Thèse de doctorat

présentée par

Ivan Valtchanov

Pour obtenir le titre de

DOCTEUR DE L'UNIVERSITÉ PARIS-SUD PARIS XI

Spécialité : Astrophysique et techniques spatiales

LES AMAS DE GALAXIES DANS LE XMM-LSS – LE SURVEY DES GRANDES STRUCTURES DE L'UNIVERS AVEC LE TÉLESCOPE XMM

Soutenue le 27 Juin 2003 devant la commission d'examen composée de :

Mme Brigitte Rocca-Volmerange	Président
M. Mark Birkinshaw	Rapporteur
M. Jean-Paul Kneib	Rapporteur
Mme Marguerite Pierre	Directeur de Thèse
Mme Danielle Alloin	Examinateur
M. Laurent Vigroux	Examinateur

CEA/DSM/DAPNIA, Service d'Astrophysique, 91191 Gif-sur-Yvette
3 juillet 2003

Remerciements

Je voudrais tout d'abord exprimer ma gratitude à Marguerite Pierre, mon directeur de thèse, pour notre agréable collaboration et pour les efforts et la patience qu'elle a investis, ainsi que les connaissances scientifiques qu'elle m'a apportées.

Mes remerciements s'adressent à Laurent Vigroux et Pierre-Olivier Lagage pour m'avoir accueilli dans le Service d'Astrophysique et rendu possible l'excellent déroulement de ma thèse. Sans votre support cela ne pouvait pas être possible !

Je dois beaucoup à mes collaborateurs au SAp, Alexandre Refregier et Sergio Dos Santos, pour les discussions scientifiques, pour l'atmosphère et l'aide journalière. J'espère que notre excellente collaboration continuera dans l'avenir.

J'ai grand plaisir à remercier spécialement Jean-Luc Starck à l'origine de mon arrivée en France et pour les discussions intéressantes et utiles sur le traitement d'images, la transformation d'ondelettes, la détection des sources et la fonction de corrélation.

Je ne peux pas manquer l'occasion de remercier Jean Ballet pour son aide dans tous les aspects de la machinerie XMM – la réduction de données XMM et les logiciels du XMM-SAS. À Doris Neumann, Monique Arnaud, Jean-Luc Sauvageot et aux autres membres du groupe X au SAp pour les réponses à mes questions et les discussions fructueuses.

Et finalement, à tout les collègues du SAp de m'avoir accueilli comme l'un des leurs et de m'avoir apporté beaucoup de joie et rendu mon séjour très agréable : merci Rafa, René, Thierry, Mark et le reste du SAp.

Résumé

Cette thèse présente les travaux sur les amas de galaxies réalisés dans le cadre d'un relevé des grandes structures de l'univers avec le télescope XMM : le *XMM Large-Scale Structure Survey* (XMM-LSS). Dans ce relevé de 64 degrés carrés, les amas de galaxies sont l'ingrédient le plus important – ce sont des sondes qui donnent des contraintes sur la cosmologie, complémentaires de celles du rayonnement cosmologique fossile (CMB) et des supernovae de type Ia (SN-Ia). En plus de leur importance cosmologique, les études multi-longueurs d'onde d'amas particuliers sont importantes sur le plan de la dynamique interne et de la croissance des structures. J'illustre ce point avec des exemples d'études d'amas de l'ére pré-XMM et Chandra. Ensuite je présente le XMM-LSS qui va étendre nos connaissances sur les grandes structures tracées par les amas à des distances de l'ordre de $z \sim 1$. Dans le cadre du XMM-LSS, j'aborde au début le problème de la détection des sources dans des images en rayons X avec XMM – ces sources (amas et quasars) seront la base de tous les suivis associés. La comparaison des procédures de détection à l'aide d'images XMM simulées nous a permis de choisir la mieux adaptée : un filtrage d'image brute avec des ondelettes en utilisant le modèle du bruit de Poisson, suivi par une détection avec `SExtractor`. Une fois la procédure de détection établie, j'ai estimé la fonction de sélection qui nous permet de prédire les contraintes cosmologiques dérivées des amas du XMM-LSS. J'ai ensuite étudié les premiers candidats amas des observations du XMM-LSS. Leur nombre d'environ 15 par $\deg^2$ est en bon accord avec les prédictions du modèle ΛCDM. A l'aide d'une procédure de visualisation des données multi-λ, les premiers candidats amas ont été programmés pour un suivi spectroscopique. Je présente les résultats d'analyse des premiers amas à $z > 0.6$ du XMM-LSS observés au VLT. Pour la première fois, grâce à la sensibilité d'XMM, nous commençons à détecter des amas de masse intermédiaire à grand redshift et dans divers états dynamiques. L'efficacité et la faisabilité du programme XMM-LSS sont ainsi démontrées d'une manière décisive.

Table des matières

Introduction

La cosmologie observationnelle est actuellement un domaine de recherche très actif et de plus en plus nous parlons de cosmologie de précision. Les derniers résultats d'observations des supernovae lointaines de type Ia (SNe-Ia) et du rayonnement cosmologique fossile (CMB) ont mis en évidence le fait que nous vivons dans un univers plat et dans une époque d'expansion accélérée. Maintenant la majorité de la communauté astronomique accepte la constante cosmologique Λ – qui est peut-être la constante la plus controversée de la physique – comme responsable de cette expansion accélérée. L'analyse des données du CMB de l'observatoire WMAP (Spergel et al. 2003) vient de mesurer les paramètres cosmologiques avec une grande précision et les conceptions convergent vers un modèle ΛCDM "standard" pour lequel les contributions à la densité totale de l'univers sont : 27% pour la matière (dont 17% de matière baryonique et 83% de matière sombre) et le reste de 73% sour forme "d'énergie du vide" représentée par le terme Λ.

Mais où se situent les amas de galaxies dans ce contexte cosmologique ? D'abord ils sont des objets massifs et rares et ils permettent de sonder la distribution de la matière dans l'univers sur de grandes échelles jusqu'à des redshifts $z \sim 1-2$. Les contraintes sur les paramètres cosmologiques que nous donnent les amas sont *indépendantes* de celles du CMB et SNe : l'information sur la cosmologie du CMB vient de l'univers très lointain $z \sim 1000$, quant aux contraintes des SNe, elles sont basées sur le fait que les supernovae de type Ia sont des chandelles standard et elle sondent pratiquement le même intervalle de redshift que les amas : $z < 2$.

C'est la raison pour laquelle nous avons proposé un survey de la structure de l'univers tracée par les amas – *XMM Large-Scale Structure Survey* (XMM-LSS) avec le meilleur instrument disponible – XMM (**X**-*ray* **M***ulti-mirror* **M***ission*[1]). Avec les programmes de suivis avancés, couvrant la majeure partie du spectre, XMM-LSS va fournir des données uniques et une vision multi-λ qui serviront à rectifier et pousser encore plus loin nos connaissances des galaxies jusqu'aux amas et la cosmologie.

Dans cette présentation je passe en revue d'abord les aspects généraux de la problématique de l'étude des amas de galaxies (Chapitre 1) et je présente le survey XMM-LSS (Chapitre 2) afin de situer mon travail. Je donne ensuite le détail de mes contributions (Chapitre 3), dont les articles sont joints à la fin. Je finis avec les conclusions et les perspectives (Chapitre 4).

[1] http ://xmm.vilspa.esa.org

1. Introduction sur les amas

Les amas de galaxies sont les entités les plus massives découplées de l'expansion générale de l'univers. Ils sont composés, par ordre d'importance de la fraction de masse, de matière noire, de gaz et de galaxies[1], dont les proportions masse baryonique/masse cachée mesurées sont comparables avec celles de l'univers dans son entier : les galaxies occupent seulement $\sim$ 5% de la masse totale des amas, le gaz est environ 15-20% et le reste est sous forme de matière sombre.

1.1 Comment se manifestent les amas ?

La Figure 1.1 nous montre l'amas Abell 1689 en optique, rayons X, en radio (millimétrique) et la distribution de la masse projetée dérivée de l'analyse de l'effet de lentille gravitationnelle ("weak lensing") à partir des données optiques. Les différentes composantes se manifestent dans différents domaines du spectre :

- *Par les galaxies en optique et infra-rouge :* Historiquement les premières mentions de sur-densités de galaxies dans les constellations *Virgo* et *Coma* viennent des observations de Herschel et Messier à la fin du XVIII siècle. Il fallut attendre le milieu du XX siècle et les études systématiques de Zwicky (1961-68) et Abell (1958) qui ont défini la notion d'"amas" et ont construit les premiers grands catalogues basés sur des sélections visuelles à partir de plaques grand champ (plaques de Schmidt). Les critères de sélection étaient plus ou moins corrects, avec des éléments subjectifs. Aujourd'hui, grâce à la digitalisation des observations astronomiques, les catalogues se font de plus en plus objectifs, avec des critères de sélection assez précis, par exemple, EDGCS : Lumsden et al. (1992) ; APM : Dalton et al. (1997) ; PDCS : Postman et al. (1996). Une bonne revue historique sur les études des amas est présenté par Biviano (2000).
- *Par le gaz en rayons X :* Avec les premières observations du ciel en rayons X à haute latitude galactique, on s'est aperçu que les amas sont parmi les sources les plus brillantes dans ce domaine du spectre (Gursky et al. 1971). L'émission X thermique observée est la preuve de l'existence d'un gaz diffus ($\sim 10^{-3}$ atomes par cm^3) dans un fort puits de potentiel qui chauffe le gaz à une température $T \sim 10^7 - 10^8$ K. A noter que l'émissivité X est proportionnelle à la densité du gaz au carré et la racine de la température : $S_X \sim n_e^2 \sqrt{T}$. Pour une revue détaillée sur les amas en X voir Rosati et al. (2002).
- *Par le gaz en radio, rayon millimétrique – l'effet Sunyev-Zel'dovich (S-Z) :* Les photons du fond diffus cosmique (CMB) interagissent avec le gaz du milieu intra-amas et gagnent

[1] Il faut aussi mentionner une quatrième composante – des particules relativistes surtout des électrons de très hautes énergies (e.g. Sarazin 1999) – mais elle est sans rapport avec mon travail.

de l'énergie par effet Compton inverse. Le résultat est une distorsion du spectre CMB (ΔT_{SZ}) maximale à $\lambda = 1.8$ mm et qui est proportionnelle à la densité du gaz et à la température : $\Delta T_{S-Z} \sim n_e T$. Par conséquent, nous pouvons étudier des variations locales de la pression ($p \sim n_e T$), ce qui n'est pas accessible avec les observations en X. En théorie ΔT_{S-Z} ne dépend pas du redshift et en combinaison avec la mesure de S_X par les observation en rayons X, cette quantité peut être utilisée pour estimer la distance angulaire et par conséquent la constante de Hubble. Pour des revues détaillées sur l'effet S-Z voir Birkinshaw (1999) et Carlstrom et al. (2002).

Il faut noter aussi qu'il existe des amas avec une émission radio diffuse et synchrotron – des sources "halo et reliques" (e.g. Giovannini et al. 1993, Ensslin et al. 1998). Les halos sont centrés sur l'émission X et s'étendent sur l'amas entier. Les reliques sont sur la périphérie de l'amas avec une polarisation de l'ordre de $\sim 20\%$ – beaucoup plus forte que pour les halos. Ces sources diffuses sont pour la plupart trouvées dans des amas chauds, lumineux en X et avec des indications des chocs dûs à des fusions. Mais il reste encore des questions sur leur origine et pourquoi il y a des amas, ayant subi une fusion récente, qui n'ont pas de halos (voir par exemple la discussion dans Liang et al. 2002).

– *Par la matière sombre :* Nous ne pouvons pas observer directement la matière sombre, mais, grâce à son effet dominant dans la dynamique des amas, il y a plusieurs méthodes qui permettent d'estimer sa contribution à la masse totale. Historiquement, la première indication de l'existence de "matière cachée" vient des études de Zwicky (1933) sur la distribution des vitesses des galaxies de l'amas dans la constellation Coma[2]. En supposant l'équilibre du viriel, on peut calculer la masse totale d'un amas à partir de la dispersion des vitesses : $M_V \sim \sigma_v^2 R_V$, où R_V est le rayon viriel et M_V est la masse du viriel.

Une autre mesure de la masse totale vient de l'émission X, en supposant un équilibre hydrostatique et une symétrie sphérique :

$$M(r) \sim kT\, r^2 \left(\frac{1}{n} \frac{dn}{dr} + \frac{1}{T} \frac{dT}{dr} \right),$$

où $M(r)$ est la masse totale dans un rayon r, $n(r)$ est le profil de la densité et $T(r)$ le profil de la température, dérivés de l'émission X (voir par exemple Article C).

La mesure directe de la distribution spatiale de la masse projetée peut être obtenue par l'intermédiaire de *l'effet de lentilles gravitationnelles*. Dans le cas de l'effet fort, le puits de potentiel de l'amas agit comme une lentille pour les sources d'arrière plan (galaxies ou quasars beaucoup plus distants que l'amas). En étudiant la distribution des images multiples d'un objet d'arrière-plan – qui dans le cas de champs gravitationnels très forts peuvent être distordues en forme d'arc – la masse projetée de la lentille dans la région centrale intérieure aux arcs ($\sim 100 - 500$ kpc) peut-être déduite avec une bonne précision. Dans le cas de l'effet faible (ou "weak shear") le passage de la lumière à travers des grandes structures sur son chemin déforme légèrement les images des galaxies d'arrière plan. En étudiant ces distorsions d'une manière statistique on peut déduire la distribution de la matière projetée, même dans les cas où il n'y a pas de forts champs gravitationnels. Les amas aussi provoquent un effet de "weak shear", qui aide à analyser la distribution de la masse sur des échelles beaucoup plus grandes que dans le cas de l'effet fort. Pour une revue détaillée sur l'effet de lentilles voir par exemple Mellier (1999).

[2]Désigné aussi comme Abell 1656 dans le catalogue d'Abell (1958).

1.2 Les amas dans le contexte cosmologique

Les propriétés globales de l'univers sont très proches d'un univers homogène et isotrope à une échelle plus grande que $\sim$ 100 Mpc. Or, l'existence des amas et des grandes structures (super-amas, grandes murailles) procure des informations importantes sur les conditions initiales et les processus de formation de ces structures.

Selon la théorie de formation hiérarchique des structures dans le modèle de matière sombre et froide (CDM, Blumenthal et al. 1984), les perturbations dans le champ de densité primordial $\delta\rho = \Delta\rho/\bar{\rho}$ donnent naissance à une hiérarchie de structures à toutes les échelles en masse, avec les petites fluctuations qui s'effondrent les premières. Le plus souvent ces fluctuations sont supposées adiabatiques et le cas le plus simple fluctuations de $\delta\rho$ est un champ gaussien, qui peut être spécifié par le spectre de puissance $P(k)$. Dans le cas de fluctuations adiabatiques sans échelles privilégiées, $P(k) \sim k^n$ et $n = 1$ – le spectre de Harrison-Zel'dovich. A cause de la présence de matière (baryonique ou non-baryonique), $P(k)$ n'est plus une simple loi de puissance parce qu'il y a des processus physiques qui introduisent des échelles caractéristiques – par exemple l'instabilité de Jeans et des amortissements des fluctuations à petites échelles. Deux paramètres décrivent ce spectre transformé : l'amplitude σ_8 qui est l'écart-type des fluctuations linéaires de la masse dans des sphères de $8h^{-1}$ Mpc aujourd'hui (à $z = 0$) et le paramètre Γ qui caractérise l'échelle où le spectre change de pente (e.g. Peacock & Dodds 1994).

Les déviations positives les plus importantes de $\delta\rho$ à grande échelle sont les germes des amas. Ils s'effondrent tard et même aujourd'hui ils sont encore dans un régime de formation par accrétion de perturbations plus petites déjà virialisées. Comme les amas sont des objets rares, leur statistique (par exemple le comptage ou la fonction de luminosité) peut contraindre fortement la normalisation du spectre des fluctuations.

1.3 Paramètres et observables

Je vais définir, sans entrer dans les détails, quelques paramètres et observables liés à l'analyse des amas. Les définitions exhaustives peuvent être trouvés dans les livres classiques sur la cosmologie, par exemple Weinberg (1972), Peebles (1993), Peacock (1999).

Paramètres cosmologiques

- <u>*La constante de Hubble*</u> $H(z)$ et sa valeur aujourd'hui $H(0) \equiv H_0$. Souvent les paramètres qui dépendent de H (distances, luminosités, masses) sont exprimées en unités $h = H_0/100$. L'inverse de la constante de Hubble : $t_H = 1/H_0$ est *le temps de Hubble* qui est un temps caractéristique et approximatif de l'âge de l'univers.
- <u>*Paramètres de densité :*</u>
  - matière non-relativiste (baryonique et non-baryonique) et relativiste (radiation) : $\Omega_{m0} = \Omega_{m0}^{NR} + \Omega_{r0} = 8\pi G\left(\rho_{m0} + \rho_{r0}\right)/3H_0^2$, où ρ_{m0} est la densité de la matière non-relativiste et ρ_{r0} est la contribution de la radiation, qui aujourd'hui n'est pas significative.
  - la contribution de la courbure : $\Omega_{k0} = -k/a_0^2H_0^2$, où a_0 est le facteur d'échelle aujourd'hui et k est la courbure.
  - l'énergie du vide : $\Omega_{\Lambda 0} = \Lambda/3H_0^2$, où Λ est la constante cosmologique.

  Il faut noter les dépendances de ces trois paramètres avec le redshift :

$$\Omega_m(z) \quad = \quad A^2\left[\Omega_{r0}\,(1+z)^4 + \Omega_{m0}\,(1+z)^3\right]$$

$$\Omega_\Lambda(z) = A^2\Omega_{\Lambda 0}$$
$$\Omega_k(z) = A^2\,(1+z)^2\,\Omega_{k0},$$

où $A = H_0/H(z)$. Les trois paramètres de densité sont liés par l'équation de Friedman : $\Omega_m + \Omega_k + \Omega_\Lambda = 1$. Par conséquent si $\Omega_m + \Omega_\Lambda = 1$ alors l'univers est plat ($k = 0$), ouvert si $\Omega_m + \Omega_\Lambda < 1$ ($k = -1$) et fermé si $\Omega_m + \Omega_\Lambda > 1$ ($k = 1$). Si nous connaissons $\Omega_m + \Omega_\Lambda$ nous pouvons prédire l'avenir de l'univers !

– *la normalisation du spectre de puissance* σ_8 (voir la section précédente) : l'analyse de WMAP donne $\sigma_8 = 0.84 \pm 0.04$ qui est en bon accord avec les résultats de comptage d'amas massifs à grand redshift (e.g. Bahcall & Bode 2003).
– *Le modèle cosmologique :* Les derniers résultats de WMAP combinés avec d'autres mesures des paramètres cosmologiques (Spergel et al. 2003) ont montré que $H_0 = 71^{+4}_{-3}$ km s $^{-1}$ Mpc^{-1}, $\Omega_{m0} = 0.27 \pm 0.04$ et $\Omega_{tot} = 1.02 \pm 0.02$. Par conséquent, $\Omega_{\Lambda 0} = 0.73$.

Le modèle cosmologique que j'adopte pour la suite est le modèle ΛCDM d'un Univers plat dominé par l'énergie du vide avec les paramètres suivants :

$$\boxed{\Omega_{m0} = 0.3,\ \Omega_{\Lambda 0} = 0.7 \text{ et } H_0 = 70 \text{ km s}^{-1} \text{ Mpc}^{-1}.}$$

– *Des temps caractéristiques :* Les échelles de temps des différents processus physiques sont des paramètres très importants parce qu'ils nous donnent une estimation de l'état dans lequel se trouvent les différentes composantes des amas et par conséquent leur interaction et l'influence sur l'évolution de l'amas.
  – le temps dynamique : $t_{dyn} \sim 1/\sqrt{G\rho}$, où ρ est la densité moyenne de l'amas qui est ≈ 200 fois la densité moyenne de l'univers.
  – le temps d'équilibre thermique du gaz : $t_{eq}(e,e) \sim T^{3/2}/n_e$ pour les électrons.
  – le temps de refroidissement : $t_{cool} \sim \sqrt{T}/n_e$

  Dans le cas des amas, on a en général $T \sim 10^7 - 10^8 K$ et $n_e \sim 10^{-3} - 10^{-2}$ cm^{-3}. Par conséquent $t_{dyn} \approx 10^9$ ans et $t_{eq} \approx 10^8$ ans au maximum pour les ions les plus massifs. Ce sont des temps largement inférieurs au temps de Hubble t_H, ce qui veut dire que le gaz dans les amas est aujourd'hui en équilibre thermique. Quant au temps de refroidissement du gaz t_{cool}, il est en général plus grand que t_{eq} et même t_H, donc le processus de refroidissement radiatif n'est pas important, sauf dans les parties centrales des amas où la densité est élevée – ce sont des amas à *"cooling flow"*.

  Contrairement au gaz, la relaxation des galaxies est un phénomène beaucoup plus compliqué. Tout d'abord, pendant la phase de formation, l'amas subi une relaxation violente où le potentiel gravitationnel varie rapidement dû aux fusions des sous-structures. Ce temps est comparable au t_H. Mais la relaxation continue ensuite avec des interactions en deux corps des galaxies d'un temps caractéristique $t_{\rm relax} = \frac{N}{\ln N}\, t_{dyn}$, où $N = 100 - 1000$ est le nombre de galaxies dans l'amas. Ce temps peut être plusieurs fois le temps de Hubble.

Observables

Ce n'est pas une liste complète de toutes les observables d'amas. J'introduis uniquement les paramètres que j'ai utilisés dans mes études.

– *Décalage spectral vers le rouge* ou *"redshift"* (z) et *la dispersion des vitesses* (σ_v) à partir des mesures des décalages spectraux des galaxies individuelles de l'amas. Par définition $1 + z = \lambda_o/\lambda_e$, où λ_o est la longueur d'onde d'une raie observée (en émission ou en absorption) et λ_e est la longueur d'onde mesurée en laboratoire.

- *La richesse* : c'est le nombre de galaxies, corrigé du fond, dans un intervalle de magnitudes $[m_3, m_3 + 2]$, où m_3 est la magnitude de la troisième galaxie la plus brillante et dans un rayon de $1.5h^{-1}$ Mpc – le rayon d'Abell.
- *Le flux* (S_X) et *la luminosité* (L_X) dans la bande X. Parce que la mesure directe des observations dans la bande X est le nombre de photons émis par seconde dans une bande d'énergie, pour obtenir S_X et L_X il faut supposer un modèle de spectre. En général c'est un spectre thermique paramétré par le redshift z, la température T, la métallicité (Z), l'absorption de notre galaxie par l'hydrogène neutre N_h et normalisé par le nombre de photons observés (Raymond & Smith 1977). S'il y a assez de photons dans le spectre X, une estimation des paramètres du modèle peut être faite en l'ajustant avec les observations. N_H est souvent fixé à la valeur galactique et $Z \sim 0.3Z_\odot$ si on n'a pas assez de photons. Normalement le redshift est connu par des observations en optique et ce sont T, Z et N_h qui restent comme des paramètres libres et peuvent être estimés par les observations.
- *Liens entre les observables, lois d'échelles* : la théorie de formation hiérarchique, auto-similaire (e.g. Kaiser 1986) prédit des relations entre les paramètres globaux des amas : $M \sim T^{3/2}$ et $L_X \sim T^2$. Or, les observations montrent que $M \sim T^2$ (Mohr et al. 1999, Finoguenov et al. 2001) et $L_X \sim T^3$ (e.g. Arnaud & Evrard 1999, Xue & Wu 2000). Malgré des effets systématiques, liés aux mesures et aux hypothèses faites dans la dérivation de la masse totale, de la température et de la luminosité, ces différences sont statistiquement significatives et il faut donc ajouter des effets non-gravitationnels – préchauffage et "feedback" de supernovae qui augmentent l'énergie du gaz et changent les pentes des relations. Logiquement ces effets sont beaucoup plus importants dans les amas de petite masse (faible gravité).
- *Le "clustering" d'amas :* La fonction de corrélation à deux points $\xi(r)$ est la mesure statistique du "clustering" la plus simple : c'est le rapport entre la distribution des séparations des objets deux à deux et la distribution des séparations d'objets aléatoirement placés dans le même champ, i.e. c'est l'excès de "clustering" sur un champ Poissonnien. Sur le plan théorique, la $\xi(r)$ est la transformation de Fourier du spectre de puissance $P(k)$ pour un champ Gaussien de fluctuations de la densité. Sur le plan observationnel, $\xi(r)$ est très bien connue pour les amas proches (décalage spectral $z < 0.2$) et est décrite par une loi de puissance : $\xi(r) = (r/r_0)^{-\gamma}$ avec l'échelle de la corrélation $r_0 = 15 - 20h^{-1}$ Mpc et le facteur de puissance $\gamma = 1.8 - 2.0$ (e.g. Collins et al. 2000). Il est important de noter que la fonction de corrélation des galaxies a la même forme – loi de puissance avec le même γ mais avec une échelle caractéristique de l'ordre de $\sim 5h^{-1}$ Mpc (e.g. Norberg et al. 2001). Ceci est un argument en faveur de la théorie de formation hiérarchique auto-similaire.

1.4 Ere pré-XMM : étude multi-longueur d'onde d'amas observés avec ROSAT et des télescopes de la classe des 4 mètres.

Pour illustrer l'analyse des amas en multi-longueur d'onde je présente deux études auxquelles j'ai participé,

Abell 1451 et 1RXS J131423.6-251521 (Article C)

Le but de cette étude : présenter les observations, la réduction des données et analyser l'état dynamique des deux amas.

Les observations : les données multi-longueurs d'onde consistent en des observations en rayons X avec ROSAT-HRI ; en optique, des observations spectroscopiques MOS (fentes multi-objets) avec le télescope de 3.6m de l'ESO (European Southern Observatory) ; en radio avec ATCA (Australia Telescope Compact Array) à 1384 et 2496 MHz (20 cm et 13 cm).

Ma contribution :

- Analyse des données ROSAT-HRI et calcul des paramètres liés à l'émission X : le flux, la luminosité et le profil de brillance de surface modélisé par un β-modèle, qui est ensuite utilisé pour dériver la masse du gaz, la masse totale et la fraction du gaz.
- Réduction et analyse des données spectroscopiques : mesures des décalages spectraux des galaxies observées et détermination des redshifts et des dispersions de vitesse des deux amas.
- Analyse globale des résultats des observations multi-λ.

Résultats :

Abell 1451 : le redshift $z = 0.1989^{+0.0005}_{-0.0007}$ et la dispersion de vitesse $\sigma_v = 1330^{+130}_{-90}$ km s^{-1} sont calculés à partir de 57 galaxies. La distribution des vitesses des galaxies est Gaussienne sans indication de sous-structure. La morphologie de l'émission X est aussi régulière avec des petites distorsions dans la partie centrale. Le temps de refroidissement, même dans la partie centrale où la densité et la température sont élevées, dépasse largement le temps de Hubble – c'est-à-dire il n'y a pas de courant de refroidissement. Les relations $L_X - T$ et $\sigma_v - T$ (la température est mesuré avec ASCA, Matsumoto et al. 2001) diffèrent considérablement des relations observées (Xue et al. 2000) ce qui montre que l'amas est dans un état dynamique perturbé et a vraisemblablement subi un choc lors d'une fusion.

RXJ1314 : le redshift moyen $z = 0.2474^{+0.0006}_{-0.0008}$ et $\sigma_v = 1100^{+140}_{-90}$ km s^{-1} sont calculés à partir de 37 galaxies. La distribution des vitesses, la distribution spatiale des galaxies dans le champ et la morphologie de l'émission X sont bi-modales ; le groupe Est à $z_E = 0.2429^{+0.0003}_{-0.0008}$, $\sigma_v = 590^{+110}_{-150}$ km s^{-1} avec 15 membres et le group Ouest à $z_W = 0.2500^{+0.0006}_{-0.0005}$, $\sigma_v = 560^{+120}_{-70}$ km s^{-1} avec 22 membres. Les deux groupes ont des galaxies géantes (cD) en leur centre mais les pics de l'émission X sont décalés par rapport aux centres optiques. Notre interprétation est que RXJ1314 est dans une phase après fusion où l'activité radio et les chocs qui ont augmenté l'énergie du milieu intra-amas ont déjà été dissipés, ce qui explique le bon accord des relations $L_X - T$ et $\sigma_v - T$ avec les relations empiriques (Xue et al. 2000).

Etude de l'amas Abell 2104

J'ai travaillé aussi sur une autre étude multi-λ d'un amas Abell 2104 (Liang et al. 2000). Ma contribution fut sur l'analyse des données photométriques.

Perspectives :

Aujourd'hui avec les deux observatoires XMM et Chandra, nous pouvons pousser beaucoup plus loin les études des amas individuels. Grâce à la meilleure sensibilité, l'information

spectrale jusqu'à 12 keV et la meilleure résolution spatiale (Chandra), les amas commencent à révéler des détails précis sur la physique du milieu intra-amas (ICM), la structure spatiale de la température et de l'abondance des éléments. Ceci procure des contraintes sur la théorie de formation et l'évolution des structures et l'importance des effets non-gravitationnels qui injectent de l'énergie dans le milieu intra-amas.

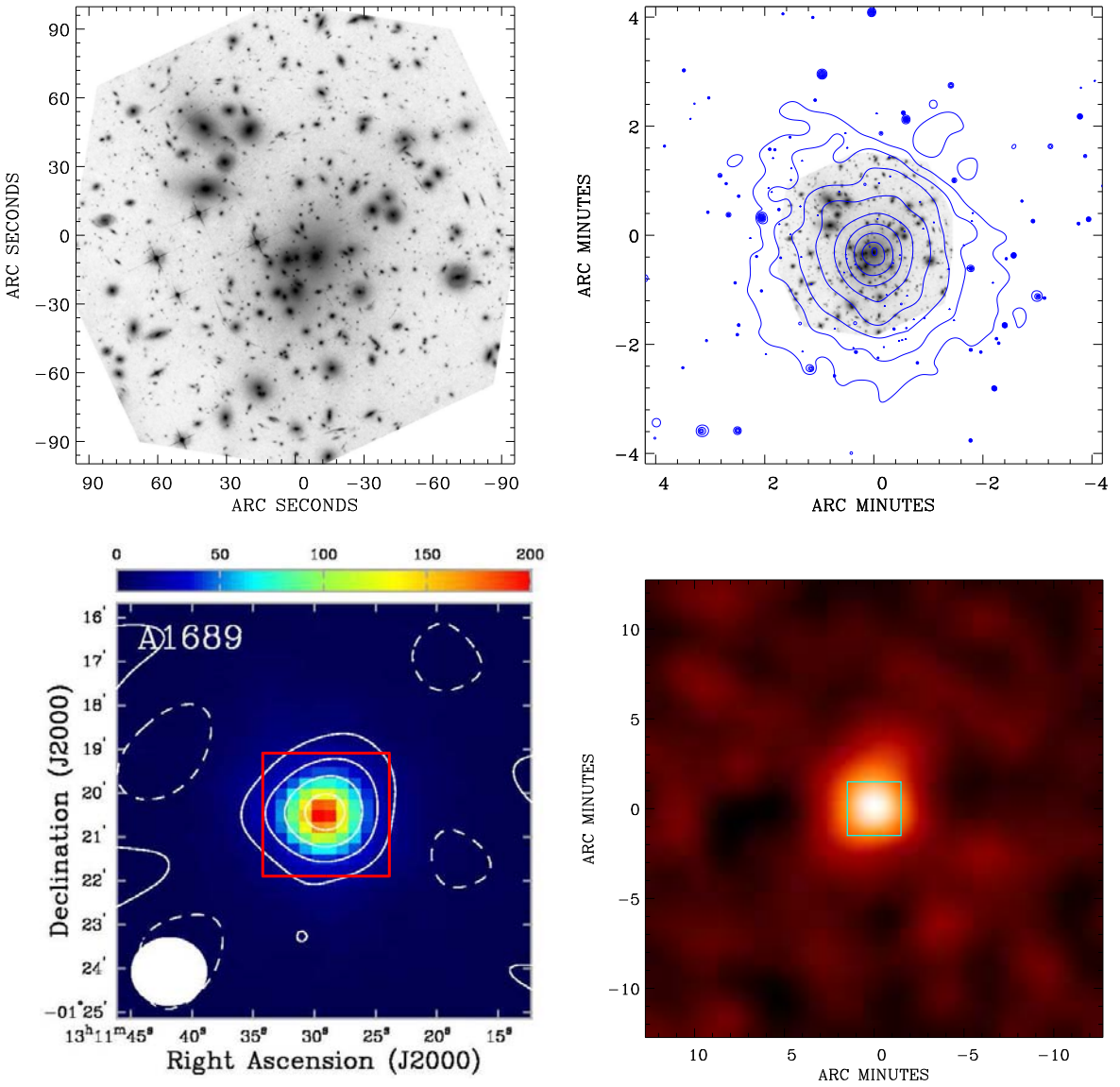

FIG. 1.1 – Exemple d'un amas (Abell 1689 à $z = 0.181$) montrant les trois constituants principaux. En haut à gauche : l'image en optique, faite avec la nouvelle caméra ACS du télescope Hubble (HST) qui montre la distribution des galaxies et l'effet de "strong lensing". En haut à droite : l'émission du gaz chaud en rayons X (montrée avec des contours) vue par le télescope Chandra superposée sur la même partie centrale de l'image à gauche. L'émission X est très piquée au centre (l'effet du courant de refroidissement). En bas, à gauche : les observations de l'effet S-Z (Reese et al. 2002). Le carré rouge indique l'échelle de l'image optique du HST. En bas, à droite : la reconstruction de la masse avec l'analyse de "weak-lensing" à partir des données ESO/MPG 2.2m en bande R (Clowe & Schneider 2001). Le carré bleu indique l'échelle de l'image optique du HST.

2. Présentation du survey XMM-LSS

La description détaillée du Survey XMM-LSS peut être trouvée dans Article A. Je résume seulement les points importants.

2.1 Pourquoi dans le domaine X ?

Dès les premières observations en rayons X, les chercheurs ont été intéressés par les amas, mais les vraies études d'échantillons complets ont commencé avec les deux observatoires *EINSTEIN* et *ROSAT*. Ces observations ont donné deux grands Surveys : *Einstein Medium Sensitivity Survey* (EMSS, Gioia et al. 1990) et *ROSAT All Sky Survey* (RASS, Voges et al. 1999). Plusieurs catalogues d'amas ont été construit à partir de ces données.

Le domaine X a plusieurs avantages sur les observations en optique pour la détection des amas :

- L'émission X étendue avec des caractéristiques spectrales d'une source thermique est une vraie signature d'un puits de potentiel, contrairement aux observations de galaxies où les sur-densités ne sont pas toujours des vraies structures liées par la gravitation. Par exemple, $\sim 10\%$ des amas du catalogue d'Abell et al. (1989) sont en fait de faux amas (Katgert et al. 1996).
- les amas de galaxies sont des sources X brillantes avec des luminosités $L_X \sim 10^{42} - 10^{46}$ erg s^{-1}. En outre, la luminosité X est bien corrélée avec la masse (Reiprich & Böhringer 2002), contrairement à la corrélation masse-richesse en optique.
- le ciel en X, à haute latitude galactique, est peuplé par deux types d'objets : amas, qui sont des sources étendues et quasars - sources non résolues. La confusion est négligeable pour une sensibilité "moyenne" ($S_X = 2 \times 10^{-15}$ erg cm^{-2} s^{-1} dans une bande d'énergie [0.5-2] keV). Par exemple, une observation de 10 ks avec XMM donne ~ 300 sources par deg^2 et pour comparaison, une image en optique dans la bande I avec la caméra CFH12k du télescope CFHT donne > 150000 sources par deg^2 pour un temps de pose comparable.

2.2 Pourquoi XMM ?

L'observatoire XMM n'a pas été conçu pour faire des très grands relevés. Mais l'idée de sonder une grande région continue avec XMM pour étudier la structure de l'univers avec les amas est pertinente car la grande sensibilité (quatre fois plus grande que Chandra à une énergie de 1 keV), un champ de $30'$ diamètre et la PSF de $6''$ FWHM sur l'axe, font de lui un instrument idéal.

2.3 Caractéristiques du Survey XMM-LSS

Une région de $8° \times 8°$ a été choisie à haute latitude galactique sans sources X brillantes, dans une zone de faible absorption d'hydrogène neutre (HI) de notre galaxie et, pour optimiser les suivis, près de l'équateur pour qu'il soit observable par les observatoires des hémisphères nord et sud.

La taille de la surface a été déterminée pour atteindre au moins la même précision sur la fonction de corrélation dans deux intervalles de redshift, $0 < z < 0.5$ et $0.5 < z < 1$, que REFLEX (Böhringer et al. 2001) – le plus grand catalogue complet d'amas en rayons X avec 450 amas dans $0 < z < 0.2$. Avec les simulations du "Hubble volume lightcone" (Evrard et al. 2002), nous avons estimé que la surface optimale entre la statistique nécessaire d'amas et la demande de temps d'observations et de l'ordre de 8×8 deg^2.

Cette surface sera pavée avec des observations XMM de 10 ks séparées par 20′ (9 pointés par deg^2). La sensibilité estimée avec des simulations d'images XMM est $\sim 3 \times 10^{-15}$ erg cm^{-2} s^{-1} pour des sources ponctuelles et $\sim 8 \times 10^{-15}$ erg cm^{-2} pour des sources étendues dans la bande d'énergie [0.5-2] keV. En comparaison avec les autres surveys d'une surface continue, XMM-LSS est 1000 fois plus profond que REFLEX et 10 fois plus que NEP (Henry et al. 2001) – la région la plus profonde de RASS (ROSAT All Sky Survey).

Le XMM-LSS est très bien placé par rapport aux autres relevés en rayons X comme nous le montre la Figure 2.1.

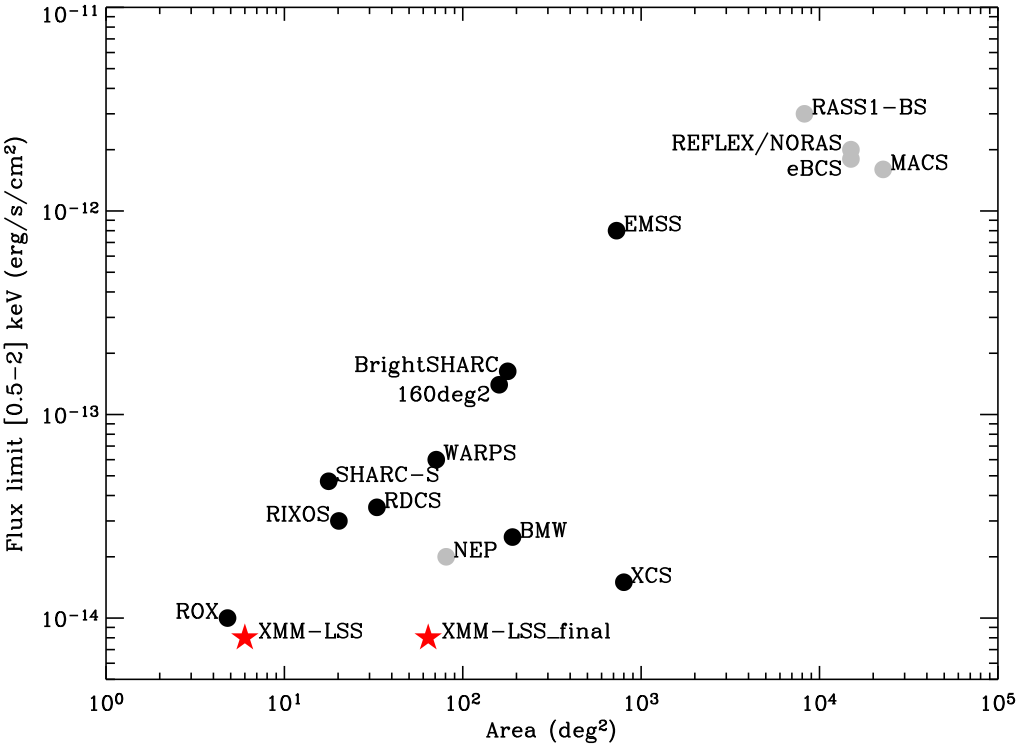

FIG. 2.1 – Revue des relevés des amas en X en fonction de la surface et le flux limite. Les relevés sur une région continue sont figurés par des cercles gris, les cercles noirs représentent des relevés "serendipitous" ; les deux étoiles indiquent la position actuelle du XMM-LSS (fin May 2003) et le but final. Pour les références voir Article A.

2.4 Objectifs scientifiques

En résumé, les buts scientifiques du XMM-LSS :

- Mesurer avec une bonne précision la fonction de corrélation des amas $\xi_{cc}(r)$ dans deux intervalles en décalage spectral entre $0 < z < 1$.
- Mesurer la fonction de corrélation des QSOs jusqu'à $z \sim 4$.
- Études multi-longueur d'onde des amas, des AGNs et des QSOs. Évolution de leurs propriétés en fonction de l'environnement et du temps. Comment sont-ils situés dans la toile cosmique définie par les amas ? Ceci procurera des informations importantes sur le mode de formation des noyaux actifs en fonction de l'environnement.
- L'existence et les propriétés des amas massifs à $z > 1$.
- Comparaison de la distribution de la matière chaude (le gaz en rayons X), lumineuse (galaxies en optique) et sombre (lentilles gravitationnelles) dans la région de XMM-LSS.

2.5 Suivis multi-longueur d'onde

Dans un survey d'une telle ampleur, la vision multi-λ est très importante, car la plupart des objectifs scientifiques reposent sur la connaissance des composantes qui se manifestent dans différents domaines du spectre. Le tableau 2.1 montre tous les suivis et peut se résumer par :

- des relevés associés de 10-20 deg^2 : études de la formation d'étoiles, des galaxies, des AGNs en fonction de l'environnement avec des observations X (le gaz chaud), infrarouge proche et lointain (galaxies lumineuses et obscures), radio (fusion, phénomènes violents).
- des relevés associés de $\sim$ 70 deg^2 : cartographie complète de la région en X (XMM : puits de potentiel), optique (CFTLS/Megacam : identification des sources X, weak lensing), radio et millimétrique (Amiba : l'effet Sunayev-Zel'dovich) pour étudier les propriétés statistiques de la population d'amas à grand z dans une région continue. Cet unique échantillon d'amas X vu en multi-λ nous permettra pour la première fois, non seulement de contraindre la cosmologie, mais aussi d'étudier les mécanismes de biais et les phénomènes non-linéaires de la physique des amas en fonction de l'échelle et de l'environnement.

TAB. 2.1 – Le XMM-LSS et les relevés associés.

Observatoire/Instrument	Coverture (planifi ée) [deg^2]	Bande/Filtre	Sensibilité fi nale
XMM/EPIC	64	[0.2-10] keV	$\sim 3\ 10^{-15}$erg cm^2 s^{-1} (1)
CFHT/CFH12K (VVDS Deep) *	2 GT	B, V, R, I	26.5, 26.0, 26.0, 25.4 (2)
CFHT/CFH12K (VVDS Wide) *	3 GO	V, R, I	25.4, 25.4, 24.8 (2)
CFHT/MegaCam	72	u*, g', r', i', z'	25.5, 26.8,26.0, 25.3, 24.3 (3)
CTIO 4m/Mosaic	~ 16	R, z'	25, 23.5 (4)
UKIRT/WFCAM	8.75	J, H, K	22.5, 22.0, 21.0 (5)
VLA/A-array *	110	74 MHz	275 mJy/beam (6a)
VLA/A-array	5.6	325 MHz	4 mJy/beam (6b)
OCRA	tous les amas du XMM-LSS	30 GHz	100 μJy (7)
AMiBA	70	95 GHz	3.0 mJy (8)
SIRTF/IRAC (SWIRE Legacy)	8.7	3.6, 4.5, 5.8, 8.0 μm	7.3, 9.7,27.5, 32.5 μJy (9a)
SIRTF/MIPS (SWIRE Legacy)	8.9	24, 70, 160 μm	0.45, 6.3, 60 mJy (9b)
Galex	~ 20	1305-3000 Å	~ 25.5 (10)

Notes :

(*) : complet

(1) : sources ponctuelles dans [0.5-2] keV

(2) : AB$_{Mag}$, ouverture de 5″

(3) : S/N = 5 dans ouverture de 1.15″

(4) : 4σ dans ouverture de 3″

(5) : Vega$_{Mag}$

(6a) : résolution de 30″ ; des observations profondes programmées

(6b) : résolution de 6.3″

(7) 5σ, limite de détection

(8) 6σ, limite de détection

(9a) 5σ

(9b) 5σ

(10) : AB$_{Mag}$

3. Ma contribution pour le survey XMM-LSS

Dans ce qui suit, je résume ma contribution qui est indiquée dans l'organigramme du XMM-LSS – Figure 3.1. Les détails peuvent être trouvés dans les articles correspondants, regroupés à la fin, dans les annexes.

3.1 Procédures de détection des objets observés en rayons X avec XMM (Article E)

L'objectif

Comparer les procédures de détection des sources dans des images XMM et choisir la meilleure en termes de performance, de détection et de classification des sources étendues et ponctuelles.

Le problème

La détection des sources en rayons X n'est pas triviale à cause des propriétés intrinsèques des télescopes X et des effets instrumentaux :

- *régime de bruit de Poisson :* dans les observations X on compte les photons un par un, en enregistrant leur temps d'arrivée, l'énergie et la position. Le nombre moyen des photons dans une image de 10 ks dans la bande d'énergie [0.5-2] keV est de l'ordre de $\sim$ 40000, ce qui correspond à moins de 0.1 photon par pixel, pour une taille de pixel de 2.5″. La fraction des photons dûs aux sources est ~25%, la reste étant des photons du fond cosmique X et des particules énergétiques.
- *la PSF :* la forme et la taille de la fonction d'étalement des points varient avec la position et l'énergie comme nous montre Figure 3.2. A $\sim 13 - 15'$ du centre du champ la PSF peut être très distordue en forme de cacahouète.
- *le vignetage :* la perte de sensibilité en fonction de la distance au centre et l'énergie des photons entrants. À 10′ du centre $\sim$ 50% des photons sont perdus comme nous le montre la Figure 3.3.
- *la géométrie des détecteurs :* mosaïque de plusieurs CCDs avec des trous entre-CCD qui introduisent des textures, surtout si les trois détecteurs sont additionnés pour augmen-

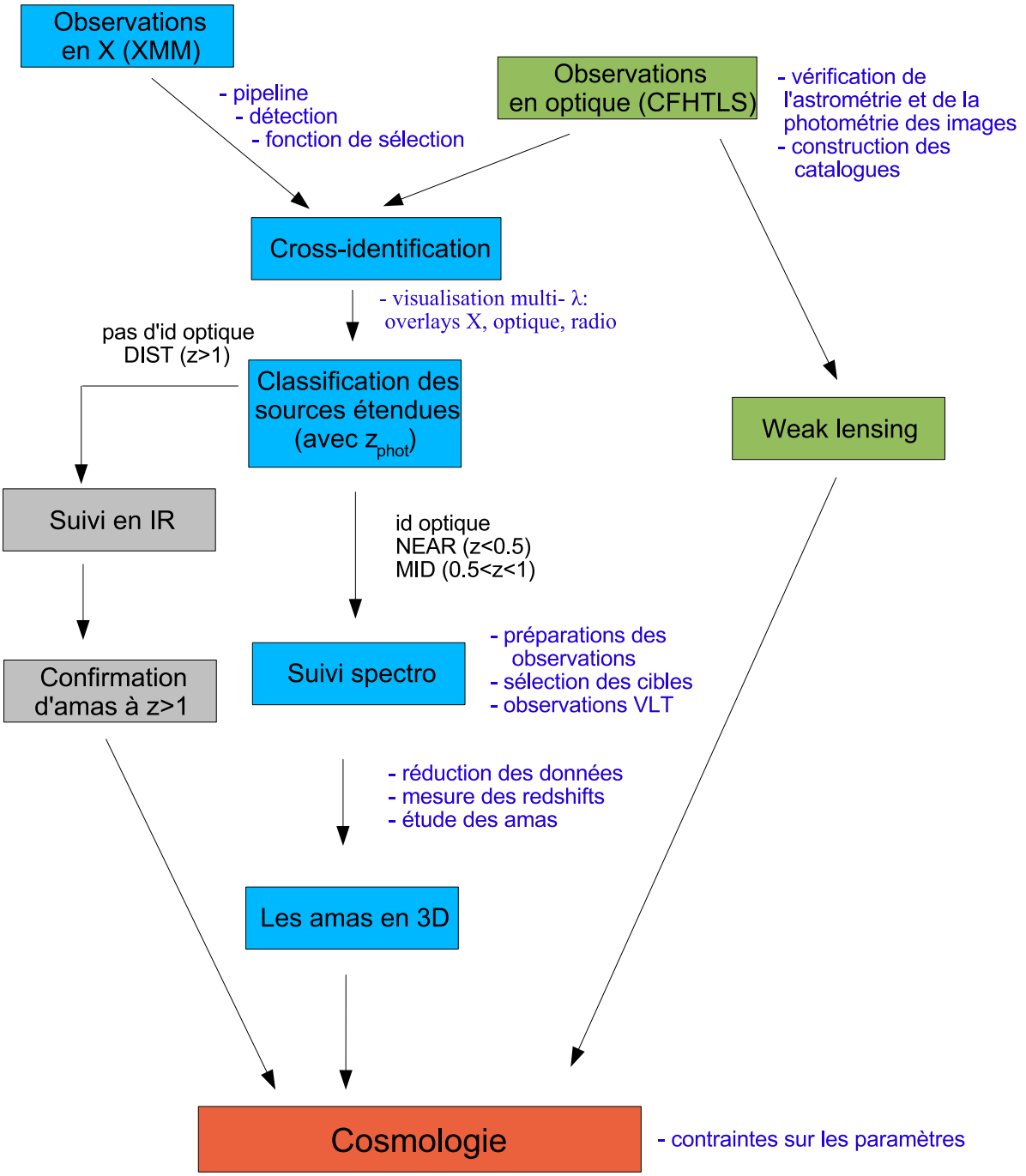

FIG. 3.1 – Organigramme du Survey XMM-LSS : des observations brutes jusqu'aux contraintes sur la cosmologie. Les tâches auxquelles j'ai contribué sont indiquées en bleu à droite de chaque étape.

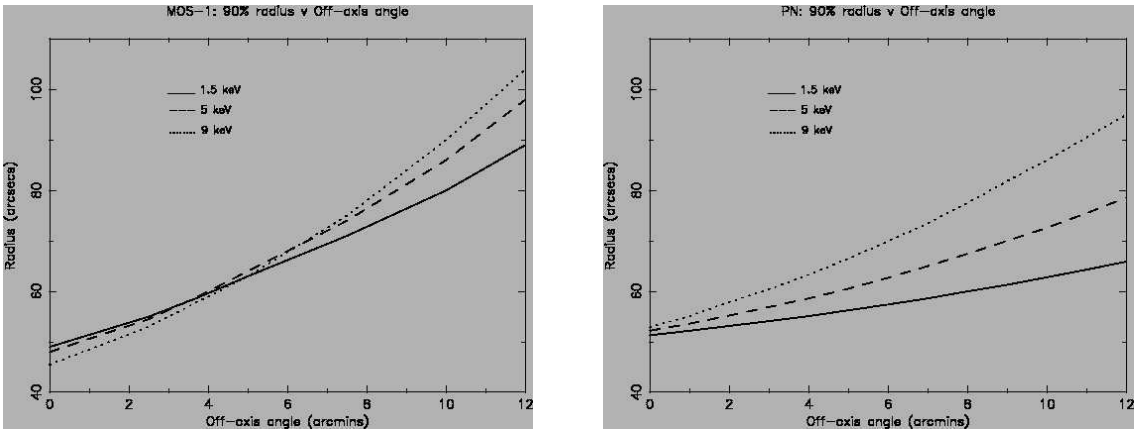

FIG. 3.2 – Le rayon (en arcsec) qui entoure 90% de l'énergie de la PSF en fonction de l'angle de l'axe et de l'énergie des photons pour deux détecteurs d'XMM : MOS (à gauche) et PN (à droite).

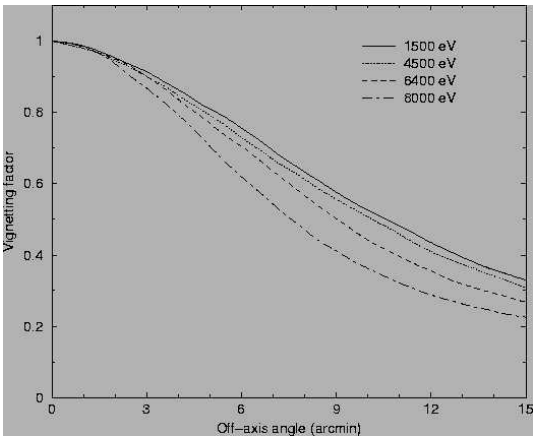

FIG. 3.3 – La fonction de vignetage d'XMM en fonction de l'angle de l'axe et de l'énergie.

ter la sensibilité. La plupart des fausses détections sont des résultats de la géométrie en supposant que nous avons réglé correctement les problèmes du bruit de Poisson.

Simulations d'images XMM

J'ai développé une procédure de simulation d'images XMM qui inclut la plupart des effets d'observations avec XMM : bruit de Poisson, la PSF, le vignetage, la géométrie des trois détecteurs d'XMM. Il y a aussi différents paramètres d'entrée, comme le temps de pose, les niveaux des fonds de particules et diffus (dû au fond diffus cosmique ou à des sources non-détectées), la taille du pixel et le rayon du champ. Les catalogues des sources étendues et ponctuelles sont aussi donnés en entrée : ce sont des tableaux `FITS` créés par l'utilisateur qui permettent une grande liberté parce que la procédure de simulation utilise la position, le nombre de photons par seconde et les paramètres du modèle-β (le rayon de coeur r_c et l'index β) pour les sources étendues. En toute rigueur, il aurait fallu faire une convolution avec la PSF car les ailes sont plus étendues que la fonction β à très grande distance.

Les sources ponctuelles sont modélisées par la PSF et les flux distribués selon la relation $\log N - \log S$ (Moretti et al. 2003) qui donne $N(> S)$ – le nombre d'objets avec un flux supérieur

à S. Une simulation d'un champ extragalactique vu par XMM est montrée Figure 3.4.

L'utilisation des images simulées d'XMM est indispensable non seulement dans une comparaison des différentes procédures de détection et dans l'ajustement du "pipeline" mais aussi pour des tâches scientifiques, comme l'estimation de la fonction de sélection, la complétude, les effets de confusion d'un survey. Cette procédure de simulation d'images est en développement continu – elle est régulièrement améliorée au fur et à mesure que notre connaissance de l'instrument et des détecteurs progresse. C'est important, parce qu'elle va nous servir tout au long du XMM-LSS.

Les outils de détection

Il y a plusieurs méthodes développées spécifiquement pour la détection des sources dans des images X :

- la méthode classique, `celldetect` (e.g. Gioia et al. 1990) implantée dans le XMM *Science and Analysis System* (XMM-SAS) : d'abord on détecte les sources dans une boite qu'on déplace sur l'image avec un niveau de signal sur bruit (S/B) assez grand, en prenant le niveau du bruit dans une région voisine. Ensuite on enlève les sources déjà détectées et on construit une carte du fond plus précise, afin de relancer `celldetect` pour la deuxième fois en utilisant cette carte pour détecter des sources beaucoup plus faibles.
- la méthode standard du XMM-SAS, `emldetect` : en utilisant les détections de `celldetect` on ajuste la PSF d'XMM (données de calibration) sur toutes les sources avec une fonction de vraisemblance. C'est un ajustement dans un espace multi-dimensionnel qui optimise *a priori* tous les paramètres des objets : la position, l'extension, l'estimation du flux et qui nous donne la vraisemblance que la source soit réelle.
- la méthode utilisant des ondelettes : bien adaptée aux images dans lesquelles il y a des sources de tailles caractéristiques différentes et un fond spatialement homogène. Il y a deux procédures publiques qui servent à la communauté astrophysique : `wavdetect` dans le traitement et analyse des données Chandra (CIAO) et `ewavelet` dans l'analyse standard d'XMM (XMM-SAS).
- la méthode hybride : filtrage des images brutes avec des ondelettes en utilisant le modèle du bruit de Poisson (Starck & Pierre 1998), suivi d'une détection et caractérisation avec `Sextractor` (Bertin & Arnouts 1996).

La meilleure méthode

La possibilité de pouvoir créer des images simulées d'XMM avec des configurations d'entrée simples (par exemple seulement avec un type de sources) jusqu'aux situations réelles nous a permis de tester le comportement des procédures de détection dans des situations difficiles et finalement de choisir la meilleure.

La conclusion est que la méthode hybride donne les meilleurs résultats en termes de performance, de détection et de caractérisation des sources étendues. Pour les sources ponctuelles les résultats d'`emldetect` ont un léger avantage (voir les tableaux comparatifs dans l'article E).

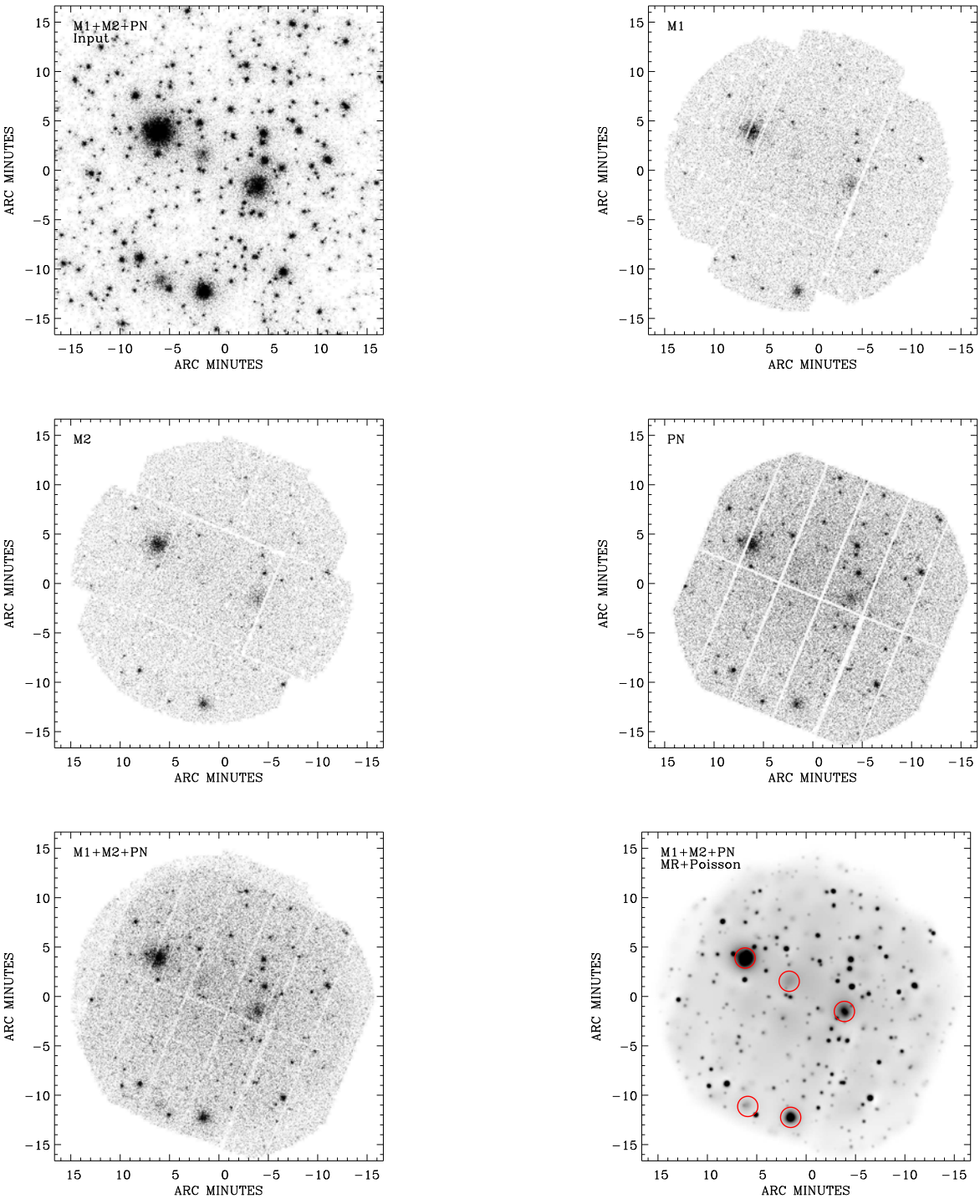

FIG. 3.4 – Image simulée d'XMM dans la bande d'énergie [0.5-2] keV, pour un temps de pose de 20 ks. La configuration d'entrée, sans bruit et pour un temps de pose long (100 ks), est montrée en haut à gauche, suivie des images dans chacun des instruments MOS1, MOS2 et PN plus l'image additionnée et filtrée avec des ondelettes en supposant un bruit de Poisson (Starck & Pierre 1998) comme indiqué dans les panneaux. Le niveau de confiance sur les coefficients d'ondelettes est 10^{-4} ($\sim 4\sigma$). Les positions des cinq sources étendues sont indiquées par des cercles dans l'image filtrée.

3.2 Contraintes cosmologiques du Survey XMM-LSS (Article D)

L'objectif

Calculer les contraintes quantitatives sur les paramètres cosmologiques à partir des amas de galaxies dans le XMM-LSS. Etablir la méthodologie pour le calcul et estimer la fonction de sélection du survey.

Pour atteindre ce but nous avons exploré deux approches : le comptage d'amas (ou l'évolution d'abondance) en fonction du redshift, $n(z)$, et la fonction de corrélation $\xi_{cc}(r)$. Les deux fonctions donnent des contraintes differentes sur la cosmologie même si à l'origine, les proprietés des amas sont definies pa un seul spectre de fluctuation de densité $P(k)$. Le comptage $n(z)$ des amas est extrêmement sensible à la normalisation de $P(k)$ (on compte des évènements très rares) ; $\xi(r)$, qui est la transformation de Fourier de $P(k)$ et par conséquent pas sensible à la normalisation, mais à la forme de $P(k)$.

Le comptage d'amas $n(z)$

La théorie : En bref, la théorie de Press & Schechter (1974) prédit le nombre d'objets virialisés (les amas en particulier) de masse M, à un redshift donné : $n(M, z)$ – la fonction de masse. Ce nombre est très sensible aux paramètres cosmologiques et en général les prédictions de la théorie sont en bon accord avec les simulations numériques (e.g. Jenkins et al. 2001). En pratique, nous ne pouvons pas mesurer directement la masse et par conséquent il faut utiliser des relations empiriques qui lient la masse aux observables, telles la température ou la luminosité. À partir de la fonction de masse $n(M, z)$ pour un modèle cosmologique et en utilisant la relation masse-température $M - T$, nous pouvons déduire la fonction de température $n(T, z)$, ou la fonction de luminosité $n(L, z)$ par l'intermédiaire de la relation masse-luminosité $M - L_X$. En intégrant ces fonctions pour toutes les luminosités ou températures supérieures à une limite nous pouvons déduire le nombre d'amas par intervalle de redshift – $n(z)$ théorique.

La fonction de sélection des amas $\phi(z, T)$: Cette fonction donne la probabilité de détecter un amas à un redshift et à une température donnés. Il faut compter sur des simulations d'images (Article E) pour estimer la fonction de sélection parce que nous connaissons le nombre exact des sources d'entrée et aussi leurs paramètres comme la température et le redshift. Le nombre des sources détectées *et* classifiées en sources étendues dans ces images simulées divisé par le nombre total d'amas d'entrée, nous donne la fonction de sélection en fonction de z et de T.

Contraintes cosmologiques : Une fois la fonction de sélection établie, nous pouvons multiplier le comptage d'amas théorique $n(z, T)$ par $\phi(z, T)$ et prédire $n(z)$ théorique, qui est ensuite comparé avec le comptage observé $n_{obs}(z)$. Pour une grille des paramètres du modèle cosmologique $(\Omega_m, \sigma_8, \Gamma, w, \cdots)$, nous pouvons calculer la différence entre prédictions et observations dans l'espace $\chi^2 = (n_{th}(z) - n_{obs}(z))^2 / n_{obs}(z)$ et établir la région la plus vraisemblable des paramètres pour un niveau de confiance donné.

La fonction de corrélation $\xi(r)$

La théorie : Nous avons utilisé l'approche de Mo & White (1996) qui prédit la fonction $\xi(r, z)$ observée en fonction du redshift, en supposant que les fluctuations de densité sont gaussiennes et par conséquent peuvent être décrites uniquement par le spectre de puissance $P(k)$. En

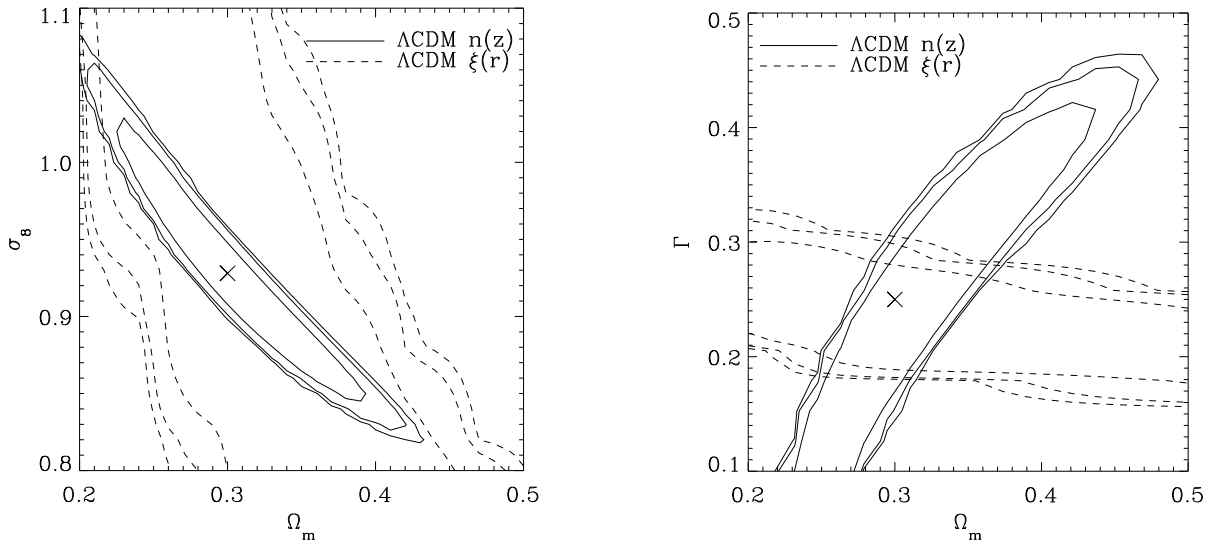

FIG. 3.5 – Contraintes dans les plans $\Omega_m - \sigma_8$ (à gauche) et $\Omega_m - \Gamma$ (à droite) du comptage $n(z)$ (les contours continus) et de la fonction de corrélation $\xi(r)$ (tirets) des amas du XMM-LSS (64 deg^2) à $z < 1$. Le modèle de référence est montré par le signe "x". Les contours montrent les niveaux de confiance à 68% (le plus intérieur), 90% et 95%.

introduisant la notion de biais effectif, $b_{eff}(z)$, nous pouvons passer de la fonction de corrélation linéaire (qui est la transformation de Fourier du spectre de puissance linéaire $P_{lin}(k)$) à la fonction observée : $\xi_{obs}(r,z) = b^2_{eff}\,\xi_{lin}(r,z)$. La fonction de corrélation $\xi(r)$ dans un intervalle $z_1 < z < z_2$ est la moyenne de $\xi(r,z)$ dans cet intervalle pondérée par le $n(z)$ (voir la section précédente).

Contraintes de $\xi(r)$: Avec la même technique que pour le comptage, en comparant la fonction observée avec les prédictions pour une grille des paramètres cosmologiques nous pouvons prédire la région de confiance correspondante aux observations envisagées.

Conclusions

Les résultats sont présentés Figure 3.5. Le comptage d'amas donne des fortes contraintes dans le plan $\Omega_m - \sigma_8$ et une dégénérescence dans le plan $\Omega_m - \Gamma$. La fonction de corrélation n'évolue pas significativement entre $0 < z < 1$ et les contraintes dans les plans $\Omega_m - \sigma_8$ et $\Omega_m - \Gamma$ sont dégénérées, mais grâce au fait que la région de confiance dans le plan $\Omega_m - \Gamma$ de $\xi(r)$ est orthogonale à celle de comptage, la dégénérescence peut être cassée. Par conséquent nous pouvons estimer les paramètres avec une précision de l'ordre de 15 à 20 %. En combinant ces contraintes cosmologiques avec celles des études du CMB et des supernovae nous pouvons d'abord vérifier si le modèle cosmologique est cohérent, i.e. s'il peut expliquer les observations de ces trois phénomènes qui reposent sur une physique différente, et ensuite diminuer encore l'intervalle de confiance et donc l'incertitude sur des paramètres.

3.3 Premiers amas à grand redshift (Article B)

Nous avons pre-selectioné les amas du XMM-LSS dans trois catégories (cf. Article A) : NEAR ($z < 0.5$), MID ($0.5 < z < 1$) et DIST($z > 1$), soit par une estimation à l'oeil, soit en utilisant les redshifts photometriques. Dans cette étude je présente cinq amas à $z > 0.6$, un sous-échantillon du groupe MID – le choix du redshift a été dicté par le point où nous commençons à perdre des amas par effet d'incomplètude (i.e. limite du flux).

L'objectif

Identifier, confirmer et obtenir les redshifts des amas dans le XMM-LSS. En particulier, les propriétés des amas à $z > 0.6$, leur état dynamique et leur évolution qui sont très importants, mais mal connus.

L'approche

J'ai développé une procédure de visualisation des données X et optique (`Auto-web`) pour faciliter la cross-identification des sources X. Cette procédure utilise des images et des catalogues des sources obtenus à partir des observations du télescope CFHT avec la caméra du grand champ CFH12k en bandes B, V, R et I. Pour chaque candidat amas (ou une position quelconque), la procédure produit les panneaux suivants :

`Auto-web` X : image en vraies couleurs d'une taille donnée, l'image brute X, l'image filtrée avec des ondelettes, l'image brute filtrée avec une gaussienne, toutes superposées avec les contours de l'émission X.

`Auto-web` optique : diagrammes couleur-couleur et couleur-magnitude à partir des catalogues optiques et les détections des sur-densités, s'il y en a, dans l'espace de redshift photométrique (z_{phot}) avec leurs probabilités correspondantes (le calcul de z_{phot} et les probabilités sont fournis par M. Bolzonella).

`Auto-web` cartes des redshifts photométriques : image optique du champ superposée avec les redshifts photométriques des galaxies.

Un exemple des trois panneaux de la procédure de visualisation pour un candidat amas (XLSS-005) est montré Figure 3.6, 3.7 et 3.8. L'analyse visuelle pour chaque candidat amas de tous les panneaux était indispensable dans l'identification des sources et le filtrage des fausses détections.

Les sources X étendues, identifiées comme des amas probables (i.e. sur-densité de galaxies dans la région de l'émission X, sur-densité dans l'espace z_{phot}) sont ensuite classées en deux groupes : `NEAR` ($z < 0.5$) et `MID` ($0.5 < z < 1$) en utilisant l'estimation du redshift photométrique. Nous avons ajouté aussi un groupe `DIST` ($z > 1$) pour les cas des sources X étendues sans contrepartie optique. Les amas des deux groupes `NEAR` et `MID` sont ensuite programmés pour des observations spectroscopiques avec des télescopes de 4 à 8 mètres. Quant aux candidats DIST, pour confirmer que ce sont des vrais amas, nous avons programmé des suivis d'imagerie en infrarouge proche.

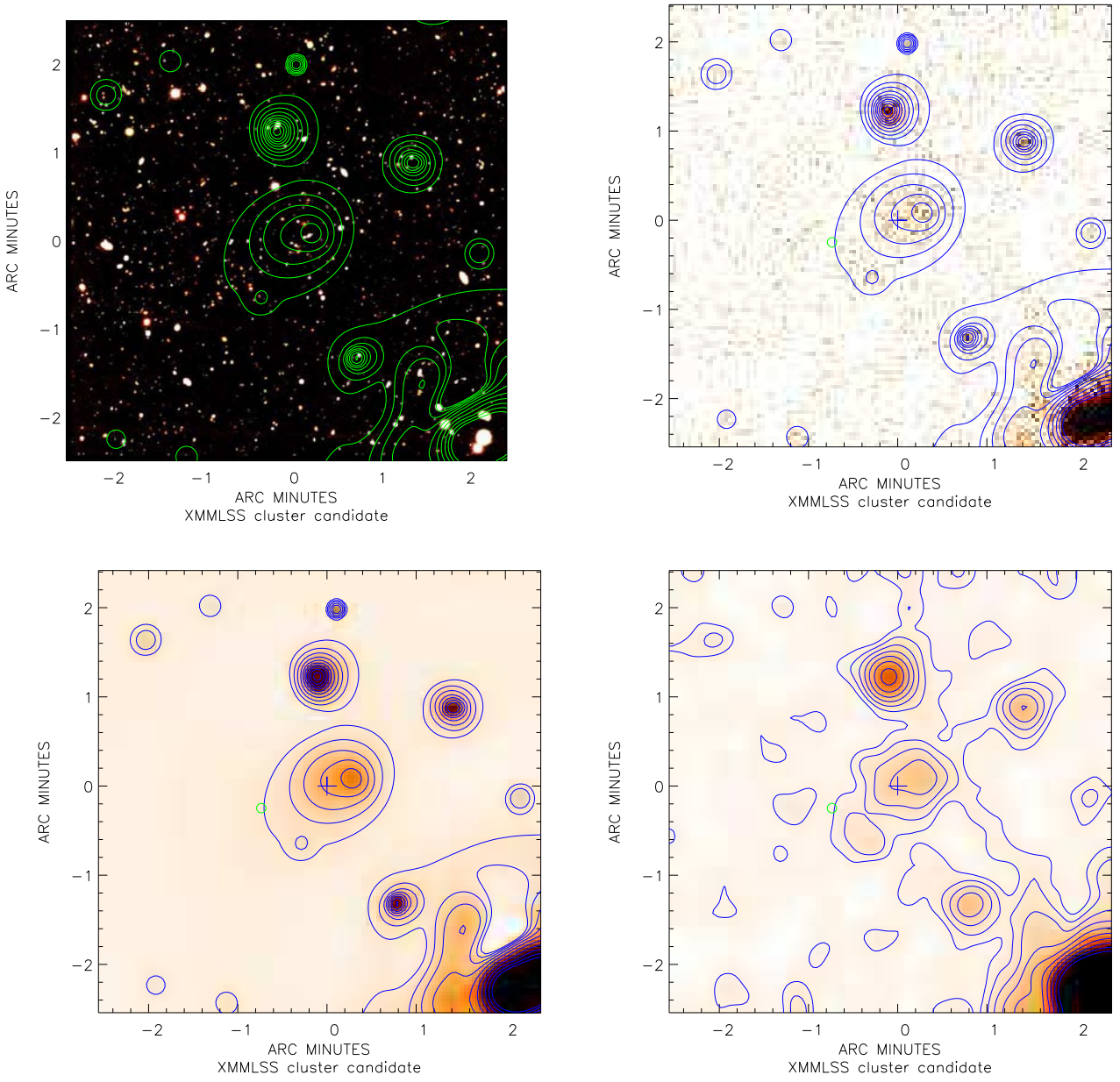

FIG. 3.6 – `Auto-web` X de XLSS-005. En haut à gauche : l'image en vraies couleurs (filtres VRI de CFH12k) avec les contours de l'image X filtrée avec des ondelettes et niveau de signification de $\sim 4\sigma$. En haut à droite : l'image brute X avec les mêmes contours du filtrage avec des ondelettes. En bas à gauche : l'image d'ondelettes superposée avec les contours. En bas à droite : l'image brute filtrée avec une gaussienne de 17.5″ FWHM. Les contours dans toutes les figures sont de 0.15 à 5 coups par pixel en échelle logarithmique. Notez la source X très forte dans le coin bas droite ($S_X[0.5-2] = 5.3 \times 10^{-13}$ erg s^{-1} cm^{-2}), c'est une des cinq sources connues du RASS dans les premiers 3 deg^2 du XMM-LSS.

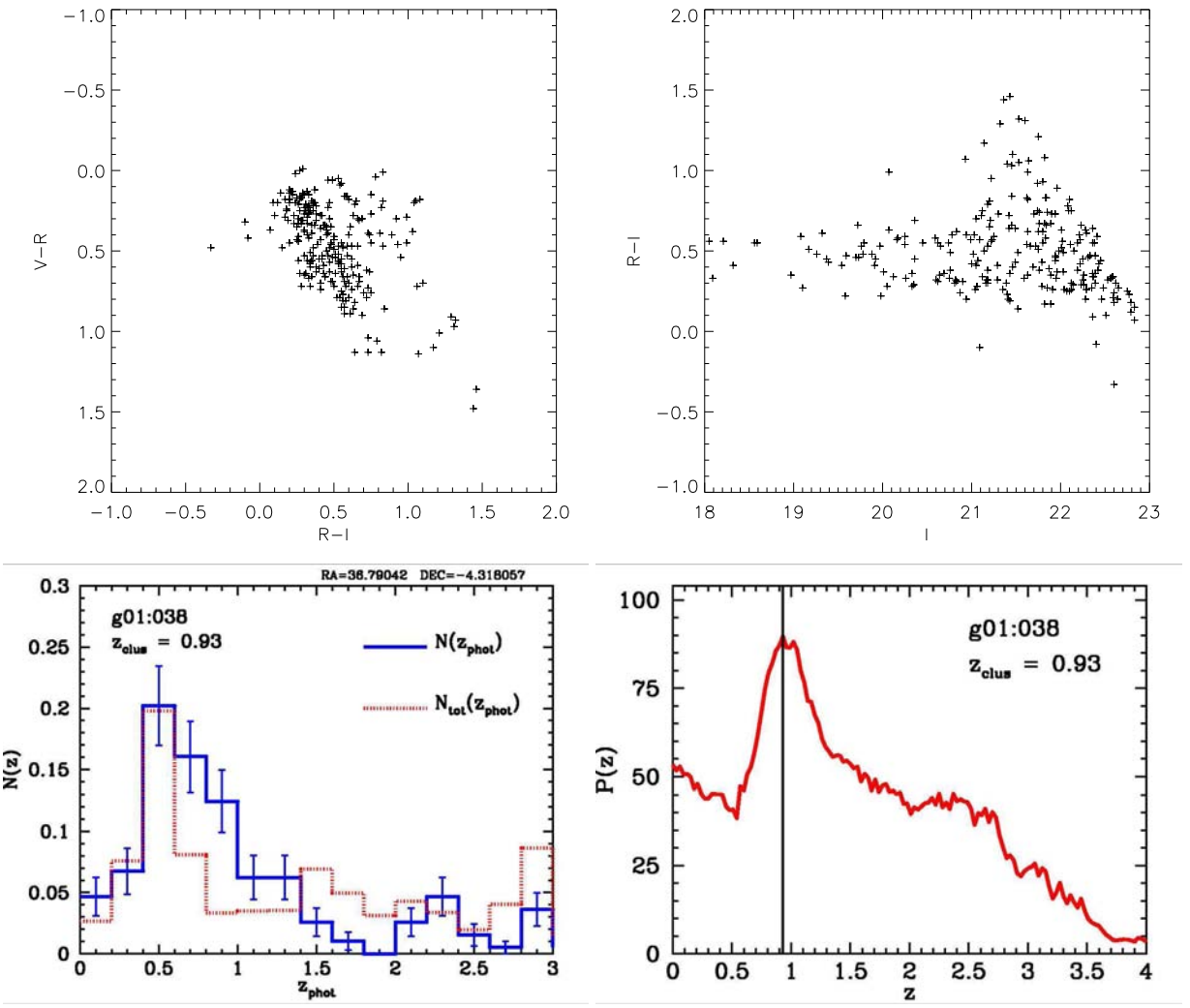

FIG. 3.7 – `Auto-web` optique de XLSS-005. En haut à gauche : le diagramme couleur-couleur (V-I, R-I) de tous les objets du champ avec R < 23^m. En haut à droite : le diagramme couleur-magnitude (R-I, I). En bas à gauche : la distribution des redshifts photométriques dans la région du candidat (histogramme continu avec les barres d'erreur) et dans le catalogue total (histogramme pointu). En bas à droite : la probabilité d'une sur-densité dans l'espace des redshifts photométriques dans une région de 1′ centrée sur l'émission X (pour plus de détails voir Article A).

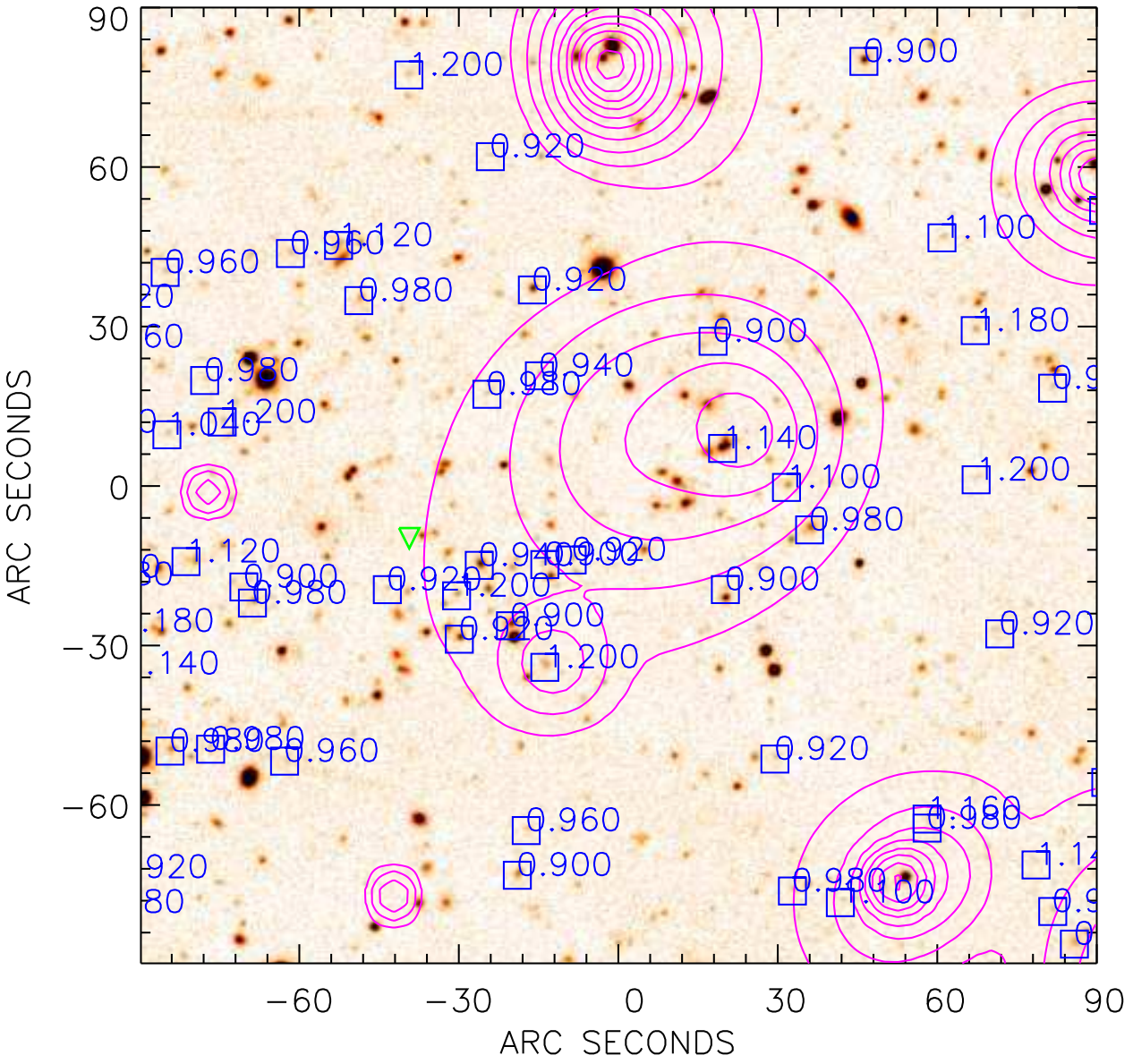

FIG. 3.8 – `Auto-web` : cartes de redshift photométriques de XLSS-005. Les objets avec des redshifts photométriques dans l'intervalle $0.9 < z < 1.2$ et dans la région centrale ($3' \times 3'$) sont indiqués. Le triangle vert est une source radio d'observations VLA (Cohen et al. 2003). Notez que les contours X cette fois sont un filtrage en ondelettes avec un niveau de signifiance de $\sim 3\sigma$ pour mieux faire apparaître les sous-structures.

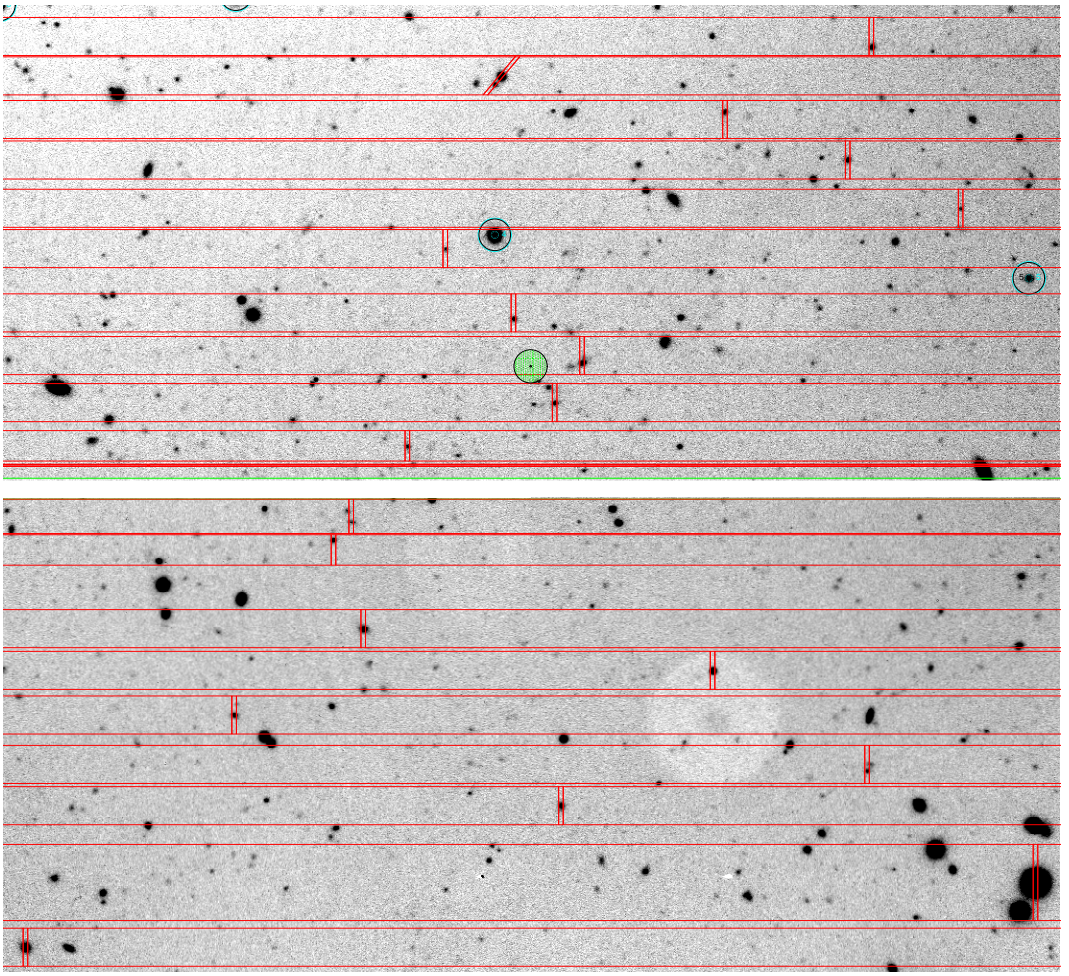

FIG. 3.9 – Un exemple de la partie centrale d'un des deux masques dans un champ de candidat amas (XLSS-05 à $z \approx 1$). J'ai préparé les fentes avec `fims` sur une image pré-observée avec le même instrument : VLT-UT4/FORS2. En utilisant le régime MXU de l'instrument FORS2 du VLT nous avons la possibilité de placer des fentes plus longues et aussi inclinées.

La préparation et les observations

Nous avons décidé d'utiliser deux masques par candidat amas pour augmenter les chances d'inclure des galaxies membres et aussi pour mieux couvrir le coeur de l'amas où la densité de galaxies est importante. J'ai préparé deux masques pour chacun des 15 candidats amas que nous avons choisi d'observer dans le premier suivi spectroscopique au VLT. Pour cette tâche j'ai utilisé `fims`[1] pour placer les fentes sur les galaxies retenues comme des membres probables, à l'aide de la procédure de visualisation. Un exemple de la partie centrale d'un masque est montré Figure 3.9. Le produit final de la préparation contient 30 masques pour les 15 candidats d'amas avec 30 fentes en moyenne par masque, ce qui fait au total quelque $\sim$ 900 fentes.

Les observations ont été faites par M. Pierre et moi-même au VLT-UT4 avec l'instrument FORS2 le 9-12 Octobre 2002 en mode "visiteur". Nous avons pu observer 12 candidats : cinq de classe `MID` et la reste de classe `NEAR`, préparés pour le cas où les conditions météo n'auraient pas permis d'observer des objets faibles.

[1] *The FORS Instrumental Mask Simulator tool* : http ://www.eso.org

Les résultats

J'ai fait la réduction et l'analyse des données spectroscopiques des 5 amas du groupe `MID`, à $z > 0.6$ (environ 300 spectres). J'ai mesuré les redshifts en utilisant la technique de cross-corrélation avec un spectre de référence ou directement avec des raies d'émission s'il y en avait. L'analyse des observations des amas `NEAR` sera présentée dans Willis et al. (2003, en préparation).

Des cinq amas, trois sont confirmés par les observations spectroscopiques : XLSS-001, XLSS-002 et XLSS-003. D'après les données X et optique ces trois amas illustrent trois états dynamiques : un amas relaxé à $z = 0.84$ (distribution des vitesses gaussienne, morphologie X régulière, pas de sous-structures, les lois d'échelle – les relations entre la luminosité X, la température et la dispersion de vitesse : L_X, T et σ_v – sont en bon accord avec les relations des amas locaux) ; un amas en voie de relaxation à $z = 0.61$ (indication de sous-structure, distribution de vitesse proche de gaussienne) et un amas en formation à $z = 0.77$ (noyau compact et présence de galaxies dans les grandes structures voisines).

Les deux autres cas, XLSS-004 et XLSS-005 sont aussi très intéressants, mais nous ne pouvons pas élucider leur nature avec ces seules données spectroscopiques. XLSS-004 est probablement un amas de faible masse, à $z = 0.9$ détecté indépendamment, à l'aide des observations à *Cerro Tololo Inter American Observatory* (CTIO) dans les filtres R et z', comme une sur-densité de galaxies avec la même couleur R-z'=1.4, qui correspond au redshift de l'amas (Andreon et al. en préparation).

Quant à XLSS-005, c'est un cas complexe à $z \approx 1$. L'émission X est étendue avec une indication de sous-structure ; la distribution des redshifts spectroscopiques est complexe avec des objets de $z = 0.92$ à $z = 1.05$. Notre interprétation est que nous voyons probablement deux amas en projection. La distribution des redshifts spectroscopiques dans la région qui inclut l'émission X, peut être expliquée si nous avons mesuré des objets du *filament* qui lie les deux amas.

En conclusion, ces premières observations et ces résultats sont très importants parce qu'ils démontrent les performances et la faisabilité du programme XMM-LSS. En une heure de temps VLT nous avons obtenu la dispersion de vitesse d'un amas à $z = 0.84$ – à noter que jusqu'à maintenant (Avril 2003) il y a seulement 5 amas connus à $z > 0.8$ avec plus de 10 mesures des redshifts concordants ! Contrairement aux amas ROSAT (de pointés profonds) du même intervalle du redshift, les premiers amas de XMM-LSS sont de faible luminosité (et donc faible masse). Ce n'est pas étonnant car 1) XMM a une meilleure sensibilité, 2) nous avons choisi une région sans amas connus et sans sources X brillantes et 3) la surface disponible jusqu'à présent est ~ 6 deg^2 et donc la probabilité d'avoir des amas massifs est très faible.

4. Conclusion et perspectives

Le XMM-LSS est un grand pas en avant pour les études de l'évolution de la structure de l'univers tracée par les amas de galaxies. D'une part, les observations de base d'XMM, qui est et qui sera l'observatoire X le mieux placé pour faire des surveys des amas à grand redshift dans la décennie à venir. D'autre part, les observations multi-longueurs d'onde pour assurer l'apport scientifique avec les instruments les plus puissants et novateurs : MegaCam, VIMOS, SIRTF, AmiBA[1]. Le XMM-LSS a commencé en 2001, il y a à peine deux ans et aujourd'hui tous les programmes de suivis sont en cours et le travail de routine se déroule sans difficultés.

Jusqu'à maintenant nous avons observé ~ 6 deg^2 avec XMM et un échantillon de quelques $\sim 80 - 90$ candidats d'amas dont 19 identifiés spectroscopiquement. Le nombre d'amas, ~ 15 par deg^2 est en très bon accord avec les prédictions cosmologiques des amas à $z < 1$ et $T > 2$ keV, en utilisant une estimation de la fonction de sélection du XMM-LSS. La plupart des amas détectés dans le XMM-LSS sont de faible luminosité (ou également faible masse), ce qui nous permettra pour la première fois de cartographier la toile cosmique à une telle échelle de masse.

La base de données avec ~ 900 amas attendus du XMM-LSS dans une région continue de 64 deg^2 jusqu'à $z \sim 1$ représentera un énorme pas en comparaison des catalogue actuellement disponibles : le plus grand est REFLEX (Böhringer et al. 2001) qui contient 450 amas jusqu'à $z \sim 0.2$. Grâce au télescope XMM, sa sensibilité, son grand champ et sa bonne résolution spatiale et spectrale, ces objectifs sont réalisables, même sans une forte pression sur les demandes d'observations. Le grand intérêt d'un tel survey a déjà suscité de nombreuses collaborations multi-longueurs d'onde qui vont nous donner une vision complète de la distribution de la matière dans le volume du XMM-LSS.

Ma contribution est pratiquement à tous les niveaux : non seulement dans la partie technique – la réduction des données X, détection des sources, cross-identification X-optique, programmation des suivis spectroscopiques, réduction des observations spectroscopiques, mais aussi dans l'analyse scientifique de l'état dynamique des amas observés, la fonction de sélection et les contraintes cosmologiques et la justification des objectifs scientifiques du XMM-LSS.

4.1 Originalité et contribution pour la communauté astrophysique

Est-ce qu'un survey doit être original ? Un survey n'a pas à être original pour produire de l'excellente science (par exemple les plaques de Schmidt). En fait, le produit final et original

[1] Voir les pages web du consortium http ://vela.astro.ulg.ac.be/themes/spatial/xmm/LSS/ pour des détails sur tous les programmes du suivi et les instruments impliqués dans le XMM-LSS.

d'un survey, est la base de données scientifiques qui sera utilisée par la communauté astrophysique. L'idée originale de XMM-LSS est d'utiliser le télescope XMM, qui d'ailleurs n'est pas conçu pour faire des surveys, et de lier les observations en rayons X avec des suivis avancés dans plusieurs longueurs d'onde (optique, infra-rouge proche et lointain, radio, millimétrique) pour une vision complète de la distribution de la matière sur des échelles > 100 Mpc.

Les sensibilités obtenues pour les différentes domaines de longueur d'onde (Table 2.1) illustrent l'avancée du XMM-LSS par rapport aux surveys antérieurs.

4.2 Perspectives

a) Des demandes d'observations spectroscopiques ont été soumises pour confirmer les amas XMM-LSS correspondant à un échantillon complet jusqu'à flux $S_X = 8 \times 10^{-15}$ erg cm^{-2} s^{-1} dans la surface disponible (6 deg^2). Le résultat sera un catalogue complet de $\sim$ 100 amas à $0 < z < 1$ qui nous permettra d'abord de tester les procédures de détection en multi-λ (X, optique, IR) et ensuite d'estimer σ_8 et d'étudier les lois d'échelles en fonction du redshift.

b) Chaque amas détecté est un objet unique et particulièrement intéressant qui mérite une description et, éventuellement, une analyse spectrale.

c) L'analyse "weak lensing" est en cours pour cartographier la distribution de la masse dans la région du XMM-LSS. La comparaison avec les amas X et optique sera très importante, surtout quant à l'existence d'objets exotiques, tels les "amas sombres" – des amas détectés par le "weak lensing" mais sans contrepartie optique ou X.

d) Le produit final – la base de données du XMM-LSS est en cours de développement et la première version publique sera disponible début 2004.

5. Références

Abell G., 1958 ApJS, 3, 211

Abell G., Corwin H. & Olowin R., 1989 ApJS, 70, 1

Arnaud M. & Evrard A., 1999 MNRAS, 305, 631

Bahcall N. & Bode P., 2003, ApJ, 588, L1

Bertin E. & Arnouts S., 1996, A&AS, 117, 393

Birkinshaw M., 1999 Physics Reports 310, 97

Biviano A., 2000. *Constructing the Universe with Clusters of Galaxies*. Eds. Durret F. & Gerbal D., Paris, France

Blumenthal et al., 1984, Nature, 311, 517

Böhringer H., Schuecker P., Guzzo L., 2001 A&A, 369, 826 (REFLEX)

Carlstrom J.E., Holder G.P. & Reese E.D., 2002 ARAA, 40, 643

Clowe D. & Schneider P., 2001 A&A, 379, 384

Cohen A.S., Röttgering H.J.A., Kassim N.E., et al. 2003, ApJ, accepté.

Collins C., Guzzo L., Böhringer H., et al., 2000 MNRAS, 319, 939

Dalton G.B., Maddox S.J., Sutherland W.J. & Efstathiou, G., 1997 MNRAS, 289, 263

Ensslin T., Biermann P., Klein U. & Kohle S., 1998, A&A, 332, 395

Evrard A., MacFarland T., Couchman H.M.P., et al., 2002 ApJ, 573, 7

Finoguenov A., Reiprich T.H. & Böhringer H, 2001 A&A, 368, 749

Gioia I.M., Maccacaro T., Schild R.E. et al., 1990 ApJS, 72, 567 (EMSS)

Giovannini G., Feretti L., Venturi T., et al., 1993, ApJ, 406, 339

Gursky H., Kellogg E., Murray S. et al., 1971 ApJ, 167, L81

Henry J.P., Gioia I.M., Mullis C.R. et al., 2001 ApJ, 553, L109 (NEP)

Jenkins A., Frenk C.S., White S.D.M. et al. 2001, MNRAS, 321, 372

Kaiser N., 1986 MNRAS, 222, 323

Katgert P., Mazure A., Perea J. et al., 1996 A&A, 310, 8

Liang H., Dogiel V.A. & Birkinshaw M., 2002, MNRAS, 337, 567

Liang H., Lémonon L., Valtchanov I., et al., 2000, A&A, 363, 440

Lumsden S.L., Nichol R.C., Collins C.A. & Guzzo L., 1992 MNRAS, 258, 1

Matsumoto H., Pierre M., Hunstead R., et al., 2001 A&A, 374, 28

Mellier Y., 1999 ARA&A, 37, 127

Mo H.J. & White S.D.M., 1996 MNRAS, 282, 347

Mohr J.J., Mathiesen B. & Evrard A., 1999 ApJ, 517, 627

Moretti A., Campana S., Lazzati D. & Tagliaferri G., 2003, ApJ, 588, 696

Norberg P., Baugh C.M., Hawkins E., et al., 2001, MNRAS, 328, 64

Peacock J.A. , 1999. *Cosmological physics*. Cambridge University Press. Cambridge.

Peacock J.A. & Dodds S.J., 1994, MNRAS, 267, 1020

Peebles P.J.E., 1993. *Principles of the physical cosmology*. Princeton University Press

Postman M., Lubin L.M., Gunn J.E. et al., 1996 AJ, 111, 615

Press W.H. & Schechter P., 1974 ApJ, 187, 425

Raymond J.C. & Smith B.W., 1977, ApJS, 35, 419

Reese E.D., Carlstrom J.E., Joy M., et al. 2002, ApJ, 581, 53

Reiprich T. & Böhringer H., 2002 ApJ, 567, 716

Rosati P., Borgani S. & Norman C., 2002, ARAA, 40, 539

Sarazin C., 1999, ApJ, 520, 529

Spergel D.N., Verde L., Peiris H.V. et al., 2003, ApJ, accepté (astro-ph/0302209)

Starck J.-L. & Pierre M., 1998, A&AS, 128, 397

Voges W., Aschenbach B., Boller Th. et al., 1999, A&A, 349, 389 (RASS)

Weinberg S., 1972. *Gravitation and cosmology*. John Wiley & Sons Inc., New York

Xue Y.-J. & Wu X.-P., 2000 ApJ, 538, 65

Zwicky F., 1933 Helv. Phys. Acta, 6, 110

Zwicky F., Herzog E., Wild P. et al., 1961-1968, *Catalogue of Galaxies and Clusters of Galaxies* (Pasadena : CalTech)

6. Liste des publications

Soumis

1. Pierre M., **Valtchanov I.**, Dos Santos S., et al., 2003, A&A, soumis
   The XMM-LSS survey I. Scientific motivations, design and first results
2. **Valtchanov I.**, Pierre M., Dos Santos S., et al., 2003, A&A, soumis
   The XMM-LSS survey II. First high redshift galaxy clusters : relaxed, relaxing and collapsing systems

Journaux en comité de lecture

1. **Valtchanov I.**, Murphy T., Pierre M., Hunstead R. & Lémonon, L., 2002, A&A, 392, 795
   Abell 1451 and 1RXS J131423.6-251521 : A multi-wavelength study of two dynamically perturbed clusters of galaxies
2. Refregier A., **Valtchanov I.** & Pierre, M., 2002, A&A, 390, 1
   Cosmology with galaxy clusters in the XMM large-scale structure survey
3. Marty P.B., Schultz J., Bayer C., Fritz A., Netopil, M., Nowotny W., Carr M., Ferrigno C., Jean C., Koprolin W., Rasmussen J., Tanvuia L., **Valtchanov I.**, Bavdaz M., Much R. & Parmar A., 2002, SPIE, 4497, 1
   In.XS : project for a future spaceborne hard X-ray all-sky survey
4. **Valtchanov I.**, Pierre M., Gastaud R., 2001, A&A, 370, 689
   Comparison of source detection procedures for XMM-Newton images
5. Watson M.G., et al., 2001, A&A, 365, 51
   The XMM-Newton Serendipitous Survey. I. The role of XMM-Newton Survey Science Centre
6. Liang H., Lémonon L., **Valtchanov I.**, Pierre M. & Soucail, G., 2000, A&A, 363, 440
   Probing the gravitational potential of a nearby lensing cluster Abell 2104
7. Starck J.-L., Bijaoui A., **Valtchanov I.** & Murtagh F., 2000, A&AS, 147, 139
   A combined approach for object detection and deconvolution
8. Kalinkov M., **Valtchanov I.** & Kuneva, I., 1998, ApJ, 506, 509
   Correlation Function of Superclusters of Galaxies
9. Kalinkov M., **Valtchanov I.** & Kuneva, I., 1998, A&A, 331, 838
   Superclusters of galaxies. II. Distribution and correlation functions

Interventions à des colloques

1. **Valtchanov I.** & Pierre M., 2003, In X-ray Surveys, in the light of the new observatories, Santander, Spain. Publié dans Astron. Nachr., 324, 124
   The XMM Large Scale Structure Survey : scientific motivation and first cluster candidates.
   présentation orale
2. **Valtchanov I.**, 2002, In Statistical Challenges in Modern Astronomy III. Eds. Eric D. Feigelson & G. Jogesh Babu, New York :Springer-Verlag
   Comparison of object detection procedures for XMM-Newton images
   poster
3. **Valtchanov I.**, Refregier A. & Pierre, M., 2001, Clusters of Galaxies and the High Redshift Universe Observed in X-rays, XXIst Moriond Astrophysical Meeting, Les Arcs, France
   The XMM-Large Scale Structure Survey : Constraining cosmology with the evolution of galaxy clusters
   présentation orale
4. **Valtchanov I.**, Gastaud R., Pierre M. & Starck, J.-L., 1999, Clustering at High Redshift, Marseille, France
   Detecting High Redshift Clusters with XMM
   poster
5. **Valtchanov I.**, 1999, Astronomical Data Analysis Software and Systems VIII, ASP Conference Series, Vol. 172. Ed. David M. Mehringer, Raymond L. Plante, and Douglas A. Roberts, 38
   Large Scale Clustering in the Universe – A Package of Codes
   présentation orale
6. **Valtchanov I.**, Kalinkov M. & Kuneva I., 1998, Numerical Astrophysics 1998, Tokyo, Japan
   Comparison of Simulated and Observed Density Profiles in Galaxy Clusters
   poster

Autres

7. Pierre M., **Valtchanov I.**, Refregier A., 2002, astro-ph/0202117, Proceedings of the Conference "New Visions of the X-ray Universe in the XMM-Newton and Chandra Era" 26-30 November 2001, ESTEC, NL
   The XMM Large Scale Structure Survey : Scientific Motivation and First Observations
8. Kalinkov M., **Valtchanov I.** & Kuneva I., 1999, Astronomical Data Analysis Software and Systems VIII, ASP Conference Series, Vol. 172. Ed. David M. Mehringer, Raymond L. Plante, and Douglas A. Roberts, 371
   References for Galaxy Clusters Database
9. Kalinkov M., **Valtchanov I.**, Kuneva I. & Tsvetanov Z., 1997, Redshift Surveys in the 21st Century, 23rd meeting of the IAU, Joint Discussion 11, E2
   K-corrections for the Sloan Digital Sky Survey

10. Kalinkov M., **Valtchanov I.** & Kuneva, I. 1996, 2nd Hellenic astronomical conference. Edited by Michael E. Contadakis, John D. Hadjidemetriou, Lyssinmachos N. Mavridis, and John H. Seiradakis. Greece : Hellenic Astronomical Society, 498
Disappearance of hierarchical clustering ?

11. Kalinkov M., **Valtchanov I.** & Kuneva I., 1996, 2nd Hellenic astronomical conference. Edited by Michael E. Contadakis, John D. Hadjidemetriou, Lyssinmachos N. Mavridis, and John H. Seiradakis. Greece : Hellenic Astronomical Society,364
Kinematics and Dynamics of Superclusters of Galaxies

12. Kalinkov M., **Valtchanov I.**, & Kuneva I., 1996, Accepted in Bulletin d'Inform. de CDS, No. 49. In CDS catalog VII/201
Cross-identification in Abell and Zwicky Clusters of Galaxies

13. Kalinkov M., Kuneva I. & **Valtchanov I.**, 1995, IAU Symposia, 164, 454
Dark Matter in Groups and Clusters of Galaxies '

14. Kalinkov M., Kuneva I. & **Valtchanov I.**, 1994, ASP Conf. Ser. 61 : Astronomical Data Analysis Software and Systems III, 3, 263
Multiple Regression Redshift Calibration for Clusters of Galaxies

A. The XMM-LSS survey
I. Scientific motivations, design and first results

Pierre M., **Valtchanov I.**, Dos Santos S. et al, 2003, A&A, submitted

The XMM-LSS survey

I. Scientific motivations, design and first results⋆

M. Pierre[1], I. Valtchanov[1], S. Dos Santos[1], B. Altieri[2], S. Andreon[3], M. Bolzonella[4], M. Bremer[5], C. Jean[6], A. M. Read[7], A. Refregier[1], J. Willis[8],[14], C. Adami[9], D. Alloin[8], M. Birkinshaw[5], L. Chiappetti[4], A. Cohen[10], A. Detal[6], P. A. Duc[1], E. Gosset[6], L. R. Jones[7], O. Le Fèvre[9], D. Maccagni[4], B. McBreen[12], H. McCracken[9], Y. Mellier[13], T. J. Ponman[7], H. Quintana[14], H. Rottgering[15], A. Smette[6], J. Surdej[6], L. Vigroux[1], H. Böhringer[17], J. Hjorth[18], C. Lonsdale[11], and S. D. M. White[16]

[1] CEA/DSM/DAPNIA, Service d'Astrophysique, Saclay, F-91191 Gif sur Yvette
[2] XMM Science Operations Centre, Villafranca, Spain
[3] Osservatorio Astronomico di Brera, Milano, Italy
[4] IASF, Milano, Italy
[5] Department of Physics, University of Bristol, UK
[6] Institut d'Astrophysique et de Géophysique, Université de Liège, Belgium
[7] School of Physics and Astronomy, University of Birmingham, UK
[8] European Southern Observatory, Santiago, Chile
[9] Laboratoire d'Astrophysique, Marseille, France
[10] Naval Research laboratory, Washington, US
[11] Infrared Processing and Analysis Center, Caltech, US
[12] Physics Department, University College, Dublin, Ireland
[13] Institut d'Astrophysique, Paris, France
[14] Pontificia Universidad Católica, Santiago, Chile
[15] Leiden Observatory, Leiden, The Netherlands
[16] Max Planck Institut für Extraterrestrische Physik, Garching bei München, Germany.
[17] Max Planck Institut für Astrophysik, Garching bei München, Germany.
[18] Astronomical Observatory, Copenhagen, Denmark

Received April 2003

Abstract. We have designed a medium deep large area X-ray survey with XMM – the XMM Large Scale Structure survey, XMM-LSS – with the scope of extending the cosmological tests attempted using ROSAT cluster samples to two redshift bins between $0 < z < 1$ while maintaining the precision of earlier studies. Two main goals have constrained the survey design: the evolutionary study of the cluster-cluster correlation function and of the cluster number density. The adopted XMM observing configuration consists of an equatorial mosaic of 10 ks pointings, separated by $20'$ and covering $8^\circ \times 8^\circ$, giving a sensitivity of $\sim 3\ 10^{-15}$ erg cm^2 s^{-1} in the [0.5-2] keV band. This will yield more than 800 clusters of galaxies and a sample of X-ray AGN with a space density of about 250 deg^{-2}. We present the expected cosmological implications of the survey in the general context of ΛCDM models and cluster evolution. The XMM-LSS survey is associated to several other major surveys, ranging from the UV to the radio wavebands which will provide the necessary resources for X-ray source identification and further statistical studies. In particular, the associated CFHTLS weak lensing and AMiBA Sunyaev-Zel'dovich surveys over the entire XMM-LSS area, will provide for the first time a coherent study of the mass distribution and of cluster physics in the universe on scales of a few hundreds of Mpc. We describe the main characteristics of our wavelet based X-ray pipeline and source identification procedures, including the classification of the cluster candidates by means of a photometric redshift analysis. This permits the selection of suitable targets for spectroscopic follow-up. We present the preliminary results pertaining to the first 15 XMM-LSS pointings : X-ray source properties, optical counterparts,highlights from the first Magellan and VLT/FORS2 spectroscopic runs as well as preliminary results from the NIR search for $z > 1$ clusters. The results are promising and, so far, in accordance with our predictions as to the survey sensitivity and cluster number density. The feasibility of the programme is demonstrated and further X-ray coverage is awaited in order to proceed with a truly significant statistical analysis.

Key words. X-ray, Large Scale Structures, clusters of galaxies, AGN

1. Introduction

1.1. The role of clusters in cosmology

We have come a long way since the Virgo cluster of galaxies was discovered as an accumulation of "nebulae" (Messier 1781), the first time the term "cluster" was used (Shapley & Ames 1926), and the first inference of large amounts of "dark matter" in the Virgo cluster (Zwicky 1933), to the point where clusters of galaxies are now routinely used as cosmological tools. This progress, is intimately related to the development and success of the standard cosmological model over the past 50 years, following ever-deeper insights into the early evolution of the Universe and the growing power of numerical simulations. From a simple theoretical point of view, clusters of galaxies - the most massive bound structures in the Universe - are objects having a mass of the order of 10^{14-16} $M_{\odot}$ growing by accretion at a rate governed by the initial density fluctuation spectrum, the cosmological parameters, the nature and amount of dark matter as well as the nature of the dark energy. Their 3-dimensional space distribution and number density as functions of cosmic time constrain cosmological parameters in a unique way. Non-gravitational effects accompanying cluster formation render the picture more complicated, but compared to galaxies, clusters still offer considerable advantages for large scale structure (LSS) studies: they can provide complete samples of objects over a very large volume of space, and they are in crucial respects simpler to understand. The extent (and mass) of clusters can be traced by their X-ray emission while the theory describing their formation (biasing) and evolution from the initial fluctuations can be tested with numerical simulations. Such a level of understanding does not exist for galaxies - which have reached a highly non-linear stage - to and even less for QSO and AGN formation. The resulting cluster LSS counts studies can constrain cosmological parameters, independently of Cosmic Microwave Background (CMB) and supernova (SN) studies since they do not rely on the same physical processes. In addition, they can also be used to test fundamental assumptions of the standard paradigm, such as the gravitational instability scenario. A quantitative overview of the cosmological implications of cluster surveys can be found for instance in Haiman et al 2001.

Conversely, given a cosmological model, a large and deep statistical sample of clusters would provide long-awaited information linking cluster physics, non-linear phenomena involved in cluster evolution, and scaling relations. Further, cluster number counts as a function of both the redshift and X-ray luminosity (or any observable), provide strong consistency tests on assumptions made in modelling the mass-luminosity (or mass-observable) relation and cosmological models involving dark energy (Hu 2003). This is very timely, since following the WMAP[1] results, independent cosmological constraints from both the early and the local universe, must be integrated into a consistent framework.

1.2. The quest for clusters

Initiated by Abell (1958) over the whole sky in the optical, the systematic search for clusters underwent a boost of activity in the X-ray waveband during the EINSTEIN (1978-1981) era. The first X-ray rockets and satellites had revealed the existence of X-ray emission associated with clusters. The UHURU (1970) data, in particular, showed that this emission is thermal and originates in a hot diffuse gas trapped in the gravitational potential of the cluster. The Extended EINSTEIN Medium Sensitivity Survey (EMSS[2]) provided some 730 serendipitous X-ray sources extracted from pointed observations down to a sensitivity of 1.5 10^{-13} erg cm^2 s^{-1} in the [0.3-3.5] keV band. A sub-sample of 67 sources identified as clusters of galaxies in the $0.14 < z < 0.6$ range, (Gioia et al 1990) suggested, for the first time, a mild evolution in the cluster number density. Next, the ROSAT All-Sky-Survey[3] (RASS, 1990-1991) provided the first sample of X-ray clusters over the entire sky (with an average PSF of 2′ FWHM) and thus, a fundamental resource for LSS studies. Cosmological implications have been investigated in detail from the southern REFLEX (3 10^{-12} erg cm^2 s^{-1} in the [0.2-2.4] keV band) and North Ecliptic Pole samples (down to 3 10^{-14}) by Böhringer et al 2001 and Henry et al 2001 respectively.

In parallel, following on the EMSS achievement, serendipitous searches for distant clusters in deep pointed ROSAT observations led to the discovery of clusters out to $z \sim 1.2$ with a modest evolution of the bulk of the high luminosity X-ray cluster population; a summary of the main X-ray cluster surveys is presented on Fig. 1.

Both approaches are consistent with hierarchical models of structure formation in a flat low density universe with $\Omega_m \sim 0.3$ and the matter density and the amplitude of mass fluctuations on 8 h^{-1} Mpc scale, $\sigma_8 \sim 0.7 - 0.8$ (see Rosati et al 2002, for a review). In parallel, the quest for clusters in the optical made its own way, from automated searches on digitised sky survey plates to deep multi-colour CCD imaging. Indeed, beyond $z \geq 0.8$, detecting clusters only from galaxy overdensity in a single band is severely hampered by the faint background population, so that the use of fine-tuned photometric redshift information becomes mandatory (see e.g. Sec. 4.2). However, given the limitations on the accuracy of such methods and various underlying hypotheses about galaxy evolution, this usually yields large numbers of high-z candidates, many of them simply being portions of cosmic filaments seen in projection. One will thus always expect - beside extensive optical spectroscopic campaigns - an ulti-

Send offprint requests to: M.Pierre, mpierre@cea.fr

⋆ paper based on observations obtained with the XMM,CFH, ESO, VLA, CTIO and Las Campanas observatories

[1] http://lambda.gsfc.nasa.gov/product/map/map_bibliography.html

[2] http://xml.gsfc.nasa.gov/archive/catalogs/9/9015/

[3] http://heasarc.gsfc.nasa.gov/docs/rosat/survey/

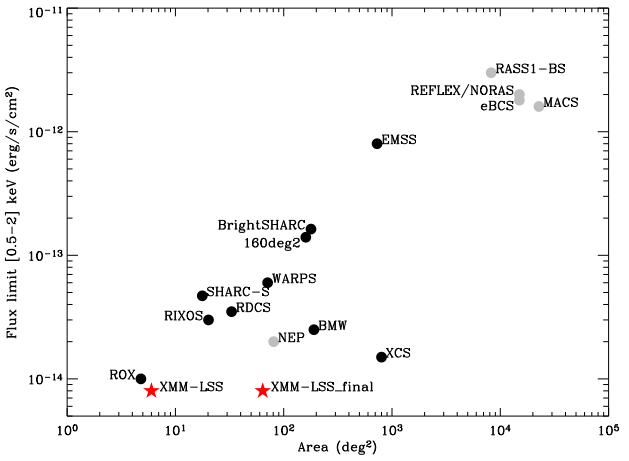

Fig. 1. Overview of existing X-ray cluster surveys as a function of coverage and limiting flux. The light filled circles indicate surveys covering contiguous area, while the dark circles represent serendipitous surveys; the stars show the position of the survey presented in this paper, the XMM-LSS survey (current stage and the foreseen final coverage). References: MACS (Ebeling et al 2001), RASS1-BS (de Grandi et al 1999), eBCS (Ebeling et al 2000), REFLEX/NORAS (Böhringer et al 2000, 2001), EMSS (Gioia et al 1990), XCS (Romer et al 2001), BMW (Panzera et al 2003), Bright SHARC (Romer et al 2000), 160deg^2 (Vikhlinin et al 1998), NEP (Henry et al 2001), WARPS (Perlman et al 2002), RDCS (Rosati et al 1998), RIXOS (Castander et al 1995), SHARC-S (Collins et al 1997), ROX (Donahue et al 2001).

mate confirmation from the X-ray band, in order to assess the presence of deep potential wells.

1.3. The power of XMM

At the time the XMM project was initiated[4], the case for surveys was not as compelling as it is today. Ten years after the completion of the RASS, and following considerable steps forward in our knowledge of cluster physics (e.g. Peterson et al 2002), XMM is in a position to open a new era for X-ray surveys. Its high sensitivity, considerably better PSF than the RASS (6″ on axis) and large field of view (30′), make it a powerful tool for the study of extragalactic LSS. In this respect, two key points may be emphasised. Firstly, a high galactic latitude field observed with XMM at medium sensitivity ($\sim 0.5-1\ 10^{-14}$ erg cm^2 s^{-1}) is "clean" as it contains only two types of objects, namely QSOs (pointlike sources) and clusters (extended sources) well above the confusion limit. Secondly, if clusters more luminous than $L_{[2-10]} \sim 3\ 10^{44}\ h_{70}^{-2}$erg/s are present at high redshift, they can be detected as extended sources out to $z = 2$, in XMM exposures of only 10 ks. XMM is a powerful wide angle X-ray imager, with a sensitivity to extended sources which will remain unrivalled in the coming decade. In parallel, progress in optical wide field imaging provides the necessary resources for the identification of faint X-ray sources. Consequently, we are now in a position to probe the evolution of the cosmic network traced by clusters and QSOs over large volumes of the Universe to high redshift.

[4] first discussions proposing some 27 telescopes in 1982; acceptance in 1988

1.4. The goals of the XMM-LSS

Each new generation of instruments brings - in some respect - at least one order of magnitude improvements compared to its predecessor. While REFLEX was the first X-ray survey to systematically address LSS with clusters in the nearby universe (450 clusters with $z \leq 0.2$), there is now a clear need to investigate the evolution of the cosmic network out to $z \sim 1$. In this context, we have designed a survey to yield some 800 clusters in two redshift bins with $0 < z < 1$: the XMM Large Scale Structure Survey (XMM-LSS). This simple goal has set the sensitivity and the coverage of the XMM-LSS and, as shown in Sec.2.1, implies an X-ray sensitivity about 3 orders of magnitude deeper than REFLEX. Consequently, this survey will determine how the cluster number density evolves - a hotly debated topic. It will also trace the LSS as defined by X-ray QSOs out to redshifts of ~ 4. The cosmological implications of the XMM-LSS are summarised in Sec. 2. In addition, the proposed X-ray survey is associated with several other major new generation surveys (optical, IR, Radio, UV). This will provide a new data set that can be used to study the evolution of clusters, cluster galaxies, and of star and AGN formation as a function of environment, in the context of structure formation. An overview of these capabilities is presented in Sec. 3. In the following sections we present a summary of results derived from the XMM AO-1 data set, demonstrating the feasibility of the project. Specifically, in Sec. 4, we describe our current X-ray source identification procedure, which led to the first spectroscopic and NIR follow-up campaigns in Autumn 2002 (Sec. 5 & 6). Future activities and immediate improvements are presented in Sec. 7.

1.5. The XMM-LSS consortium

The wide scope of the project has motivated the assembly of a large consortium to facilitate both the data reduction/management and the scientific analysis of the survey. The XMM-LSS Consortium comprises some fifteen European and Chilean institutes. The project is presented in detail on the following website: `http://vela.astro.ulg.ac.be/themes/spatial/xmm/LSS/index_e.html`

2. Survey design and cosmological implications

2.1. Defining the survey

Given our driving goal of extending the REFLEX achievements to high redshift (Sec. 1.4), the following objectives were decisive in designing the survey.

• **Measure the cluster correlation function in two redshift bins spanning $0 < z < 1$, with a good level of accuracy.** This implies a minimum of about 400 clusters for each bin.

• **Probe a comoving length which is significantly larger than 100 h^{-1}Mpc at $z \sim 1$, the characteristic scale in the galaxy power spectrum of the local universe (e.g. Landy et al 1996).** This constraint corresponds to an opening survey angle of $\sim 10°$ at $z = 1$ (i.e. 400 h^{-1}Mpc)

• **Find the best compromise between the two above constraints in order to minimise the necessary XMM observing time.** Quantitatively, we used the Press-Schechter formalism (Press & Schechter 1974) and the mass-temperature relation from simulations to predict the counts of clusters and their X-ray properties in several CDM models (Refregier et al 2002). We computed the detection efficiency of clusters, using realistic simulations of XMM images, and studied how this differs from a conventional flux limit. In order to fulfil the first 3 conditions above, and assuming the current favoured ΛCDM cosmological model, the optimal survey design was found to be an $8° \times 8°$ area, paved with 10 ks XMM pointing separated by 20 arcmin (i.e. 9 pointings per deg^2). The expected ultimate sensitivity is $\sim 3\ 10^{-15}$ erg cm^2 s^{-1} for pointlike sources in the [0.5-2] keV band. This is about 1000 and 10 times deeper than the REFLEX (Böhringer et al 2001) and NEP (Henry et al 2001) single area surveys respectively and provides much better angular resolution ($6''$ vs $2'$).

• **Find an adequate survey location.** An equatorial field is optimal, as ground-based follow-up resources from both hemispheres may be used. High galactic latitude and the absence of bright X-ray sources (e.g. nearby clusters) are also required. Moreover, the visibility of the field by XMM must be $\geq 15\%$. Given this, only one area in the sky turned out to be favorable: a field centred around $\alpha = 2^h18^m00^s$,$\delta = -7°00'00''$ (at $b = -58°$) with neutral hydrogen column $2 \times 10^{20} < N_H \mathrm{cm}^{-2} < 5 \times 10^{20}$. Whereas this region appears to be the best compromise between many astronomical and instrumental constraints, it should be noted that it is not optimal for far infra-red observations (above 25 μm) because of cirrus contamination. The X-ray survey is centred on two deeper areas (one and two square degrees) deriving from XMM guaranteed time programmes (GT). Several surveys are located in the same region (Sec.3) of which an overview map is presented on Fig. 2.

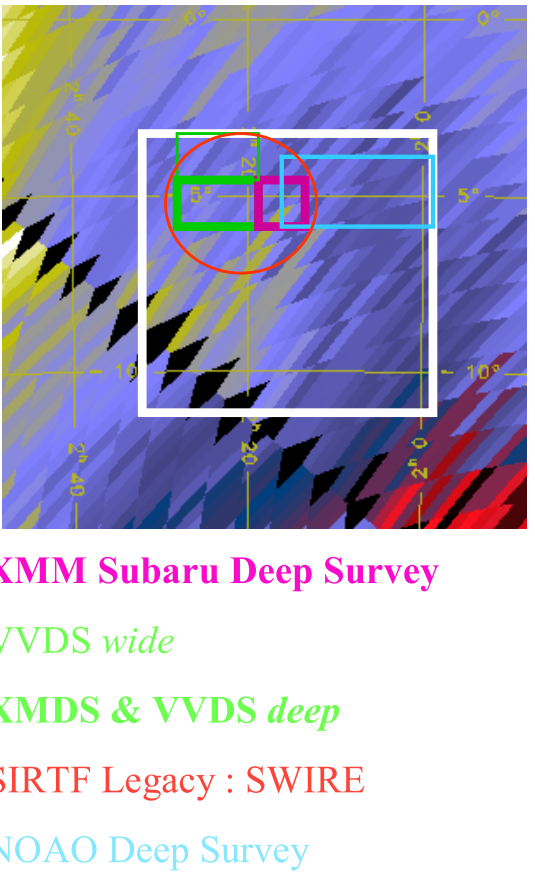

Fig. 2. Large white square indicating the location of the XMM-LSS survey is overlaid on a map of N_H($1.4\ 10^{20} < N_H < 3.5\ 10^{20}$ for the XMM-LSS field). The survey area surrounds two deep XMM surveys based on guaranteed time: the XMM_SSC/Subaru Deep Survey (80 ks exposures in 1 deg^2) and the XMM Medium Deep Survey (XMDS; 20 ks exposures in 2 deg^2) also corresponding to the VIRMOS-DESCART Deep Survey[*deep*], the latter being a collaboration between several instrumental teams: XMM-OM (Liège), XMM-EPIC (IASF-MILANO),XMM-SSC (Saclay); CFHTLS (Saclay, IAP); VIRMOS (LAM, IASF-MILANO,OAB). The area overlap will greatly assist in quantifying the completeness of the survey. Also indicated, are the positions of the associated DESCART-VIRMOS Deep Survey [*wide*], the SWIRE SIRTF Legacy Survey and the NOAO deep survey (Sec. 3).(Note that the center of the whole XMM-LSS survey has been shifted by 2 degree southward from its initial position because of the presence of the variable type M7 star Mira Ceti (02 19 20.8-02 58 39) which can reach I=1, thus very damageable for the optical mapping.)

2.2. Constraining cosmology - Quantitative assessments

The prospects that the XMM-LSS cluster catalogue offers for determining cosmological parameters have been studied in detail byRefregier et al 2002. We recall here the main issues.

• The cluster counts set strong constraints on the value of the $\Omega_m - \sigma_8$ combination. This combination will also

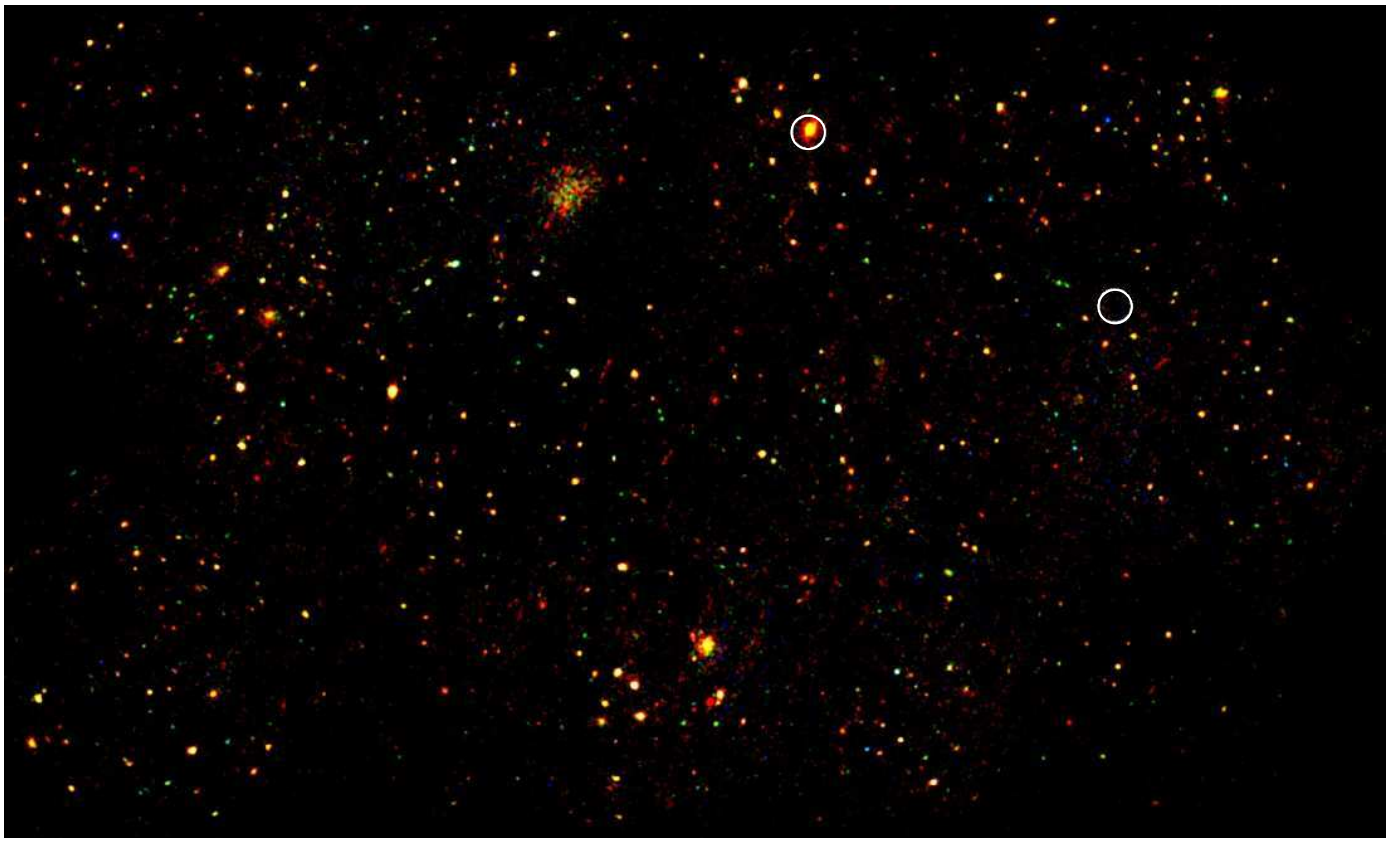

Fig. 3. First view of the deep X-ray sky on large scales. Image obtained combining the first 15 XMM-LSS fields mosaiced in true X-ray colours: red [0.3-1.0] keV, green [1.0-2.5] keV, blue [2.5-10.0] keV. The circles indicate the sources found in the RASS; the brightest one being a star, HD14938. The displayed region covers 1.6 deg^2. This is the first time that such an X-ray depth has been achieved over such an area. The improvement with respect to the RASS is striking, with a source density of the order of ~ 300 deg^{-2} in the [0.5-2] keV band. The wealth of sources includes supersoft and very hard sources, as well as sources with a wide range of intrinsic extents, giving an indication of the scientific potential of the XMM-LSS survey.

provide a consistency check for the ΛCDM model, and a discrimination between this model and the OCDM model.

• The addition of the cluster 2-point correlation function provides a constraint on Γ, the shape of the initial density fluctuation power spectrum.

• With the current survey design, the *simultaneous* expected precision on Ω_m, σ_8 and Γ is about 15%, 10%, 35% respectively. It is important to note that the present uncertainties on σ_8 globally result in a factor of 2 uncertainty in our predicted cluster numbers of $\sim$15 deg^{-2} (i.e. from 600 to 1200 clusters detections expected within $0 < z < 1$). The high sensitivity to σ_8 is not surprising, as it is precisely this which makes cluster counts a good measure of this parameter. This uncertainty can be reduced by analysing about 15 deg^2 of the XMM-LSS, the minimum area required to improve upon the current measurements of σ_8 in the presence of shot noise and cosmic variance.

• The sensitivity of the XMM-LSS survey allows the entire cluster population (≥ 2 keV) to be detected out to a redshift of 0.6, and will unveil the nearby group population. Rather few galaxy groups have been well-studied in the nearby universe, whereas they are believed to constitute the majority of the mass, and of the baryon reservoir. They are also the building block of richer clusters. With increasing redshift, the XMM-LSS is less sensitive to low mass systems. Consequently, the low-z and high-z samples to be used for the study of the LSS, will pertain to different cluster mass ranges. But as outlined above, this does not prevent the derivation of strong cosmological constraints. Further, in a more comprehensive approach, the XMM-LSS high-z clustering properties will be compared to the

REFLEX ones, which accurately sample the most massive nearby clusters.

3. Associated multi-wavelength surveys : an overview

While optical information remains the primary data base for X-ray source identification, contribution from other wave bands may be critical, for example in the far infrared domain, where many heavily absorbed X-ray QSO, not visible in the optical, are expected to show up. Beyond the necessary identification step, multi-wavelength information provides an overview of the energy emission and absorption processes in astronomical objects, which is vital to our understanding of their physics, formation and evolution. The contiguous design of the XMM-LSS, optimised for large scale studies, provides considerable advantages for complementary observations, compared to serendipitous fields, and the project has developed numerous collaborations at other wavelengths. The main characteristics of associated surveys are summarised in Table 1 and their main science applications are outlined below.

Optical, NIR and UV imaging: The imaging of the 8×8 deg^2 XMM-LSS area is one of the priorities of the Canada-France-Hawaii Legacy Survey[5] (CFHTLS). It will be performed by MegaCam, the one degree field imager built by CEA and installed at the new CFHT prime focus. Imaging of the XMM-LSS region will start by mid 2003. The CFHTLS will provide the deep high quality optical multi-colour imaging counterpart of the X-ray sources at a rate of 25 deg^2/yr in at least three colours. Data pipelines and processing have been developed by the TERAPIX[6] consortium which provides object catalogues and astrometric positions for the entire surveyed region. Currently, the optical data used for the identification work, and presented in this paper, mostly pertain to the CFH12K VIRMOS-DESCART VLT Deep Surveys (VVDS [*deep*] and [*wide*], Fig. 2 and Tab.1, (Le Fèvre et al 2003)). An optical cluster catalogue is under construction using the CFH12K (and later MegaCam) observations using both spatial clustering analysis and multi-colour matched filter techniques, in addition to photometric redshift estimates. Moreover, the MegaCam data will form the basis of a weak lensing analysis[7], whose cosmological constraints will be compared to those provided by the X-ray data on the same region. This will be the first, coherent study of LSS on such scales. R and z' imaging taken by us at CTIO are also being analysed, forming the basis of an independent cluster catalogue (Sec. 5.1, Andreon et al 2003). In addition, deep NIR VLT imaging (J & K) of $z > 1$ cluster candidates found in the XMM-LSS is performed as a confirmation prior to spectroscopy. Finally, a sub area of 8.5deg^2 of the XMM-LSS field is a high priority target of the Deep Extragalactic Survey part of the UKIRT Deep Sky Survey (UKIDSS[8]). In the UV domain, the XMM-LSS field will be one of the targets of the Galex[9] Deep Survey, whose main goal is to map the global history of star formation out to $z \sim 2$.

Spectroscopy: The standard spectroscopic follow-up is designed to perform redshift measurements for all identified $0 < z < 1$ X-ray clusters in Multi-Object-Spectroscopy mode, using 4m and 8m class telescopes. Current identification procedures and first results are described in later Sections. We shall subsequently undertake programmes of advanced spectroscopy that will focus on individual objects, and include high resolution spectroscopy, the measurement of cluster velocity dispersions and QSO absorption line surveys, as well as NIR spectroscopy of our $z > 1$ cluster candidates.

Radio: In the radio waveband, the complete survey region is being mapped using the VLA at 74MHz and 325MHz. First results of this low frequency coverage are described by Cohen et al 2003. Radio observations are not only particularly relevant for tracing merger events triggered by structure formation, but also as a useful indicator of galactic nuclear or star-formation activity.

Sunyaev-Zel'dovich: Observations (S-Z) are also planned. Clusters in the XMM-LSS field will be targets of the prototype OCRA (One-Centimeter Radiometer Array) instrument. The full XMM-LSS field will be mapped by the OCRA (in 2004-2004), and will be an early target of the Array for Microwave Background Anisotropy (AMiBA) (Liang 2001). This will enable not only the measurement of the Hubble constant, but also a statistical analysis of the physics of the ICM as a function of redshift. In the long term, these observations will also provide invaluable information on the low density structures such as cluster outskirts and groups, and their connections to supercluster filaments. These measurements are complementary to the X-ray and weak lensing surveys, connecting the mass distribution of clusters to the structure of the hot gas they contain. The three data sets together will also provide a direct and independent check of the extragalactic distance scale.

Infrared: In the infrared, the SWIRE[10] SIRTF Legacy Programme will cover $\sim$ 9 deg^2 of the XMM-LSS in 7 MIR and FIR wavebands from 4 to 160 μm (Lonsdale et al 2003). The estimated IR source densities per square degree in this area are around 1100/400/130 and 670/150/130 for starbursts/spiral-irregular/AGN in the $0 < z < 1$ and $1 < z < 2$ redshift intervals, respectively (Xu et al 2003). This represents a unique X-ray/IR combination in depth and scales to be probed. The coordinated SWIRE/XMM-LSS observations will clarify an important aspect of environmental studies, namely how star formation in cluster galaxies depends on distance from the cluster centre, on the strength of the gravita-

[5] http://cdsweb.u-strasbg.fr:2001/Science/CFHLS/
[6] http://terapix.iap.fr
[7] http://www.iap.fr/LaboEtActivites/ThemesRecherche/Lentilles/LentillesTop.html
[8] http://www.ukidss.org/
[9] http://www.srl.caltech.edu/galextech/galex.htm
[10] http://www.ipac.caltech.edu/SWIRE

Observatory/Instrument	(Planned) Coverage	Band	Final Sensitivity
XMM/EPIC	64 deg^2	[0.2-10] keV	$\sim 3\ 10^{-15}$erg cm^2 s^{-1} [1]
CFHT/CFH12K (VVDS Deep) *	2 deg^2 GT	B, V, R, I	26.5, 26.0, 26.0, 25.4 [2]
CFHT/CFH12K (VVDS Wide) *	3 deg^2 GO	V, R, I	25.4, 25.4, 24.8 [2]
CFHT/MegaCam	72 deg^2	u*, g', r', i', z'	25.5, 26.8,26.0, 25.3, 24.3 [3]
CTIO 4m/Mosaic	$\sim$ 16 deg^2	R, z'	25, 23.5 [4]
UKIRT/WFCAM	8.75 deg^2	J, H, K	22.5, 22.0, 21.0 [5]
VLA/A-array *	110 deg^2	74 MHz	275 mJy/beam [6a]
VLA/A-array	5.6 deg^2	325 MHz	4 mJy/beam [6b]
OCRA	all XMM-LSS clusters	30 GHz	100 μJy [7]
AMiBA	70 deg^2	95 GHz	3.0 mJy [8]
SIRTF/IRAC (SWIRE Legacy)	8.7 deg^2	3.6, 4.5, 5.8, 8.0 μm	7.3, 9.7,27.5, 32.5 μJy [9a]
SIRTF/MIPS (SWIRE Legacy)	8.9 deg^2	24, 70, 160 μm	0.45, 6.3, 60 mJy [9b]
Galex	$\sim$ 20 deg^2	1305-3000 Å	$\sim$ 25.5 [10]

Table 1. XMM-LSS X-ray and associated surveys Notes: * : complete[1]: for pointlike sources in [0.5-2] keV[2]: AB_{Mag}, 5″ aperture[3]: S/N = 5 in 1.15″ aperture[4]: 4 sigma in 3″ aperture[5]: $Vega_{Mag}$ [6a]: 30″ resolution; deeper observations planned[6b]: 6.3″ resolution[7] 5σ, detection limit[8] 6σ, detection limit[9a] 5σ[9b] 5σ[10]: AB_{Mag}

tional potential, and on the density of the ICM. In this respect the XMM-LSS represents the optimum SWIRE field, where galaxy environment, deep NIR imaging and optical spectroscopic properties will be the main parameters in modelling the MIR/FIR activity. Here also, the location of IR AGNs within the cosmic web will help establish their nature. The FIR/X/optical/radio association will also provide valuable insights into the physics of heavily obscured objects, as well as the first coherent study of biasing mechanisms as a function of scale and cosmic time, for hot (XMM), dark (weak lensing), luminous galactic (optical/NIR) and obscured (SWIRE) material.

In summary, the XMM-LSS multi-λ data set will offer the first evolving view of structure formation from supercluster to galaxy scales. Its comprehensive approach constitutes a decisive new step in the synergy between space and ground-based observatory resources and therefore a building block of the forthcoming Virtual Observatory.

4. X-ray source lists

In addition to the XMDS Guaranteed Time survey consisting of 18 pointings (Fig. 2), 33 Guest Observer XMM-LSS pointings have been allocated in the first two XMM AOs. At the time of writing (March 2003) all 20 ks GT and 10 ks AO-1 observations have been performed. The preliminary results presented in this section pertain to the first 15 GO XMM-LSS pointings displayed in Fig. 3. Most of the X-ray observations were performed in good conditions. Effective exposure times range from 5 to 16 ks (after removal of bad time intervals, mainly due to flares). The mean exposure time weighted over the area is about 12 ks and 9 ks for the MOS and pn detectors respectively, which is close to the nominal survey exposure time of 10 ks. These contiguous observations were used out to an off-axis angle of 13.3′ and cover a total area of 1.6 deg^2.

4.1. Source detection and statistics

The XMM-LSS pipeline (Dos Santos et al 2003) is based on a 3 stage filtering/detection/measurement process initiated by Valtchanov et al 2001. After applying the standard XMM reduction procedure[11], photon images are generated in several energy bands. These are subsequently wavelet filtered (in counts, to preserve Poisson statistics) computing the significance threshold (10^{-4}) in wavelet space by histogram auto-convolution, followed by an iterative reconstruction of the image (MR1, see Starck & Pierre 1998). The filtered images are then exposure-corrected and a mask map (discarding bad pixels and regions with too low an exposure) is constructed. These steps are performed for each detector independently, allowing us to obtain count-rate images without assuming a spectrum for the sources. Then, the three exposure-corrected images of the same field (MOS1, MOS2 and pn) are summed for the first detection step. Sextractor (Bertin & Arnouts1996), with parameters adjusted for X-ray filtered images, is then used to obtain a preliminary list of sources. The detection threshold is set to a low value, in order to avoid missing faint sources. The Sextractor source list is then fed into the XMM SAS EMLdetect task. For each source, this task performs a maximum likelihood PSF fit on each detector independently, thus yielding a quantitative measurement of the source in all detectors, taking into account the PSF variation with energy and off-axis radius, as well as other detector characteristics. The parameters that are varied for each source are: position, number of counts and extension. Position and extension are forced to be the same in each detector, while the number of counts is adjusted to an individual best-fit value for each EPIC instrument. Derived parameters are: source count rate (total and in each instrument), likelihood of detection (total and in each instrument), likelihood of source extent, and extension in arcsec. Since EMLdetect simply assumes a Gaussian

[11] http://xmm.vilspa.esa.es/external/xmm_sw_cal/sas_frame.shtml

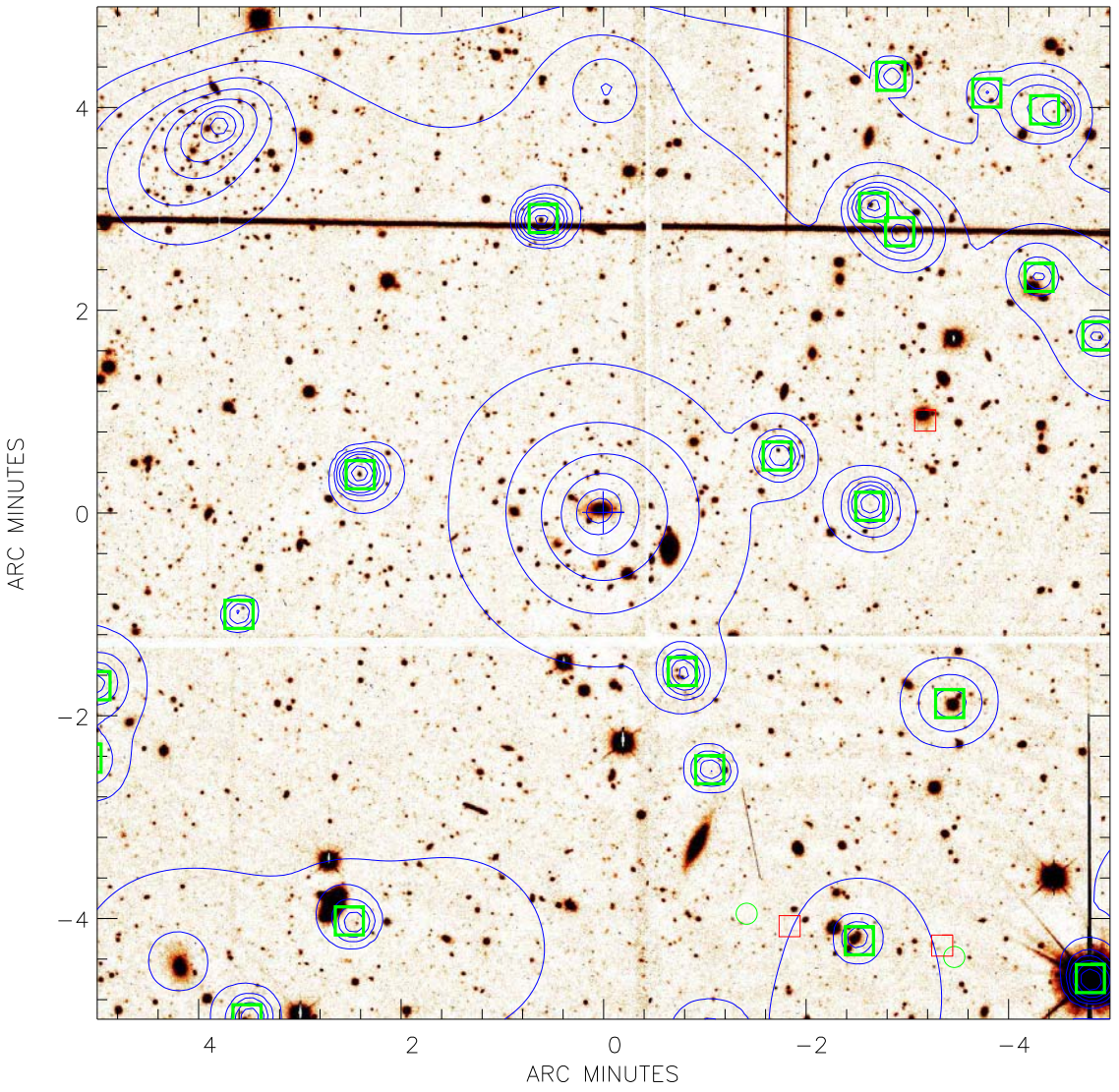

Fig. 4. This image ($10' \times 10'$) provides an overview of the source types encountered in the survey and of the identification procedure. Overlaid on a 1h exposure CFH12KI-band image (processed by Terapix) are blue XMM flux contours in [0.5-2] keV, obtained by the MR1 multi-scale wavelet filtering algorithm; the procedure allows the automatic recognition of point-like sources (green squares); the significance of the lowest wavelet contour is 10^{-4} (equivalent to 3.7σ for Gaussian noise, cf Starck & Pierre 1998). The image is centred on a bright extended X-ray source, corresponding to an obvious nearby cluster (a *NEAR* candidate) for which we measured a redshift of 0.33. Another - much more distant - cluster is apparent in the upper left corner (a *MID* candidate); this object was found to have a redshift of 0.84. Top middle, another extended source without a clear optical counterpart, typically a *DISTANT* candidate. The density of pointlike sources is high, some of them having an obvious optical counterpart, others, none. The red squares and green circles indicate VLA NVSS and 325 MHz radio sources respectively. In the lower right corner, there is a conspicuous double lobe radio galaxy, which is also an X-ray source.

profile for extended sources, we combine the results of Sextractor and EMLdetect and end up, for each extended source over the detection threshold with several geometrical parameters, including extension, major and minor axis length and principal angle. At this stage of processing, we adopt a conservative approach,retaining all sources detected by EMLdetect with a maximum likelihood[12] of 8; source counts being subsequently normalised by the exposure map. We finally select only sources having at least 20 counts (for the 3 detectors, in the [0.5-2] keV band). With

[12] corrected value: http://xmm.vilspa.esa.es/external/xmm_news/news_list/xmm_news_029.shtml

the analysis performed on the first 15 pointings, we detect some 250 sources per square degree down to a flux limit of 5 10^{-15} erg cm^2 s^{-1} in the [0.5-2] keV band (assuming a power-law spectrum with a photon index of $\Gamma = 1.7$). The current log N-log S curve is shown on Fig. 5.

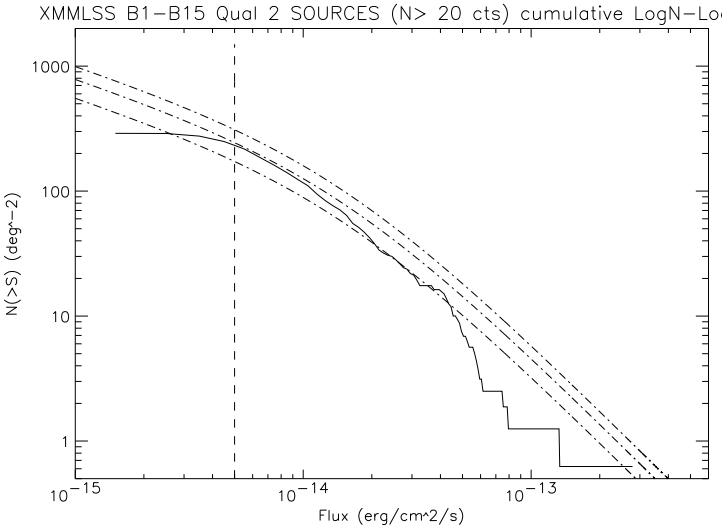

Fig. 5. Cumulative log N-log S distribution, in the [0.5-2] keV band, for the sources pertaining to the first 15 XMM-LSS pointings. The central dot-dashed line is the analytical fit of the deep log N-log S distribution, by Moretti et al 2003, bracketed by the 68% confidence level allowed by the uncertainty on the amplitude of the curve. The apparent lack of bright sources is explained by the small size of the current studied area and the fact that the region has been particularly selected for its low density of bright X-ray sources. Currently the completeness limit is reached around 5×10^{-15} erg cm^2 s^{-1}. Further refinements of the detection procedure, combined with extensive simulations, should allow us to lower this limit by a factor of two.

4.2. Extended sources and visual check

As clusters of galaxies constitute the core of the project, special care is devoted to the detection and assessment of faint extended sources. The MR1/Sextractor/EMLdetect hybrid method described above provides a series of parameters used to establish a preliminary list of extended sources. Currently, the procedure is performed on the [0.5-2] keV catalogue which offers optimal sensitivity considering the observed cluster emission spectra over the $0 < z < 1$ range, the various components of the background (galactic, particle, solar flares), and galactic absorption. We have developed an automated interface to produce X-ray/optical overlays for every extended source candidate (Fig.4). At the end of the pipeline procedure, each overlay is inspected by eye in order to catch possible instrumental artifacts which could have escaped the pipeline rejection algorithm. Finally, a list of plausible extended sources is issued with an indication of whether they correspond to an obvious overdensity of galaxies. We currently find an extended source density of about 15-20 deg^{-2}, with conspicuous optical cluster (or group) counterparts on the CFH12K I images. At this stage, given the small area explored, it is not possible to make firm statements about these results. The fact that we tend to find somewhat more extended objects than formally predicted, would suggest that either we sample the cluster population below the 2keV limit that was set in our theoretical predictions, using a given set of M-T-L(z) relations, (a small reduction in the limit to 1.8 keV, could account for this difference); or that we are more sensitive than assumed. An example of the good sensitivity we reach for extended sources is displayed in Fig. 6. This shows that we can flag extended sources down to a flux limit of $\sim 4 \times 10^{-15}$ erg cm^2 s^{-1} in the [0.5-2] keV band. The study of the log N-log S distribution of extended sources and of their selection function will be the subject of a forthcoming paper.

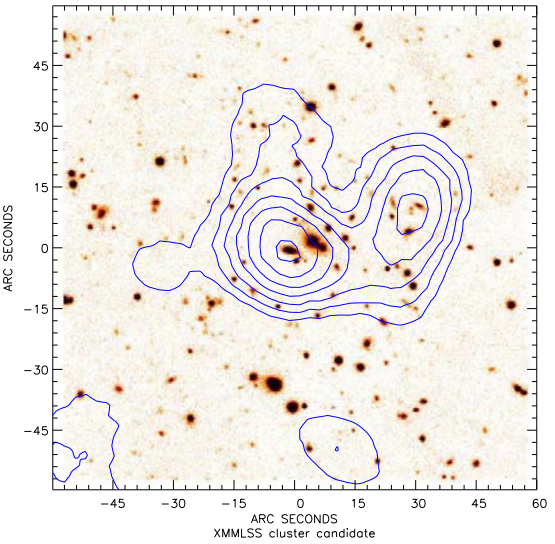

Fig. 6. The figure shows an XMM source detected as extended with only ~ 50 net counts in the combined image of the 3 detectors. The overlay on the optical image confirms the presence of a distant cluster ($z \sim 0.8 - 0.9$), and even reveals X-ray structure associated with 2 distinct groups of galaxies. The collected photons correspond to an emitted flux of $\sim 4 \times 10^{-15}$ or $\sim 1.2 \times 10^{-14}$ erg cm^2 s^{-1}, for a source falling on-axis or at an off-axis distance of 11′ respectively, assuming a typical thermal cluster spectrum.

5. Source classification

5.1. Clusters

The depths of both the XMM-LSS and of the CFHTLS and CTIO data, have been tuned to sample most of the cluster population out to a redshift of 1 (Sec. 2.1 and Tab. 1). Beyond this, massive clusters can still be detected in the X-ray band (Valtchanov et al 2001). A cluster located

at $z \sim 2$ and having a temperature of 7 keV will show up with an apparent temperature of about 2.5 keV, which falls in the most sensitive part of the XMM response. Hence, for such a cluster, the X-ray K-correction is only ~ 0.7 (Jones et al 1998). In contrast, $z > 1$ clusters do not appear as significant overdensities of galaxies in the optical band. Increasing the depth of the optical survey would not significantly improve the situation, as most of the galaxy light is shifted into the infrared band. We have therefore adopted the following approach and definitions:

1) A $z \leq 1$ cluster candidate is defined as an extended X-ray source corresponding to a significant visual excess of galaxies in the optical wavebands. The multi-colour BVRIz' information is used to enhance the visual contrast of the cluster galaxy density with respect to the background population and to construct optical cluster catalogues following different methods : the Red Cluster Sequence (Gladders & Yee 2000, Andreon et al 2003), clustering analysis in redshift slices (Adami et al1998), and matched filter (Lobo et al 2000).These catalogues are currently used as ancillary information and cross-correlated with the X-ray extended source catalogue. Further, the optical data allow us to assign photometric redshifts to the X-ray cluster candidates in an independent way. First, we apply the public code Hyperz (Bolzonella et al 2000) to the entire BVRI galaxy catalogue. For each galaxy, we derive the photometric redshift, corresponding to the minimum χ^2 computed comparing the observed photometry to the fluxes expected from a set of reference templates (GISSEL98, Bruzual & Charlot 1993). Second, we search for the cluster signature by placing a number of apertures in the field of the X-ray detection in order to determine the maximum overdensity in photometric redshift space relative to the "field" distribution (Bolzonella et al 2003) and Fig. 7). This approach does not assume that the distribution of cluster galaxy members apparent in the optical data is centred on the X-ray detection and it makes no prior assumption of the apparent optical extent of the candidate cluster. The redshift bin in $N(z_{\rm phot})$ has been set similar to the precision expected from photometric redshifts, given the set of filters and their depths (typically $\Delta z = 0.2$). Finally, from the region with the largest overdensity detected, we selected the candidate cluster members in different classes of confidence, considering their $z_{\rm phot}$, their error bars and probability functions. An impressive example of the power of the method is displayed on Fig.7 and 8. This procedure enables the pre-selection of the cluster candidates into *NEAR* and *MID* distance classes, corresponding to the $0 < z < 0.5$ and $0.5 < z < 1$ ranges respectively, and provides a useful tool for ascribing targets to the various telescopes available for the spectroscopic follow-up.

2) A small fraction of the extended sources (≤ 1 per pointing) do not present any significant optical counterpart – occasionally, one or two galaxies visible in the I or z' band, sometimes nothing at all. These are typically interesting $z > 1$ cluster candidates and are classified into the third category, *DISTANT*, to be imaged in the NIR bands. If confirmed, they will be the subject of dedicated spectroscopic follow-up programmes.

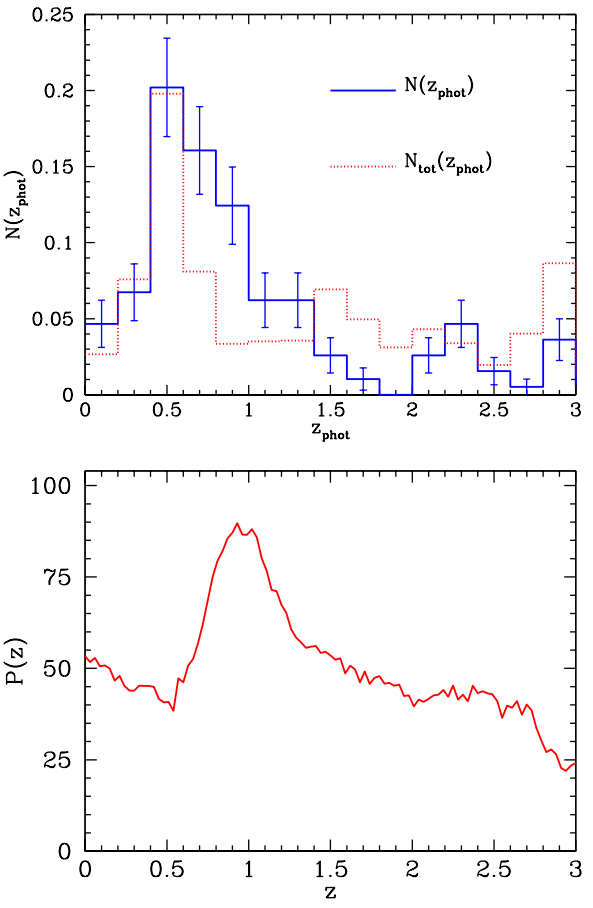

Fig. 7. Photometric redshift determination around the position of an X-ray cluster candidate (see text). Top: the photometric redshift distribution of the region where the overdensity has been detected (solid line), compared to the reference redshift distribution, obtained from the total catalogue (dotted line). The redshift distributions have been normalised to the respective number of objects. To select the significant overdensities, we plot the Poissonian error bars of the small region $N(z_{\rm phot})$. Bottom: combined photometric redshift probability as a function of redshift of galaxies selected within an aperture of radius $1'$ whose position within the field maximises the probability of the redshift "peak". Individual galaxy probabilities are determined from the chi-squared statistic returned from the photometric redshift template fitting procedure (Bolzonella et al 2003). VLT/FORS2 observations showed that this X-ray source indeed corresponds to a structure at $z \sim 0.9 - 1$. See Fig. 8

5.2. AGNs and QSO

Active galactic nuclei constitute by far, the dominant population of X-ray sources at the XMM-LSS sensitivity. Given the XMM PSF, and consequently, the positional accuracy, there is some ambiguity in the identification of pointlike sources, as can be appreciated in Fig. 4 (note the

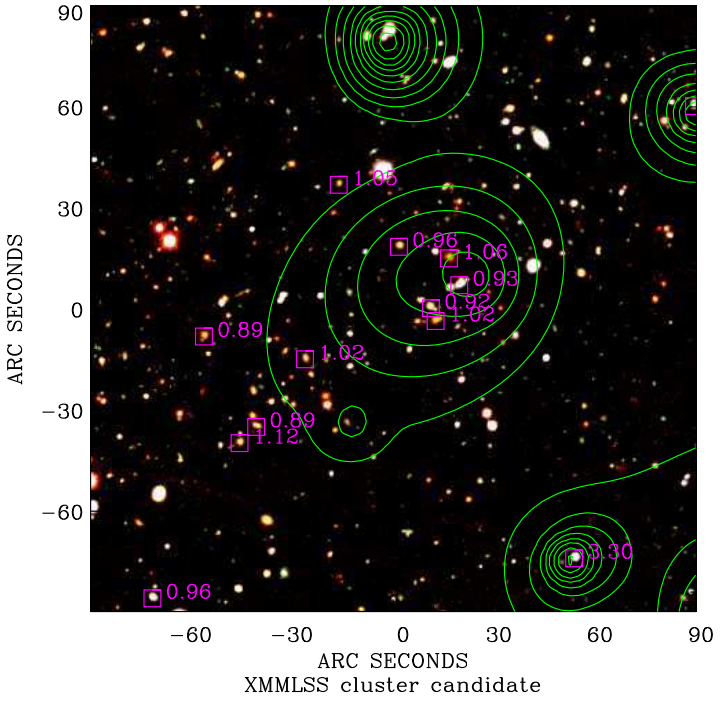

Fig. 8. The most distant X-ray complex identified so far, showing a clear concentration of galaxies in the $0.9 < z < 1$ range (Green X-ray contours overlaid on a CFH12K VRI composite). Bottom right is the most distant X-ray QSO currently measured in the XMM-LSS at a redshift $z = 3.3$ (see Fig. 11); its isophotes are distorted by the immediate vicinity of an X-ray bright emission line galaxy located at $z = 0.054$.

sources having two or three possible optical counterparts, or for which the optical ID is below the limit of the optical survey). This is a well known draw-back, thoroughly studied in deep surveys; but here, the situation is simpler since the XMM-LSS flux limit is well above the confusion limit.

6. First spectroscopic campaigns

6.1. Strategy

The first spectroscopic observations dedicated to the identification and redshift measurement of the XMM-LSS galaxy clusters took place during the fall of 2002. Three nights were allocated at ESO on the VLT/FORS2 instrument and 2 nights at Las Campanas with the Magellan/LDSS2 instrument. We summarise here the most important outcomes. Galaxy cluster candidates were pre-selected as described above, comprehensive information (X-ray, optical, photometric redshift) being gathered into an HTML database, allowing a rapid overview of the cluster properties. From this, we selected a number of clusters spanning different optical morphology and flux ranges, in order to optimise the allocated spectroscopic time, and to give a representative overview of the XMM-LSS cluster population. For the first spectroscopic campaign, it was decided to conservatively obtain two masks per cluster in order to sample well the cluster galaxies in the central region, and ensure confident redshift determination. Thanks to the high throughput of the FORS2 instrument in the [0.8-1] μm range, all *MID* galaxy clusters candidates were directed to the VLT sample. The *NEAR* ones were assigned to the Magellan sample, and also as backup sources for VLT, in case of possible low-quality weather conditions. In order to investigate and quantify the most efficient method for the future, galaxies to be measured were selected using different approaches: simple magnitude cut, colour selection or photometric redshift criteria.

No dedicated spectroscopic runs were planned in 2002 for the QSO and AGN population. However, many point-like X-ray sources surrounding the selected clusters and present in the corresponding instrumental field of view were included in the spectroscopic masks. For each $7' \times 7'$ field centred on a galaxy cluster candidate, we first cross-correlated the X-ray point-like source catalogues with the optical ones obtained from the CFH12K data. We then searched for optical counterparts within a radius of $5''$ from each X-ray point-like source and produced catalogues of associations. Using the latter, we overlaid on the optical images the positions of the X-ray sources and their associated optical counterparts, if any. Then, we visually checked on the optical images each X-ray position (no more than ten per field) associated with 0, 1 or more optical counterparts. Depending on the "quality" of the X/optical associations, we sorted the AGN/QSO candidates into different categories characterising the priority for spectroscopic observations of the optical counterparts. There were three main classes: (1) unambiguous cases where a unique and relatively bright optical source lies within a radius of $5''$; (2) ambiguous or doubtful cases when there were several possible optical counterparts and/or when the optical counterpart(s) was (were) rather faint; (3) rejected cases when there was no, or a much too faint, optical counterpart. The fraction represented by each class was $\sim$ 35, 25 and 40% respectively. A catalogue containing the first two classes of AGN/QSO candidates was considered for spectroscopic observations of each field. Given the constraints imposed by the cluster spectroscopy (especially, optimal sampling of the cluster cores) and the zones of avoidance within the FORS2 field of view, an average of 2-3 pointlike sources were measured per cluster field. This corresponds to about 30-45 sources per deg^2.

6.2. Overview of the results

Weather and working conditions at the VLT were optimal. In three nights, 12 cluster fields (5 *MID*, 7 *NEAR* – $z > 0.35$) were observed, containing on average about 30 slits per mask, yielding some 700 spectra. In addition 2 new nearby compact groups were also observed (with 7 and 8 galaxies per group), prepared as a backup pro-

gramme. The overall strategy proved successful. An example of spectrum is shown in Fig. 9. Encouragingly, an estimate of the velocity dispersion of a newly discovered 0.84 redshift cluster can be achieved in 2 hours, supporting the follow-up of large numbers of distant clusters with relatively little observing time. Seven *NEAR* clusters were observed at Magellan, where one night out of the allocated two suffered from poor meteorological conditions. With an average number of slits of 15 per masks, some 200 spectra were obtained.

Current results on the redshift distribution are shown on Fig.10. Given the selection procedure adopted for this first identification campaign, this cannot be ascribed any cosmological interpretation yet. The photometric cluster distance estimates proved useful and reliable indicators for the cluster classification (cf Fig. 7, 8). A comprehensive X-ray/optical study of the current *NEAR* and *MID* samples is presented by Willis et al 2003 and Valtchanov et al 2003 respectively. The optical properties of the cluster galaxies (luminosity function and colour distribution) are discussed by Andreon et al 2003.

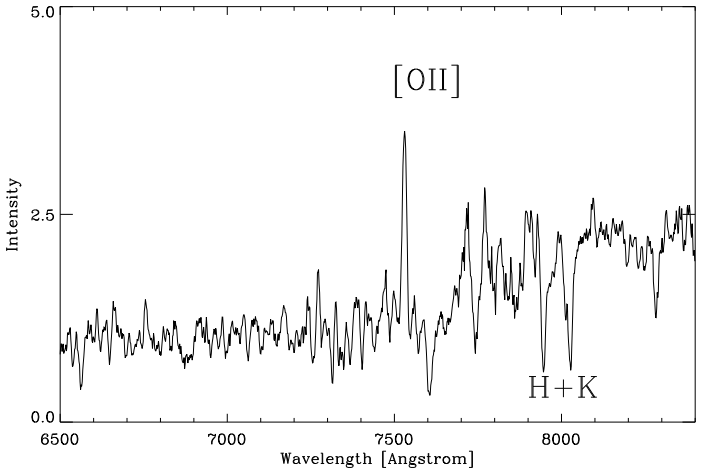

Fig. 9. One of the most distant cluster galaxy measured, at a redshift of $z = 1.02$ (see Fig. 8). This good quality spectrum was obtained in 1.5h with the R600RI+19 grism on the VLT/FORS2 instrument. The object has magnitudes of V=24.19, R=23.34, I=22.21 and displays characteristics of an elliptical galaxy having a component of young stars (E+A type).

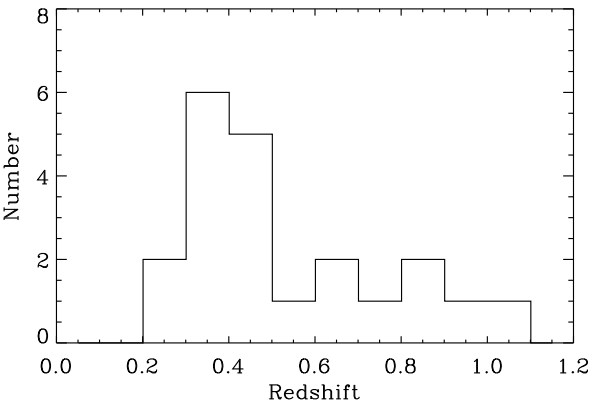

Fig. 10. Redshift distribution of the 19 spectroscopically confirmed clusters during the 2002 Magellan/LDSS and VLT/FORS2 runs.

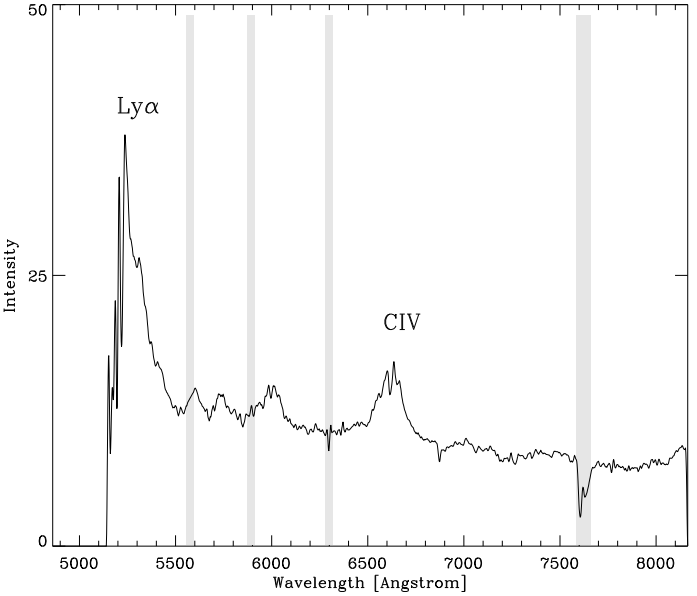

Fig. 11. Most distant X-ray AGN detected so far, at a redshift of $z = 3.3$ (see Fig. 8); grey bands indicate the position of strong atmospheric lines.

The optical spectra of the measured X-ray AGNs showed a plethora of properties. The most distant X-ray source measured so far has a redshift of 3.3 (Fig. 11). The AGN sample is currently under analysis (Jean et al 2003).

7. First NIR imaging campaign

In November 2002, we carried out an initial, exploratory observing run with SOFI on the NTT, in order to search for *DISTANT* clusters selected from candidates in the first set of available XMM data. The details will be presented elsewhere (Bremer et al 2003). Here we note that by selecting faint, extended X-ray sources associated with either blank fields in the CFHT data, or with fields showing a hint of clustering at faint ($I > 22$) magnitude levels in the same data, we were successful at reliably detecting such clusters. Moreover, the X-ray fluxes of these objects are such that if they were placed at higher redshifts they would still be detectable in the XMM-LSS exposures. Thus the survey will enable us to map the cluster distribution to redshifts well above $z = 1$. An example is shown In Fig. 12 and13.

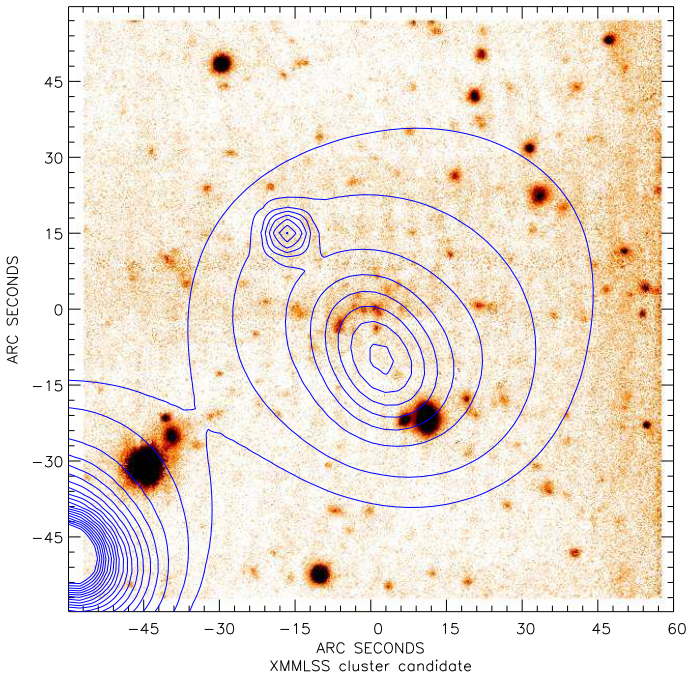

Fig. 12. Extended X-ray source with a very faint optical counterpart in the I-band. The NIR image of the field is shown in Fig. 13.

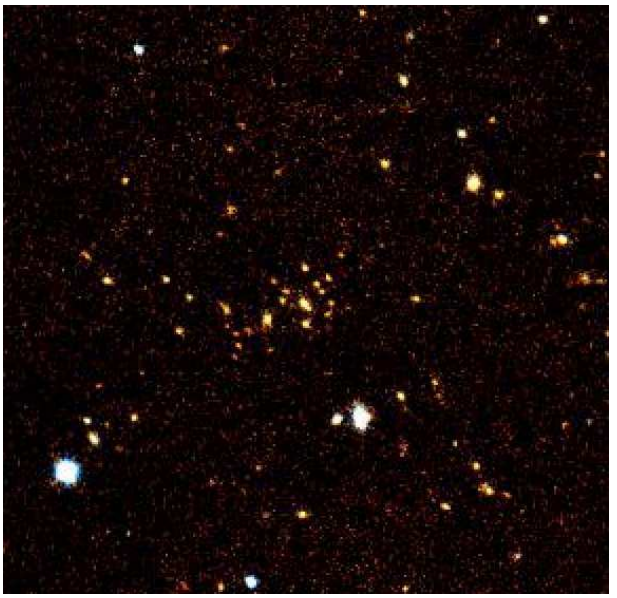

Fig. 13. J-K colour image of the *DISTANT* cluster candidate flagged in Fig. 12. This presents a significant overdensity of red objects. The brightest cluster member has Ks$\sim 17.5 \pm 0.3$, and the other objects within $20''$ are generally fainter than Ks ~ 18.5. These properties are consistent with a cluster at $z = 1$ or above.

8. Conclusion and prospects

8.1. The newly discovered clusters

Following the completion of the AO-1 period, the main outcome of the XMM-LSS project can be summarised as follows : XMM observations of only 10 ks, coupled with a similar time spent on imaging at CFHT or CTIO, can detect a significant fraction of the cluster population out to $z \sim 1$ (a flux of 0.8×10^{-14} erg cm^{2}s^{-1} corresponds to a cluster mass of 6.7×10^{13} M$_\odot$ [T = 2.7 keV] at $z = 1$, assuming typical scaling laws). Moreover, adding two hours of FORS2 spectroscopic time, provides a reliable estimate of cluster velocity dispersion at $z = 0.85$. This represents a substantial increase in efficiency compared to former high-z cluster searches. The feasibility of the XMM-LSS programme is now fully demonstrated, and the current data set already provides a valuable sample for cosmological studies. For the first time, we are detecting the numerous population of low luminosity (mass) objects out to $z \sim 0.5$; this will allow a dense mapping of the matter distribution. So far (within ~ 4 deg^2, including the GT area), no massive object has been detected and, following a detailed inspection of the optical images, no giant arcs have been found in the identified clusters. These results are consistent with the Press-Schechter formalism (folded with the current favoured cosmological model) predicting 2.8 and 0.0001 cluster per deg^2 between $0 < z < 1$ for clusters more massive than $10^{14} M_\odot$ and $10^{15} M_\odot$ respectively, if we assume that in only massive clusters are potential strong lenses. Of course, an additional necessary condition is the steepness of the mass profile.

Immediate foreseen improvements are the following: in the next version of the X-ray pipeline, the source flux detection limit will be significantly lowered. This requires further work on the background estimation. In parallel, extensive simulations are being performed to improve the characterisation (extent and flux) of the faintest sources as well as to determine the survey selection function. This is complicated by the necessity of taking proper account of the Poisson nature of the data and the fact that the signal to be analysed comes from 3 different detectors.

8.2. Cluster identification refinements

In a second step, we shall systematically investigate overlaps and differences between the optical cluster catalogues and the X-ray extended source catalogue. There are two main reasons why variations should be observed: (i) faint groups or distant clusters may not be unambiguously detected as extended sources because of their low flux or, alternatively, because they host a cooling flow, which makes them appear unresolved. Currently, we are confident that any regular object having a typical core radius of the order of $125 h_{100}^{-1}$ kpc and producing a net number of counts of ≥ 70 is detected by the pipeline as an extended source (Valtchanov et al 2001); (ii) there are intrinsic differences between the X-ray and optical catalogues since the methods used to construct them rely on specific assumptions as to galaxy colour and evolution, or on the properties of the IGM at high redshift. Understanding the discrepancies will not only increase the efficiency of our cluster finding pro-

cedure, but also shed light on the much debated topic of cluster formation and evolution. This will also contribute to the improvement of our photometric redshift determination procedure. Finally, output from the weak lensing analysis will reveal large mass concentrations, optimally within the $0.1 < z < 0.5$ range. Again, the comparison between the X-ray and optical catalogues will be most instructive. Given the current understanding of structure formation, it is difficult to devise a physical process that would prevent gas being trapped or heated within large concentrations of dark matter. However, the surveyed volume is ideally suited to systematically search for "dark clump".

8.3. Active galactic Nuclei

Due to the primary goal of the spectroscopic observations performed so far (confirmation and redshift determination of X-ray selected galaxy clusters), few AGN/QSO candidates could actually be observed. For this reason, a spectroscopic survey of a unique sample of X-ray selected AGN/QSOs within a large contiguous area of some 10 deg^2, typically complete down to $F_{[2-10]keV} \sim 10^{-14}$ erg cm^2 s^{-1}, $F_{[0.5-2]keV} \sim 5\times10^{-15}$ erg cm^2 s^{-1} and $I_{AB} = 22.5$ is foreseen. Because of the large surface density of AGN/QSO candidates detected in the XMM-LSS field (typically > 200 deg^{-2} with $0 < z < 1$), compared to previous surveys, it should be more sensitive to contrasts between voids and peaks than previous surveys, such as 2dF. This will enable us to study with high precision the correlation function of these objects over scales in the [2-400] Mpc range, to probe the environmental influence on various type of AGN, and to compare these correlations with those for normal galaxies. The distinct redshift distributions of X-ray selected type I and type II AGN will be very accurately determined, and this will provide interesting constraints on models of black hole formation compared with models of star formation. The proposed studies will provide a comparison of the clustering properties, as a function of redshift, of X-ray, optical (2dF) or radio selected AGN/QSO.

8.4. Survey products

A dedicated *mysql* database with a Java front end interface is available via a site at IASF Milano[13] with a mirror at ESO Santiago. This will include the X-ray source catalogue, and complete catalogues of surveys performed by the LSS Consortium in other wavebands, together with selected subsets from the surveys performed by other Consortia made available under agreement. It will also give access to a selection of data products. The database, currently accessible and used internally by the Consortium, will be gradually opened to the public. The first public release, based on the AO-1 pointings (X-ray source lists and available identifications) is foreseen for the beginning of 2004.

[13] http://cosmos.mi.iasf.cnr.it/~lssadmin/Website/LSS/

Acknowledgements. SDS is supported by a post-doctoral position from the Centre National d'Etudes Spatiales. MP and IV are grateful to the ESO/Santiago Office for Science, for a 2 week stay in October 2002, were the the analysis of the VLT data presented here was initiated.

References

Adami C., Mazure A., Katgert P., Biviano A., 1998, A&A 336, 63
Andreon S. et al A&A 2003 *in preparation*
Arnaud, M. & Evrard, A., 1999, MNRAS, 305, 631
Bertin M., Arnouts S., 1996, A&AS, 117, 393
Böhringer, H., Voges, W., Huchra, J. P., McLean, B., Giacconi, R., Rosati, P., Burg, R., Mader, J., Schuecker, P., Simiç, D., Komossa, S., Reiprich, T. H., Retzlaff, J., Trümper, J., 2000, ApJS, 129, 435
Böhringer H., Schuecker P., Guzzo L., Collins C. A., Voges W., Schindler S., Neumann D. M., Cruddace R. G., De Grandi S., Chincarini G., Edge A. C., MacGillivray H. T., Shaver P., 2001,A& A 369, 826
Bolzonella, M., Miralles, J.-M. & Pelló, R. 2000, A&A 363, 476
Bolzonella et al, 2003, A&A *in preparation*
Bremer M. et al , 2003 A&A *in preparation*
Bruzual, G. & Charlot, S. 1993, ApJ 405, 538
Castander, F. J., et al. 1995, Nature, 281, 59
Cohen A. et al 2003, ApJ *submitted*
Collins, C. A., Burke, D. J., Romer, A. K., Sharples, R. M.,Nichol, R. C., 1997, ApJ, 479, L117
de Grandi, S., Böhringer, H., Guzzo, L., Molendi, S., Chincarini, G., Collins, C., Cruddace, R., Neumann, D., Schindler, S., Schuecker, P., Voges, W., 1999, ApJ, 514, 148
Donahue, M., Mack, J., Scharf, C., Lee, P., Postman, M., Rosati, P., Dickinson, M., Voit, G. M., Stocke, J. T., 2001, ApJ, 552, L93
Dos Santos et al 2003, A&A *in preparation*
Ebeling, H., Voges, W., Bohringer, H., Edge, A. C., Huchra, J. P.,Briel, U. G. 1996, MNRAS, 281, 799
Ebeling, H., Edge, A. C., Bohringer, H., Allen, S. W., Crawford,C. S., Fabian, A. C., Voges, W., Huchra, J. P. 1998, MNRAS, 301, 881
Ebeling, H., Edge, A. C., Henry, J.P 2001, ApJ, 553, 668
Ebeling, H., Edge, A. C., Allen, S. W., Crawford, C. S., Fabian, A. C., Huchra, J. P., 2000, MNRAS, 318, 333
Eke, V.R., Cole, S., & Frenk, C.S., 1996, MNRAS, 282, 263
Gioia, I. M.; Henry, J. P.; Maccacaro, T.; Morris, S. L.; Stocke,J. T.; Wolter, A., 1990, ApJ Let 356, L35-L38
Gladders M.D., Yee H.K., 2000, AJ 120, 2148
Haiman Z., Mohr J. J., Holder G. P., 2001, ApJ, 553, 545
Henry J. P., Gioia I.M., Mullis C.R., Voges W., Briel U.G.,Böhringer H., 2001, ApJ Let 553, L109
Hu W., 2003, astroph/0301416
Jean C. et al 2003, A&A *in preparation*
Jones, L. R., Scharf, C., Ebeling, H., Perlman, E., Wegner, G.,Malkan, M., Horner, D. 1998, ApJ, 495, 100
Landy S.D. et al., 1996, ApJ 456, L1
Le Fevre, O., Mellier, Y., McCracken, H.J., Foucaud, S., Gwyn, S., Radovich, M., Dantel-Fort, M., Bertin, E., Cuillandre, J.C., Le Brun, V., Mazure, A., Moreau, C., Pierre, M., Tresse, L., Veillet, C., 2003, *A&A, submitted*

Liang H., 2001, astro-ph/0110518
Lonsdale C. et al 2003, PASP, *submitted*
Lobo C., Iovino A., Lazzati D., Chincarini G., 2000, A&A 360, 896
Moretti A., Campana S., Lazzati D., Tagliaferri G., 2003astoph/0301555
Panzera, M. R., Campana, S., Covino, S., Lazzati, D., Mignani, R.P., Moretti, A., Tagliaferri, G. 2003, A&A, 399, 351
Perlman, E. S., Horner, D. J., Jones, L. R., Scharf, C., Ebeling, H., Wegner, G., Malkan, M., 2002, ApJS, 140, 265
Peterson J.R., Ferrigno C., Kaastra J.S., Paerels F.B.S., KahnS.M., Jernigan J.G., Bleeker J.A.M., Tamura T., 2002,astro-ph/0202108
Press, W.H., & Schechter, P., 1974, ApJ, 187, 425
Refregier A., Valtchanov I., Pierre M., 2002, A&A 390, 1
Refregier A., Dos Santos S.,Valtchanov I., Pierre M., 2003*in preparation*
Romer, A. K., Nichol, R. C., Holden, B. P., Ulmer, M. P., Pildis,R. A., Merrelli, A. J., Adami, C., Burke, D. J., Collins, C. A., Metevier, A. J., Kron, R. G., Commons, K. 2000, ApJS, 126, 206
Romer, A. K., Viana, P. T. P., Liddle, A. R.; Mann, R. G., 2001, ApJ, 547, 594
Rosati P., della Ceca R., Norman C., Giacconi R., 1998, ApJ Let492, 21L
Rosati P., Borgani S., Norman C., 2002, astroph/0209035
Starck J.-L., Pierre M., 1998, A&A 128, 397
Sheth R. K. Tormen G., 1999, MNRAS 308, 119
Valtchanov I., Pierre M., Gastaud R., 2001 A&A 370, 689
Valtchanov I. et al 2003, A&A *in preparation*
Xu C.K., Lonsdale C. J., Shupe D. L., Franceschini A., Martin C.,Schiminovich D., 2003 *ApJ in press* (astro-ph/0212344)
Vikhlinin, A., McNamara, B. R., Forman, W., Jones, C., Quintana,H., Hornstrup, A. 1998a, ApJ, 502, 558
Willis J. et al 2003, A&A *in preparation*

B. The XMM-LSS survey
II. First high redshift galaxy clusters : relaxed and collapsing systems

Valtchanov I., Pierre M., Dos Santos S. et al, 2003, A&A, submitted

Astronomy & Astrophysics manuscript no. XMM-LSS˙II June 19, 2003
(DOI: will be inserted by hand later)

The XMM-LSS Survey

II. First high redshift galaxy clusters: relaxed and collapsing systems⋆

Ivan Valtchanov[1], Marguerite Pierre[1], Jon Willis[2], Sergio Dos Santos[1], Laurence Jones[3], Christophe Adami[4], Bruno Altieri[5], Stefano Andreon[6], Micol Bolzonella[7], Pierre-Alain Duc[1], Eric Gosset[8], Christophe Jean[8], and Jean Surdej[8]

[1] CEA/Saclay, Service d'Astrophysique, F-91191, Gif-sur-Yvette, France
[2] ESO, Ave. Alonso de Cordova 3107, Casilla 19, Santiago 19001, Chile
[3] School of Physics and Astronomy, University of Birmingham, Birmingham
[4] LAM, Traverse du Siphon, 13012 Marseille, France
[5] ESA, Villafranca del Castillo, Spain
[6] INAF-Osservatorio Astronomico di Brera, via Brera 28, 20121 Milano, Italy
[7] Istituto di Astrofisica Spaziale e Fisica Cosmica, Sezione di Milano, via Bassini 15, 20133 Milano
[8] Université de Liège, Allée du 6 Août, 17, B5C, 4000 Sart Tilman, Belgium

Received, June 19, 2003, Accepted, June 19, 2003

Abstract. We present the first five spectroscopic identifications of new clusters of galaxies at $z > 0.6$ found in the XMM Large-Scale Structure Survey (XMM-LSS). All five candidates are extended X-ray sources in the XMM images. For three of them we have sufficient spectroscopically confirmed member galaxies that an estimate of the velocity dispersion is possible: XLSS-001 at $z = 0.61$ with 29 concordant redshifts, XLSS-002 at $z = 0.77$ with a compact core and 8 galaxies with concordant redshifts at $1.5'$ from the centre and XLSS-003 at $z = 0.84$ with 17 cluster members. The three clusters are at intermediate X-ray luminosities: $L_X \sim 1 - 3 \times 10^{44}$ erg s^{-1} and follow the low redshift scaling relations between L_X, T and σ_v. They have lower temperatures and subsequently are less massive than the previously known clusters at similar redshifts. Thus for the first time we are starting to detect in a systematic way intermediate mass clusters in the high redshift Universe.
Two candidates, XLSS-004 and XLSS-005, cannot be confirmed by these spectroscopic observations, although XLSS-004 is detected independently as an overdensity of galaxies of a colour R-z'=1.4 that matches the redshift of the central galaxy $z = 0.89$. XLSS-005 is a complex system at a redshift around unity associated with an unequivocally extended X-ray source with probable substructure. The X-ray morphology and the distribution of the galaxies with spectroscopic and photometric redshifts in this region point toward an interpretation of two clusters in projection: one at $z \sim 0.95$ and a more distant one at $z \sim 1.02$. Because of their small separation on the sky we are probably detecting for the first time a large-scale structure filament at a redshift of unity as traced by the two clusters.

Key words. X-rays: galaxies: clusters; Cosmology: large-scale structure of Universe; Surveys

1. Introduction

Statistical samples of distant galaxy clusters can serve as a powerful tool to study the large-scale structure of the Universe. To obtain cluster samples deep enough and over a large area with optical or near-infrared observations is quite a difficult task (e.g. Gunn et al. 1986, Postman et al. 1996, Gonzales et al. 2001, Stanford et al.1997). Projection effects and the small field-of-view of the current NIR imagers interplay to make relatively large contiguous surveys of distant clusters a dubious game.

X-ray observations, by their nature, are much more appropriate and less contaminated by projection effects. From EINSTEIN and ROSAT based X-ray cluster surveys we have gained knowledge about individual objects, scaling relations, the large-scale distribution, the clustering properties and the evolution of galaxy clusters (see Rosati et al. 2002 for a review). With the XMM and Chandra X-ray observatories in orbit we can push the observational limits further. The increased sensitivity can be exploited not only in single deep fields but large areas of the sky can also be surveyed with relatively short exposure times. A

Send offprint requests to: Ivan Valtchanov, e-mail: ivaltchanov@cea.fr

⋆ Based on observations obtained with XMM-Newton, CFHT, ESO (program ID: 70.A-0283)

fainter cluster/group population at intermediate redshifts that was not accessible to the previous X-ray missions will thus be detected. In return, this will give us a unique view of the cosmic web as traced by this population.

One of the most important questions is to investigate the clustering properties of the nearby and distant Universe. This is the main scientific goal of the XMM Large-Scale Structure Survey (Pierre et al. 2003, hereafter paper I) – to compute the cluster-cluster correlation function in two redshift bins within $0 < z < 1$. The XMM-LSS survey geometry and depth was chosen such that to have a statistically significant number of objects in these two regions, necessary to improve our knowledge over the results of the ROSAT-ESO Flux Limited X-ray Survey (REFLEX) which covers a much larger area but only reaches $z < 0.2$ (Böhringer et al. 1998).

To achieve the objectives of the XMM-LSS we have developed an efficient procedure that uses the full instrument sensitivity and indeed allows us to detect extended sources down to flux levels of 8×10^{-15} erg s^{-1} cm^{-2} for 10 ks exposures with XMM (Valtchanov et al. 2001, Dos Santos et al. 2003). The detection is quite crucial because even the mere counting of clusters at different redshifts, the so called cluster abundance evolution, can be used to constrain the cosmological parameters (e.g. Refregier et al. 2002 and references therein) that are complementary and independent to the constraints from the cosmic microwave background and the supernovae studies.

The first spectroscopic follow-up of the candidate clusters at $z < 1$ was programmed for observations on Las Campanas/Magellan and on the ESO/VLT telescopes. The subject of this paper is to present the first results for a sample of 5 clusters at $z > 0.6$.

The paper is organised as follows: first we present the X-ray data reduction and source detection (Sect. 2), then in Sect. 3 the optical identification, spectroscopic target selection procedure and the observations are described. In Sect. 4, we present the data analysis results from the spectroscopic and X-ray observations. Next we discuss each individual object (Sect. 5) and end up with the conclusions (Sect. 6). Except where is mentioned, we use a ΛCDM cosmology ($H_0 = 70$ km s^{-1} Mpc^{-1}, $\Omega_m = 0.3$, $\Omega_\lambda = 0.7$) for all cosmologically dependent parameters.

2. X-ray data

The sources for the first spectroscopic run were chosen from all XMM-LSS pointings received by August 2002. This includes 15 AO-1 pointings of 10ks exposures and another 15 of 20 ks exposures from the Guaranteed Time XMM Medium Deep Survey (XMDS, see paper I for details). All observations were of good quality, except two fields that suffered from high background contamination affecting $> 50\%$ of the exposure time.

2.1. Data reduction

A detailed description of the pipeline used in the XMM-LSS data reduction will be presented in Dos Santos et al. (2003). Here we just briefly mention the main steps. The X-ray observations were reduced by the standard XMM Science Analysis System (XMM-SAS) tasks `emchain` and `epchain` for MOS and PN detectors respectively. High background periods related to soft protons were excluded from the event lists and raw photon images in different energy bands were then created. Subsequently the raw images for each instrument were filtered using "à trous" (with holes) iterative wavelet technique with a Poisson noise model and a threshold of 10^{-4} (equivalent to 3.7σ in the Gaussian case) for the significant wavelet coefficients (Starck & Pierre 1998, Starck et al. 1998). Each filtered image is then exposure corrected and a mask map that includes bad pixels, CCD gaps and non-exposed CCD regions (generally parts outside the field-of-view of the telescope) are created. Wavelet-filtered, exposure-corrected images for each instrument in a given energy band are added together to form a total band image to be used in the first stage of the detection procedure.

2.2. Source detection

Clusters of galaxies are extended sources in X-ray images and their detection and correct classification is not trivial because of various peculiarities of the X-ray observations: Poisson noise regime, varying PSF as a function of off-axis angle, vignetting effect, and detector geometry (gaps). We use images in the [0.5-2] keV energy band which is well suited for clusters and groups (Scharf 2002). The detection procedure is based on the prescription of Valtchanov et al. (2001) and has three stages: wavelet filtering (see the previous section), detection and measurements. The wavelet filtered image is fed to `SExtractor` (Bertin & Arnouts 1996) for detection, characterization and classification improved by using weighted images that incorporate the detector masks and bad pixels.

The third step in the detection procedure consists of a maximum-likelihood fit of the PSF to each source, as implemented in the XMM-SAS `emldetect` package, using the `SExtractor` source list as input. The main objective is to improve the source characteristics and classification measurements and obtain the likelihood of the detection and of the extension (see Dos Santos et al. 2003 for details).

In total, from all available X-ray observations, we find some 55 X-ray cluster candidates from about 3.5 deg^2 (30 XMM pointings), which corresponds to ~ 15 clusters per sq.deg., in good agreement with the cosmological predictions (see paper I for details).

3. Optical data

3.1. Optical imaging

Deep images from the CFH12k camera on the Canada-France-Hawaii Telescope (CFHT) in BVRI from the VIRMOS-VLT Deep Survey (VVDS: Le Fèvre et al. 2001, McCracken et al. 2003) were used for optical identifications. The observations were processed by the Terapix team[1] to produce astrometrically and photometrically calibrated images and to create object catalogs by means of `SExtractor`. The definition and magnitude limits of the VVDS may be found in the web pages of the VIRMOS consortium[2]. The X-ray cluster candidates were assigned to *NEAR* ($z < 0.5$) and *MID* ($0.5 < z < 1$) samples by visual inspection of the optical images and also using photometric redshift estimates (paper I). The visual scan of the data was also indispensable for removal of spurious extended sources introduced by instrumental effects or by the iterative wavelet filtering procedure. In addition to the CFH12k data, we obtained observations at the CTIO 4m telescope in R and z' which allowed us to search for a red sequence of galaxies at a given X-ray position (Andreon et al. 2003a).

3.2. Spectroscopic target selection

Our driving objective was to confirm the clusters and to measure their redshifts. We chose the ESO-VLT/FORS2 instrument in MXU multi-object spectroscopy mode because of the liberty to place a large number of slits with different sizes and orientations and so to optimize the target selection, especially in regions of high galaxy density. Using `fims` (the FORS Instrumental Mask Simulator tool), we placed about 30 slits on average in each mask, eventually placing inclined and longer ones. We also randomly sampled the X-ray QSO population presented in the same area with the remaining available slits.

We have developed a visualization procedure to facilitate the selection of spectroscopic targets, optimizing the chances to pick up cluster member galaxies. It uses all the available information in the field, combining optical (one band or pseudo-colour VRI image) and X-ray images, colour-magnitude and colour-colour diagrams, and photometric redshift peaks and probabilities (see paper I for details). In this "multi-parametric space", first we have taken the objects above the photometric limit, imposed by exposure time and observational strategy constraints. Secondly, we have looked for objects with a plausible colour (V−I or R−I) for ellipticals at the estimated photometric redshift and also used the pseudo-colour images for all candidates for which we have V, R and I observations. The utility of colour information is justified as, out to redshift of unity, the major population of cluster cores is made of ellipticals with an old stellar population (e.g. Dressler et al. 1997, Postman et al. 1998). Moreover, cluster ellipticals at high redshift show-up as an overdensity of red objects in VRI composite images, proving useful in the target selection process. Examples of RGB images for some of the candidate clusters can be found in the web pages of the XMM-LSS consortium[3]

3.3. Spectroscopic observations

The ESO-VLT/FORS2 spectroscopic observations in MXU mode were performed on 9-12 October 2002. For the 3 allocated nights in "visitor" mode we selected some 12 candidates from the *NEAR* and *MID* samples. *NEAR* clusters were included in order to provide targets in case of a poor weather and will be presented elsewhere (Willis et al. 2003). The observing log and object designations for the 5 clusters pertaining to this paper, that fall in the *MID* sample and at $z > 0.6$, are shown in Table 1.

We have used the holographic grism 600RI+19 with the GG435 blocking filter that gives a good response from about 5000 to 8500 Å and a dispersion of 1.64 Å/pixel with the standard instrument resolution. The spectral resolution for slits of $1.4''$ width as measured from the arc or sky lines was ~ 6 Å FWHM. The high resolution of the grism ($\lambda/\Delta\lambda = 1000$) makes subsequent sky subtraction easier.

For each mask we split the total observing time into two exposures in order to remove the cosmic ray contaminations with `IRAF/imcombine` task and `crreject` algorithm that is appropriate for rejecting cosmic ray events even with two images. The spectral reduction was performed using the standard tools from `IRAF`: zero level exposure, flat-fielding, cosmic ray removal, aperture selection and sky subtraction using the `apextract` package. For wavelength calibration, we have used He-Ne-Ar lamp exposures observed at the end of the corresponding night. The wavelength calibration was performed with a Chebyshev polynomial of 3rd degree and the residuals were kept inside ± 1.0 Å with an rms $\sim 0.3-0.5$ Å. A standard star was observed in the beginning and at the end of each night with the same instrumental configuration in order to remove the instrumental response and therefore to transform the spectra to relative flux units.

As an example, in Fig. 1 we show the spectra of the brightest cluster galaxies (BCG).

4. Results

4.1. Redshifts

The sky subtracted, wavelength and flux calibrated spectra were used to derive the redshifts. First we obtained a redshift estimate based on the CaII H+K doublet, when present, and then we used the cross-correlation technique as implemented in the `RVSAO` package (Kurtz & Mink 1998) using an elliptical galaxy template spectrum (Kinney et al. 1996). To improve the cross-correlation

[1] http://terapix.iap.fr

[2] http://www.astrsp-mrs.fr/virmos/vvds.htm

[3] http://vela.astro.ulg.ac.be/themes/spatial/xmm/LSS

Table 1. ESO-VLT observing log. The exposure time is given for each mask.

ID[a]	Cluster	R.A. (J2000.0)	Decl.	Seeing arcsec	Exposure min.
		09-Oct-2002			
001	XLSSJ022457.1−034853	02:24:57.1	−03:48:53	1.0-1.2	2x60
005	XLSSJ022709.7−041805	02:27:09.7	−04:18:05	0.7-1.1	2x90
		10-Oct-2002			
004	XLSSJ022530.2−050713	02:25:30.2	−05:07:13	0.8-2.7	90+60
		10-Oct-2002			
002	XLSSJ022532.5−035510	02:25:32.5	−03:55:10	0.7-1.2	2x60
003	XLSSJ022737.6−031807	02:27:37.6	−03:18:07	0.7-1.1	2x60

[a] - In the following, all clusters are referred to via the reference XLSS-plus the identification number, e.g. XLSS-001, etc.

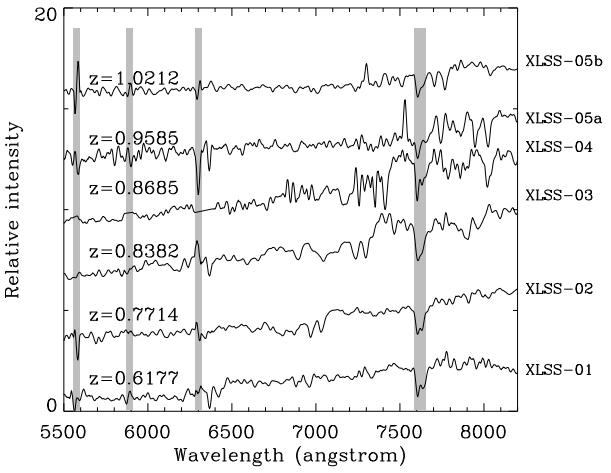

Fig. 1. Spectra, with the corresponding redshift, of the brightest or centrally located cluster galaxies with respect to the observed wavelength. The regions with residuals from the sky subtraction are masked with grey bands and the spectra are smoothed with a boxcar of ~ 11Å.

Table 2. Cluster redshift characteristics. N_{gal} shows the total number of galaxies used to derive the redshift. The number in parenthesis shows the number of emission line galaxies.

Name	Redshift	σ_v km/s	N_{gal}
XLSS-001	$0.6128^{+0.0006}_{-0.0006}$	867^{+80}_{-60}	29(9)
XLSS-002*	$0.7722^{+0.0001}_{-0.0003}$	524^{+267}_{-116}	11(5)
XLSS-003	$0.8387^{+0.0007}_{-0.0007}$	780^{+137}_{-75}	17(5)
XLSS-004	~ 0.88	—	2
XLSS-005	~ 1.0	—	7(5)

(*) – taking only the objects having redshifts in $[0.76, 0.78]$.

signal, we have masked the wavelength ranges of the strongest sky lines, where residuals from the sky subtraction could occur, and also the region of a strong atmospheric absorption at 7750-7800 Å.

The redshift distributions in each field are shown in Fig. 2. To illustrate the redshift space overdensities we have applied an adaptive kernel smoothing over the redshifts – the so called adaptive kernel density estimation (e.g. Silverman 1986, Pisani 1993). There is both a clear redshift grouping and a spatial grouping associated with the X-ray emission in XLSS-001, XLSS-002 and XLSS-003. For these three cases only we show zoomed in an inset a redshift histogram of the overdensity with a fixed bin size. The derived mean redshift and the velocity dispersion, by means of the bi-weighted estimators of location and scale (Beers et al. 1990), are shown in Table 2; the quoted errors are 1σ bias-accelerated bootstrap errors (Efron & Tibshirani 1986).

For XLSS-004 and XLSS-005, the peaks in the redshift distribution do not correspond to any significant spatial clustering, and no peak can be unambiguously associated with an X-ray source. Nevertheless, we show in Table 2 the most plausible redshift based on measurements of galaxies most likely associated with the cluster X-ray emission (see Figs. 8 and 9).

4.2. X-ray analysis

For each cluster an X-ray spectrum was extracted from a region large enough to include the cluster emission. A background spectrum was taken from an adjacent annulus. We removed in advance the contribution of all other sources within the cluster and background regions. A photon redistribution matrix (RMF) and ancillary region file (ARF) were created using `XMMSAS:rmfgen/arfgen`, including corrections for bad pixels and detector geometry. Finally the spectra from the three instruments MOS1, MOS2 and PN were regrouped to have at least 25 counts per bin. The extracted spectra were used to derive the observed characteristics shown in Table 3 without any recourse to a reference model.

To derive the global cluster X-ray characteristics, the binned spectra in each instrument were fitted to a `mekal` model of thermal plasma emission with photo-electric absorption using `XSPEC` (Arnaud 1996, also see the `XSPEC` manual[4] for the `mekal` model and corresponding refer-

[4] http://heasarc.gsfc.nasa.gov/docs/xanadu/xspec/manual/

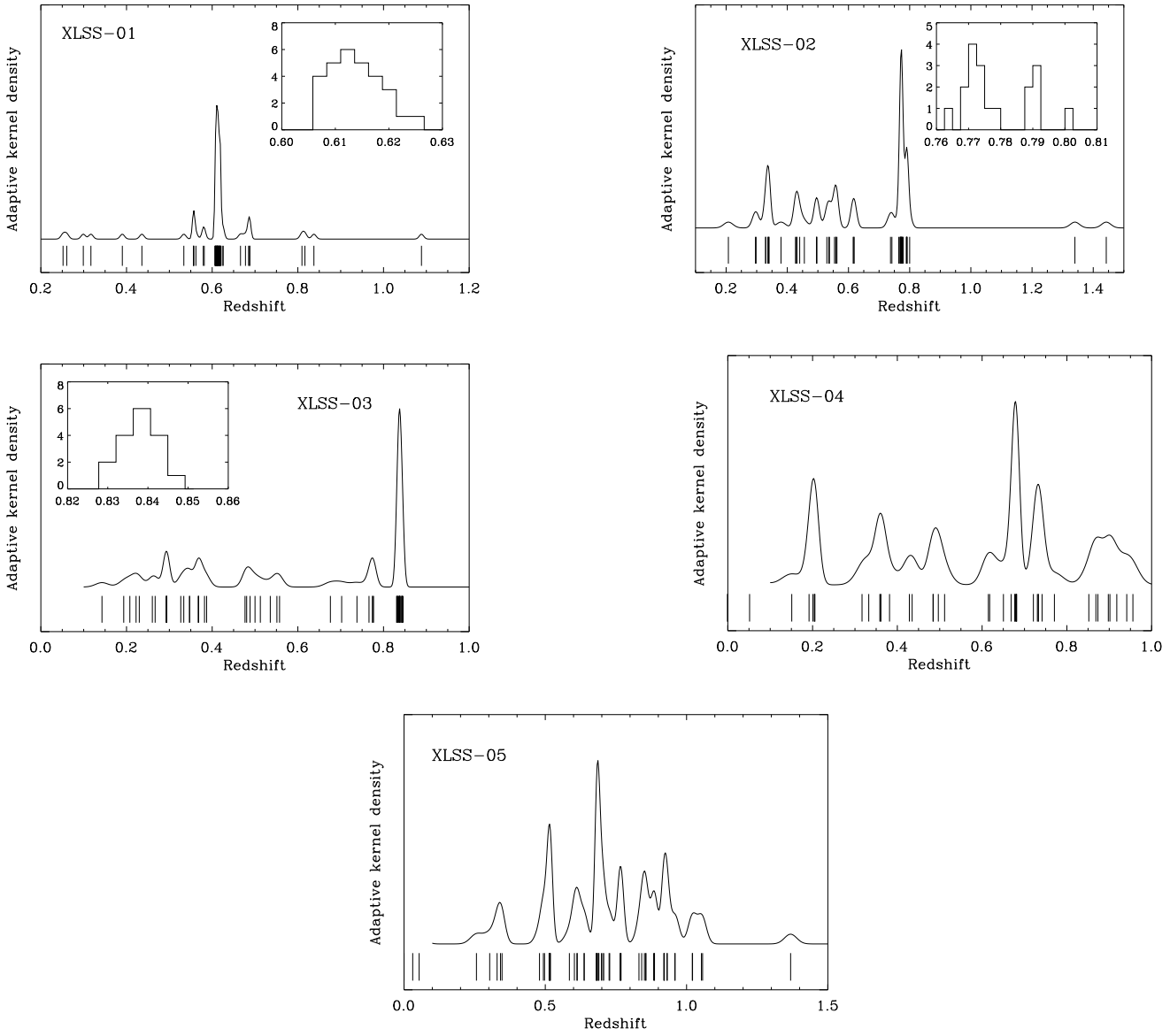

Fig. 2. Redshift distributions of the spectroscopically observed objects for all five clusters. The adaptive kernel density estimation (Silverman 1986) is shown as a continuous line over the redshift measurements. In cases where an overdensity in redshift space corresponds to a spatial correlation we show a histogram of the zoomed redshift region: for XLSS-001 from 0.6 to 0.63, bin size 0.0026; XLSS-002: $0.76 < z < 0.81$, bin size 0.0025; XLSS-003: $0.82 < z < 0.86$, bin size 0.0043.

ences). The energy range used in the fit is $[0.3 - 10]$ keV for MOS instruments, but for PN we used $[0.3 - 7.5]$ keV in order to avoid an instrumental emission feature at $8 - 9$ keV. We have kept only two free parameters in the fitting: the temperature and the normalisation. The mean Galactic absorption of $N_H = 2.5 \times 10^{20}$ cm^{-2} (Dickey & Lockman 1990), the metal abundance of $Z = 0.3 Z_\odot$ and the redshift were fixed. For parameter estimation, we used the Cash statistic, modified to allow background subtraction (see the `XSPEC` manual). The results for XLSS-001, XLSS-002 and XLSS-003 are shown in Table 4. For the other two candidates the photon statistics are insufficient to allow any plausible parameter estimation. The X-ray spectra, `mekal` fit and the corresponding χ^2 residuals are shown in Fig. 3.

The bolometric X-ray luminosity L_X was calculated using the full energy range, constrained only by the instrument response matrices (generally from ~ 0.05 to ~ 20 keV rest frame). The cluster masses were estimated from the local $L_X - M$ relation (Reiprich & Böhringer 2002) assuming no evolution.

4.3. Scaling relations

The scalings between the bolometric luminosity, temperature and velocity dispersion from the clusters in the compilation of Wu et al. (1999) are shown in Fig. 4, to-

Table 3. X-ray parameters of the *MID* sample. "Region" is the extraction radius in arcmin and in comoving Mpc in brackets. "R_{50}" is the object's half-light radius in arcsec in the [0.5-2] keV band. The "Exposure" is the average of the weighted live time events in the extraction region.

Name	Redshift	Region	R_{50}	Counts [0.2-10] keV	Exposure MOS1+MOS2+PN
		arcmin(Mpc)	arcsec	ALL(MOS1+MOS2+PN)	ks
XLSS-001	0.6128	1.7(0.78)	32.2	1812(472+467+873)	2x13.3+7.9
XLSS-002	0.7722	1.1(0.60)	16.6	633(177+152+304)	2x13.3+7.9
XLSS-003	0.8378	1.1(0.65)	23.6	575(136+128+311)	2x11.5+8.3
XLSS-004	~ 0.88	0.5(0.27)	—	233(40+83+110)	2x20.8+16.6
XLSS-005	~ 1.0	0.83(0.56)	21.1	353(50+76+227)	24.5+24.9+21.5

Table 4. Derived, model dependent, cluster X-ray characteristics. No data is presented for XLSS-004 and XLSS-005 because of the poor photon statistics. The errors on the temperature are 1σ, the errors for the flux F_X and the luminosity L_X were calculated varying the normalisation parameter in its 1σ confidence interval while the temperature were kept fixed at its best fit value.

Name	Redshift	kT	F_X^a keV	L_X^b	M^c
XLSS-001	0.6128	$3.4^{+1.1}_{-0.8}$	$8.9^{+1.0}_{-0.7}$	$3.5^{+0.3}_{-0.3}$	12.3
XLSS-002	0.7722	$2.2^{+1.3}_{-0.6}$	$2.6^{+0.7}_{-0.4}$	$1.7^{+0.4}_{-0.3}$	8.0
XLSS-003	0.8378	$4.1^{+4.7}_{-1.8}$	$4.4^{+1.0}_{-0.8}$	$3.7^{+0.9}_{-0.6}$	12.1

[a] – the unabsorbed flux F_X in the [0.5-2] keV band and in units of 10^{-14} erg s^{-1} cm^{-2}.
[b] – the luminosity L_X is pseudo-bolometric ([0.01-30] keV) and in units of 10^{44} erg s^{-1}.
[c] – the mass M in units of $10^{14}\,M_\odot$.

gether with the objects pertaining to this paper. XLSS-001, XLSS-002 and XLSS-003 are in good agreement with the scaling relations $L_X - \sigma_v$, $L_X - T$ and $\sigma_v - T$ (Xue & Wu 2000, Arnaud & Evrard 1999), although caution must be taken because of possible biases on the temperature introduced by the insufficient photon statistics (see e.g. Fairley et al. 2000). What is important to note is that the three clusters are at lower temperatures and luminosities than the other known clusters at high redshift. In that sense we are starting to reach moderately massive systems at high redshift, whilst from ROSAT or EINSTEIN deep surveys the distant clusters are rather more luminous and consequently more massive systems.

5. Individual objects

The optical/X-ray overlays for all candidates are shown in Figs.5-9. The optical images are from CFH12k in the I-band, and the X-ray contours are from wavelet filtered, summed MOS1&2+PN images (see Sec. 2). For XLSS-001, XLSS-002 and XLSS-003, the objects from the inset histograms of their redshift distribution (Fig. 2) are denoted as boxes and triangles, the latter for the galaxies with emission lines. When there was no obvious redshift peak (XLSS-004 and XLSS-005) we indicate in the figure the redshift measurements of each spectroscopically observed galaxy.

Based on the morphology, redshift distribution and the visual appearance, we define three broad cluster classes: relaxed, relaxing and collapsing.

5.1. Relaxed cluster: XLSS-003

This has the appearance of a relaxed, distant cluster at $z = 0.8378$ with a velocity distribution close to a Gaussian. Normality tests (Anderson-Darling and Shapiro-Wilk, see e.g. D'Agostino & Stephens 1986) accept the null hypothesis of the distribution being drawn from a normal distribution at 90% confidence, but this must be taken with caution as the number of objects is small. The X-ray emission is slightly elongated and there is no evidence of substructure. The brightest cluster galaxy coincides with the X-ray emission peak and is at rest with respect to the cluster mean ($z_{BCG} = 0.8382$, $\Delta v = 65$ km s^{-1}).

As can be seen from Tabs. 3 and 4, the low photon statistics do not allow the temperature to be constrained, although if we assume an equipartition between the galaxy velocities and the gas, i.e. $kT = \mu m_p \sigma_v^2$, we derive a temperature of $kT = 3.9 \pm 1.5$ keV – in excellent agreement with the best fit value.

5.2. Relaxing cluster: XLSS-001

Morphologically XLSS-001 at $z = 0.6136$ looks like present day still relaxing clusters: there is an obvious centre formed by the brightest cluster galaxies displaced at $\sim 30''$ from the X-ray emission peak, there is a subclump to the north-east and the brightest cluster galaxy (BCG) that has a typical giant elliptical galaxy absorption spectrum (see Fig. 1) is at 750 km s^{-1} from the mean cluster redshift. The velocity distribution is quite broad, but the normality tests accept at the 90% confidence level the null hypothesis that the observed distribution is consistent with a normal distribution.

There are three other X-ray sources projected over the cluster emission. One is the subclump to the north-east,

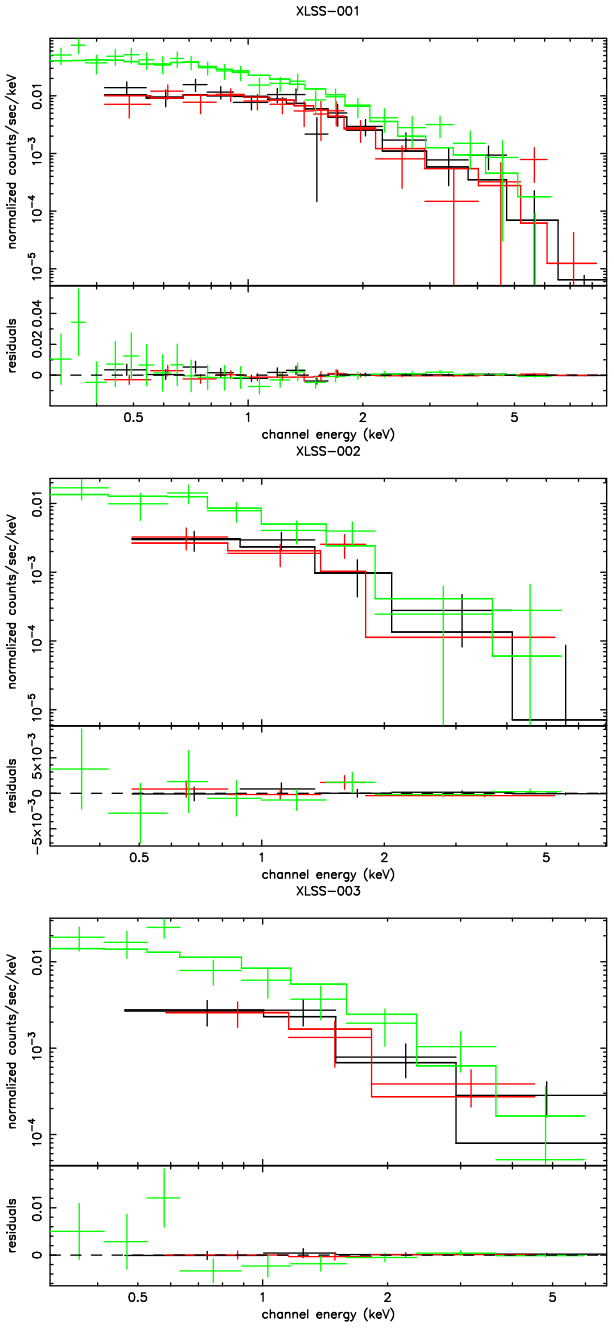

Fig. 3. X-ray spectra, model fit (continuous histogram) and the corresponding residuals for MOS1 (black), MOS2 (red) and PN(green). From top to bottom the objects are XLSS-001, XLSS-002 and XLSS-003. The spectra were initially regrouped to have at least 25 photons per energy bin.

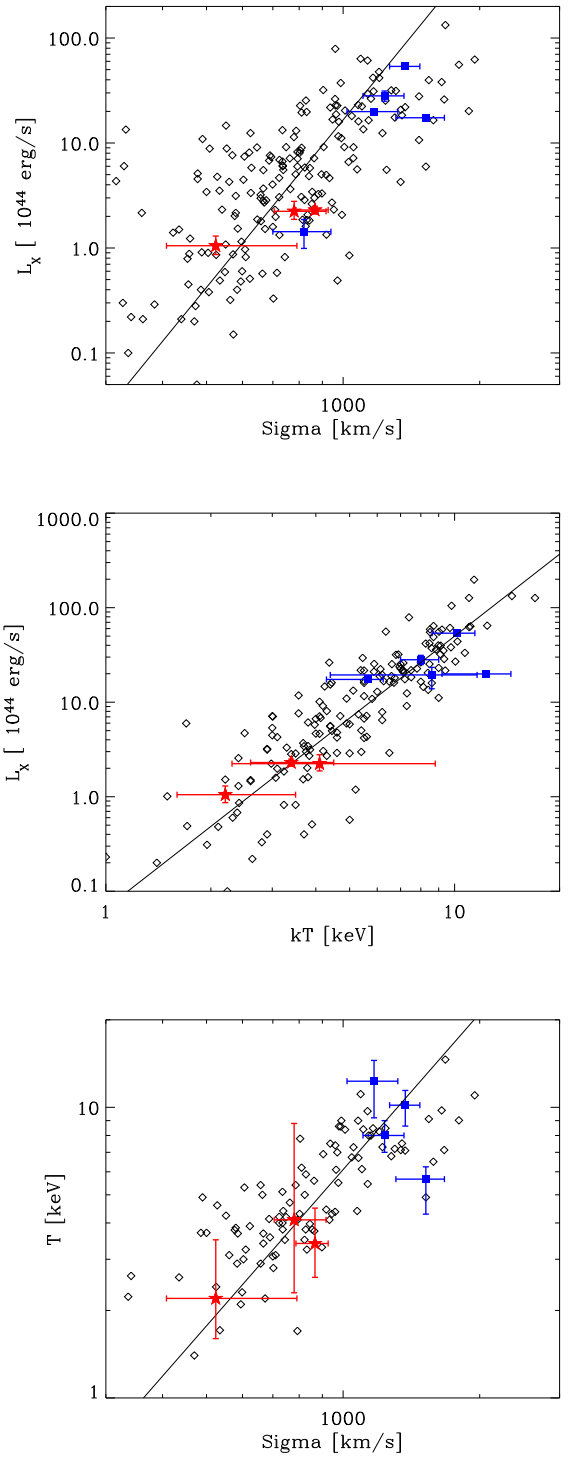

Fig. 4. The scaling relations: luminosity-velocity dispersion ($L_X - \sigma_v$, upper panel), luminosity-temperature ($L_X - T$, middle panel) and velocity dispersion-temperature (lower panel). The clusters from the compilation of Wu et al. (1999) are denoted as diamonds and those at $z \geq 0.5$ are shown as blue boxes with error bars. The best fit from Xue & Wu (2000) for $L_X - \sigma_v$ and $\sigma_v - T$ and from Arnaud & Evrard (1999) for $L_X - T$ are shown as lines. The objects pertaining to this paper are shown as filled red stars with the corresponding error bars. For this comparison only, their luminosity was transformed to Einstein-de Sitter cosmology with $H_0 = 50$ km s^{-1} and $\Lambda = 0$ ($q_0 = 0.5$).

which is most likely associated with a group falling into the cluster potential as there are three cluster members within the X-ray contours (two of which are emission line galaxies) and no obvious optical counterpart at the X-ray peak. Another X-ray source is visible to the north and is probably associated with a nearby galaxy. Finally to the south-east there is a bright point-like source for which we do not have the optical spectrum.

The X-ray characteristics of the cluster are well constrained as we have about 1600 photons in the spectrum

and the cluster is of low temperature. The low luminosity of the cluster is in agreement with its temperature but is at variance with the velocity dispersion, as compared to the scaling relations of local clusters (Fig. 4). This may be regarded as an another argument for the cluster being in the process of relaxation. The gas may have already settled down in the potential whilst the galaxies have still to relax.

5.3. Collapsing cluster: XLSS-002

Although XLSS-002 resembles a point-like source in X-rays, its half-light radius is $R_{50} \approx 17''$ (see Table 3, to be compared to the PSF half-energy width of $16''$) but the extension log-likelihood (from `emldetect`) is 7.4, corresponding to a probability of 6×10^{-4} of being a point-like source. The 8 centrally located galaxies form a crown-like figure, and five are in a very narrow redshift range $0.771 - 0.775$ most likely forming a compact core. There are galaxies at similar redshifts all over the field as can be seen in Fig. 6. None of the other X-ray sources present in the field are cluster members.

The temperature is quite tightly constrained by the X-ray spectral fit as the cluster has a rather low temperature even though the photon statistics are poor – 480 photons in the [0.2-10] keV band in total. There is a large fraction of emission-line galaxies in the centre (5 from 8) and probably some of them, if shown to be AGNs, might contribute to the overall X-ray emission.

The brightest cluster galaxy, at a redshift coinciding with the mean of the centrally located galaxies ($z_{BCG} = 0.7714$, Fig. 1) has a typical giant elliptical galaxy absorption spectrum.

Based on the morphology and the redshift distribution, the most plausible interpretation is that the cluster is in its early stage of formation: a compact core is already formed and the accretion of matter from the nearby large-scale structure is underway. The relations between cluster global characteristics, L_X, T and σ_V (Fig. 4) are consistent with those observed from local clusters.

5.4. Other cases

XLSS-004 The cluster X-ray emission lies between two bright X-ray sources identified as QSOs at $z = 1.12$ (the closest to the north-west, with 486 counts in the [0.5-5] keV band and V = 21.2, R = 20.9, I = 20.8) and at $z = 1.19$ (to the south-east, with 378 counts and V = 18.5, R = 18.5, I = 18.0). These two QSOs are located in diametrically opposed directions at $0.9'$ and $1.2'$ from the centre of the cluster X-ray emission, respectively. Such a configuration is very unlikely to occur by chance. Given our estimated surface density of approximately 30 X-ray sources per deg^2 over a field of 2.8 deg^2 in the XMM-LSS survey with detected counts greater than 300, the probability of detecting two X-ray sources within $2'$ from the cluster X-ray centre is about 1%. Given that these two quasars are located just behind a putative foreground cluster at z = 0.9 (see below), gravitational lensing could possibly affect the real positions and fluxes of these two background objects. However, the hypothesis that these QSOs could be two images of a single source lensed by a foreground cluster does not hold as their optical spectra show a significant redshift difference $\Delta z \simeq 0.07$. A more detailed discussion on this unusual association will be presented elsewhere (Jean et al. 2003).

We cannot confirm the reality of the cluster from the spectroscopic observations only – the galaxy coincident with the peak of the X-ray emission is at $z = 0.868$ and there is only one other galaxy $30''$ to the south-east at a similar redshift, $z = 0.873$. XLSS-004 is, however, independently detected on a scale of 1 arcmin diameter (marked as a thick green circle in Fig. 8) as an overdensity of galaxies with a similar colour of R−z'$= 1.4^m$, corresponding to $z \approx 0.9$ (Andreon et al. 2003a). The cluster optical luminosity function also suggests a high redshift, compatible with $z = 0.9$ (Andreon et al. 2003b).

There is a peak in the redshift distribution at $z \approx 0.68$ (see Fig. 2) but it does not correspond to any spatial grouping.

XLSS-005 This is a very interesting and complicated case with probably two structures in projection, at $z \sim 0.95$ and $z \sim 1.02$. The morphology of the X-ray emission also suggests a bi-modality, with a central extended source and a possible subclump to the south-east. It is not trivial, however, to disentangle the centre, where galaxies at $z = 0.92 - 0.96$ and $z = 1.02 - 1.06$ are mixed. The redshift space distance between the two groups is rather significant: $\Delta z \sim 0.1$ (~ 15000 km s^{-1}) which rules out the galaxies belonging to the same cluster.

This cluster has already been observed in the K' band with ESO-NTT/SOFI in the framework of the XMM-LSS VIRMOS Deep Survey over an area of 0.25 deg^2. The exposure of 1.5 hours resulted in a catalog down to a limiting magnitude K'$_{AB} \approx 22.7$. A search for overdensities in photometric redshift slices of $\Delta z_{phot} = 0.2$ was made, with z_{phot} calculated from BVRIK' photometry. As a result, there is a strong detection with signal-to-noise (S/N) ~ 5 of an overdensity at $z \approx 0.9$ centred on the south-east extension of the X-ray emission. Observations in J and K at ESO-NTT/SOFI (Andreon et al. 2003b) also indicate two overdensities of galaxies with colours compatible with $z \approx 1$.

Our preliminary interpretation is that we are observing two clusters in projection: one at $z \sim 0.92 - 0.95$, forming the main body of the extended X-ray source, and the more distant one at $z = 1.02 - 1.05$, that is partially covered. The redshifts of the spectroscopically observed objects, that span all of the interval from $z \sim 0.92$ to $z \sim 1.05$, could be an indication of a filament connecting both clusters. However, their number is insufficient for any strong claim. This is a good target for deep integral field spectroscopy observations (e.g. IFU of the VIMOS instrument) that will help us resolve this extremely interesting case.

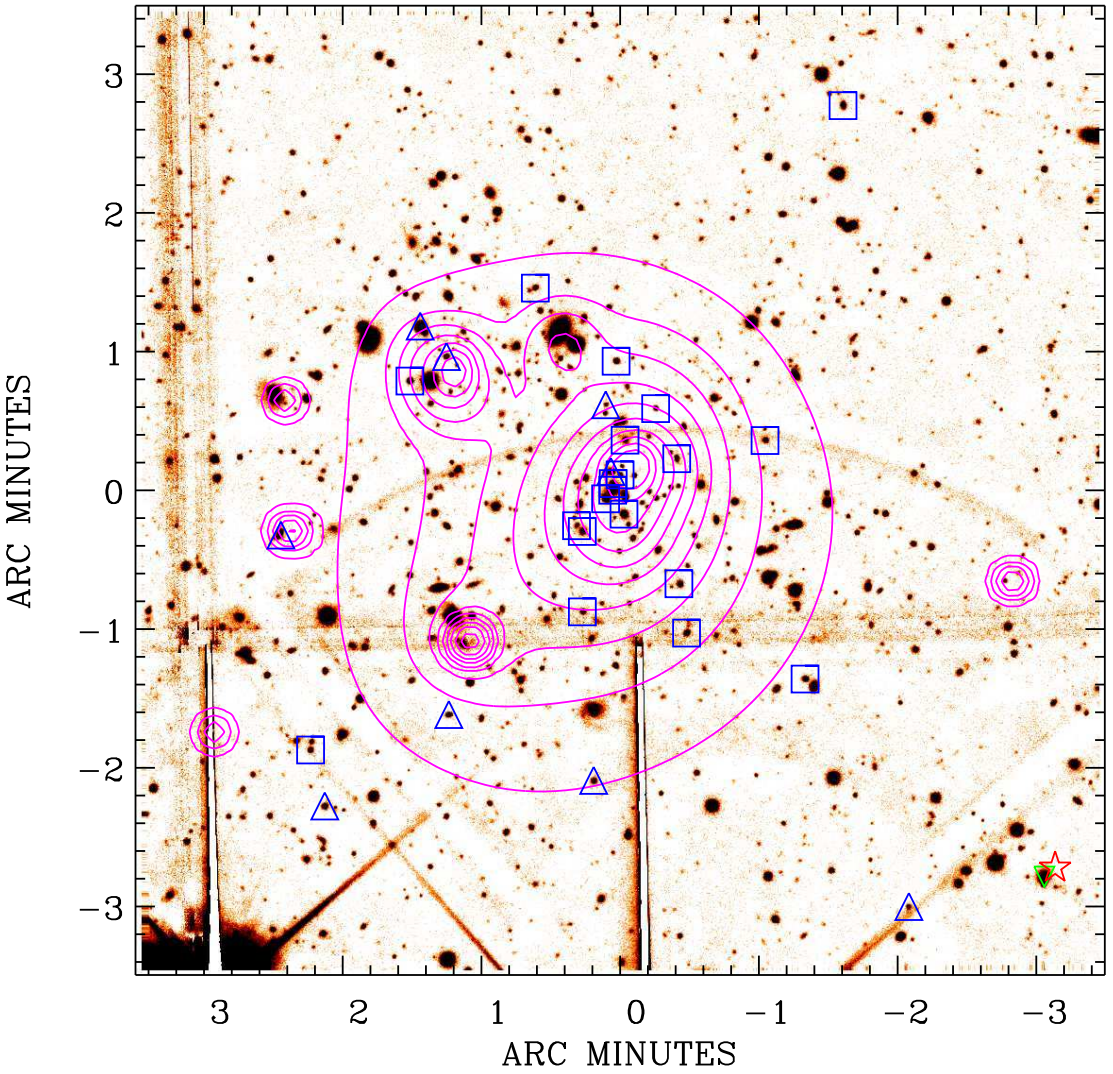

Fig. 5. XLSS-001. CFH12k I-band image of a $7' \times 7'$ field is shown. North is up and east to the left. The X-ray contours run from 0.5 to 5 counts/pixel (2.5″ pixel size) with 10 levels in log space. Objects in the $0.6 \leq z \leq 0.63$ redshift range are denoted by boxes and triangles (for emission-line objects).

The large fraction of emission line objects is also striking. Of 7 objects in the centre with redshifts between $0.92-1.06$, 5 have detectable [OII]3727Å emission in their spectra.

6. Conclusions

We present spectroscopic confirmation of the first discovered high redshift, X-ray selected clusters in the XMM Large-Scale Structure Survey. The detection and classification in X-rays, the subsequent optical identification and spectroscopic target selection demonstrate the efficiency of the follow-up procedure.

6.1. Highlights

- Five newly discovered X-ray clusters from the *MID* sample at $z > 0.6$ were observed at ESO-VLT for 11.5 hours in total. For three of them, we measured more than 15 galaxies with concordant redshifts and thus obtained a viable estimate of the velocity dispersion.
- Thanks to the optimized target selection, we were able to get an estimate of the velocity dispersion of XLSS-003 at $z = 0.84$ in a reasonable VLT time of 2 hours. To show the potential of the XMM-LSS it is interesting to note that to date (March 2003) there are 5 known clusters in the literature (two of them are X-ray selected) at $z > 0.8$ with more than 10 spectroscopically

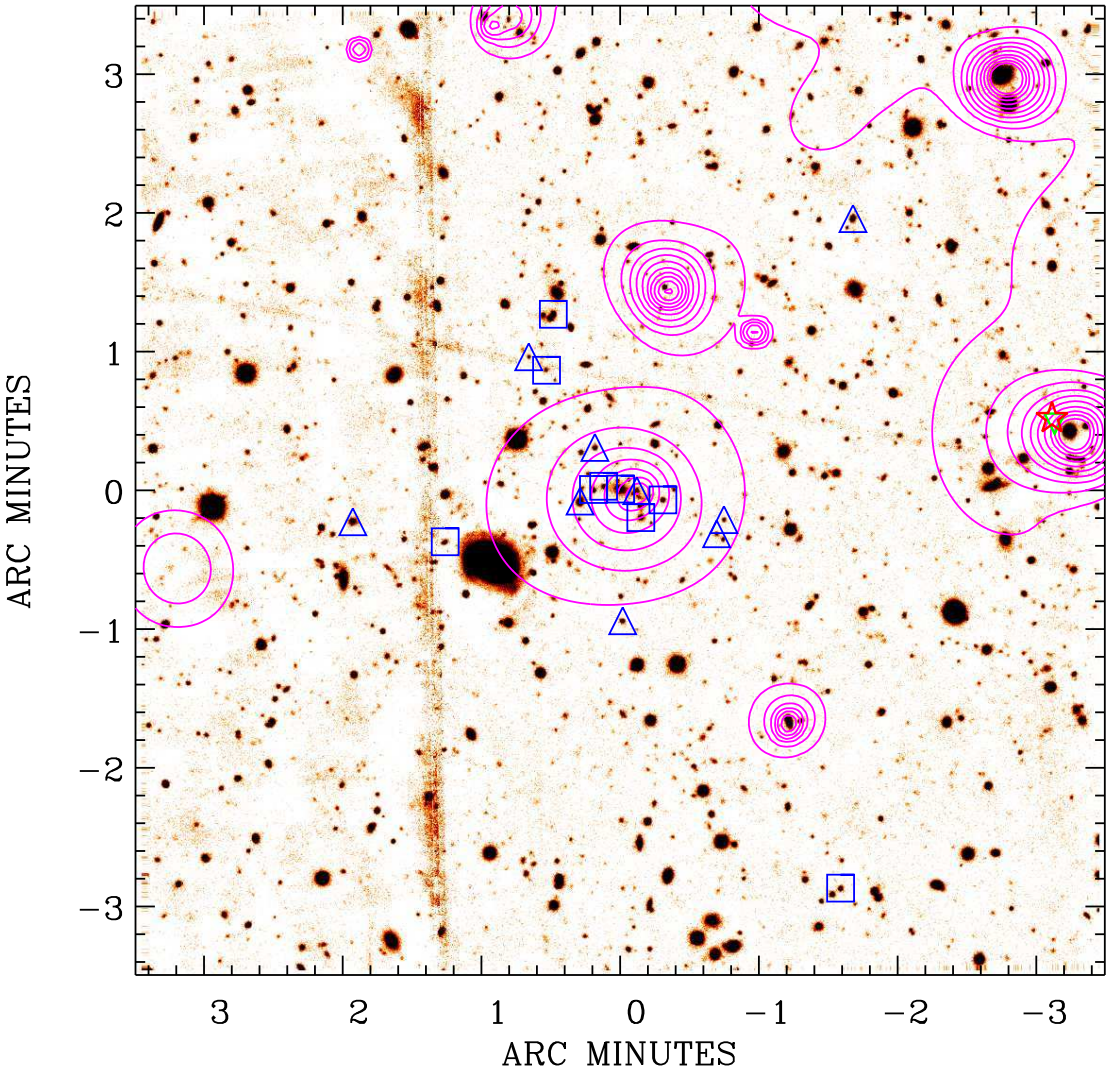

Fig. 6. XLSS-002. A $7' \times 7'$ field is shown and the objects at $0.76 \leq z \leq 0.81$ are denoted by boxes and triangles (for emission-line objects). The X-ray contours run from 0.1 to 5 photons/pixel with 10 levels in log space, with the lowest cluster contour at 0.1 photons/pixel.

measured concordant redshifts, allowing an estimate of the velocity dispersion.

– We have detected a complex structure at a redshift of unity – XLSS-005. Most likely there are two clusters at $z \sim 0.9$ and $z \sim 1$ observed in projection, the signature of which is also detected in X-rays. Galaxy overdensities in the same region in photometric redshift slices around $z \sim 0.9 - 1$, together with the large span of spectroscopic redshifts of the objects in the central region, are indications that we are seeing a large-scale filament in projection.
– One cluster, XLSS-004, is not confirmed by the spectroscopic run alone, but the CTIO Rz' observations detect it as an overdensity of R−z'=1.4^m galaxies, matching the redshift, $z \sim 0.9$, of the centrally located galaxy.
– From Tables 3 and 4, and Fig. 4, it is obvious that for the first time we are unveiling moderate mass clusters in the redshift range $0.5 < z < 1$. Most of these objects are weak, moderately extended X-ray sources and consequently would have been missed or incorrectly classified in deep ROSAT pointings because of the insufficient photon statistics in addition to the worse PSF. Thus with XMM-LSS we are starting to fill the cluster database with objects at high redshift from the middle of the mass function. This is very important, first for cosmological constraints and second, for non-gravitational physics in clusters (as the effects like pre-

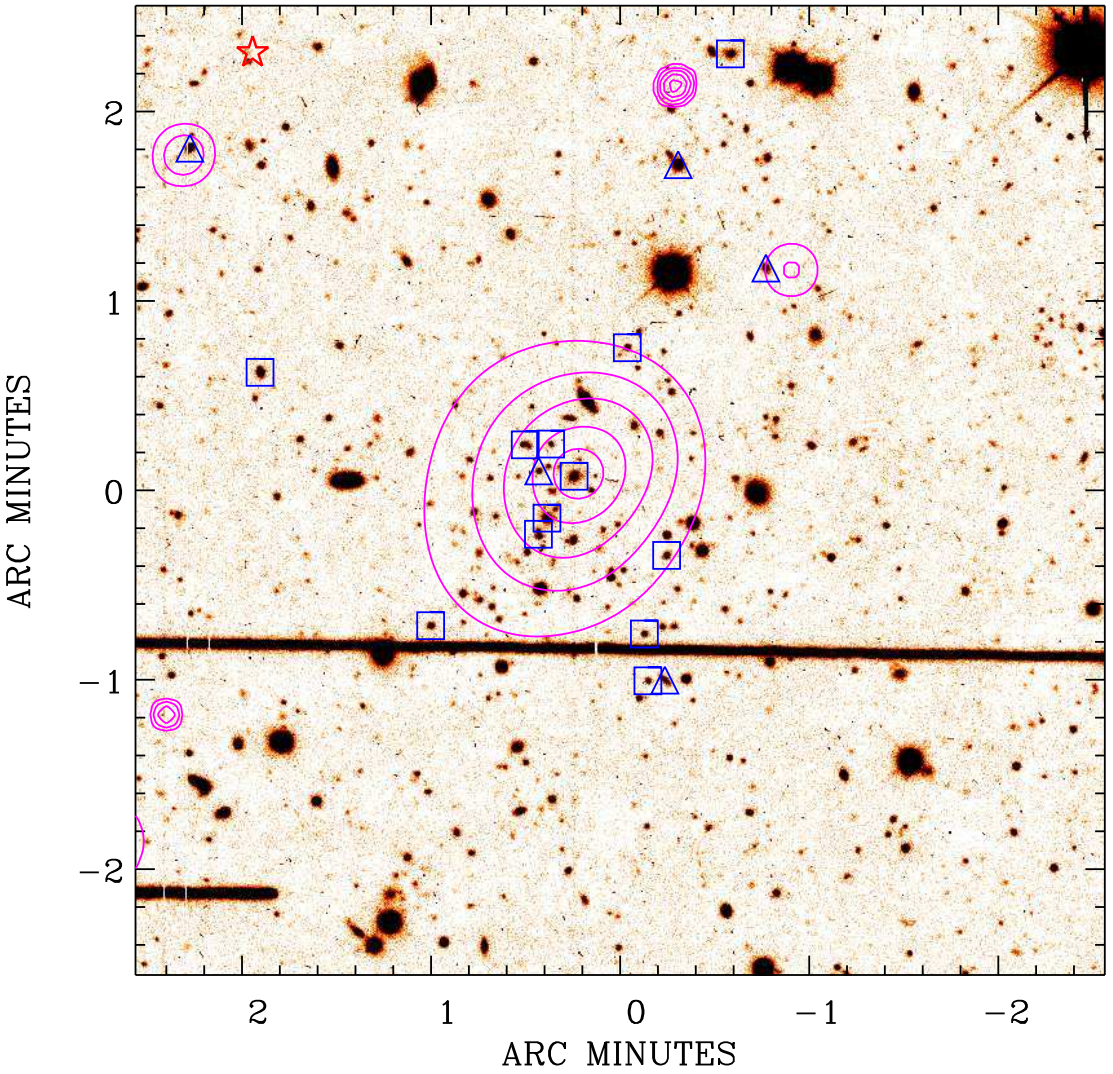

Fig. 7. XLSS-003. Only the central $5' \times 5'$ region of the field is shown and the objects in $0.82 \leq z \leq 0.86$ are denoted by boxes and triangles (for emission-line objects). The X-ray contours run from 0.1 to 5 photons/pixel with 10 levels in log space, and the lowest cluster contour is at 0.1 photons/pixel.

heating and feedback are presumably more important in lower mass systems).

6.2. Prospects

In the near future, our goal will be to confirm, via spectroscopic identifications, all XMM-LSS clusters down to $\sim 8 \times 10^{-15}$ erg s^{-1} cm^{-2} over the 3 sq.deg. of the AO-1 observations. This will form a complete sample of about 30 X-ray selected clusters at $0 < z < 1$. A follow-up of the most interesting objects at $z \sim 1$ is also previewed with integral-field spectroscopy.

Acknowledgements. SDS is supported by a post-doctoral position from the Centre National d'Etudes Spatiales. MP and IV are grateful to the ESO/Santiago Office for Science, for a 2 week stay in October 2002, were the analysis of the VLT data presented here was initiated.

This research has made use of the X-Rays Clusters Database (BAX) which is operated by the Laboratoire d'Astrophysique de Midi-Pyrénées (LAOMP), under contract with the Centre National d'Etudes Spatiales (CNES) and of the NASA/IPAC Extragalactic Database (NED) which is operated by the Jet Propulsion Laboratory, California Institute of Technology, under contract with the National Aeronautics and Space Administration.

References

Andreon, S. et al. 2003a, in preparation
Andreon, S. et al. 2003b, in preparation

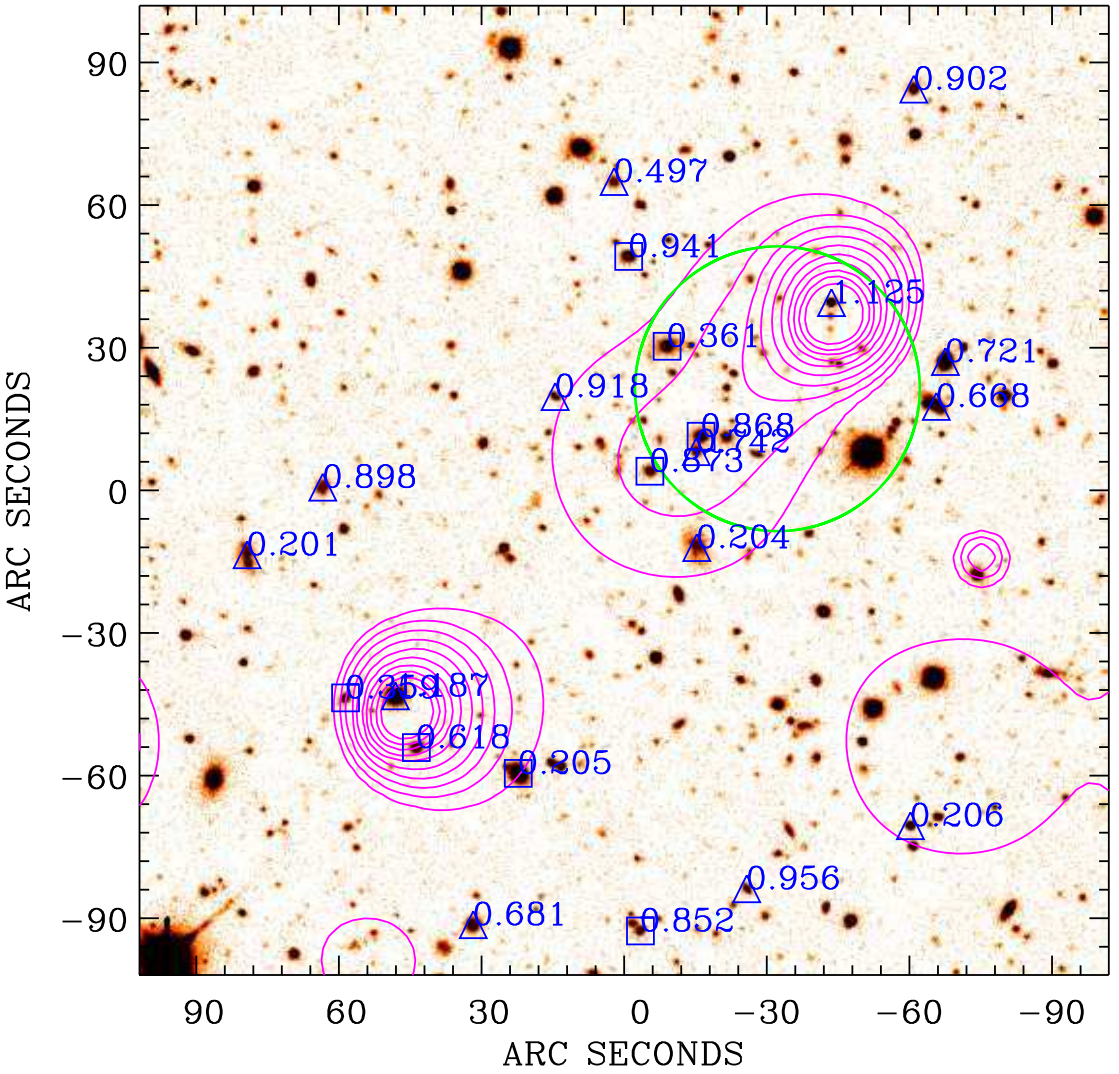

Fig. 8. XLSS-004. Only the central $3.4' \times 3.4'$ region of the field is shown and the redshifts for all spectroscopically observed objects are indicated. The triangles denote emission-line objects. The X-ray contours run from 0.15 to 5 photons/pixel with 10 levels in log space, with the lowest cluster contour at 0.15 photons/pixel. The optical detection from CTIO Rz' data is shown as a green circle.

Arnaud, K.A. 1996, in ASP Conf. Ser., Vol. 101, Astronomical Data Analysis Software and Systems V,eds. Jacoby G.H. & Barnes J. (San Francisco: ASP), 17 (XSPEC)

Arnaud, K.A. 2001, ApJ, submitted

Arnaud, M. & Evrard, A. 1999, MNRAS, 305, 631

Beers, T.C., Flynn & K., Gebhardt, K. 1990, AJ 100, 32 (ROSTAT)

Bertin, E. & Arnouts, S. 1996, A&AS, 117, 393 (SExtractor)

Böhringer, H., Schueker, P., Guzzo, L., et al. 2001, A&A, 369, 826

D'Agostino, R.B. & Stephens, M.A. 1986, Goodness-of-fit Techniques (New York: Marcel Dekker)

Danese,L., De Zotti, G. & di Tullio G. 1980, A&A, 82, 322

Dickey. J.M. & Lockman. F.J. 1990, ARA&A, 28, 215

Dos Santos, S. et al. 2003, in preparation

Dressler, A., Oemler, A., Couch, W., et al. 1997, ApJ, 490, 577

Efron, B. & Tibshirani, R. 1986, Stat. Sci., 1, 54

Fairley, B.W., Jones, L.R., Scharf, C., et al. 2000, MNRAS, 315, 669

Gladders, M.D. & Yee, H.K.C. 2000, AJ, 120, 2148

Gonzalez, A.H., Zaritsky, D., Dalcanton, J.J., & Nelson, A.E. 2001, ApJS, 137, 117

Gunn, J.E., Hoessel, J.G., & Oke, J.B. 1986, ApJ, 306, 30

Jean, C., et al. 2003, in preparation

Kinney, A., Calzetti, D., Bohlin, R., et al. 1996, ApJ, 467, 38

Kurtz, M.J. & Mink, D.J. 1998, PASP, 110, 934

Le Fèvre, O., Mellier, Y., McCracken, H.J., et al. 2001, in "New Era of Wide-Field Astronomy", Eds. R.G. Clowes, A.J. Adamson, G.E. Bromage, ASP conference series, Vol. 232, p449

McCracken, H.J., Radovich, M., Bertin, E., et al. 2003, A&A, submitted

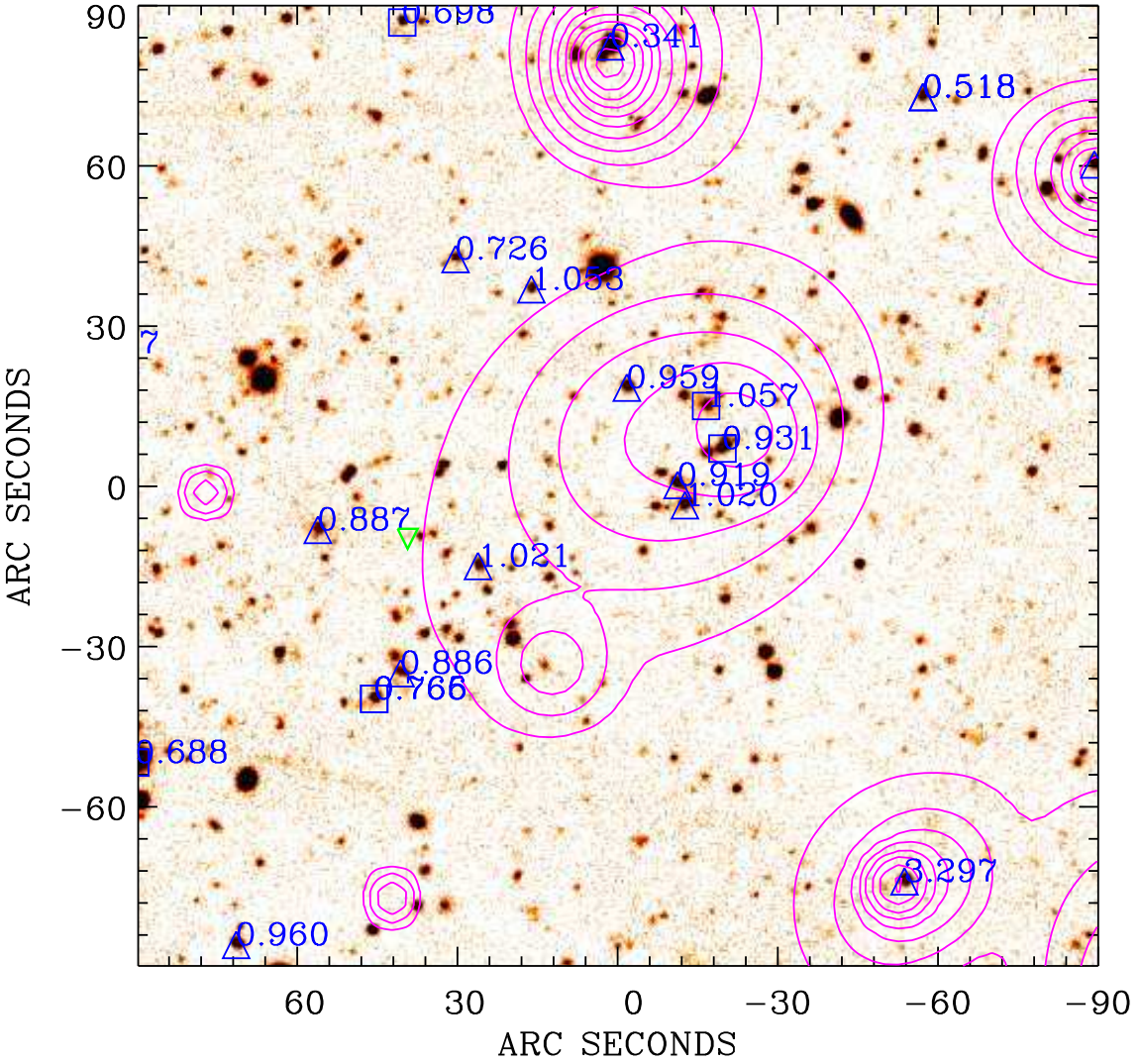

Fig. 9. XLSS-005. Only the central $3' \times 3'$ region of the field is shown and the redshifts for all spectroscopically observed objects are indicated. The triangles denote emission-line objects. The X-ray contours run from 0.15 to 5 photons/pixel with 10 levels in log space, with the lowest cluster contour at 0.15 photons/pixel.

Pierre, M., Valtchanov, I., Dos Santos, S., et al 2003, A&A, submitted (paper I)

Pisani, A. 1993, MNRAS, 265, 706

Postman, M., Lubin, L.M., Gunn, J.E., et al. 1996, AJ, 111, 615

Postman, M., Lubin, L. & Oke, J. 1998, AJ, 116, 560

Raymond, J.C. & Smith, B.W. 1977, ApJS 35, 419

Refregier, A., Valtchanov, I. & Pierre, M. 2002, A&A, 390, 1

Reiprich, T.H. & Böhringer, H. 2002, ApJ, 567, 716

Rosati, P., Borgani, S. & Norman C. 2002, ARAA, 40, 539

Scharf, C. 2002, ApJ, 572, 157

Silverman, B. 1986, Density Estimation for Data Analysis and Statistics (London: Chapman & Hall)

Stanford, S.A., Elston, R., Eisenhardt, P.R., et al. 1997, AJ, 114, 2232

Starck, J.-L. & Pierre, M. 1998, A&AS 128, 397

Starck, J.-L., Murtagh, F. & Bijaoui, A. 1998, Image Processing and Data Analysis. The Multiscale Approach. Cambridge University Press

Tonry, J.L. & Davis, M. 1979, AJ, 43, 393

Valtchanov, I., Pierre, M. & Gastaud, R. 2001, A&A, 370, 689

Willis, J. et al. 2003, in preparation

Wu, X.-P., Xue, Y.-J. & Fang, L.-Z. 1999, ApJ, 524, 22

Xue, Y.-J. & Wu, X.-P. 2000, ApJ, 538, 65

C. Abell 1451 and 1RXS J131423.6-251521 : A multi-wavelength study of two dynamically perturbed clusters of galaxies

Valtchanov I., Murphy T., Pierre M., Hunstead R. & Lémonon L., 2002, A&A, 392, 795

Astronomy & Astrophysics manuscript no. Valtchanov June 18, 2003
(DOI: will be inserted by hand later)

Abell 1451 and 1RXS J131423.6−251521: a multi-wavelength study of two dynamically perturbed clusters of galaxies

I. Valtchanov[1], T. Murphy[2⋆], M. Pierre[1], R. Hunstead[2], and L. Lémonon[1]

[1] CEA/DSM/DAPNIA, Service d'Astrophysique, F-91191 Gif-sur-Yvette, France
[2] School of Physics, University of Sydney, NSW 2006, Australia

Received June 18, 2003/ Accepted June 18, 2003

Abstract. We present results from optical, X-ray and radio observations of two X-ray bright ($L_X \sim 10^{45}$ erg s^{-1}) galaxy clusters. Abell 1451 is at redshift $z = 0.1989$ and has line-of-sight velocity dispersion $\sigma_v = 1330$ km s^{-1} as measured from 57 cluster galaxies. It has regular X-ray emission without signs of substructure, a Gaussian velocity distribution, lack of a cooling flow region and significant deviations from the observed scaling laws between luminosity, temperature and velocity dispersion, indicating a possible merging shock. There is only one spectroscopically confirmed cluster radio galaxy, which is close to the X-ray peak.
1RXS J131423.6−251521 (for short RXJ1314−25) has $z = 0.2474$ and $\sigma_v = 1100$ km s^{-1} from 37 galaxies. There are two distinct galaxy groups with a projected separation of ≈ 700 kpc. The velocity histogram is bi-modal with a redshift-space separation of ~ 1700 km s^{-1}, and the X-ray emission is double peaked. Although there are no spectroscopically confirmed cluster radio galaxies, we have identified a plausible relic source candidate.

Key words. galaxies: clusters: individual: Abell 1451, 1RXS J131423.6−251521 — X-rays: galaxies — radio: galaxies — galaxies: redshifts — general: clusters

1. Introduction

Clusters of galaxies form a representative population which traces the highest initial density fluctuation peaks. They are excellent tools for exploring the distant Universe and are used to constrain cosmological models. A significant fraction of clusters shows evidence of substructure (e.g. Geller & Beers 1982, Dressler & Shectman 1988, West 1994; for a recent review see Pierre & Starck 1998) and complexity in the distribution of the different constituents — galaxies, gas, dark matter (Baier et al. 1996). Combined multi-wavelength observations are needed to disentangle the dynamical state of clusters. Analysis of the velocity and space distribution of the galaxies is very important but, in contrast to the optical, the X-ray analysis is less prone to projection effects and probes better the cluster mass distribution (because the X-ray surface brightness depends on the square of the matter density). The presence of substructure is also revealed in the radio properties of clusters (Röttgering et al. 1994, Reid et al. 1998), but the radio sources in turn may also influence the X-ray emission (Rizza et al. 2000).

This paper is the third in a series of papers (Pierre et al. 1997, Lémonon et al. 1997) dedicated to studies of distant, bright X-ray clusters discovered in the ROSAT All-Sky Survey (RASS, Voges et al. 1999). A sample of ≈ 10 clusters with $L_X > 10^{44}$ erg s^{-1} was selected (Pierre et al. 1994) in the redshift range $0.1 < z < 0.3$. In this paper we present multi-wavelength observations of two of these clusters — Abell 1451 and 1RXS J131423.6−251521 (hereafter shortened to RXJ1314−25). General data associated with both clusters are given in Table 1.

The plan of the paper is as follows: in Section 2 we present optical observations, data reduction, redshift catalogues and data analysis for the two clusters. In Section 3 and 4 we present ROSAT-HRI observations and data analysis and ATCA radio observations and data analysis respectively. Finally in Section 5 we discuss the multi-wavelength view of Abell 1451 and RXJ1314−25. Throughout the paper we use $H_0 = 50$ km s^{-1} Mpc^{-1} and $q_0 = 0.5$.

2. Optical observations, data reduction and analysis

2.1. Observations and reduction

Multi-Object Slit (MOS) spectra for both clusters were acquired using the ESO 3.6-m telescope at La Silla in

Send offprint requests to: Ivan Valtchanov, ivaltchanov@cea.fr
⋆ Now at Institute of Astronomy, University of Edinburgh, Royal Observatory, Blackford Hill, Edinburgh, EH9 3HJ

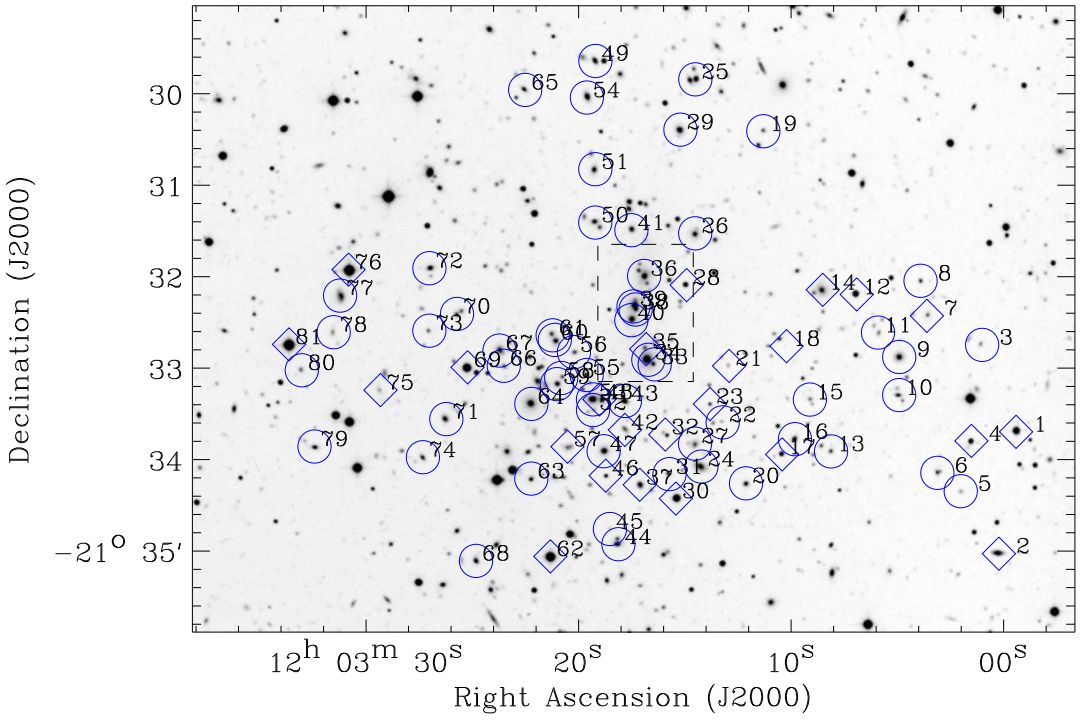

Fig. 1. Abell 1451: V-band image from the Danish 1.5-m telescope showing the objects included in the spectroscopic study. Numbers correspond to the object identification in Table 3; those denoted as diamonds are either stars or non-cluster members. The dashed box is the central part, shown zoomed in Fig. 2.

two runs, one in 1993 and one in 1999 (Table 2). The first run was equipped with EFOSC1 (ESO Faint Object Spectrograph and Camera), Tektronix 512×512 CCD (pixel size 27 μm and 0.61″/pixel) and Grism B300, covering the range 3740–6950 Å, with central wavelength 5250 Å and dispersion of 6.2Å/pixel. The observations in 1999 were performed with EFOSC2, CCD #40 2048×2048 (pixel size 15 μm, 0.157″/pixel) and Grism O300 which covers 3860–8070Å with central wavelength 5000 Å and dispersion 2.06 Å/pixel. However, the final wavelength range depends on the position of each slit on the mask. The seeing was $1.0 - 1.2''$ for both 1993 and 1999 runs. The corresponding airmasses and the exposure times for each mask/slit configuration are given in Table 2.

All spectra were processed within the ESO-MIDAS or IRAF environment to produce the final wavelength calibrated, sky subtracted spectra. A HeAr lamp was used for wavelength calibration, and a second-order cubic spline or polynomial fit to 5–12 comparison lines gave rms residuals <1Å.

We have determined redshifts using the Tonry & Davis (1979) cross-correlation technique as implemented in the RVSAO package (Kurtz & Mink 1998). Before processing with RVSAO we have masked out spectral ranges where significant residuals from sky subtraction could occur, and also any possible emission lines. Generally we have cross-correlated our observed spectra with 3 to 6 galaxy and star templates with good signal-to-noise, and also with the composite absorption-line template (fabtemp97) dis-

Table 2. Summary of the multi-slit spectroscopic observations

Date	Object	RA (J2000)	Dec (J2000)	Airmass	MOS masks/slits	Exposure (s)
1993 Mar 29	Abell 1451	12:03:15	−21:31:36	1.2	1/15	900
1993 Mar 29	RXJ1314−25	13:14:29	−25:16:25	1.1	1/15	2x900+1800
1999 Apr 19/20	Abell 1451E	12:03:12	−21:33:25	1.34	2/20+21	3x1800/4x2100
1999 Apr 19/20	Abell 1451W	12:03:23	−21:33:25	1.40	2/21+19	2x3600/4200
1999 Apr 19/20	RXJ1314−25N	13:14:22	−25:14:55	1.06	2/17+18	2x3600/4x2100
1999 Apr 19/20	RXJ1314−25S	13:14:22	−25:17:55	1.04	2/17+18	4x1800/4x2100

Table 1. Properties of the two clusters. References: Abell (1958), Abell et al. (1989) for the coordinates and richness; Bautz & Morgan (1970) for classification for Abell 1451; coordinates for RXJ1314−25 are from RASS (Voges et al. 1999); T_X and L_X in the 2–10 keV band are from Matsumoto et al. (2001); redshift and σ_v are from this paper; the apparent magnitude of an L^* galaxy was calculated using $M^*(B_j) = -21.8$, obtained by adjusting the Lumsden et al. (1997) value of $M^*(B_j) = -20.16$ to the cosmological parameters used in this paper.

	Abell 1451	RXJ1314−25
R.A. (J2000)	12:03:16.0	13:14:23.6
Dec. (J2000)	−21:30:42	−25:15:21
BM Class	III	—
Richness	3	—
Redshift	0.1989	0.2474
σ_v km s^{-1}	1330	1100
B_j^*	19.5	20.2
L_X (10^{45}) erg s^{-1}	1.5	1.8
T_X keV	13.4	8.7

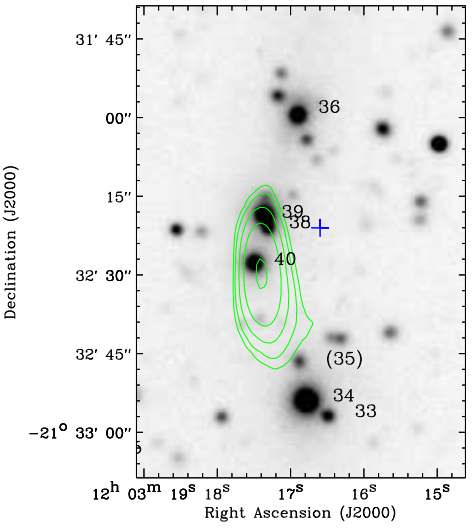

Fig. 2. Abell 1451: zoomed image of the central part of Fig. 1. The plus sign marks the X-ray emission centre (see Section 3) and the contours are ATCA 13cm radio observation with levels = 0.3, 0.5, 1, 2, 5 and 10 mJy/beam, rms noise level is 60μJy/beam (see Section 4). The object in brackets is a background galaxy.

tributed with RVSAO. For each target object we adopted the redshift value from the best (highest correlation coefficient) template. The redshifts were then checked by identifying the prominent absorption features (CaII H & K, G band, MgI triplet) in each spectrum. If emission lines were present in the spectra, redshifts were determined from them.

The errors in redshift were computed from $\Delta z = k/(1+r)$, where r is the cross-correlation coefficient and k was determined empirically by adding noise to a high signal-to-noise spectrum and correlating it with template spectra with known velocities. For our observational configurations we found $k = 0.003$, which gives a velocity error of about 200 km s^{-1} for a redshift estimate with $r = 3$. We have checked our redshift measurements and uncertainties using a few galaxy spectra repeated in different runs or masks and they are all in excellent agreement, consistent with the derived errors.

We have not converted our measurements to the heliocentric system because the correction is about 1 km s^{-1} for the 1993 run and −8.8 km s^{-1} for the 1999 run, well below the uncertainties.

The final redshift catalogue of objects for Abell 1451 is shown in Table 3 and for RXJ1314−25 in Table 4, with corresponding finding charts in Figs 1 and 3.

2.2. Optical data analysis

2.2.1. Abell 1451

Cluster membership was determined by using an interactive version of the Beers et al. (1990) ROSTAT package (Valtchanov 1999) and confirmed by the 3-σ clipping method of Yahil & Vidal (1977). The cluster redshift distribution is shown in Fig. 4 and some relevant characteristics, taking redshift errors into account, are given in Table 5. The distribution is very close to Gaussian, which has been quantified by various statistical tests for normality (D'Agostino & Stephens 1986) — the Wilk-Shapiro test accepts normality at the 99% level and the Anderson-Darling test at the 95% level.

There is no single dominant cluster galaxy. The brightest cluster members (BCMs, #34, #39, #36 and #40) are linearly aligned in projection (see Fig. 2) and their spectra are typical elliptical galaxy absorption spectra with no emission lines. The projected galaxy density distribution from SuperCOSMOS (Hambly et al. 2001) data shows an elongation in the same direction. The velocity dispersion

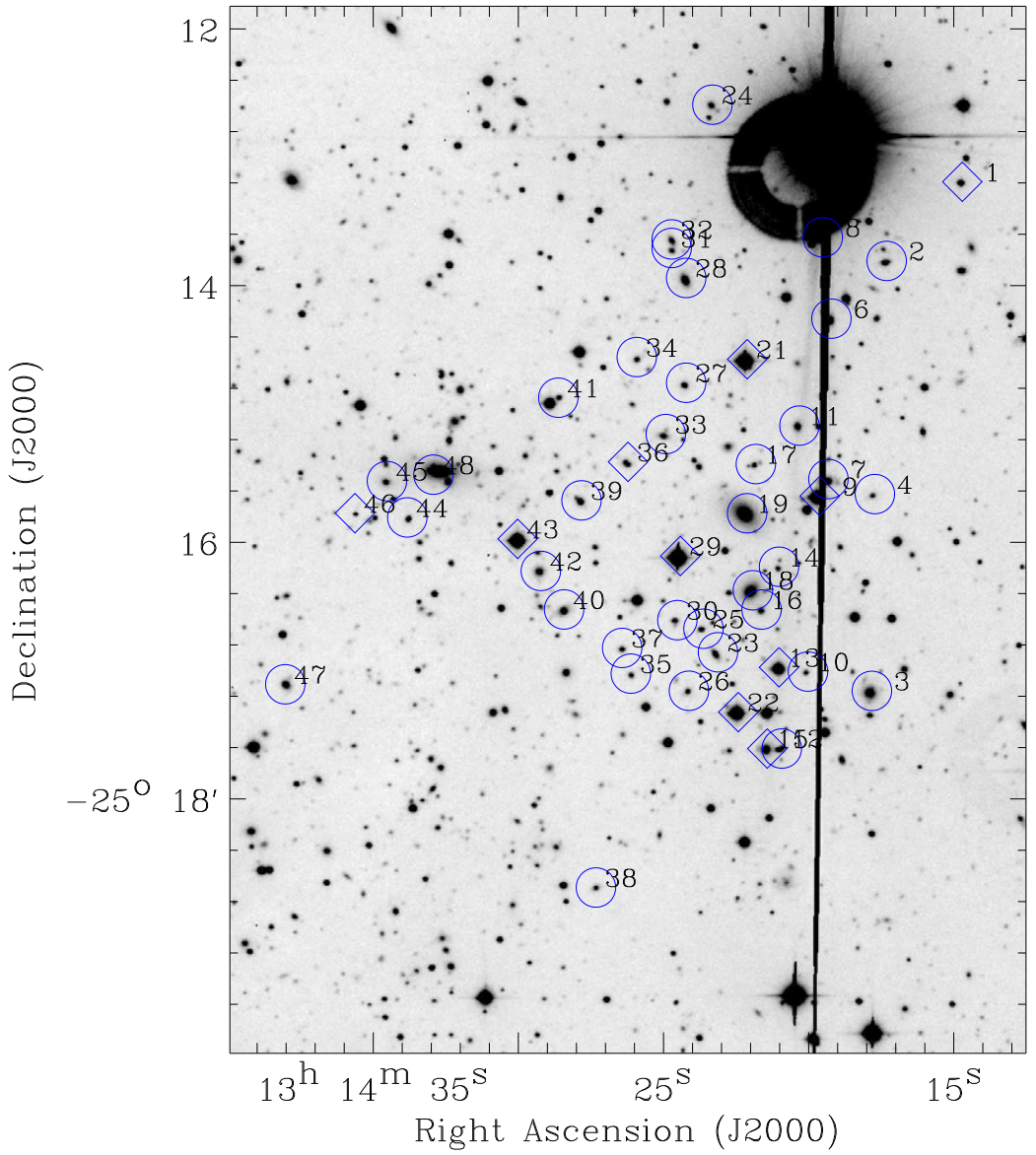

Fig. 3. RXJ1314−25: I-band image from the Danish 1.5-m telescope showing the objects in the spectroscopic study. Numbers correspond to the object identifications in Table 4; those marked with diamonds denote either stars or non-cluster members. Note that we have not plotted galaxy #20 because it is not resolved spatially from galaxy #19.

among the BCMs is $\sim$ 800 km s^{-1}, somewhat less than the overall cluster velocity dispersion.

2.2.2. RXJ1314−25

Statistics of the redshift distribution are shown in Table 6 and the redshift histogram in Fig. 5. The distribution clearly shows two peaks and the test for the hypothesis of a unimodal distribution — the dip test (Hartigan 1985) — gives an insignificant probability of a single mode. Going further, we have applied the KMM method for detecting bimodality (Ashman et al. 1994), which confirmed the dip test negative result for unimodality and also gave us the probable group membership, assuming a bi-modal distribution. In Table 6 we show the same statistics for both groups. Although the number of cluster members is relatively small for giving high weight to the KMM result, the segregation of the galaxies on the sky supports that conclusion (see Fig. 6).

Table 5. Abell 1451: Some statistical characteristics of the redshift distribution, corrected for measurement errors (Danese et al. 1980). The scale measure is in the cluster rest frame, i.e., $S_{BI} = c\sigma_z/(1+z)$ (Harrison 1974). The errors (1σ) are calculated by using the accelerated bias-corrected bootstrap technique with 1000 bootstrap resamplings (Efron & Tibshirani 1986)

Characteristic	Value
N = 57	
Bi-weighted location: C_{BI}	$\overline{z} = 0.1989^{+0.0005}_{-0.0007}$
Bi-weighted scale: S_{BI}	1330^{+130}_{-90} km s^{-1}
Maximum gap	564 km s^{-1}

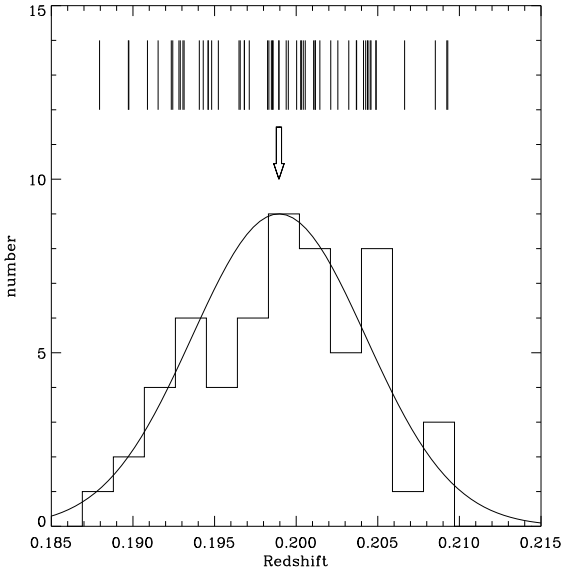

Fig. 4. Abell 1451: Redshift histogram for cluster members; the bin size is 0.0019. The bi-weighted location (C_{BI}) is shown by an arrow. The lines above the histogram are the actual 1-D redshift distribution and the continuous line is the Gaussian function with bi-weighted location (C_{BI}) and bi-weighted scale (S_{BI}) from Table 4.

Table 6. RXJ1314−25: Statistics of the redshift distribution, as for Table 5. The subdivision into two groups follows from KMM (Ashman et al. 1994)

Characteristic	Value
Total, N = 37	
C_{BI}	$\overline{z} = 0.2474^{+0.0006}_{-0.0008}$
S_{BI}	1100^{+140}_{-90} km s^{-1}
Maximum gap	523 km s^{-1}
Group 1 (East), N = 15	
C_{BI}	$\overline{z} = 0.2429^{+0.0003}_{-0.0008}$
S_{BI}	590^{+110}_{-150} km s^{-1}
Maximum gap	516 km s^{-1}
Group 2 (West), N = 22	
C_{BI}	$\overline{z} = 0.2500^{+0.0006}_{-0.0005}$
S_{BI}	560^{+120}_{-70} km s^{-1}
Maximum gap	523 km s^{-1}

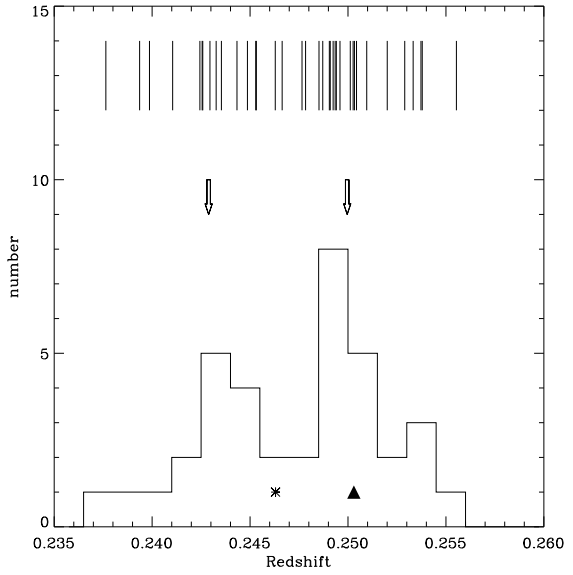

Fig. 5. RXJ1314−25: Redshift histogram for cluster members; the bin size is 0.0015. The C_{BI} locations for the two groups (see Table 6) are indicated by arrows. The two brightest cluster galaxies are marked: #48 with an asterisk and #19 with a filled triangle.

Table 7. ROSAT-HRI X-ray observing log

Cluster	Date	Exposure (s)
Abell 1451	1997 Jul 14–16	25603
RXJ1314−25	1996 Jan 27–31	29294

The optical image of the cluster (Fig. 3) shows two dominant galaxies (#48 and #19, marked also in Table 4) as the brightest cluster galaxies (BCG). Both have typical giant elliptical galaxy absorption line spectra, without any apparent emission lines. The second-ranked BCG (#19, $z = 0.2503$) is at rest with respect to the galaxy members of the western group, while the first-ranked galaxy (#48, $z = 0.2463$) differs by ~ 800 km s^{-1} from the mean redshift of the eastern group, but lies closer to the overall cluster mean. The separation between the two groups in velocity space is ~ 1700 km s^{-1}, substantially greater than their combined velocity dispersions. With optical data alone we can not determine whether the two groups are gravitationally connected.

3. X-ray data and analysis

The X-ray observing logs for both clusters are given in Table 7. For both ROSAT/HRI images we have used 5″/pixel binning of the event list in order to reduce the noise as much as possible without losing information on the cluster extension. The raw photon images were then filtered using wavelet analysis with Poisson noise modeling (Starck & Pierre 1998) at 10^{-4} ($\sim 4\sigma$) significance level for the wavelet coefficients.

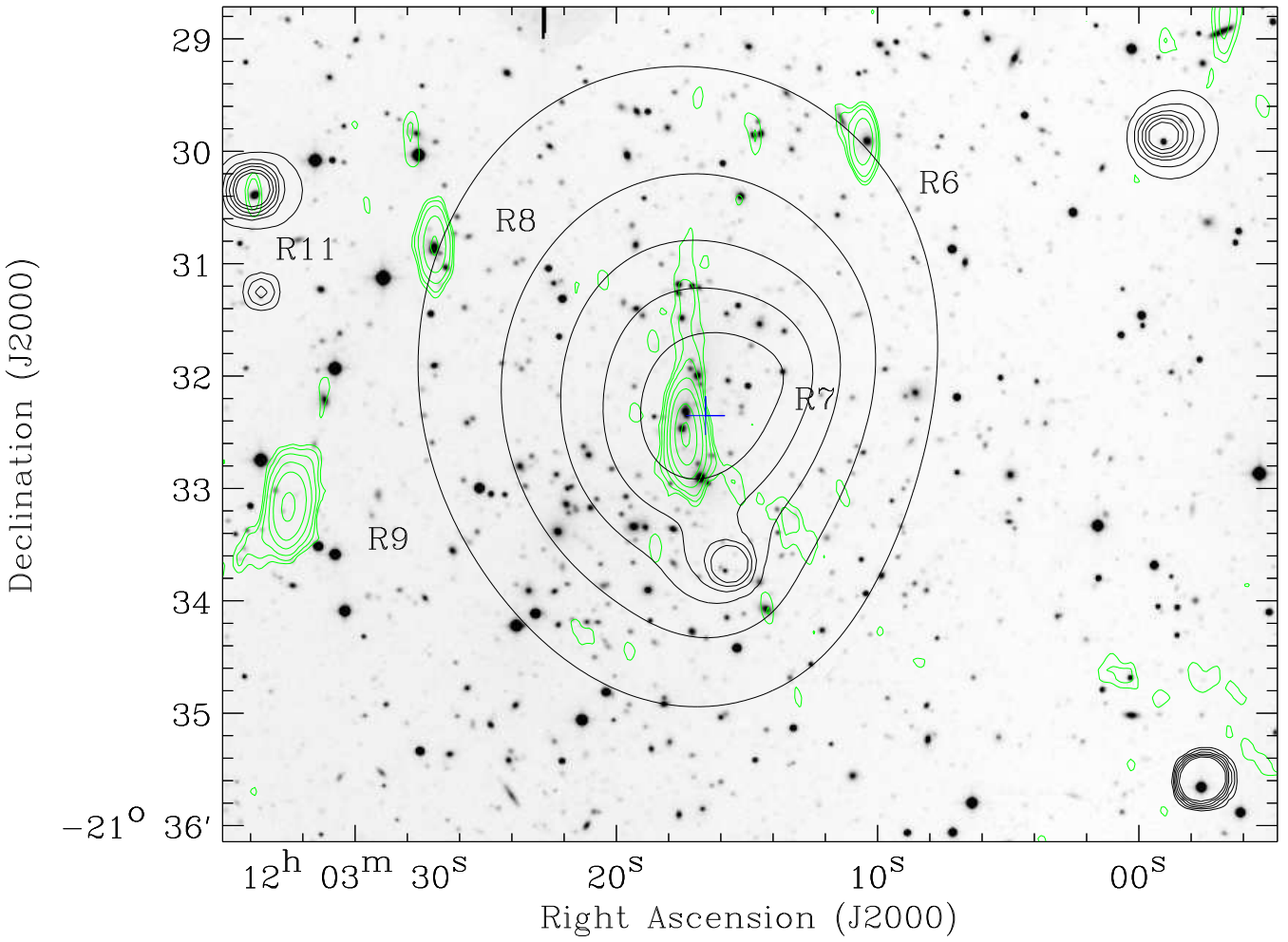

Fig. 7. Abell 1451: Optical V-band image from the Danish 1.5-m telescope overlaid with HRI X-ray contours (heavy) and 20 cm ATCA radio contours (lightweight). The X-ray contours run from 0.006 to 0.02 counts s^{-1} $arcmin^{-2}$ in logarithmic steps; the innermost cluster contour is at 0.0134 counts s^{-1} $arcmin^{-2}$. The peak of the extended X-ray emission, used for the profile measurements, is marked with a cross. The radio contour levels are 0.2, 0.3, 0.5, 1, 2, 5 and 10 mJy/beam; the rms noise level is 80 μJy/beam.

3.1. X-ray morphology

The X-ray contours are shown overlaid on optical images and radio observations (see Sec.4) in Fig. 7 for Abell 1451 and in Fig. 8 for RXJ1314−25.

3.1.1. Abell 1451

The X-ray image in Fig. 7 shows a very strong point source $\sim 1'30''$ south of the cluster centre which coincides with a QSO at $z = 1.17$ (object #32 in Table 3). The cluster emission is regular, with the inner contours slightly twisted but no sign of substructure. The X-ray emission peaks at R.A. $= 12^h03^m16\overset{s}{.}6$ and Dec. $= -21°32'21''$, which is $36''$ (150 kpc) north of the brightest cluster galaxy (#34 in Table 3) and $12''$ west of the second brightest galaxy (#39), and $\sim 1'40''$ from the catalogued cluster position (Abell et al. 1989).

3.1.2. RXJ1314−25

The cluster X-ray emission is quite irregular, showing two central peaks and a SE–NW elongation. Unfortunately, there is an X-ray emitting star projected in front of the cluster (object #29 in Table 4) only $\sim 24''$ from the adopted X-ray centre. The strong point source SE of the cluster centre is a Sy1 galaxy (object #47 in Table 4) and a cluster member. There is no indication of substructure in the X-ray emission associated with the eastern group or the brightest cluster galaxy (see Fig. 6).

3.2. X-ray properties

To estimate the basic physical cluster parameters we model the X-ray surface brightness using the isothermal β-model (King 1962, Cavaliere & Fusco-Femiano 1976)

$$S(r) = S_0 \left(1 + (r/r_c)^2\right)^{0.5-3\beta} + S_b, \quad (1)$$

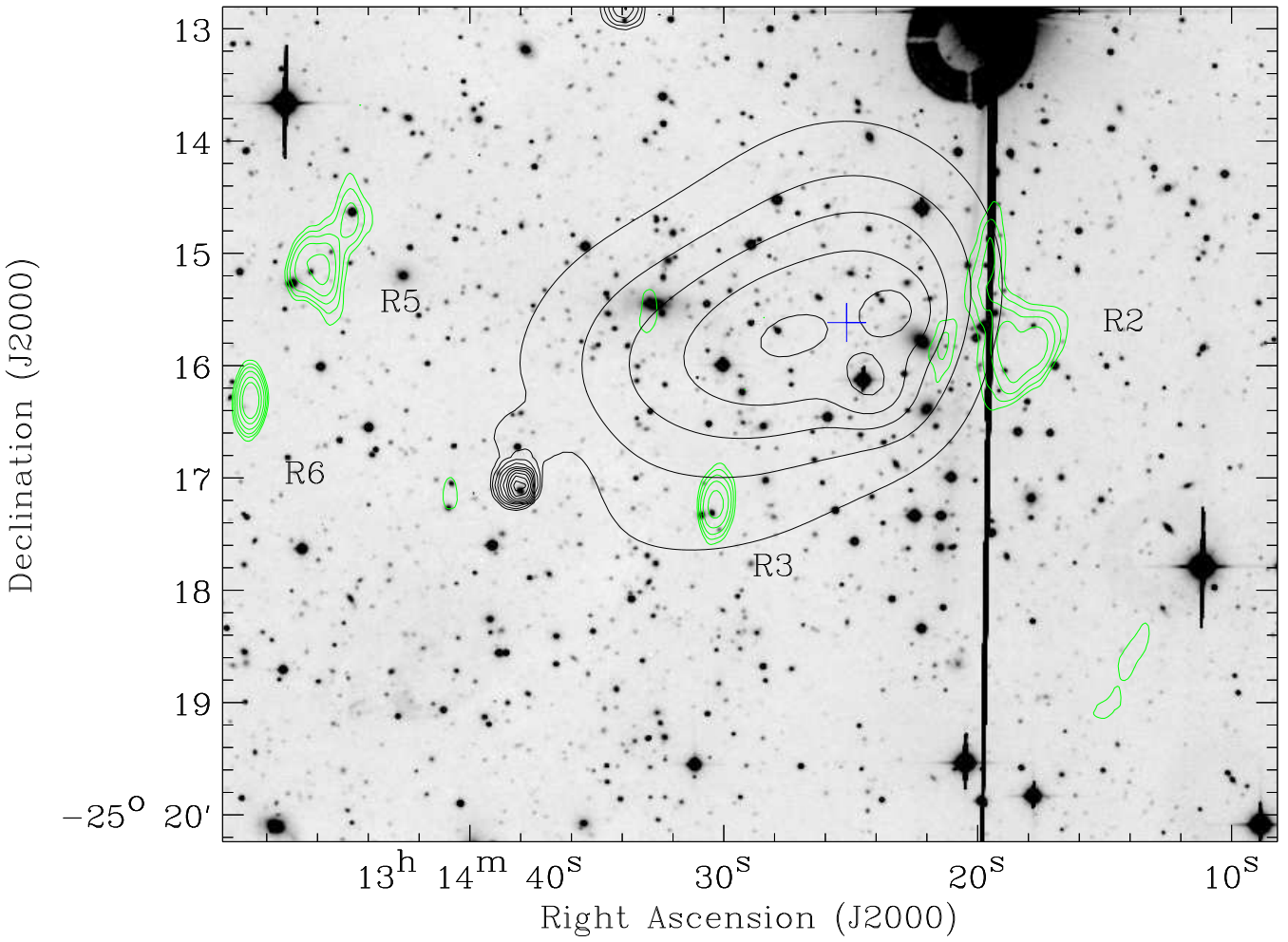

Fig. 8. RXJ1314−25: Optical I-band image from the Danish 1.5-m telescope overlaid with HRI X-ray contours (heavy) and 20 cm ATCA contours (lightweight). The X-ray contours run from 0.004 to 0.065 counts s^{-1} $arcmin^{-2}$ in logarithmic steps; the innermost cluster contour is at 0.012 counts s^{-1} $arcmin^{-2}$. The centre of the X-ray emission taken for the profile measurements is marked with a cross. The radio contour levels are 0.35, 0.5, 0.7, 1, 1.5 and 2 mJy/beam; the rms noise level is 90 μJy/beam.

where $S(r)$ is the azimuthally averaged X-ray surface brightness as a function of the radial distance r from the centre, S_0 is the central brightness, S_b is the background contribution and r_c is the core radius. To fit the model profile to the data we define a proper cluster centre and exclude any discrete sources projected over the cluster X-ray emission. Finally, we obtain an average profile by summing the cluster X-ray photons in concentric rings and fit the model (Eq. 1) with S_0, S_b, β and r_c as free parameters, taking into account the Poissonian errors of the rings counts. The X-ray surface brightness profiles of Abell 1451 and RXJ1314−25 are shown in Figs. 9–10, with the corresponding parameters in Table 8.

To derive the count-rate in the [0.1–2.4] keV ROSAT/HRI band we integrate the fitted surface brightness profile analytically, excluding the background. The integration is usually carried out to a given radius $r_{\rm lim}$, where the surface brightness profile reaches the detection limit; for both clusters we put $r_{\rm lim} = 300''$. For the overall

Table 8. β-profile best-fit parameters with the corresponding 95% confidence intervals.

Parameter	Abell 1451	RXJ1314−25
r_c (arcsec)	59 ± 20	81 ± 28
r_c (kpc)	240 ± 90	400 ± 140
β	0.50 ± 0.08	0.77 ± 0.23

count rate C we have

$$C(< r_{\rm lim}) = \int_0^{r_{\rm lim}} 2\pi r S(r) dr = \frac{\pi S_0 r_c^2}{3/2 - 3\beta} \times \left[\left(1 + (r_{\rm lim}/r_c)^2\right)^{3/2-3\beta} - 1\right]. \quad (2)$$

By means of EXSAS (Zimmermann et al. 1994), the observed count-rate is then used to normalize the spectral model — a Raymond & Smith (1977) thermal plasma emission, convolved by the ROSAT/HRI response function, with temperature and metallicity from ASCA data (Matsumoto et al. 2001) and line-of-sight Galactic absorp-

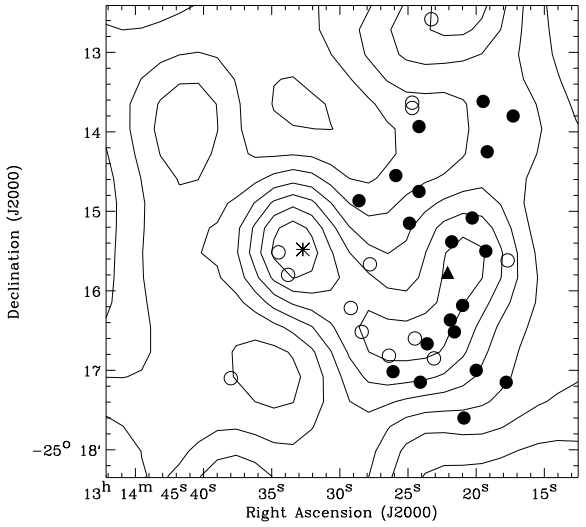

Fig. 6. RXJ1314−25: Sky distribution for cluster members. Open circles denote the members of the eastern group, while the filled circles are those belonging to the western group as assigned by KMM (see Table 6). The contours are the adaptive kernel density estimate (Silverman 1986, Pisani 1996) of the SuperCOSMOS galaxy distribution. The asterisk and filled triangle mark the positions of the first- and second-ranked BCGs respectively (#48 and #19 in Table 4). Note that galaxy #20 is too close to galaxy #19 to be plotted separately.

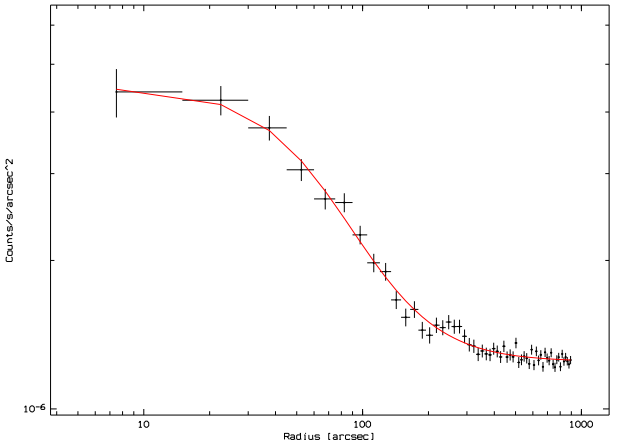

Fig. 9. Abell 1451: Circularly averaged surface brightness profile in the energy band [0.1–2.4] keV. Bin size is 15″ and the solid line is the King profile fit (Eq. 1) with parameters in Table 8.

tion by H I from Dickey & Lockman (1990). The spectrum is then integrated to derive the flux and cluster rest frame luminosity in the "standard" X-ray bands [0.5–2] and [2–10] keV. The profile model, together with the emission model, was used to derive the emission measure, $\int_V n_e n_p dV$, and the proton density distribution:

$$n_p(r) = n_p(0)\left(1 + (r/r_c)^2\right)^{-3\beta/2}. \quad (3)$$

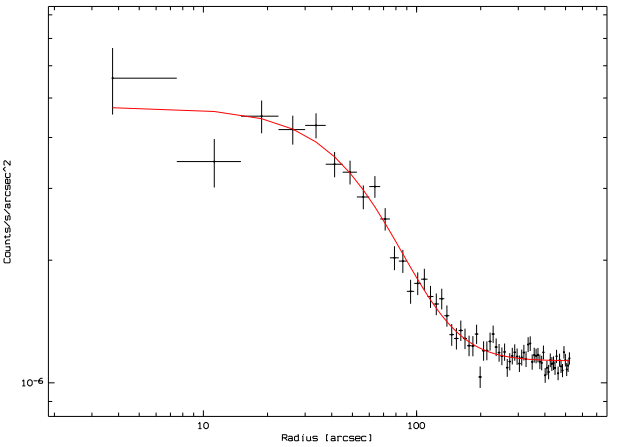

Fig. 10. RXJ1314−25: Circularly averaged surface brightness profile in the [0.1–2.4] keV energy band. Bin size is 7.5″ and the solid line is the King profile fit (Eq. 1). The deviation of the inner two points from the model is due to the irregular morphology in the cluster centre.

Assuming a hydrogen gas then $\rho_{\rm gas} = 2.21\mu m_p n_p$ and we can calculate the mass of the gas inside a given radius R:

$$M_{\rm gas}(r < R) = \int_0^R 4\pi\rho_{\rm gas}(r)dr. \quad (4)$$

The total gravitating mass of the cluster within radius r can be estimated, assuming hydrostatic equilibrium, as

$$M_{\rm tot}(r) = \frac{r^2 kT}{G\mu m_p}\left(\frac{1}{n}\frac{dn}{dr} + \frac{1}{T}\frac{dT}{dr}\right), \quad (5)$$

with $n = n_e + n_p = 2.21 n_p$ and $\mu = 0.61$ for the abundances. Ignoring any radial temperature dependence we can derive:

$$M_{\rm tot}(r) = 3\beta r^3 kT/G\mu m_p(r^2 + r_c^2). \quad (6)$$

The derived and model parameters for the X-ray emission of both clusters are shown in Table 9. There are small differences in luminosity when compared with ASCA data. This can be explained, firstly, by the smaller limiting distance (4′) for flux integration adopted in Matsumoto et al. (2001) and secondly, by the fact that for both clusters there are discrete X-ray sources within the extended cluster emission which were not resolved by ASCA and so their contribution was not subtracted.

Derived cluster masses should be considered with caution, as the combined X-ray/optical analysis tends to indicate that neither cluster has reached equilibrium.

Although the X-ray emission in both clusters is not centrally peaked, we have tried to estimate the cooling flow radius — the zone where the time for isobaric cooling is less than the age of the universe (Sarazin 1986, Fabian 1994). For any reasonable choice of the Hubble constant and gas parameters (n_p, T_X, Z) there is no such zone.

Table 9. X-ray data for both clusters. N_H is taken from Dickey and Lockman (1990). ASCA data for T_X and L_X in the [2−10] keV band (Matsumoto et al. 2001) are indicated correspondingly. The count-rate C is in [0.1–2.4] keV band. The luminosities in [0.5–2], [2–10] keV and bolometric bands were obtained by extrapolation of the King profile out to 5′.

Parameter	Abell 1451	RXJ1314−25
$r_{\rm lim} = 5'$ (Mpc)	1.3	1.5
N_H (10^{20} cm^{-2})	4.5	6.7
T_X (keV) ASCA	$13.4^{+1.9}_{-1.5}$	$8.7^{+0.7}_{-0.6}$
Count-rate $C(r < r_{\rm lim})$ (cts s^{-1})	0.126	0.083
F_X [0.5–2] keV (10^{-12} erg cm^{-2} s^{-1})	4.4	3.2
F_X [2–10] keV (10^{-12} erg cm^{-2} s^{-1})	11.2	6.8
L_X [0.5–2] keV (10^{44} erg s^{-1})	6.8	7.4
L_X [2–10] keV (10^{44} erg s^{-1})	17.2	16.0
L_X [2–10] keV (10^{44} erg s^{-1}) ASCA	15.0†	18.0‡
L_{bol} (10^{44} erg s^{-1})	39.8	34.0
$n_p(0)$ (10^{-3} cm^{-3})	5.09	5.31
$M_{\rm tot}(< r_{\rm lim})$ (10^{14}M$_\odot$)*	8.6	9.7
$M_{\rm gas}(< r_{\rm lim})$ (10^{14}M$_\odot$)*	2.2	2.6
$M_{\rm gas}/M_{\rm tot}(< r_{\rm lim})$	0.25	0.27

† ASCA/GIS luminosity out to 4′, including the contribution from the QSO ∼ 1′30″ south of the centre.
‡ ASCA/GIS luminosity out to 4′, including the contribution from the Sy1 galaxy ∼ 3′15″ south-east of the centre.
* Assuming hydrostatic equilibrium.

Table 10. Details of the ATCA radio observations of the two clusters.

Cluster (Obs. Date)	Frequency (GHz)	RMS Noise mJy/beam	Restoring Beam $b_{\rm maj}$ (″)	$b_{\rm min}$ (″)	PA (deg)
Abell 1451	1.384	0.08	27.8	9.4	−0.5
(1999 Feb 25)	2.496	0.06	15.4	5.2	−0.5
RXJ1314−25	1.384	0.09	23.8	9.4	0.9
(1999 Feb 26)	2.496	0.06	13.2	5.2	0.8

4. Radio observations and data analysis

4.1. Observations and reduction

The Australia Telescope Compact Array (ATCA) consists of five 22 m antennas on a 3 km east-west railway track, and a sixth antenna 3 km from the western end of the track. Each cluster was observed in 1999 February for 12 hours with the ATCA in the 6C configuration, giving baselines ranging from 153 m to 6 km. Simultaneous observations at 1.384 GHz and 2.496 GHz were made for each cluster.

The radio data were processed using standard `MIRIAD` (Sault et al. 1995) software and techniques. The primary flux density calibrator was PKS B1934−638, with PKS B1245−197 as the secondary phase calibrator. The data were then CLEANed and RESTORed. Table 10 lists details of the ATCA observations, including the size and orientation of the elliptical Gaussian restoring beams and the rms noise in the final images.

4.2. Data Analysis

The `AIPS` task `VSAD` was used to generate a radio source list for each cluster, above a nominal cutoff of 0.5 mJy at 1384 MHz. An elliptical Gaussian was fitted to each source as described by Condon (1997). For sources which were extended or complex, the integrated flux density was estimated by using `kview` (Gooch 1996) to sum inside a rectangular region defined around the source. The radio sources for Abell 1451 and RXJ1314−25 within one Abell radius ($R_A = 1.7/z$ arcmin) of the cluster centre[1] are listed in Table 11. Positions are measured from the 1384 MHz image except for sources R1 and R9 in Abell 1451 which are measured at 2496 MHz; quoted errors are the quadratic combination of the formal `VSAD` error and a nominal 0.5″ calibration uncertainty. Errors in flux density are taken directly from the `VSAD` output; if no error is quoted for $S_{\rm int}$ the measurement was made using `kview`.

A search was carried out for optical identifications of the radio sources in Table 11 using the SuperCOSMOS catalogue (Hambly et al. 2001). A search radius of 10 arcsec was used. The results are shown in Table 12.

4.2.1. Abell 1451

The 1.384 GHz (20 cm) radio contours overlaid on the DSS image of the cluster field are shown in Fig. 11; the 1.384 GHz (20 cm) radio contours for the central part of the cluster are shown in Fig. 7 together with the X-ray contours. The central radio source (R7 in Table 11) is extended north-south with a peak that best matches galaxy #40 from Table 3. The apparent wide-angle tail (WAT) morphology relies on the lowest (2.5σ) contours and is therefore uncertain. Such morphologies are usually associated with the central dominant cluster member. An alternative interpretation, suggested by the 13 cm observation shown only for the central part of the cluster on Fig. 2, is that R7 is a head-tail source identified either with galaxy #40 or the brighter galaxy #39 which is ∼ 10″ north. Higher resolution radio observations are needed to settle this issue.

Apart from R7, there are no other cross-identifications between the spectroscopic catalogue and radio source list. However, there are several likely cluster identifications, including the head-tail source (R1) located ∼8′ NW of the cluster centre. The weakest source in the field, R11, is a clear AGN candidate — it is a strong X-ray source with a flat radio spectrum; SuperCOSMOS classifies the optical counterpart as a galaxy. R9 is an extended source with no obvious optical counterpart. We initially considered it as a possible relic source (Enßlin et al. 1998), but the 13 cm image suggests an identification with a very faint object visible on both the B and R sky survey images. The QSO (#32, $z = 1.17$) is radio quiet.

[1] For Abell 1451 we have adopted the X-ray peak as the centre of the cluster.

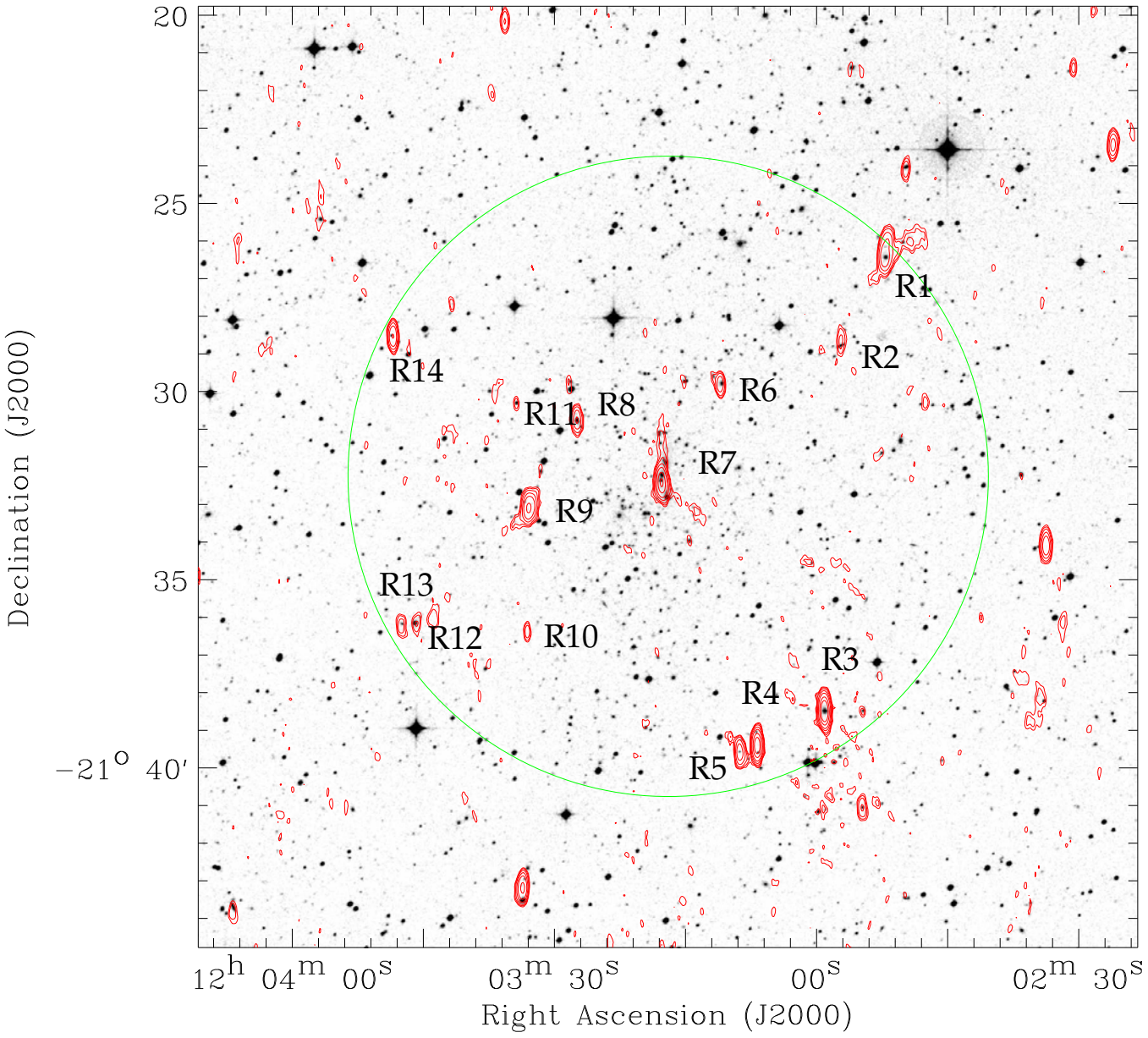

Fig. 11. Abell 1451: DSS image overlaid with ATCA 20cm radio contours. The Abell radius with X-ray emission peak as a cluster centre is shown as a green circle. The objects are designated by their respective names from Table 11. The radio contour levels are 0.2, 0.3, 0.5, 1, 2, 5 and 10 mJy/beam; the rms noise level is 80 μJy/beam.

4.2.2. RXJ1314−25

The 1.384 GHz (20 cm) radio contours overlaid on the DSS image of the cluster field are shown in Fig. 12; the central region of RXJ1314−25, together with X-ray contours, are shown in Fig. 8 overlaid on the optical image from Fig. 3. Background noise in the central region of the 20 cm image is affected by sidelobes of the 200 mJy source NVSS J1314−2522 located SW of the cluster centre, just outside one Abell radius. For this reason the lowest contour level in Fig. 8 has been set at $\sim 4\sigma$.

As shown in Table 11, the projected radio source density is lower than for Abell 1451. There are no positive identifications with spectroscopically confirmed cluster members, although there is a weak source just below the 0.5 mJy threshold, very close to the brightest cluster galaxy BCG2 (galaxy #48; see Fig. 8). There is also a striking mirror symmetry of sources R2 and R5 (Table 11) with respect to this galaxy, resembling the lobes of an FR II radio galaxy (see e.g. Fig. 8). At the redshift of the galaxy, $z = 0.2466$, the linear size of $6'15''$ would correspond to $\sim$1 Mpc, a typical scale for a giant radio galaxy (Schoenmakers et al. 2001). Such an interpretation is questionable, however, as the galaxy is clearly not located in an underdense environment (see Fig. 6), as required for the growth of giant sources. Neither source has an obvious optical counterpart in the 20 cm image, but R5 appears double at 13 cm, with a plausible optical identifica-

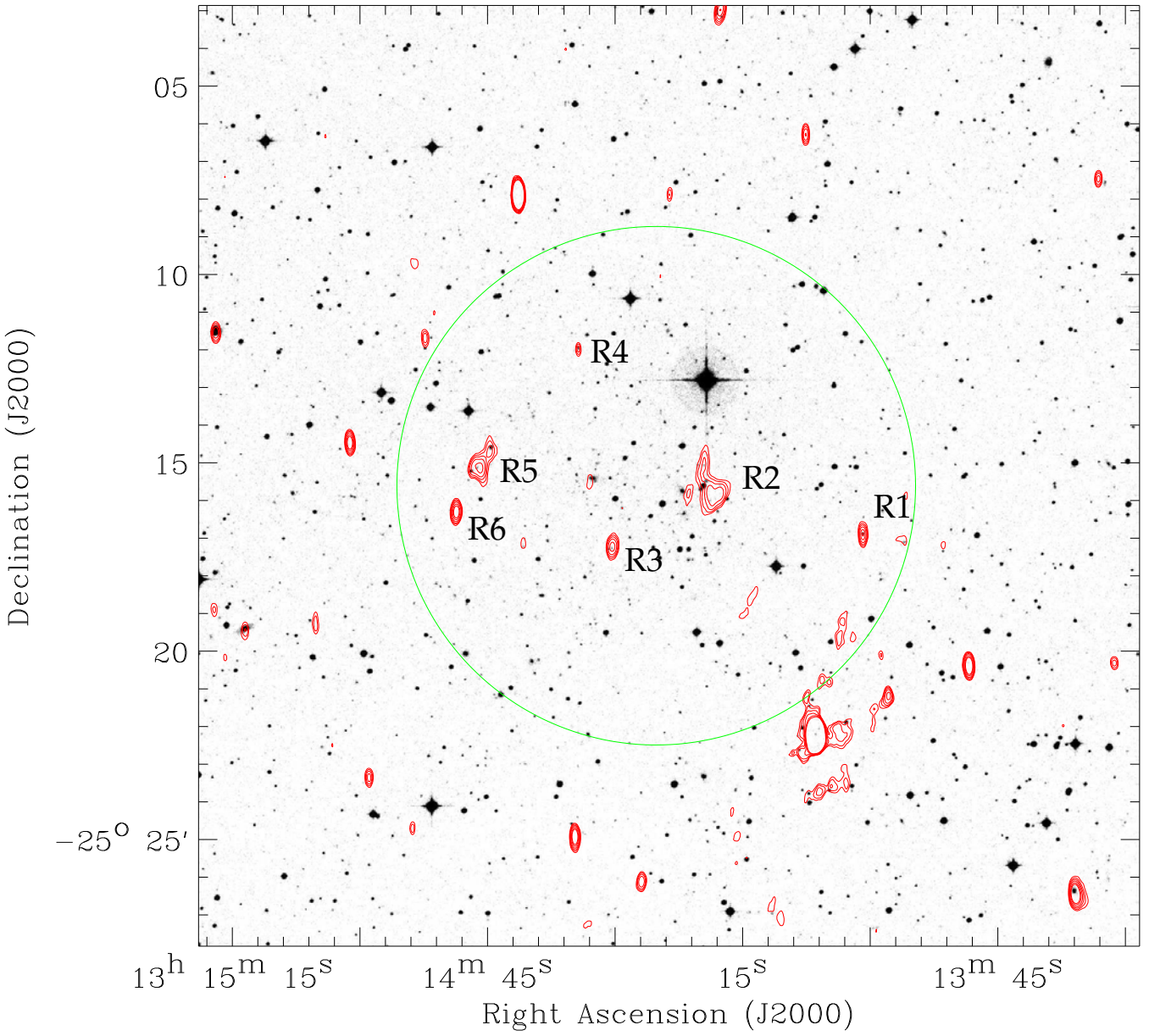

Fig. 12. RXJ1314−25: DSS image overlaid with ATCA 20cm radio contours. The Abell radius is shown as a green circle. The objects are designated by their respective names from Table 11. The radio contour levels are 0.35, 0.5, 0.7, 1, 1.5 and 2 mJy/beam; the rms noise level is 90 μJy/beam.

tion midway between the components. On the other hand, with its extended radio emission, steep spectrum and position in the cluster, R5 is an excellent candidate for a relic source. Its true extent is difficult to judge from the ATCA 20 cm image because of sidelobe confusion, but there is a suggestion of low surface brightness, extended emission in the vicinity of BGC#1 and the western X-ray peak.

5. Discussion

5.1. Abell 1451

The dynamical state of Abell 1451 is very similar to that of Abell 665 (Gomèz et al. 2000) and to the more distant Abell 1300 (Lémonon et al. 1997, Reid et al. 1998), suggesting that it may also be in the final stage of establishing equilibrium after a merger event.

Support for the merger scenario comes from different morphological and physical reasons which are summarized below:

– There is no single dominant galaxy. The brightest cluster galaxy (#34, Table 3) is 35″ away from the X-ray centroid, and 580 km s^{-1} from the cluster mean redshift.
The putative identification for the central radio source (#40, Table 3) is offset by 1300 km s^{-1} from the cluster mean redshift.

Table 11. Radio sources for Abell 1451 and RXJ1314−25 within 1 Abell radius of the cluster centre. Source coordinates are from VSAD. The peak ($S_{\rm peak}$) and integrated ($S_{\rm int}$) flux densities were measured using either VSAD or kview as described in the text. For Abell 1451 we adopt the X-ray emission peak as the centre.

N	RA (err s)	Dec (err ″)	ν	$S_{\rm peak}$(err)	$S_{\rm int}$(err)
	(J2000)		GHz	mJy/bm	mJy
		Abell 1451			
R1	12:02:51.67(0.04)	−21:26:35.8(1.0)	1.384	3.9	12.1
			2.496	1.6	9.6
R2	12:02:56.73(0.06)	−21:28:46.7(1.9)	1.384	0.60(0.06)	1.10(0.19)
			2.496	—	—
R3	12:02:58.94(0.04)	−21:38:35.8(0.5)	1.384	25.8(0.08)	28.3(0.15)
			2.496	12.2(0.06)	14.4(0.12)
R4	12:03:06.66(0.05)	−21:39:29.8(0.5)	1.384	18.6(0.08)	18.6(0.14)
			2.496	7.80(0.06)	8.27(0.11)
R5	12:03:08.65(0.05)	−21:39:40.6(0.6)	1.384	3.75(0.08)	4.24(0.15)
			2.496	1.95(0.06)	2.31(0.12)
R6	12:03:10.59(0.04)	−21:29:54.4(0.7)	1.384	1.90(0.08)	1.97(0.14)
			2.496	0.98(0.06)	1.02(0.11)
R7	12:03:17.35(0.04)	−21:32:31.3(0.5)	1.384	11.4(0.07)	15.4
			2.496	5.51(0.06)	7.2
R8	12:03:26.97(0.04)	−21:30:49.9(0.7)	1.384	2.21(0.07)	2.65(0.15)
			2.496	1.19(0.06)	1.36(0.11)
R9	12:03:32.53(0.04)	−21:33:09.1(0.5)	1.384	6.11(0.07)	9.7
			2.496	2.56(0.04)	6.2
R10	12:03:32.85(0.05)	−21:36:26.2(1.6)	1.384	0.73(0.08)	0.73(0.10)
			2.496	0.36(0.06)	0.40(0.11)
R11	12:03:33.84(0.05)	−21:30:22.1(1.7)	1.384	0.39(0.08)	0.36(0.13)
			2.496	0.30(0.05)	0.47(0.13)
R12	12:03:45.47(0.07)	−21:36:11.7(2.1)	1.384	0.52(0.07)	0.80(0.17)
			2.496	—	—
R13	12:03:47.24(0.05)	−21:36:15.1(1.3)	1.384	0.78(0.07)	1.01(0.16)
			2.496	0.31(0.05)	1.09(0.19)
R14	12:03:47.91(0.04)	−21:28:33.1(0.5)	1.384	5.53(0.08)	5.32(0.14)
			2.496	2.70(0.06)	2.79(0.12)
		RXJ1314−25			
R1	13:14:00.90(0.04)	−25:16:53.7(0.7)	1.384	2.09(0.09)	2.38(0.1)
			2.496	0.84(0.06)	1.13(0.1)
R2	13:14:18.62(0.05)	−25:15:47.0(1.0)	1.384	1.16(0.03)	13.0
			2.496	—	—
R3	13:14:30.31(0.04)	−25:17:14.2(0.7)	1.384	1.93(0.08)	4.4
			2.496	0.54(0.04)	1.7
R4	13:14:34.31(0.06)	−25:11:59.9(1.6)	1.384	0.69(0.09)	0.64(0.2)
			2.496	0.62(0.07)	0.57(0.1)
R5	13:14:45.90(0.05)	−25:15:05.5(0.7)	1.384	1.57(0.04)	6.8
			2.496	0.48(0.04)	1.5
R6	13:14:48.64(0.04)	−25:16:18.3(0.6)	1.384	3.20(0.09)	3.65(0.2)
			2.496	1.47(0.05)	2.20(0.1)

Table 12. Radio-optical identifications in Abell 1451 and RXJ1314−25. N refers to the identification number given in Table 11 and Δr is the radius-vector offset between radio and SuperCOSMOS optical positions. T refers to the SuperCOSMOS image classification: 1=galaxy; 2=star.

N	RA	Dec	B_J	Δr	T
	Optical (J2000)		(mag)	(″)	
		Abell 1451			
R1	12:02:51.56	−21:26:35.4	19.26	1.6	1
R2	12:02:56.81	−21:28:55.8	18.42	9.1	1
R3	12:02:58.92	−21:38:36.4	18.18	0.7	1
R5	12:03:08.68	−21:39:40.0	20.12	0.7	2
R6	12:03:10.35	−21:29:54.2	19.13	3.4	1
R7	12:03:17.47	−21:32.27.4	19.41	4.2	1
R8	12:03:26.98	−21:30:51.5	18.19	1.6	1
R11	12:03:45.70	−21:36:11.9	18.98	3.5	1
R12	12:03:47.14	−21:36:12.8	20.28	2.8	1
R13	12:03:48.11	−21:28:33.1	20.40	3.2	2
		RXJ1314−25			
R1	13:14:00.89	−25:16:54.3	19.81	0.6	2
R2	13:14:23.78	−25:07:51.8	21.07	2.9	1
R3	13:14:30.36	−25:17:17.4	21.40	3.3	1
R4	13:14:34.27	−25:11:58.9	20.07	1.1	1
R5	13:14:46.17	−25:15:09.1	21.37	5.1	1

– Nearly regular X-ray emission, without substructures but slightly twisted inner part.
– No cooling flow region.
– Deviations from the observed scaling relations L_X–T and σ_v–T (Xue & Wu 2000), shown in Table 13. The cluster is significantly less luminous than expected from its measured temperature. The very high observed temperature (13.4 keV) is probably an indication of a shock that occurred in the recent past. We cannot exclude a possible overestimation of the published ASCA temperature due to the presence of the background X-ray point source. However, the small difference (in the wrong sense) between the ASCA luminosity and our estimate with the QSO emission excluded (see Table 9) seems unlikely to account for a temperature overestimate of more than 4 keV. A new and more accurate measurement of the temperature is clearly needed.
– Based on numerical simulations (Roettiger et al. 1997, Belsole et al. 2002), the regular X-ray morphology and high X-ray temperature are fully compatible with expectations from a past merger.

We can also determine the dynamical status of the cluster by comparing its kinetic and potential energies. From the measured velocity dispersion we find $\beta_{\rm spec} = \mu m_p \sigma_v^2 / kT = 0.84 \pm 0.25$, while from the X-ray emission, with the correction factor from Bahcall & Lubin (1994), we have $\beta_X^c = 1.25\beta_X = 0.63 \pm 0.1$. These values are consistent within the uncertainties, indicating that the gas and galaxy motions are close to equipartition.

If a merger occurred recently we might expect signatures at radio wavelengths, such as radio halo/relic sources, and possibly tailed sources (e.g. Enßlin et al. 1998, Reid et al. 1998, Röttgering et al. 1994). There is no evidence for a radio halo, although there is a tailed source (R7) near the cluster centre which could have disrupted it (Giovannini 1999, Liang et al. 2000).

5.2. RXJ1314−25

RXJ1314−25 is morphologically and dynamically very different from Abell 1451. It shows a clear bi-modal structure — there are two groups in velocity space separated by ~ 1700 km s^{-1} (cf. Table 6 and Fig. 5) which are also separated in the projected galaxy distribution (cf. Fig. 6). The dominant galaxies of each group are separated by

Table 13. Scaling relations for Abell 1451 and RXJ1314−25. σ_v–T is from Xue & Wu (2000), while $L_{\rm bol}$–T is from Arnaud & Evrard (1999). The temperature from ASCA is in keV, $L_{\rm bol}$ in units of 10^{44} erg s^{-1} and σ_v in km s^{-1} are from this paper.

Cluster	T (obs)	σ_v (obs)	σ_v (σ_v–T)	$L_{\rm bol}$ (obs)	$L_{\rm bol}$ ($L_{\rm bol}$–T)
Abell 1451	13.4	1330	1670	39.8	116
RXJ1314−25	8.7	1100	1261	34.0	33.5

~ 1000 km s^{-1} in redshift space, and $2'25''$, or $\approx$700 kpc, in projected distance.

The X-ray emission is elongated, with the centroid located between the two dominant galaxies. The elongation, however, is rotated by $\approx 20^\circ$ from the axis connecting the two BCGs. This may simply be due to the decoupling between the galaxies and gas during the merger.

There are no cluster radio sources within the X-ray extension, with the possible exception of the weak (uncatalogued) source at the position of galaxy #48. If we are witnessing an interaction between two sub-clusters, we might expect stronger radio activity than observed. However, residual sidelobes from a strong background source $\sim 7'$ south of the centre hamper the detection of any very extended emission. In addition, a more compact ATCA antenna configuration is needed to improve sensitivity to low surface brightness emission. There are, however, two extended radio sources, one of which (R2) has a steep radio spectrum and no optical counterpart, and is therefore a plausible candidate for a relic source.

The observed L_X, T and σ_v for RXJ1314−25 are in good agreement with the L_X–T and σ_v–T scaling relationships (Table 13), suggesting that the merger has progressed to the stage where the transient shock heating and radio activity have dissipated. On the other hand, if the cluster is in a pre-merging phase, then it is unusual that the X-ray elongation is not aligned with the group centres and that there is no sign of X-ray substructure around the eastern group, as revealed, for example, in numerical simulations (Roettiger et al. 1997, Takizawa 2000). The scattered appearance of the projected galaxy distribution of the eastern group compared to the western group (Fig. 6) also supports a post-merging scenario.

In conclusion, our observations suggest that neither cluster is relaxed following a recent merger. However, their properties and scaling laws are quite different, illustrating the diversity in the merging and relaxation processes in cluster formation and evolution. The current data for the two clusters are compatible with the expectations from the merger of a small group with a bigger cluster for Abell 1451, and nearly equal mass groups for RXJ1314−25. Deep XMM and Chandra observations, coupled with detailed numerical simulations are needed to assess these hypotheses and better understand the many aspects of the physical processes occurring during accretion and relaxation over the course of a cluster merger.

Acknowledgements. We would like to thank Romain Teyssier, John Hughes and Pierre-Alain Duc for numerous discussions about simulations, data reduction and analysis. We are especially indebted to Hector Flores and Dario Fadda for providing us with the observation of galaxy #48 in RXJ1314−25 (CFHT, June 2001). We thank the referee Reinaldo de Carvalho for valuable comments.

References

Abell, G.O., 1958, ApJS 3, 211
Abell G.O., Corwin H.G., Olowin R.P., 1989, ApJS 70, 1
Arnaud M., Evrard, A., 1999, MNRAS 305, 631
Ashman K.M., Bird K.M., Zepf S.E., 1994, AJ 108, 2348
Bahcall N., Lubin L., 1994, ApJ 426, 513
Baier F.W., Lima Neto G.B., Wipper H., Braun M., 1996, AN 317,77
Bautz L.P., Morgan W.W., 1970, ApJ 162, L149
Beers T.C., Flynn K., Gebhardt K., 1990, AJ 100, 32 (ROSTAT)
Belsole E., Sauvageot J.-L., Teyssier R., 2002, (astro-ph/0203297)
Cavaliere A., Fusco-Femiano R., 1976, A&A 49, 137
Condon J.J, 1997, PASP 109, 166
Donahue, M., Voit, G.M., Gioia, I., et al., 1998, ApJ 502, 550
D'Agostino R.B. & Stephens M.A., 1986, Goodness-of-fit Techniques, Marcel Dekker, New York
Maddox, G., Sutherland, W.J., Efstathiou, G., Loveday, J. 1990b, MNRAS, 243, 692
Danese L., De Zotti G., di Tullio G., 1980, A&A 82, 322
Dickey J.M., Lockman F.J., 1990, ARA&A 28, 215
Dressler A. & Shectman S.A., 1988, AJ 95, 985
Efron B., Tibshirani R., 1986, Stat. Sci. 1, 54
Enßlin T.A., Biermann P.L., Klein U., & Kohle S., 1998, A&A 332, 395
Fabian A.C., 1994, ARA&A 32, 277
Geller M.J., Beers T.C., 1982, PASP 94, 421
Giovannini, G., 1999, in "Diffuse thermal and relativistic plasma in galaxy clusters", eds H. Böhringer, L. Feretti, P. Schuecker, MPE Report 271, p. 13
Girardi M., Fadda D., Giuricin G., et al., 1996, ApJ 457, 61
Gómez P.L., Hughes J.P., Birkinshaw M., 2000, ApJ 540, 726
Gooch R., 1996, PASA 14(1), 106
Hambly, N.C., MacGillivray, H.T., Read, M. A. et al., 2001, MNRAS, 326, 1279
Hartigan P.M., 1985, Appl. Stat. 34, 3
Hughes J.P., Yamashita K., Okumura Y., et al., 1988, ApJ 327, 615
Harrison E.R., 1974, ApJ 191, L51
King I.R., 1962, AJ 67, 471
Kurtz M.J., Mink D.J., 1998, PASP 110, 934
Liang H., Hunstead R., Birkinshaw M., Andreani P., 2000, ApJ 544, 686
Lémonon L., Pierre M., Hunstead R., et al., 1997, A&A 326, 34
Lumsden S.L., Collins C.A., Nichol R.C., Eke V.R., Guzzo L., 1997, MNRAS, 290, 119
Matsumoto H., Pierre M., Tsuru T.G., Davis, D., 2001, A&A, 374, 28
Pierre M., Böhringer H., Ebeling H., et al., 1994, A&A 290, 725
Pierre M., Oukbir J., Dubreuil D., et al., 1997, A&AS 124, 283
Pierre M., Starck, J.-L., 1998, A&A 330, 801

Pisani A., 1996, MNRAS 278, 697
Raymond J.C., Smith B.W., 1977, ApJS 35, 419
Reid A.D., Hunstead R.W., Pierre M.M., 1998, MNRAS 296, 531
Rizza E., Loken C., Bliton M., et al., 2000, AJ 119, 21
Roettiger K., Loken C., Burns J.O., 1997, ApJS 109, 307
Röttgering H., Snellen I., Miley G., et al., 1994, ApJ 436, 654
Sarazin C.L., 1986, Review of Modern Physics 58, 1
Sault R.J., Teuban P.J., Wright M.C.H., 1995, in ASP Conf. Ser., Vol. 77, Astronomical Data Analysis Software and Systems IV, ASP Conference Series, Vol. 77, eds. R.A. Shaw, H.E. Payne, & J.J.E. Hayes (San Francisco: ASP), 433
Schoenmakers A.,P., de Bruyn A.,G., Röttgering H.,J.,A., van der Laan H., 2001, A&A 374, 861
Silverman B., 1986, Density Estimation for Data Analysis and Statistics (London: Chapman & Hall)
Starck J.-L., Pierre M., 1998, A&AS 128, 397
Takizawa M., 2000, ApJ 532, 183
Tonry J., Davis M., 1979, AJ 84, 1511
Valtchanov I., 1999, in ASP Conf. Ser., Vol. 172, Astronomical Data Analysis Software and Systems VIII, eds. D.M. Mehringer, R.L. Plante, & D.A. Roberts (San Francisco: ASP), 38
Voges W., Aschenbach B., Boller Th., et al., 1999, A&A 349, 389
West M.J., 1994, In Proc. XIV Moriond Astrophysics Meeting, Clusters of Galaxies, eds. Durret F., Mazure A. & Trân Than Vân J., (Gif-sur-Yvette: Editions Frontières), p. 23
Xue Y.-J., Wu X.-P., 2000, ApJ 538, 65
Yahil A., Vidal N.V., 1977, ApJ 214, 347
Zimmermann H.U., Becker T., Belloni T., et al., 1994, EXSAS User's Guide.

Table 3. A1451 spectroscopic catalogue. The columns are: reference number ("*" denotes 1993 observations); J2000 coordinates; redshift from cross-correlation or line measurements; the corresponding error; B_J magnitude, or R when B_J is not available; flag; and notes. Flag codes are: 0 – star, 1 – galaxy member of the cluster, 2 – galaxy member of the cluster with emission lines, 3 – emission line galaxy not in the cluster, 5 – other galaxy. Magnitudes are taken from the SuperCOSMOS Sky Survey (Hambly et al. 2001), "†" indicates possible magnitude problem due to blending.

No.	R.A. (J2000)	Dec. (J2000)	z	Δz	B_J	Flag	Notes
01	12:02:59.4	-21:33:41	0.0009	0.0003	17.81	0	
02	12:03:00.2	-21:35:01	0.1482	0.0008	19.16	5	
03	12:03:01.0	-21:32:44	0.1968	0.0007	21.82	1	
04	12:03:01.5	-21:33:47	0.0020	0.0005	19.01	0	
05	12:03:02.0	-21:34:20	0.1983	0.0008	—	1	
06	12:03:03.1	-21:34:08	0.2015	0.0004	20.78	1	
07	12:03:03.6	-21:32:25	0.3362	0.0010	21.68	5	
08	12:03:03.9	-21:32:02	0.2011	0.0007	21.35	1	
09	12:03:04.9	-21:32:52	0.1915	0.0004	19.58	1	
10	12:03:04.9	-21:33:17	0.2046	0.0009	20.71	1	
11	12:03:05.9	-21:32:36	0.1983	0.0009	22.35	1	
12	12:03:06.9	-21:32:11	0.0014	0.0004	18.34	0	
13	12:03:08.1	-21:33:54	0.2003	0.0006	21.29	1	
14	12:03:08.5	-21:32:08	0.2133	0.0007	19.19	5	
15	12:03:09.1	-21:33:20	0.1928	0.0008	21.20	1	
16	12:03:09.8	-21:33:46	0.2006	0.0004	20.36	1	
17	12:03:10.4	-21:33:56	0.0007	0.0004	20.10	0	
18	12:03:10.2	-21:32:45	0.3071	0.0005	—	5	
19*	12:03:11.3	-21:30:24	0.1985	0.0007	21.64	1	
20	12:03:12.1	-21:34:15	0.2049	0.0004	20.62	1	
21	12:03:12.9	-21:32:58	0.3053	0.0003	22.07	3	[OII],[OIII]
22	12:03:13.2	-21:33:35	0.1879	0.0008	22.72	1	
23	12:03:13.8	-21:33:23	0.0018	0.0005	21.35	0	
24	12:03:14.2	-21:34:04	0.2066	0.0006	18.99	2	[OII],H_β,[OIII],H_α
25*	12:03:14.5	-21:29:50	0.2032	0.0004	20.08†	1	
26*	12:03:14.5	-21:31:31	0.2037	0.0007	19.91	1	
27	12:03:14.5	-21:33:49	0.2044	0.0004	19.96	2	[OII],[OIII],H_α
28	12:03:14.9	-21:32:05	0.0019	0.0005	19.61	0	
29*	12:03:15.2	-21:30:23	0.1909	0.0004	19.37	1	
30	12:03:15.4	-21:34:25	0.0009	0.0007	17.39	0	
31	12:03:15.7	-21:34:09	0.2037	0.0003	21.05	1	
32	12:03:15.9	-21:33:43	1.1710	0.001	20.33	3	QSO: CIII],MgII
33	12:03:16.4	-21:32:57	0.1946	0.0004	—	1	
34	12:03:16.7	-21:32:54	0.1966	0.0005	18.53	1	
35	12:03:16.8	-21:32:47	0.2986	0.0007	20.76	5	
36*	12:03:16.9	-21:31:59	0.1989	0.0006	19.19†	1	
37	12:03:17.1	-21:34:16	0.2133	0.0003	19.82	3	
38*	12:03:17.3	-21:32:21	0.1948	0.0006	—	1	
39*	12:03:17.4	-21:32:19	0.1995	0.0004	18.78†	1	
40*	12:03:17.5	-21:32:28	0.2041	0.0006	19.41	1	
41*	12:03:17.5	-21:31:29	0.1994	0.0005	20.44	1	
42	12:03:17.8	-21:33:40	0.3025	0.0007	20.60	3	[OII],[OIII]
43	12:03:17.8	-21:33:21	0.1923	0.0005	20.02	1	
44	12:03:18.1	-21:34:55	0.1952	0.0005	19.68	1	
45	12:03:18.5	-21:34:45	0.1931	0.0005	21.19(R)	1	
46	12:03:18.7	-21:34:10	0.0010	0.0006	20.90	0	
47	12:03:18.8	-21:33:54	0.2003	0.0003	19.70	1	
48	12:03:19.0	-21:33:20	0.3341	0.0004	20.79	5	
49*	12:03:19.2	-21:29:38	0.1989	0.0006	20.58	1	
50*	12:03:19.2	-21:31:24	0.2085	0.0007	20.37	1	
51*	12:03:19.2	-21:30:49	0.1941	0.0008	20.12	1	
52	12:03:19.3	-21:33:27	0.1965	0.0006	22.22	1	
53	12:03:19.3	-21:33:20	0.1897	0.0004	19.02	1	
54*	12:03:19.6	-21:30:02	0.1931	0.0005	19.73	1	
55	12:03:19.6	-21:33:04	0.1971	0.0007	20.69	1	
56	12:03:20.2	-21:32:49	0.1986	0.0004	21.13	1	
57	12:03:20.5	-21:33:51	0.3353	0.0004	20.92	5	
58	12:03:20.8	-21:33:06	0.2004	0.0006	21.60	1	
59	12:03:21.0	-21:33:10	0.1924	0.0005	20.31	1	
60*	12:03:21.1	-21:32:41	0.2092	0.0009	20.19	1	
61	12:03:21.2	-21:32:38	0.2012	0.0005	20.92	1	
62	12:03:21.3	-21:35:03	0.0001	0.0008	16.28	0	
63	12:03:22.2	-21:34:12	0.1897	0.0003	20.75	1	
64	12:03:22.2	-21:33:23	0.2049	0.0003	19.16	1	
65*	12:03:22.5	-21:29:57	0.1943	0.0006	20.64	1	
66	12:03:23.5	-21:32:58	0.1929	0.0008	21.23	1	
67	12:03:23.7	-21:32:48	0.2021	0.0004	19.81	1	
68	12:03:24.8	-21:35:06	0.1985	0.0006	20.39	1	
69	12:03:25.2	-21:32:59	-0.0011	0.0003	16.84	0	
70	12:03:25.7	-21:32:24	0.2043	0.0007	20.27	1	
71	12:03:26.2	-21:33:33	0.2000	0.0003	19.77	2	[OII],[NeIII],H_β,[OIII],H_α
72	12:03:27.0	-21:31:54	0.2045	0.0007	20.13	1	
73	12:03:27.0	-21:32:35	0.2044	0.0006	21.86	1	
74	12:03:27.3	-21:33:58	0.2011	0.0004	20.89	1	
75	12:03:29.3	-21:33:14	0.5167	0.0005	19.41(R)	5	
76	12:03:30.8	-21:31:55	-0.0001	0.0003	15.69	0	
77	12:03:31.2	-21:32:12	0.1968	0.0003	18.99	2	[OII],[NeIII],H_γ,H_β
78	12:03:31.5	-21:32:36	0.2093	0.0010	21.57	1	
79	12:03:32.4	-21:33:51	0.2025	0.0004	20.52	1	
80	12:03:33.0	-21:33:01	0.1946	0.0004	21.29	1	
81	12:03:33.6	-21:32:44	0.0017	0.0003	15.38	0	

Table 4. RXJ1314−25 spectroscopic catalogue; see caption for Table 3.

No.	R.A. (J2000)	Dec. (J2000)	z	Δz	B_J	Flag	Notes
01	13:14:14.7	-25:13:11	0.0020	0.0007	19.10	0	
02	13:14:17.3	-25:13:48	0.2529	0.0009	20.71	1	
03	13:14:17.8	-25:17:09	0.2537	0.0005	19.78	1	
04	13:14:17.7	-25:15:37	0.2394	0.0008	21.66	1	
05	13:14:18.1	-25:20:18	-0.0005	0.0005	19.67	0	
06	13:14:19.2	-25:14:15	0.2496	0.0005	20.07	1	
07	13:14:19.3	-25:15:30	0.2501	0.0005	20.17	1	
08	13:14:19.5	-25:13:37	0.2520	0.0007	17.76(R)	1	
09	13:14:19.6	-25:15:38	0.0001	0.0003	16.19	0	
10	13:14:20.0	-25:17:00	0.2491	0.0008	22.30	1	
11	13:14:20.3	-25:15:05	0.2555	0.0007	20.92	1	
12	13:14:20.9	-25:17:36	0.2533	0.0005	20.83	1	
13	13:14:21.0	-25:16:58	-0.0014	0.0003	17.25	0	
14	13:14:21.0	-25:16:11	0.2477	0.0006	22.22	1	
15	13:14:21.4	-25:17:36	0.2939	0.0002	21.65	5	z from lines
16	13:14:21.6	-25:16:31	0.2493	0.0005	21.31	1	
17	13:14:21.8	-25:15:23	0.2538	0.0008	21.65	1	
18	13:14:21.9	-25:16:22	0.2504	0.0004	19.27	1	
19	13:14:22.1	-25:15:46	0.2503	0.0004	18.43	1	BCG #1
20	13:14:22.1	-25:15:45	0.2487	0.0004	—	1	
21	13:14:22.1	-25:14:34	-0.0012	0.0003	15.57	0	
22	13:14:22.4	-25:17:19	0.0008	0.0003	15.94	0	
23*	13:14:23.1	-25:16:51	0.2443	0.0004	20.85	1	
24	13:14:23.3	-25:12:35	0.2453	0.0006	20.99	1	
25	13:14:23.6	-25:16:40	0.2503	0.0005	21.35	1	
26	13:14:24.1	-25:17:09	0.2485	0.0006	21.51	1	
27	13:14:24.2	-25:14:45	0.2466	0.0005	21.20	1	
28	13:14:24.2	-25:13:56	0.2492	0.0004	20.23	1	
29	13:14:24.4	-25:16:06	-0.0010	0.0003	15.33	0	
30	13:14:24.5	-25:16:36	0.2453	0.0006	21.44	1	
31	13:14:24.7	-25:13:42	0.2424	0.0005	—	1	
32	13:14:24.7	-25:13:38	0.2376	0.0005	—	1	
33*	13:14:24.9	-25:15:09	0.2494	0.0007	20.80	1	
34	13:14:25.9	-25:14:33	0.2478	0.0005	21.63	1	
35	13:14:26.1	-25:17:01	0.2491	0.0006	21.74	1	
36*	13:14:26.2	-25:15:22	0.0008	0.0009	21.08	0	z from lines
37	13:14:26.4	-25:16:49	0.2426	0.0006	21.53	1	
38	13:14:27.3	-25:18:41	0.2449	0.0007	22.11	1	
39*	13:14:27.8	-25:15:40	0.2429	0.0005	20.87	1	
40*	13:14:28.4	-25:16:31	0.2435	0.0004	20.47	1	
41	13:14:28.6	-25:14:52	0.2510	0.0006	—	1	
42*	13:14:29.2	-25:16:13	0.2425	0.0005	20.60	1	
43	13:14:30.0	-25:15:58	0.0000	0.0007	15.52	0	
44*	13:14:33.8	-25:15:48	0.2411	0.0006	21.48	1	
45*	13:14:34.5	-25:15:31	0.2399	0.0007	20.91	1	
46*	13:14:35.6	-25:15:46	-0.0001	0.0007	22.24	0	
47*	13:14:38.0	-25:17:06	0.2433	0.0002	19.33	2	Sy1: [OII],[NeIII],H_β,[OIII]
48	13:14:32.9	-25:15:28	0.2463	0.0004	18.30	1	BCG #2

D. Cosmology with galaxy clusters in the XMM large-scale structure survey

Refregier A., **Valtchanov I.** & Pierre M., 2002, A&A, 390, 1

Astronomy & Astrophysics manuscript no. ms June 4, 2003
(DOI: will be inserted by hand later)

Cosmology with Galaxy Clusters in the XMM Large-Scale Structure Survey

Alexandre Refregier[1], Ivan Valtchanov[2], & Marguerite Pierre[2]

[1] Institute of Astronomy, Madingley Road, Cambridge CB3 OHA, UK; ar@ast.cam.ac.uk
[2] Service d'Astrophysique, Bat. 709, CEA Saclay, F-91191, Gif-sur-Yvette, France; ivaltchanov, mpierre@cea.fr

Received, , Accepted,

Abstract. The upcoming XMM Large Scale Structure Survey (XMM-LSS) will provide a unique mapping of the distribution of X-ray sources in a contiguous 64 deg^2 region. In particular, it will provide the 3-dimensional location of about 800 galaxy clusters out to a redshift of about 1. We study the prospects that this cluster catalogue offers for measuring cosmological parameters. We use the Press-Schechter formalism to predict the counts of clusters and their X-ray properties in several CDM models. We compute the detection efficiency of clusters, using realistic simulations of XMM X-ray images, and study how it differs from a conventional flux limit. We compute the expected correlation function of clusters using the extended halo model, and show that it is expected to evolve very little out to $z \simeq 2$, once the selection function of the survey is taken into account. The shape and the amplitude of the correlation function can be used to brake degeneracies present when cluster counts alone are considered. The combination of cluster counts evolution and of the correlation function yields measurements of Ω_m, σ_8 and Γ with a precision of about 15%, 10% and 35%, respectively, in a ΛCDM model. This combination will also provide a consistency check for the ΛCDM model, and a discrimination between this model and the OCDM model. The XMM-LSS will therefore provide important constraints on cosmological parameters, complementing that from other methods such as the Cosmic Microwave Background.

Key words. X-rays: galaxies: clusters; Galaxies: clusters: general; Cosmology: cosmological parameters; Cosmology: large-scale structure of Universe; Surveys

1. Introduction

Clusters of galaxies are the most massive bound objects in the Universe and provide a powerful cosmological probe (see e.g. Borgani & Guzzo 2001 for a review). In particular, the number counts of clusters and its evolution yield a robust measure of both the amplitude of the matter power spectrum and of the geometry of the universe (e.g. Oukbir & Blanchard 1997; Eke et al. 1998; Viana & Liddle 1999; Kitiyama & Suto 1997). The spatial correlation function of clusters quantifies the clustering of these objects and yields complementary constraints on cosmology (e.g. Mo, Jing & White 1996; Suto et al. 2000; Robinson 2000; Moscardini et al. 2000; Collins et al. 2000).

In this paper, we explore the prospects of measuring cosmological parameters with the upcoming XMM Large Scale Structure Survey (XMM-LSS; Pierre 2000). This survey consists of 10 ksec exposures of an 8×8 deg^2 region with the XMM-Newton observatory, along with an extensive follow-up programme in the optical, IR and radio bands. In particular, it will provide the 3-dimensional location of about 800 clusters out to a redshift of about 1. Thanks to its uniform sensitivity across a contiguous region, this survey thus provides a unique database to measure the evolution of both the number counts and the correlation function of clusters.

To study how the clusters found in XMM-LSS can constrain cosmological models, we use the Press & Schechter (1974) formalism to predict the expected cluster counts in the survey. This is done using the selection function of the survey derived from detailed simulations of cluster detections in XMM-Newton images (see Valtchanov, Pierre & Gastaud 2001, VPG). Using the Mo & White (1996) formalism, we compute the expected spatial correlation function for the detected clusters. We then study how the cluster counts and correlation function, taken together, constrain cosmological parameters. Our results complement that of Moscardini et al. (2000) who considered the expected cluster counts and correlation function for XMM-LSS, but who assumed a simple flux limit, and did not compute the resulting joint constraints on cosmological parameters.

The paper is organized as follows. In §2 we summarize the characteristics of the XMM-LSS. In §3, we describe the simulations for cluster detection and derive the

cluster selection function. In §4 we compute the expected cluster counts using the selection function combined with the Press-Schechter formalism. In §5 we compute the correlation function for this cluster sample and show how it constrains cosmological parameters. Our conclusions are summarized in §6.

2. The XMM Large Scale Structure Survey

The XMM-LSS Survey is a unique medium-deep cluster survey combining X-ray observations with an extensive optical, IR, and radio follow-up programme (Pierre 2000). The survey geometry - coverage and depth - was chosen to allow the measurement of the cluster two-point correlation function, with better than 15% error on the correlation length, in two redshift intervals between $z = 0$ and 1.

The position of the 8×8 deg^2 surveyed area on the sky ($\alpha = 2^h20^m$, $\delta = -5^o$) is at a sufficiently high galactic latitude ($\approx -60^o$) in a region of moderate galactic absorption and without known bright X-ray sources. It will be covered by 24×24 partially overlapping XMM pointings with individual exposure times of 10 ks, reaching a sensitivity of 3×10^{-15} erg s^{-1} cm^{-2} in the $[0.5-2]$ keV band for point sources, or of about 5×10^{-15} erg s^{-1} cm^{-2} for cluster-like extended sources. Down to this limit, some 300 objects (mainly QSOs) per deg^2 are expected according to the latest deep surveys (e.g. Hasinger et al. 2001, Giacconi et al. 2001), and a total of about 10-15 clusters per deg^2 out to $z \simeq 1$. The survey is also well suited to probe the existence of massive clusters within the important $1 < z < 2$ redshift range.

An extensive multi-wavelength follow-up programme has been undertaken by the XMM-LSS consortium[1]. Special care is given to the optical identification of the X-ray sources: deep multi-color imaging of the entire region will be performed by the Canada-France-Hawaii Legacy Survey[2] and subsequent redshift measurements by the VIRMOS/VLT instrument and other large telescopes to which the consortium has access. The main priorities are: (1) identification and redshift measurement of all X-ray clusters between $0 < z < 1$, (2) NIR observations of distant ($z > 1$) cluster candidates and, subsequently, determination of their redshift, (3) serendipitous spectroscopic observations of the X-ray QSOs, in order to study their clustering properties within the deep potential-well network traced by the clusters.

3. Simulations

In order to estimate the detection probability of clusters in the survey, we performed a series of X-ray image simulations. While a detailed description can be found in VPG, we first review here the main features of the simulations. We then show how they can be used to derive the selection function for the survey.

3.1. Cluster Detection in Simulated Images

The simulations reproduce the main characteristics of the XMM-EPIC instruments, such as the Point-Spread Function (assuming circular symmetry) and vignetting as a function of energy and off-axis angle. These were parametrized using the latest available on-flight calibrations. For the diffuse and particle background, we have used the data from Watson et al. (2001).

The point-like sources were laid at random inside the field-of-view. Their fluxes were drawn from the $\log N - \log S$ data in Lockman Hole (Hasinger et al. 2001) and Chandra deep field south (Giacconi et al. 2001). Their spectrum was taken to be a power law with photon index 2.

Clusters of galaxies were modeled as spherically symmetric objects assuming a β-profile (e.g. Cavaliere & Fusco-Femiano 1976) with fixed core radius $r_c = 250\,h^{-1}$ kpc and slope $\beta = 0.75$. A thermal plasma spectrum (Raymond & Smith 1977) was assumed. The spectrum was normalized using the non-evolving luminosity-temperature ($L-T$) relation of Arnaud & Evrard (1999). When generalized to arbitrary cosmological model, it is given by

$$L = 2.87 \times 10^{44} \left(\frac{T}{6\mathrm{keV}}\right)^{2.88} \left(\frac{D_L}{D_{L,\mathrm{EdS}}}\right)^2 h^{-2}\mathrm{erg\ s^{-1}}, \quad (1)$$

where L is the bolometric luminosity, T is the X-ray temperature, and D_L and $D_{L,\mathrm{EdS}}$ are the luminosity distances in the desired and Einstein-de Sitter cosmological models, respectively.

We took the neutral hydrogen column density to be $N_H = 5 \times 10^{20}$ cm^{-2} and element abundances $Z = 0.3 Z_\odot$. Using XSPEC (Arnaud 1996), we calculated the total expected count rates for the extended and point-like sources for the three XMM EPIC instruments[3] with thin filters in [0.5-2] keV energy band, for an integration time of 10 ks.

For each temperature and redshifts, we placed 13 clusters on a grid inside the inner $20'$ of the field-of-view. The detection was performed in the same way as in VPG, i.e. using multi-scale (wavelet) filtering assuming Poisson noise statistics (Starck & Pierre 1998), followed by `SExtractor` (Bertin & Arnouts 1996) detection and classification. As was pointed out in VPG, this is currently the most suitable method to detect, characterize and classify extended sources in XMM images. The raw photon and wavelet filtered images for clusters with $T = 3$ keV at a redshifts of $z = 1$ and 1.5 are shown in Figs. 1 and 2.

To cross-identify the detected objects with the input clusters we have used a searching radius of $12''$. If a correspondence is found, we perform a classification based

[1] Official web page of the consortium: http://vela.astro.ulg.ac.be/themes/spatial/xmm/LSS/

[2] http://cdsweb.u-strasbg.fr:2001/Instruments/Imaging/Megacam

[3] See e.g. the XMM-Newton User's Handbook: http://xmm.vilspa.esa.es/user/uhb/xmm_uhb.html

on the half-light radius and the stellarity index, to determine whether the object is extended. (For the choice of the searching radius and the classification criteria, see VPG). A cluster is finally considered to be detected if the positional *and* the classification criteria are obeyed. This procedure is close to the planned analysis of the incoming XMM data, which will make use of the multi-color optical data to derive cluster positions.

3.2. Selection Function

To compute the selection function, we performed a set of 10 simulation images for a set of temperatures T from 2 to 12 keV and redshifts z ranging from 0.6 to 2.0. For each value of T and z, the selection $\phi(T, z)$ of clusters for the survey was then calculated by comparing the number of detections (and correct classifications) $N_{\rm det}(T, z)$ to the number of input clusters $N_{\rm in}(T, z)$, so that

$$\phi(T, z) = N_{\rm det}(T, z)/N_{\rm in}(T, z). \quad (2)$$

Fig. 3 shows the resulting selection function, which gives the probability for a cluster with temperature T and redshift z to be detected and classified as an extended object in the survey catalogue. Approximately, 90% of all clusters with $T > 3$ keV are detectable out to $z \sim 0.6$. The selection function is close to about 1 for $T > 2$ keV and $z < 0.5$ (not shown). Since we are only interested in clusters (and groups), we set the selection function to 0 for $T < 2$ keV at all redshifts. This corresponds to a minimum luminosity of about $10^{44}\ h^{-2}$ erg s^{-1} (see Eq. [1]) and can thus be easily implemented in practice. As can be seen on the figure, low temperature clusters become progressively harder to detect as the redshift increases (compare Figs. 1 and 2). For example, at $z = 2$ only clusters with $T > 6$ keV yield a completeness better than 90%.

It is instructive to compare our selection function to that corresponding to a constant flux limit, as assumed in many previous studies. The flux $S_{[0.5-2]}$ of a cluster in the $[0.5 - 2]$ keV band at redshift z can be derived from its temperature using the $L - T$ relation (Eq. [1]), the Raymond-Smith spectrum and the luminosity-distance relation. Using this correspondence, we can express the selection function in terms of the flux rather than temperature. The resulting selection function $\phi(S_{[0.5-2]}, z)$ is shown in Fig. 4. Our selection function clearly does not exactly correspond to a sharp flux limit. Instead, the completeness is a smooth function of flux and depends on the redshift. As is conspicuous on Fig. 4, an exact and constant flux limit of $S_{[0.5-2]} = 5 \times 10^{-15}$ erg s^{-1} cm^{-2} would clearly overestimate the detection efficiency, especially for brighter clusters at large redshifts.

In the following, we will use our selection function which includes most of the relevant instrumental and observational limitations. For comparison, we will also consider the selection function corresponding to the above flux limit, along with that corresponding to temperature limit $T > 2$ keV. The latter selection is useful to study the effect of the removal of small clusters on our predictions.

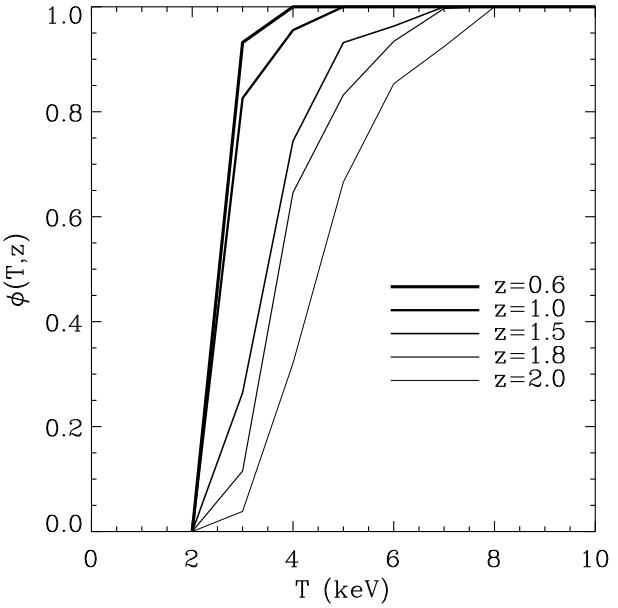

Fig. 3. Selection function $\phi(T, z)$ for ΛCDM model derived from the simulations. This function is the probability that a cluster with temperature T and redshift z is detected and classified as an extended object in the survey catalogue.

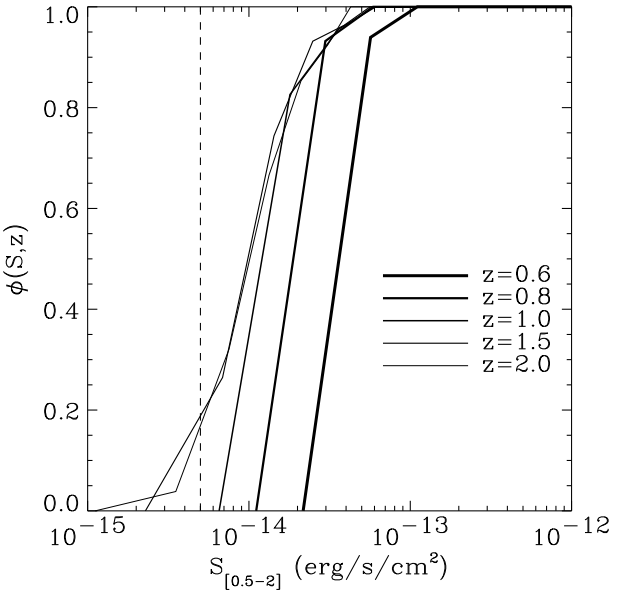

Fig. 4. Selection function $\phi(S, z)$ expressed in terms of the flux S in the [0.5-2] keV band for ΛCDM model. The vertical line shows the flux limit of 5×10^{-15} erg s^{-1} cm^{-2} usually assumed for the extended objects detection in the survey; it illustrates deviations from a strict flux limit when realistic observing conditions are taken into account (esp. source confusion).

4. Cluster Counts

We first compute the expected cluster number counts in the survey. This is done using the cluster selection function derived in the previous section combined with the Press-Schechter formalism. We first briefly review the main assumptions involved in our calculation of the mass function and of the temperature function of clusters. We then com-

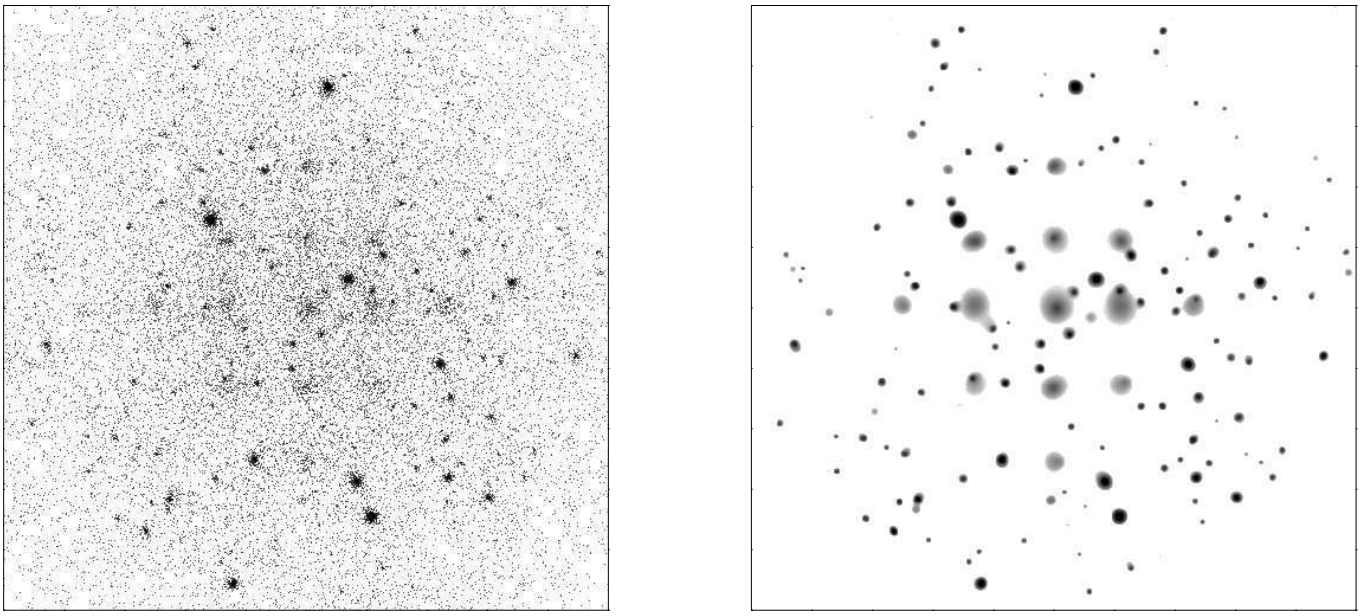

Fig. 1. Simulated extragalactic XMM-LSS raw image (left) and the corresponding wavelet filtered image with Poisson noise model and 10^{-4} ($\sim 4\sigma$) significance (Starck & Pierre 1998). The energy band is $[0.5-2]$ keV, the exposure time 10ks, and the three XMM instruments are added together (MOS1, MOS2 and pn). Point-like sources follow the observed $\log N - \log S$ relation and the extended sources (clearly visible on the wavelet filtered image) are clusters of galaxies with $T_X = 3$ keV at $z = 1$ (see text for details).

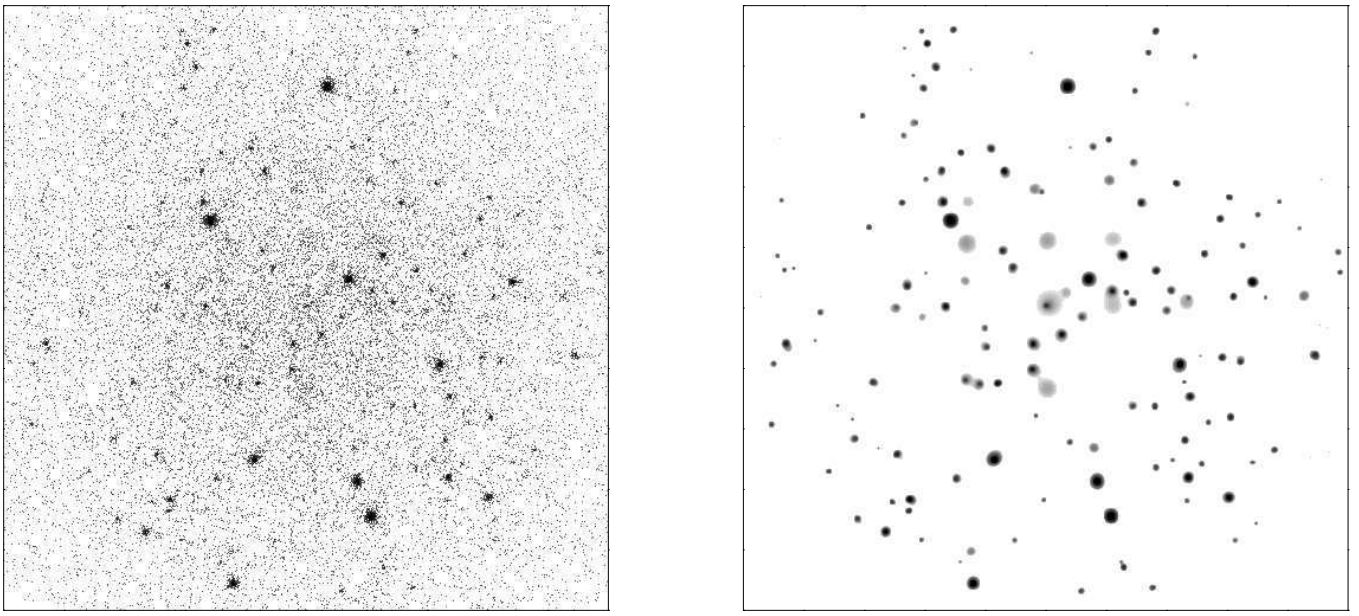

Fig. 2. Same as Fig. 1 but with clusters at $z = 1.5$.

pute the expected projected number of clusters on the sky, as function of redshift. Finally, we show how the resulting redshift distribution constrains cosmological parameters within CDM models.

4.1. Mass Function

The Press-Schechter formalism provides an analytic expression for the abundance of dark matter halos (Press & Schechter 1974). At a given redshift z, the differential number of dark matter halos of mass M per unit comoving volume is

$$\frac{dn}{dM} = \sqrt{\frac{2}{\pi}} \frac{\overline{\rho}}{M} \frac{d\nu}{dM} e^{-\frac{\nu^2}{2}} \tag{3}$$

where $\overline{\rho}$ is the present mean matter density. The peak height is defined as $\nu(M) = \delta_c/\sigma(M)$, where $\sigma(M)$ is the linear rms fluctuation in a sphere containing a mean mass M. We compute $\sigma(M)$ for an arbitrary cosmological model by integrating the linear power spectrum $P_{\rm lin}(k)$ derived from the BBKS transfer function (Bardeen et al. 1986;

Table 1. Cosmological Models

Model	h	Ω_m	Ω_Λ	σ_8	Γ
τCDM	0.5	1	0	0.52	0.23
ΛCDM	0.7	0.3	0.7	0.93	0.23
OCDM	0.7	0.3	0	0.87	0.23

with the conventions of Peacock 1997), evolved with the linear growth factor $D(z)$. The density threshold δ_c depends weakly on cosmology (i.e. on Ω_m and Ω_Λ) and was computed using the fitting formulae of Kitiyama & Suto (1996).

4.2. Temperature Function

The X-ray temperature of a cluster at redshift z is taken to be the virial temperature which is given by (see e.g. Eke, Cole & Frenk 1996)

$$kT \simeq \frac{7.75}{\beta_v}(1+z)\Omega_m^{\frac{1}{3}}\left(\frac{M}{M_{15}}\right)^{\frac{2}{3}}\left(\frac{\mu}{0.59}\right)\left(\frac{\Delta_c}{178}\right)^{\frac{1}{3}}\text{keV}, \quad (4)$$

where the average virial overdensity $\Delta_c(z,\Omega_m,\Omega_\Lambda)$ can be evaluated using the fitting formulae of Kitiyama & Suto (1996), $M_{15} = 10^{15}h^{-1}M_\odot$ and the value $\mu = 0.59$ for the number of particles per proton mass corresponds to a hydrogen mass fraction of 76%. The factor β_v is equal to about 1 for a truncated singular isothermal sphere. We adopt this value as it provides a good fit to numerical simulations (Eke, Cole & Frenk 1996; Bryan & Norman 1997).

Combining Eqs. (3) and (4) we can derive the differential temperature function

$$\frac{dn}{dT} = \frac{dn}{dM}\frac{dM}{dT}. \quad (5)$$

It is often more convenient to consider the number density of clusters with temperatures above a given minimum, $n(>T) = \int_T^\infty dT' \, \frac{dn(T')}{dT}$.

To illustrate the dependence of our prediction on cosmological parameters, we consider the three cosmological models listed in Tab. 1, i.e a tilted (τ) CDM, ΛCDM and OCDM . The normalization of these models is determined by σ_8, the amplitude of mass fluctuations on $8h^{-1}$ Mpc scale. Our chosen numerical values correspond to the constraints derived from current cluster surveys, namely $\sigma_8 \simeq 0.52\Omega_m^{-0.52+0.13\Omega_m}$ for the flat case and $\sigma_8 \simeq 0.52\Omega_m^{-0.46+0.10\Omega_m}$ for the for the open case (Eke et al. 1996). The shape of the matter power spectrum is controlled by the shape parameter Γ which, unless otherwise specified, we fix at 0.23, as indicated by galaxy clustering surveys (see Viana & Liddle 1996 and reference therein).

4.3. Projected Cluster Counts

From the temperature function $\frac{dn}{dT}$ (Eq. [5]), we can compute the projected surface density of clusters on the sky. Noting that the comoving volume element is $dV = R^2 d\chi d\Omega$, where $d\Omega$ is the infinitesimal solid angle, χ is the comoving radius and $R(\chi)$ is the comoving angular-diameter radius, we find that the number of clusters per unit solid angle, temperature and redshift interval is

$$\frac{dN}{dTdz} = R^2\frac{d\chi}{dz}\frac{dn}{dT}, \quad (6)$$

where $\frac{d\chi}{dz} = -\frac{c}{H_0}\left[(1-\Omega)a^{-2} + \Omega_m a^{-3} + \Omega_\Lambda\right]^{-\frac{1}{2}}$ as derived from the Friedmann equations. As a result the observed surface density of clusters per unit redshift

$$\frac{dN_{\rm obs}}{dz} = \int dT \frac{dN}{dTdz}\phi(T,z) \quad (7)$$

where $\phi(T,z)$ is the survey selection function (Eq. [2]).

4.4. Predictions

The predicted projected counts as a function of redshift are shown on Fig. 5 for the three cosmological models whose parameters are listed in Tab. 1. The counts correspond to the full 64 deg^2 of the completed XMM-LSS survey. The counts from the three models agree at low redshifts ($z < 0.2$), as expected since the three models were normalized with the number of clusters in the local universe. On the other hand, the number counts differ greatly at larger redshifts. The τCDM model predicts much smaller number of clusters at $z > 0.2$, while the ΛCDM and OCDM models differ for $z > 0.6$. The predicted counts at $z > 1$ are larger in the OCDM model compared to that in the ΛCDM case, due to the somewhat slower evolution of the growth factor in the open model. These differences illustrate the well known fact that the evolution of cluster counts is a powerful probe of Ω_m and Ω_Λ.

In the 64 deg^2 of the survey, the expected number of detected clusters with $0 < z < 1$ is about 900, 1000 and 175 for the ΛCDM , OCDM and τCDM model, respectively. For $1 < z < 2$, the expected counts are about 400, 900 and < 10, for each model respectively. Fig. 7 shows how these predictions for the ΛCDM model depend on σ_8 and Ω_m. Clearly, the number counts are very sensitive on these two parameters. Taking $\sigma_8 = 0.93 \pm 0.07$ for $\Omega_m = 0.3$ (Eke et al. 1996), the expected number of clusters in this model is between 600-1200 for $0 < z < 1$ and 200-700 for $1 < z < 2$.

The effect of the selection function on these predictions are shown in Fig. 6. The number counts for the ΛCDM model are shown as a function of redshift, for our selection function $\phi(T,z)$ (as in Fig. 5), for the flux limited case and for the temperature limited case. The flux limited counts overpredict the counts for $0.4 < z < 1.4$, as expected from Fig. 4 (see discussion in §3.2). This demonstrates the importance of considering all the observational details when making such predictions, especially confusion by point-like sources, an unavoidable drawback for a highly sensitive instrument. Notice that the temperature limited counts agree with the other two for $z < 0.4$. This shows that our

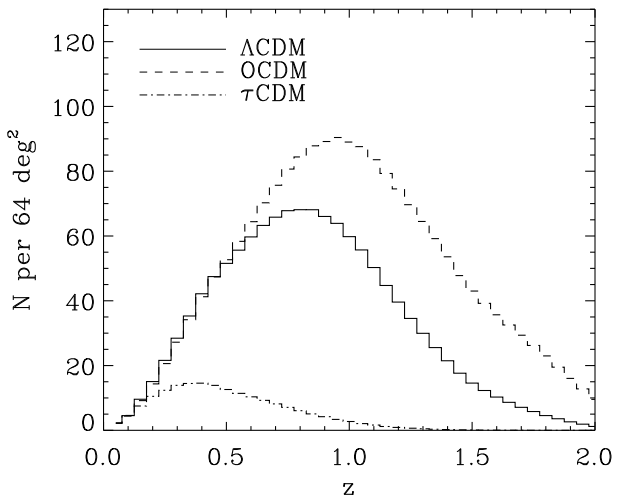

Fig. 5. Projected number counts of clusters as a function of redshift in the three cosmological models. The selection function $\phi(T, z)$ for the XMM-LSS derived from image simulations was used for each model.

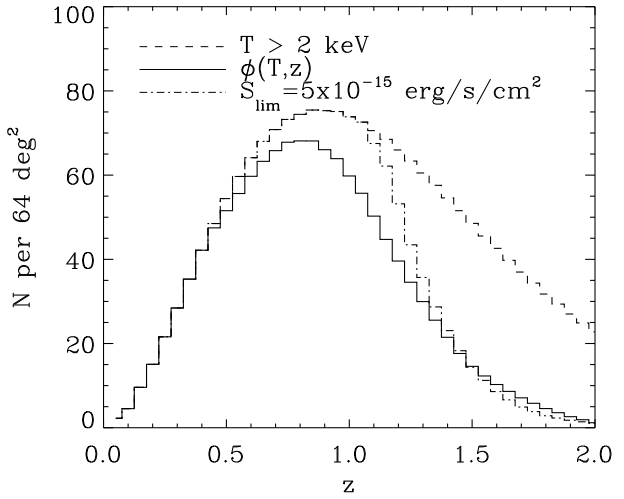

Fig. 6. Projected number counts of clusters for the ΛCDM model with different selection criteria: with the selection function $\phi(T, z)$ (as in figure 5), with a temperature limit only ($kT > 2$ keV), and with a flux limit ($S_{[0.5-2]} > 5 \times 10^{-15}$ erg s^{-1} cm^{-2}).

counts are limited mainly by the temperature at low redshifts. Not surprisingly, the T-limited counts overpredict the abundances for $z > 0.4$.

Note that the fluxes of the clusters measured in XMM-LSS will be rather uncertain (see VPG). This will prevent us from making accurate determinations of the luminosity, and therefore of the temperature and of the mass, of each cluster. In this paper, we therefore consider statistical quantities (such as the counts and the correlation function) which are averaged over the population of clusters detectable in the survey, and therefore do not require this information. A study of the further constraints which can be derived from the (uncertain) flux measurements is left to future work.

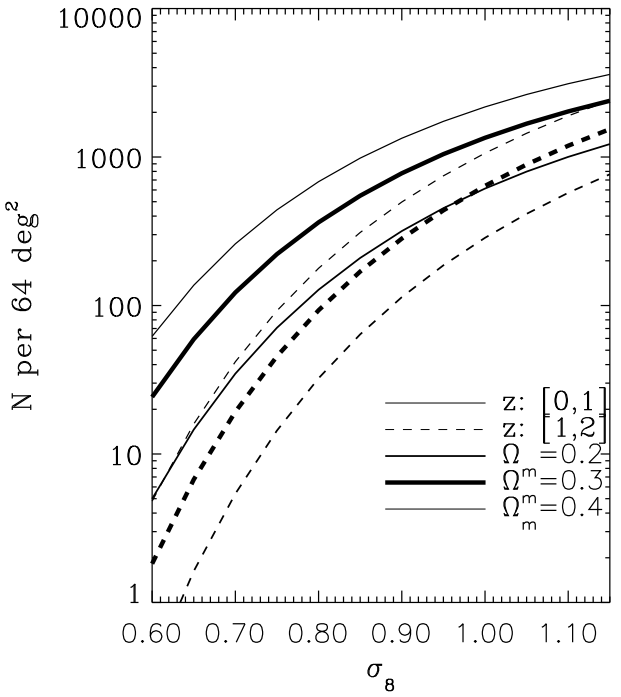

Fig. 7. Cluster counts expected for the XMM-LSS as a function of σ_8 and Ω_m in the ΛCDM model. The XMM-LSS simulated selection function was used in all cases. Counts for the $0 < z < 1$ and $1 < z < 2$ redshift intervals are shown as the solid and dashed lines, respectively. In each case, models with $\Omega_m = 0.4$, 0.3 and 0.2, are shown from top to bottom, respectively.

4.5. Cosmological Constraints from Cluster Counts

We now wish to study how the cluster counts can be used to constrain cosmological parameters. For this purpose, we generated cluster counts from the predicted counts from Eq. (7) in ΛCDM model for several redshift bins (as shown in Fig. 5 for different models). We used the XLSS selection function $\phi(T, z)$ and survey area, and considered redshift bins of width $\Delta z = 0.1$ from $z = 0$ to $z = 1$ assuming Poissonian errors for the number counts in each bin. Note that the Poisson errors neglect the uncertainty arising from cosmic variance; this is a good approximation since this latter uncertainty is small for a survey area as large as that of the XLSS (compare the correlation length $\sim 20h^{-1}$ Mpc to the survey size, $\sim 200h^{-1}$ Mpc at $z \simeq 0.5$). We then calculated the χ^2-difference between the simulated counts and that expected in a ΛCDM model for a range of values for σ_8 and Ω_m. This approach is rather computer intensive, but it is more accurate than the faster Fisher matrix method, which approximates the confidence regions as ellipses and can be incorrect when the parameter space is non-Gaussian (Holder et al. 2001).

The resulting constraints on these cosmological parameters are shown as the solid lines in Fig. 8. The input ΛCDM model is that of Tab. 1 and is shown with a cross. The 90% and 95% confidence regions are shown as solid lines. The cluster counts alone will provide tight constraints on both parameters, with 95% uncertainties of about 0.06 and 0.05 for σ_8 and Ω_m, respectively. As

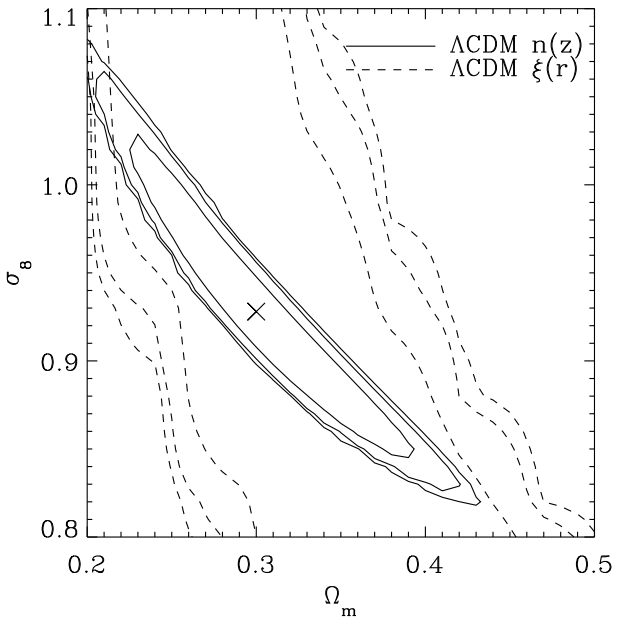

Fig. 8. Constraints on the cosmological parameters Ω_m and σ_8 for the ΛCDM model, from the cluster counts (solid lines) and from the correlation function (dashed lines). In each case, the 68%, 90% and 95% confidence level contours are shown along with the assumed model (cross).

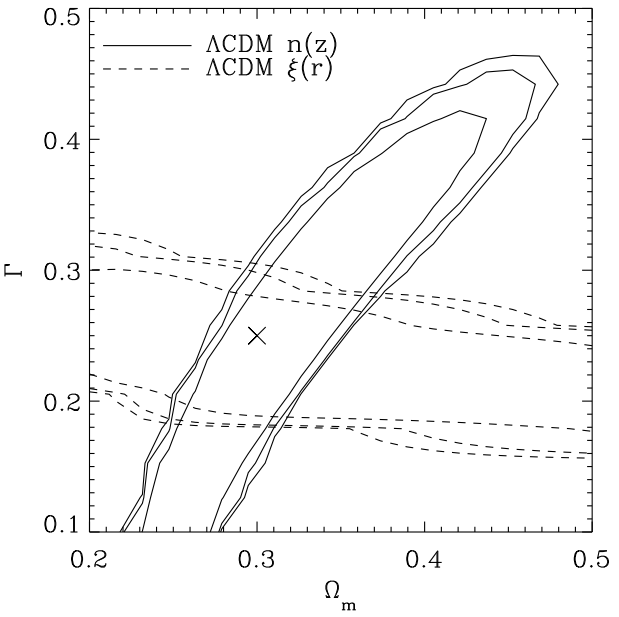

Fig. 9. Constraints on Γ and Ω_m for the ΛCDM , from the cluster counts (solid lines) and from the correlation function (dashed lines). As before, the 68%, 90% and 95% confidence level contours are shown (solid lines) along with the assumed model (cross).

can be seen from the elongation of the contours, the two parameters are however somewhat degenerate. Any additional information on either parameters, can thus be used to reduce their respective uncertainty.

It is also interesting to investigate how cluster counts can constrain Γ, the shape parameter of the matter power spectrum. For this purpose, we follow the same χ^2 procedure, this time varying Γ and Ω_m, while σ_8 follows the Eke et al. (1996) relation (see §4.2). The resulting confidence contours for the ΛCDM model are shown as the solid lines in Fig. 9. Clearly, these two parameters are quite degenerate with counts alone, hampering the determination of Ω_m, which can only be determined with an accuracy of about 40% (95% CL). More information is therefore required to alleviate these limitations. One obvious possibility is to use other measures of large-scale structure such as galaxy catalogues to constrain Γ. This has the disadvantage of relying on assumptions about the bias of galaxies and on an external data set. In the next section, we show how the degeneracy can be broken by measuring the correlation function of the galaxy cluster population.

5. Cluster Correlation function

We now turn to the cluster correlation function which quantifies the spatial clustering of clusters in the survey. We first use the extended halo model of Mo & White (1996) to predict the observed cluster correlation function at a given redshift. We then consider the average correlation function in a finite redshift range, compute its uncertainties, and study the constraints its measurement can place on cosmological parameters.

5.1. Observed Correlation Function : at a single redshift

According to the Mo & White (1996) halo formalism, the correlation function of two sets of clusters with masses M and M' and with comoving separation r is given by

$$\xi(r, M, M', z) \simeq b(M, z)b(M', z)\xi_{\rm lin}(r, z), \tag{8}$$

where $\xi_{\rm lin}(r, z) = \xi_{\rm lin}(r, 0)D^2(z)$ is the linear correlation function which is the Fourier Transform of the linear power spectrum $P_{\rm lin}(k, z)$. The mass dependent bias parameter of the halos is given $b(M, z) = 1 + (\nu^2 - 1)/\delta_c$, with the conventions of §4.1. Note that the separation of the clusters is assumed to be small compared to the scale in which any evolution takes place.

It is easy to show that the resulting observed correlation function in a narrow redshift interval is given by (Suto et al. 2000; Moscardini et al. 2000 and reference therein)

$$\xi_{\rm obs}(r, z) = b^2_{\rm eff}(z)\xi_{\rm lin}(r, z), \tag{9}$$

where the effective bias is

$$b_{\rm eff}(z) = \int dM \frac{dn_{\rm obs}}{dM} b(M) \Big/ \int dM \frac{dn_{\rm obs}}{dM} , \tag{10}$$

and where the observed differential number counts are given by $\frac{dn_{\rm obs}}{dM} = \frac{dn}{dT}\frac{dT}{dM}\phi(T, z)$. Note that, in our analysis, we neglect redshift-space distortions which were shown to yield only about 10% corrections on the amplitude of the correlation function (Suto et al. 2000; Moscardini et al. 2000)

In general, the evolution of $\xi_{\rm obs}(r, z)$ is determined by two competing effects. First, the growth of structures induces the linear correlation function $\xi_{\rm lin}(r, z)$ to decrease

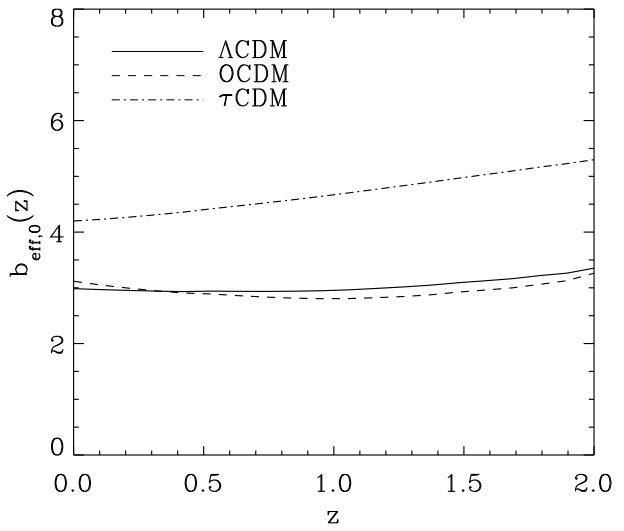

Fig. 10. Evolution of $b_{\rm eff,0}(z)$, the effective bias of the cluster correlation function $\xi_{\rm obs}(r,z)$ with respect to the linear mass correlation function $\xi_{\rm lin}(r,0)$ at $z=0$. This quantifies the evolution of the cluster correlation function. It is shown for the three cosmological models as a function of redshift.

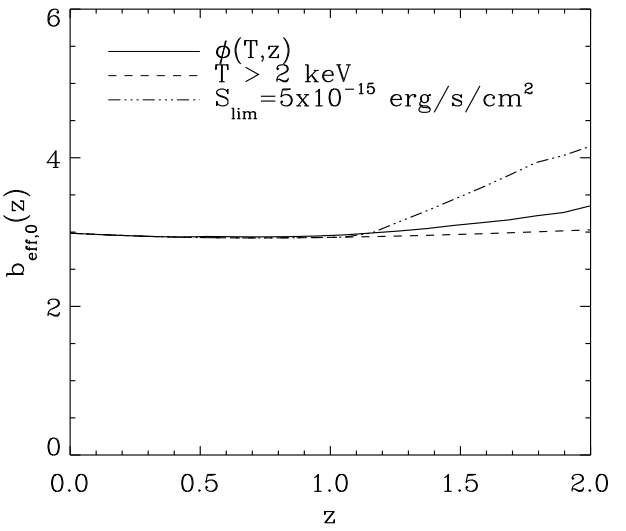

Fig. 11. Evolution of $b_{\rm eff,0}(z)$ in the ΛCDM model for different selection schemes: the XMM-LSS selection function, a temperature limited survey, and a flux limited survey.

as the redshift increases. On the other hand, the clusters which are detectable at large redshifts are more massive and therefore more strongly biased. The effective bias $b_{\rm eff}(z)$ thus tends to be larger at high redshift. To study the interplay between these two effects it is convenient to define

$$b_{\rm eff,0}(z) \equiv \left[\frac{\xi_{\rm obs}(r,z)}{\xi_{\rm lin}(r,0)}\right]^{\frac{1}{2}} = b_{\rm eff}(z)D(z). \qquad (11)$$

This quantity provides the bias of the observed cluster correlation with respect to the linear correlation function at $z=0$, and therefore quantifies the evolution of the correlation function.

The behaviour of $b_{\rm eff,0}(z)$ is shown on Fig. 10 for the three cosmological models and for the XMM-LSS selection function. The curves are remarkably flat for all models, showing that the cluster correlation function evolves only very weakly from $z=0$ to $z=2$. It is interesting to study whether this lack of evolution depends on the selection function. Fig. 11 shows $b_{\rm eff,0}(z)$ for each selection scheme for the ΛCDM model. The evolution is also very weak for the temperature limited case. For the flux-limited sample, the evolution is somewhat stronger for $z>1$. This evolution is lost when the full selection function $\phi(T,z)$ is used. In all cases, there is effectively no evolution for $0<z<1$. We shall thus, in the following, derive the constraints on cosmology integrating the correlation function over the $0<z<1$ range.

5.2. Observed Correlation Function: Redshift Average

To maximize the sensitivity, it is useful to measure the correlation function over a wide redshift range. In this case, we must take into account the pair-weighted evolution of the correlation function $\overline{\xi}(r,z)$ within the light-cone section of interest. The average correlation function in the redshift interval $z_{\rm min}<z<z_{\rm max}$ is thus given by (Suto et al. 2000; Moscardini et al. 2000 and reference therein)

$$\overline{\xi}_{\rm obs}(r) = \frac{\int_{z_{\rm min}}^{z_{\rm max}} dz\ \frac{d\chi}{dz} R^2 n_{\rm obs}^2(z)\xi_{\rm obs}(r,z)}{\int_{z_{\rm min}}^{z_{\rm max}} dz\ \frac{d\chi}{dz} R^2 n_{\rm obs}^2(z)}, \qquad (12)$$

where the observed number density of clusters is $n_{\rm obs}(z) = \int\ dT \frac{dn}{dT}\phi(T,z)$.

The resulting correlation functions for the three cosmological models are shown on Fig. 12. The XMM-LSS selection function was used in all cases, along with a redshift range of $0<z<1$. The correlation functions for the 3 models have very similar shape, as expected since the same value for Γ was assumed in all cases. Notice that the τCDM correlation function has a lower amplitude than that for the other two models. This is expected since the former model has a lower value for σ_8 (see Tab. 1). The ΛCDM and OCDM models have very similar values of σ_8 and thus yield correlation functions with very similar amplitudes.

5.3. Uncertainties

We now wish to estimate the uncertainty involved in measuring the cluster correlation function. The simplest way to measure the correlation function is to count the number of pairs in excess of random in the survey volume. (This is sometimes taken as the definition of the correlation function). An estimator for $\overline{\xi}_{\rm obs}(r)$ in a bin of radii between r and $r+\Delta r$ is thus

$$\hat{\overline{\xi}}_{\rm obs}(r,\Delta r) \equiv \frac{N_{\rm pairs}^{\rm obs}(r,\Delta r)}{N_{\rm pairs}^{\rm ran}(r,\Delta r)} - 1, \qquad (13)$$

where $N_{\rm pairs}^{\rm obs}$ and $N_{\rm pairs}^{\rm ran}$ are the number of pairs (i.e. with clustering) and for a random distribution (i.e. without

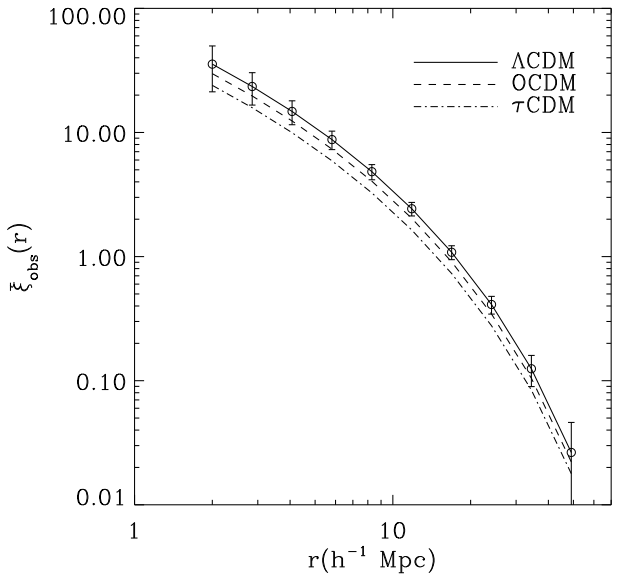

Fig. 12. Prediction for the cluster correlation function averaged in redshift interval $0 < z < 1$. The three cosmological models are shown. For clarity, the expected measurement error bars for the full 64 deg^2 of the XMM-LSS are shown only for the ΛCDM model. .

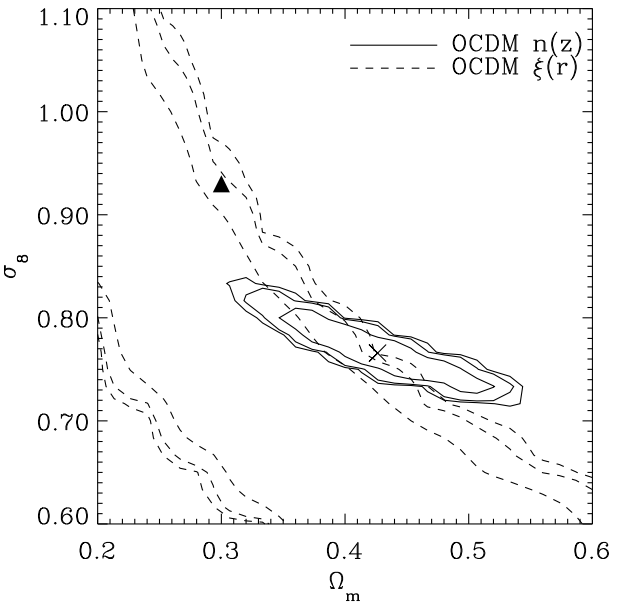

Fig. 13. Constraints on Ω_m and σ_8 resulting from a fit of the OCDM model to the ΛCDM predictions. Both the cluster counts (solid lines) and the correlation function (dashed lines) are shown. In each case, the 68%, 90% and 95% confidence level contours are shown, along with the χ^2 minimum (cross) and the input values for the ΛCDM model (filled triangle).

clustering), respectively, in the observed radius interval. Ignoring boundary effects, the random number of pairs is given by

$$N^{\rm ran}_{\rm pairs}(r,\Delta r) \simeq 2\pi A r^2 \Delta r \int_{z_{\rm min}}^{z_{\rm max}} dz \frac{d\chi}{dz} R^2 n^2_{\rm obs}(z), \qquad (14)$$

where A is the solid angle of the survey.

For weak signals, the error in measuring $\hat{\bar{\xi}}_{\rm obs}(r,\Delta r)$ will be dominated by Poisson statistics, and will thus be given by (see e.g. Peebles 1980)

$$\sigma[\hat{\bar{\xi}}_{\rm obs}(r,\Delta r)] \simeq \frac{1+\xi(r)}{\sqrt{N^{\rm obs}_{\rm pairs}(r,\Delta r)}} = \sqrt{\frac{1+\xi(r)}{N^{\rm ran}_{\rm pairs}(r,\Delta r)}}. \qquad (15)$$

This provides us with an expression for the error in the correlation function for a finite survey. The resulting errors for the ΛCDM model and for the full 64 deg^2 of the XMM-LSS are shown in Fig. 12.

5.4. Combined Cosmological Constraints

We now study how the measurement of the cluster correlation function constrains cosmological parameters. As for the cluster counts (§5.4), we use a χ^2-fit to simulated measurements of the correlation function to derive confidence regions in parameter space. We considered a redshift interval of $0 < z < 1$ and computed the errors using Eq. (15).

The resulting confidence contours for a joint fit of Ω_m and σ_8 are shown as the dashed lines in Fig. 8, for the ΛCDM model. The constraints from the correlation function are rather weak on this plane alone, with little dependence on σ_8. These constraints are however somewhat orthogonal to that from cluster counts and are thus complementary.

The constraints from the correlation function on Γ and Ω_m are shown in Figure 9. The confidence contours show little dependence on Ω_m and are therefore nearly orthogonal to that from cluster counts alone. With the combined counts and correlation function constraints, Ω_m, σ_8 and Γ can be measured with a precision of about 15%, 10%, and 35%, respectively at the 95% confidence level. The cluster correlation function thus provides the required information to break the degeneracy present when cluster counts alone are considered.

Until now, we have focused on the ΛCDM model, thus implicitely assuming prior knowledge that the universe is flat. While flatness is strongly indicated by measurements of the Cosmic Microwave Background anisotropies (e.g. Jaffe et al. 2001), it is interesting to establish whether our predictions depend on this assumption. To study this, we fitted an OCDM model to the ΛCDM predictions for both the cluster counts and the correlation function. The resulting constraints on σ_8 and Ω_m are shown in Fig. 13. For the cluster counts, the best fit values for both of these parameters are now biased (compare the best fit, cross, to the input values, triangle). This bias again hampers the determination of Ω_m using cluster counts alone. Thanksfully, the correlation function can again help overcome this limitation. Indeed, the contours for $\xi(r)$ are now somewhat incompatible with that from the counts (compare to Fig. 8). The consistency between the counts and correlation function constraints can thus be used as a diagnostic and as a discriminant between the ΛCDM and the OCDM model.

6. Conclusions

Following the REFLEX survey (Guzzo et al. 1999, Böhringer et al. 2001) based on the ROSAT All-Sky-Survey, the XMM-LSS survey will be some 1000 times deeper and thus opens wide prospects for cosmology. Indeed, it will provide an independent measurement of cosmological parameter and thus complement Cosmic Microwave Background and Supernova experiments. It will also provide a test of important ingredients of the standard cosmological model, such as the gravitational instability paradigm and the gaussianity of initial fluctuations.

To study the constraints XMM-LSS will set on cosmological parameters, we first derived the selection function for the survey using detailed simulations of cluster detection in XMM-Newton images. We found that our selection function differs significantly from a simple flux-limit selection, which is commonly assumed. We then computed the expected number counts of clusters in several CDM models. We found that, for the currently favoured ΛCDM model, we expect about 600-1200 clusters to be detectable in XMM-LSS at $0 < z < 1$ and about 200-700 at $1 < z < 2$, the uncertainty being dominated by the current errors on σ_8 and Ω_m.

Clusters counts beyond $z > 0.5$ depend on cosmological parameters and can thus be used to constrain models. Within a ΛCDM model, we found that the redshift dependence of the XMM-LSS cluster counts will allow us to measure σ_8 and Ω_m with a precision of about 6% and 18% (95% CL), respectively, if the shape parameter Γ is known. In the absence of prior knowledge on Γ, the precision on these parameters degrades considerably, if only cluster counts are considered.

This limitation can be circumvented by considering the cluster correlation function. One of the strength of XMM-LSS is indeed to offer a uniform coverage over a wide contiguous area (64 deg^2), with an extensive spectroscopic follow-up. This will allow us to measure the correlation function in several redshift bins out to $z = 1$. Using the extended halo formalism of Mo & White (1996), we computed the correlation function of clusters detectable in XMM-LSS. We find that, for the selection function of XMM-LSS, the correlation function is not expected to evolve significantly from $z = 0$ to 2. This results from the competing effects of the growth of mass perturbations and the stronger bias of the detectable massive clusters at large redshifts. It will thus be important to compare the correlation function measured in two redshift bins between $z = 0$ and $z = 1$: the verification of the lack of evolution provides a test of the bias model for haloes and of the gravitational instability paradigm.

The amplitude and shape of the cluster correlation function can be used to lift the degeneracies present when cluster counts alone are considered. Within a ΛCDM model, the correlation function measured in XMM-LSS at $0 < z < 1$, combined with the cluster counts, will constrain Ω_m, σ_8 and Γ with a precision of about 15%, 10% and 35%, respectively (95% CL). Moreover, the combination of the counts and the correlation function will provide a consistency check for the ΛCDM model, and a discrimination between this model and the OCDM model.

In our analysis, we have assumed that the $L - T$ and $M - T$ relations were known. By the time the XMM-LSS is completed, better insights will be gained in this respect, thanks to deep pointed cluster observations. It would nevertheless be useful to study how our results are affected by the uncertainties in these relations (see the analysis of Diego et al. 2001). In particular, it would be important to study how physical processes, such as feedback from early star formation and reionization, can modify these relationships and therefore yield detectable changes in the cluster counts and correlation function (see e.g. Muanwong et al. 2001 and reference therein). Another important issue is the existence of high redshift cooling flows which may affect the detectability of distant clusters and their $L - T$ relationship (e.g. Henry 2000). Finally, the behaviour of the correlation function as a function of both cluster mass and redshift deserves further investigation. The study of these pending questions is left for future work.

Acknowledgements

AR was supported by a TMR postdoctoral fellowship from the EEC Lensing Network, and by a Wolfson College Research Fellowship.

References

Arnaud, K.A., 1996, in ASP Conf. Ser., Vol. 101, Astronomical Data Analysis Software and Systems V,eds. Jacoby G.H. & Barnes J. (San Francisco: ASP), 17 (XSPEC)
Arnaud, M. & Evrard, A., 1999, MNRAS, 305, 631
Bardeen, J.M., Bond, J.R., Kaiser, N., & Szalay, A.S., 1986, ApJ, 304, 15
Bertin, E., Arnouts, S., 1996, A&AS, 117, 393
Borgani, S., & Guzzo, L. 2001, Nature, 409, 39
Böhringer, H., Schueker, P., Guzzo, L. et al., 2001, A&A, 369, 826
Bryan, G.L., & Norman, L., 1997, ASP Conf Ser. 123: Computational Astrophysics; 12th Kingston Meeting on Theoretical Astrophysics, 363
Cavaliere, A., Fusco-Femiano, R., 1976, A&A, 49, 137
Collins, C. A., Guzzo, L., Böhringer, H., Schuecker, P., Chincarini, G., Cruddace, R., De Grandi, S., MacGillivray, H. T., Neumann, D. M., Schindler S., Shaver P., Voges W., 2000, MNRAS, 319, 939
Diego, J.M., Martínez-Gonzáles, E., Sanz, J.L., Cayón, L., & Silk, J., 2001, MNRAS, 325, 1533
Eke, V.R., Cole, S., & Frenk, C.S., 1996, MNRAS, 282, 263
Eke, V.R., Navarro, J.F., & Frenk, C.S., 1998, ApJ, 503, 569
Giacconi, R., Rosati, P., Tozzi, P. et al., 2001, ApJ, 551, 624
Guzzo, L., Böhringer, H., Schuecker, P. et al., 1999, ESO Messenger, 95, 27
Hasinger, G., Altieri, B., Arnaud, M., et al. 2001, A&A, 365, L45
Henry, J.P., 2000, ApJ, 534, 565
Holder, G., Zoltán, H., Mohr, J.J., 2001, ApJL, submitted (astro-ph/0105396)

Jaffe, A., et al. 2001, Phys.Rev.Lett. 86, 3475
Kitiyama, T., & Suto, Y., 1996, ApJ, 469, 480
Kitayama, T., & Suto, Y., 1997, ApJ, 490, 557
Mo, H.J. & White, S.D.M., 1996, MNRAS, 282, 347
Mo, H.J., Jing, Y.P. & White, S.D.M., 1996, MNRAS, 282, 1096
Moscardini, L., Matarrese, S., & Mo, H.J., 2000, astro-ph/0009006
Muanwong, O., Thomas, P.A., Kay, S.T., Pearce, F.R., Couchman, H.M.P., ApJ, 552, L27
Oukbir, J., & Blanchard, A. 1997, A&A, 317, 1
Peacock, J.A., 1997, MNRAS, 284, 885
Peebles, P.J.E. 1980, The Large-Scale Structure of the Universe (Princeton: Princeton Univ. Press)
Pierre, M., 2000, Procs. of "Mining the sky", Joint MPA/ESO/MPE conference, preprint astro-ph/0011166
Press, W.H., & Schechter, P., 1974, ApJ, 187, 425
Raymond, J.C., Smith, B.W., 1977, ApJS, 35, 419
Robinson, J. 2000, submitted to MNRAS, astro-ph/0004023
Sadat, R., Blanchard, A., & Oukbir, J., 1998, A&A, 329, 21
Starck, J.-L., Pierre, M., 1998, A&AS 128, 397
Suto, Y., Yamamoto, K., Kityama, T., & Jing, Y.P., 2000, ApJ, 534, 551
Valtchanov, I., Pierre, M. & Gastaud, R., 2001, A&A, 370, 689 (VPG)
Viana, P.T.P & Liddle, A.R., 1996, MNRAS, 281, 323
Viana, P.T.P & Liddle, A.R., 1999, MNRAS, 303, 535
Watson, M.G., Auguères, J.-L., Ballet, J., et al. 2001, A&A, 365, L51

E. Comparison of source detection procedures for XMM-Newton images

Valtchanov I., Pierre M. & Gastaud R., 2001, A&A, 370, 689

.

Astronomy & Astrophysics manuscript no. MS10417 June 4, 2003
(DOI: will be inserted by hand later)

Comparison of source detection procedures for *XMM-Newton* images

I. Valtchanov, M. Pierre, and R. Gastaud

CEA/DSM/DAPNIA Service d'Astrophysique, 91191 Gif-sur-Yvette, France

Received 31 october 2000 / Accepted 8 February 2001

Abstract. Procedures based on current methods to detect sources in X-ray images are applied to simulated *XMM-Newton* images. All significant instrumental effects are taken into account, and two kinds of sources are considered – unresolved sources represented by the telescope PSF and extended ones represented by a β-profile model. Different sets of test cases with controlled and realistic input configurations are constructed in order to analyze the influence of confusion on the source analysis and also to choose the best methods and strategies to resolve the difficulties.
In the general case of point-like and extended objects the mixed approach of multiresolution (wavelet) filtering and subsequent detection by `SExtractor` gives the best results. In ideal cases of isolated sources, flux errors are within 15-20%. The maximum likelihood technique outperforms the others for point-like sources when the PSF model used in the fit is the same as in the images. However, the number of spurious detections is quite large.
The classification using the half-light radius and `SExtractor` stellarity index is succesful in more than 98% of the cases. This suggests that average luminosity clusters of galaxies ($L_{[2-10]keV} \sim 3 \times 10^{44}$ erg/s) can be detected at redshifts greater than 1.5 for moderate exposure times in the energy band below 5 keV, provided that there is no confusion or blending by nearby sources.
We find also that with the best current available packages, confusion and completeness problems start to appear at fluxes around 6×10^{-16} erg/s/cm^2 in [0.5-2] keV band for *XMM-Newton* deep surveys.

Key words. Methods: data analysis, Techniques: image processing, X-rays: general

1. Introduction

X-ray astronomy has entered a new era now that *Chandra* and *XMM-Newton* are in orbit. Their high sensitivities and unprecedented image qualities bear great promises but also pose new challenges. In this paper, we outline problems of object detection in X-ray images that were not previously encountered. In doing so, we compare the performances of various detection techniques on simulated *XMM-Newton* test images, incorporating the main instrumental characteristics.

The X-ray observations consist of counting incoming photons one by one, recording their time of arrival, position and energy. Later, the event list is used to create images for a given pixel scale and energy band. Various X-ray telescope effects complicate this simple picture – the point spread function (PSF) and the telescope effective area (the vignetting effect), both dependent on the off-axis angle and incoming photon energy; detector effects like quantum efficiency variations, different zones not exposed to X-ray photons; environmental and background effects like solar flares and particle background. Even for relatively large exposures, the X-ray images could contain very few photons, and some sources could contain only a few tens of photons spread over a large area. Consequently, it is important for the source detection and characterization procedures to be able to cope with these difficulties.

As an example, the same hypothetical input situation is shown schematically in Fig. 1 for *ROSAT* [1], *XMM-Newton* [2] and *Chandra* [3] . *XMM-Newton* 's rather large PSF, coupled with its higher sensitivity, leads to the detection of more objects but also to blending and source confusion, which become severe for long exposures depending on the energy band. Confusion problems in the hard band above 5 keV are less important, given the smaller number of objects and smaller count rate of energetic photons. Thus, we concentrate our analysis mainly on source detection problems for the more complicated case of the *XMM-Newton* energy bands below 5 keV.

Send offprint requests to: I. Valtchanov, ivaltchanov@cea.fr

[1] http://wave.xray.mpe.mpg.de/rosat
[2] http://xmm.vilspa.esa.es/
[3] http://chandra.harvard.edu/

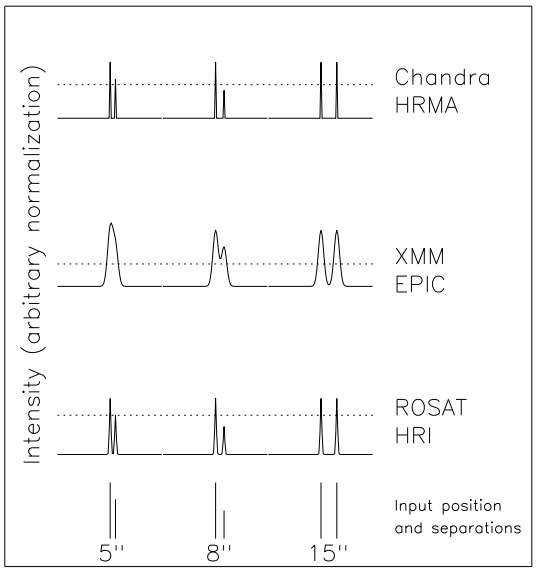

Fig. 1. Typical representation of objects seen by *ROSAT* -HRI, *XMM-Newton* -EPIC and *Chandra* -HRMA. The objects are represented by δ-functions and folded by the corresponding instrumental PSF and efficiency. Full-width-at-half-maximum (FWHM) of the on-axis PSFs are $1\farcs7$ for *ROSAT* -HRI, $0\farcs5$ for *Chandra* -HRMA and $6''$ for *XMM-Newton* -EPIC. The dotted line represents schematically the detection limit.

Each X-ray mission provides data analysis packages – EXSAS for *ROSAT* (Zimmermann et al. 1994), CIAO for *Chandra* (Dobrzycki et al. 1999) and *XMM-Newton* Science Analysis System (XMM-SAS[4]). They include procedures for source detection, and in this paper we estimate and compare their performances on simulated images using various types of objects. These procedures make use of techniques such as Maximum Likelihood (ML), Wavelet Transformation (WT), Voronoi Tessellation and Percolation (VTP).

In Section 2 we describe the X-ray image simulations. A short presentation of the detection procedures is given in Sec. 3. Tests using only point sources are presented in Sec. 4, and extended sources in Sec. 5. We have analyzed realistic simulations of a shallow and a deep extragalactic field with only point sources in Sec. 6 and with extended objects in Sec. 7 for an exposure of 10 ks. Finally, we investigate the problems of confusion and completeness in two energy bands – [0.5-2] and [2-10] keV for two exposures – 10 ks and 100 ks (Sec. 8). Sec. 9 presents the conclusions. ($H_0 = 50$ km/s/Mpc, $h = 0.5$, $q_0 = 0.5$ and $\Omega_0 = 1$ are used).

2. Simulation of X-ray images

The simulations are essential to understand and qualify the behavior of the different detection and analysis packages. We have developed a simulation program that generates X-ray images for given exposure times with extended and point-like objects. It takes into account the main instrumental characteristics of *XMM-Newton* and the total sensitivity of the three EPIC instruments. The procedure is fast and flexible and is made of two independent simulation tasks: object generation (positions, fluxes, properties) and instrumental effects. A possibility to apply the instrumental response directly over images is also implemented, especially useful when one wants to use sky predictions from numerical simulations (cf. Pierre et al. 2000).

Table 1. The general parameters for the simulated images.

Parameter	
Image scale	$4''$/pixel
Image size	512x512
Exposure time	10ks & 100ks
Energy bands	[0.5-2] & [2-10] keV
PSF on axis	$6''$ (FWHM)
	$15''$ (HEW)
Total background (pn+2MOS)	
$[0.5-2]$ keV	1.78×10^{-5} cts/s/pixel
	0.0041 cts/s/arcmin^2
$[2-10]$ keV	2.4×10^{-5} cts/s/pixel
	0.0055 cts/s/arcmin^2

A summary of the simulated images parameters are given in Tab. 1.

The point-like sources are assumed to be AGNs or QSOs with a power law spectrum with a photon index of 2 and flux distribution following the $\log N - \log S$ relations of Hasinger et al. (1998, 2001) and Giacconi et al. (2000) in the two energy bands.

The PSF model is derived from the current available calibration files[5]. On-board PSF data is generally in very good agreement with the previous ground based calibrations (Aschenbach et al. 2000). We must stress that the model PSF is an azimuthal average and in reality, especially for large off-axis angles, its shape can be very distorted. However, in the analytic model (Erd et al. 2000), the off-axis and energy dependences are not available yet. This is not crucial, as the energy dependence in the bands used is moderate and we confine all the analysis inside $10'$ from the centre of the field-of-view where the PSF blurring is negligible.

The extended objects are modeled by a β-profile (Cavaliere & Fusco-Femiano 1976) with fixed core radius $r_c = 250\,h^{-1}$ kpc and $\beta = 0.75$. A thermal plasma spectrum (Raymond & Smith 1977) is assumed for different temperatures, luminosities and redshifts. The source spectra (extended and point-like) are folded with the spectral response function for the total sensitivity of the three *XMM-Newton* EPIC instruments (MOS1, MOS2 and pn with thin filters) by means of XSPEC (Arnaud 1996) to produce the count rates in different energy bands. The actual choice of the energy bands is not important for this comparison study, although some objects can be more efficiently detected in particular energy ranges.

[4] http://xmm.vilspa.esa.es/sas/

[5] http://xmm.vilspa.esa.es/ccf/

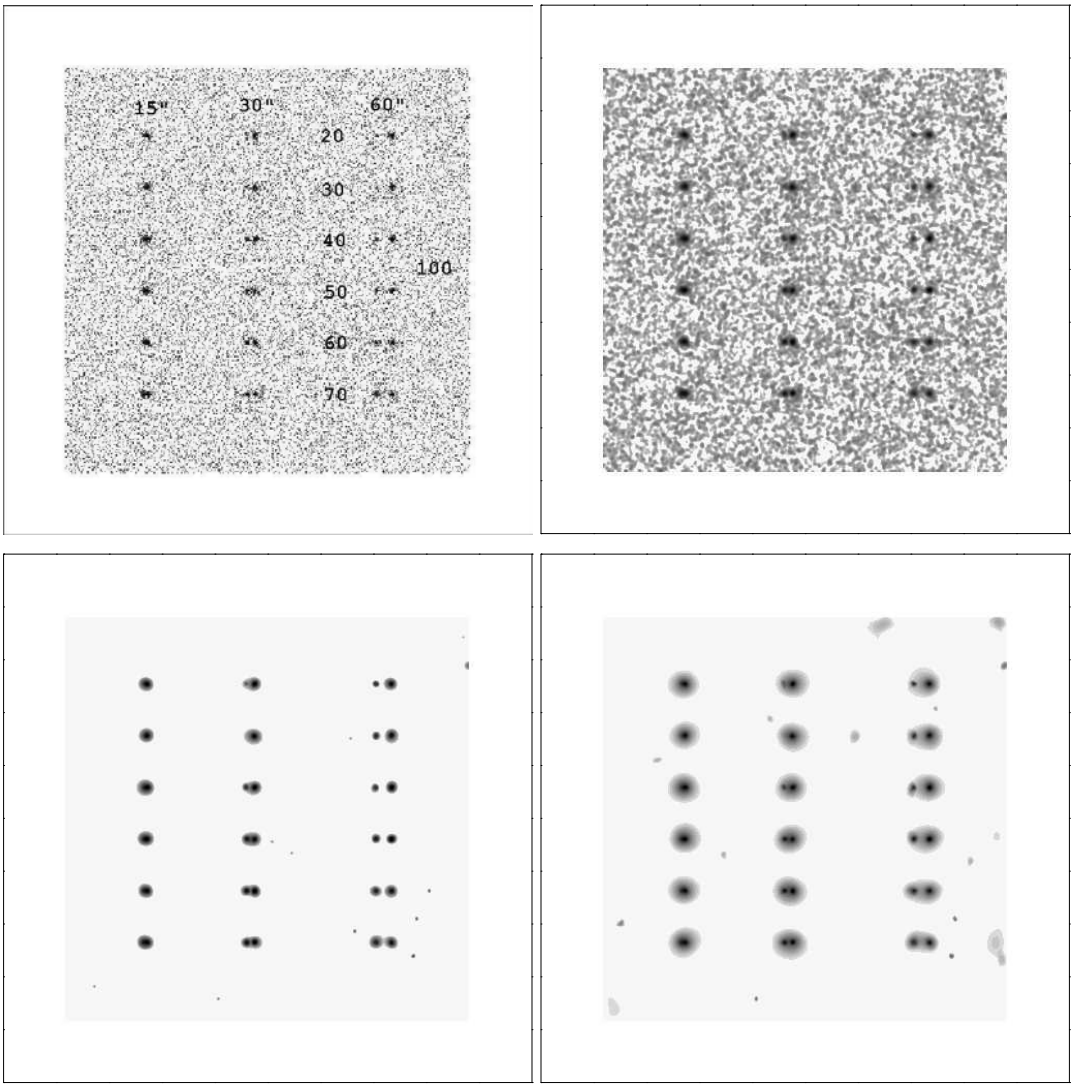

Fig. 2. Test 1. The raw X-ray photon image with object counts for 10 ks exposure time (upper left). There are three sets of two columns of objects at separations of 15″ (HEW of the PSF), 30″ and 60″. The Gaussian convolution with FWHM= 12″ (upper right), `MR/1` wavelet filtering (lower left) and `WAVDETECT` detection image (lower right) both with a significance threshold of 10^{-4} are shown.

As an example, we show in Tab. 2 the resulting count rates for extended sources assuming that they represent an average cluster of galaxies.

The background in the simulations includes realistic background values derived from the *XMM-Newton* in-orbit measurements in the Lockman Hole (Watson et al. 2001).

The calculated count rates for the objects and the photons of the background are subject to the vignetting effect – some photons are lost due to the smaller telescope effective area at given off-axis angle, depending on the incoming photon's energy. We have parametrized the vignetting factor – the probability that a photon at an off-axis angle θ to be observed – as polynomials of fourth order in two energy bands: [0.5-2] and [2-10] keV, using the latest *XMM-Newton* on-flight calibration data. For example, a photon at $\theta = 10'$ has a 53% chance of being observed in [0.5-2] keV and 48% in [2-10] keV.

Further instrumental effects such as quantum efficiency difference between the CCD chips, the gaps between the chips, out-of-time events, variable background, pile-up of the bright sources are not taken into account – their inclusion is not relevant for our main objective.

3. Detection procedures

Without attempting to provide a review of the available techniques in the literature, we briefly describe here the procedures we have tested. They are summarized in Tab. 3.

3.1. Sliding cell detection and maximum likelihood (ML) method

Historically, the sliding cell detection method was first used for *Einstein Observatory* observations (e.g. EMSS –

Table 3. Designation, implementation and short description of the procedures or method used for detection and analysis.

Procedure	Implementation	Version	Method
`EMLDETECT`	XMM-SAS v5.0	3.7.2	Cell detection + Maximum likelihood
`VTPDETECT`	*Chandra* CIAO	2.0.2	Voronoi Tessellation and percolation
`WAVDETECT`	*Chandra* CIAO	2.0.2	Wavelet
`EWAVELET`	XMM-SAS v5.0	2.4	Wavelet
`G+SE`	Gauss + `SExtractor`	2.1.6	Mixed – gauss convolution followed by `SExtractor` detection
`MR/1+SE`	MR/1 + `SExtractor`	2.1.6	Mixed – multi-resolution filtering followed by `SExtractor` detection

Table 2. Count rates for extended sources in three energy bands calculated assuming an average luminosity ($L_{[2-10]keV} = 2.8 \times 10^{44}$ erg/s, $T_X = 5$ keV) $\beta-$profile cluster of galaxies with a Raymond-Smith spectrum, $N_H = 5 \times 10^{20}$ cm^{-2} and spectral response functions for the three EPIC detectors with thin filters.

z	Core radius	Count-rate, photons/s		
	arcsec	[0.4-4] keV	[0.5-2] keV	[2-10] keV
0.6	32.8	0.1687	0.1316	0.0362
0.7	31.3	0.1238	0.0963	0.0253
0.8	30.4	0.0942	0.0734	0.0185
0.9	29.7	0.0737	0.0577	0.0139
1.0	29.3	0.0593	0.0465	0.0107
1.1	29.1	0.0486	0.0382	0.0085
1.2	29.0	0.0406	0.0319	0.0068
1.3	29.0	0.0343	0.0270	0.0055
1.4	29.1	0.0293	0.0231	0.0046
1.5	29.2	0.0253	0.0200	0.0038
1.6	29.4	0.0220	0.0175	0.0032
1.7	29.6	0.0193	0.0154	0.0027
1.8	29.9	0.0171	0.0137	0.0023
1.9	30.2	0.0152	0.0122	0.0020
2.0	30.5	0.0137	0.0109	0.0018

Gioia et al. 1990). It is included in *ROSAT* , *Chandra* and *XMM-Newton* data analysis tools and a good description can be found in the specific documentation for each of those missions.

The X-ray image is scanned by a sliding square box and if the signal-to-noise of the source centered in the box is greater than the specified threshold value it is marked as an object. The signal is derived from the pixel values inside the cell and noise is estimated from the neighboring pixels. Secondly, the objects and some zone around them are removed from the image forming the so-called "cheese" image which is interpolated later by a suitable function (generally a spline) to create a smooth background image. The original image is scanned again but this time using a threshold from the estimated background inside the running cell to give the map detection object list.

The procedure is fast and robust and does not rely on *a priori* assumptions. However it has difficulties, especially in detecting extended features, close objects and sources near the detection limit. Many refinements are now implemented improving the sliding cell method: (1) consecutive runs with increasing cell size, (2) matched filter detection cell where the cell size depends on the off-axis angle. However, the most important improvement was the addition of the maximum likelihood (ML) technique to further analyze the detected sources.

The ML technique was first applied to analyze *ROSAT* observations (Cruddace et al. 1988, 1991, Hasinger et al. 1993). It was used to produce all general X-ray surveys from *ROSAT* mission (e.g. RASS – Voges et al. 1999, WARPS survey – Ebeling et al. 2000). The two lists from local and map detection passes can be merged to form the input objects list for the ML pass. It is useful to feed the ML procedure with as many candidate objects as possible, having in mind that large numbers of objects could be very CPU-expensive. The spatial distribution of an input source is compared to the PSF model – the likelihood that both distributions are the same – is calculated with varying the input source parameters (position, extent, counts) and the corresponding confidence limits can be naturally computed. A multi-PSF fit is also implemented which helps in deblending and reconstructing the parameters of close sources. In the output list, only sources with a likelihood above a threshold are kept.

The ML method performs well and has many valuable features, however, it has some drawbacks – it needs a PSF model to perform the likelihood calculation and thus favours point-like source analysis, extent likelihood could be reliably taken only for bright sources, it cannot detect objects which are not already presented in the input list (e.g. missing detections in the local or map passes). Here we have used `EMLDETECT` – an implementation of the method specifically adapted for XMM-SAS (Brunner 1996). In the map mode sliding cell pass we used a low signal-to-noise ratio ($\sim 3\sigma$) above the background in order to have as many as possible input objects for the ML pass. The likelihood limit (given by $L = -\ln P$, where P is the probability of finding an excess above the background) was taken to be 10, which corresponds roughly to 4σ detection. A multi-PSF fitting mode with the maximum of 6 simultaneous PSF profile fits was used.

3.2. VTP

VTP – the Voronoi Tessellation and Percolation method (Ebeling & Wiedenmann 1993, Ebeling 1993) is a general method for detecting structures in a distribution of points (photons in our case) by choosing regions with enhanced

surface density with respect to an underlying distribution (Poissonian in X-ray images). It treats the raw photon distribution directly without any recourse to a PSF model or a geometrical shape of the objects it finds. Each photon defines a centre of a polygon in the Voronoi tessellation image and the surface brightness is simply the inverse area of the polygon (assuming one single photon per cell). The distribution function of the inverse areas of all photons is compared to that expected from a Poisson distribution and all the cells above a given threshold are flagged and percolated, i.e. connected to form an object. This method was successfully used with *ROSAT* data (Scharf et al. 1997) and is currently incorporated in the *Chandra* DETECT package (Dobrzycki et al. 1999).

Apart from these advantages, VTP has some drawbacks which are especially important for *XMM-Newton* observations: (1) because of the telescope's high sensitivity and rather large PSF with strong tails, the percolation procedure tends to link nearby objects; (2) excessive CPU time for images with relatively large number of photons; (3) there is no simple way to estimate the extension of objects.

3.3. Wavelet detection procedures

In the past few years a new approach has been extensively used: the wavelet technique (WT). This method consists in convolving an image with a wavelet function:

$$w_a(x,y) = I(x,y) \otimes \psi(\frac{x}{a}, \frac{y}{a}), \quad (1)$$

where w_a are the wavelet coefficients corresponding to a scale a, $I(x,y)$ is the input image and ψ is the wavelet function. The wavelet function must have zero normalization and satisfy a simple scaling relation

$$\psi_a(x,y) = \frac{1}{a}\psi_1(\frac{x}{a}, \frac{y}{a}). \quad (2)$$

The choice of ψ is dictated by the nature of the problem but most often the second derivative of the Gaussian function or the so called "Mexican hat" is used.

The WT procedure consists of decomposing the original image into a given number of wavelet coefficient images, w_a, within the chosen set of scales a. In each wavelet image, features with characteristic sizes close to the scale are magnified and the problem is to mark the significant ones, i.e. those which are not due to noise. In most cases, this selection of significant wavelet coefficients cannot be performed analytically because of the redundancy of the WT introducing cross-correlation between pixels. For Gaussian white noise, w_a are distributed normally, allowing easy thresholding. This is not the case for X-ray images which are in the Poissonian photon noise regime.

Various techniques were developed for selecting the significant wavelet coefficients in X-ray images. In Vikhlinin et al. (1997) a local Gaussian noise was assumed; Slezak et al. (1994) used the Ascombe transformation to transform an image with Poissonian noise into an image with Gaussian noise; in Slezak et al. (1993), Starck & Pierre (1998) a histogram of the wavelet function is used. In recent years a technique based on Monte Carlo simulations is used successfully (e.g. Grebenev et al. 1995, Damiani et al. 1997, Lazzati et al. 1999).

Once the significant coefficients at each scale are chosen, the local maxima at all scales are collected and cross-identified to define objects. Different characteristics, such as centroids, light distribution etc., can be computed, as well as an indication of the source size at the scale where the object wavelet coefficient is maximal.

WT has many advantages – the multiresolution approach is well suited both for point-like and extended sources but favours circularly symmetric ones. Because of the properties of the wavelet function a smoothly varying background is automatically removed. Extensive description of wavelet transform and its different applications can be found in Starck et al. (1998).

In this work we have tested two WT procedures:

`WAVDETECT`: one of the *Chandra* wavelet-based detection techniques (Freeman et al. 1996, Dobrzycki et al. 1999). It uses a "Mexican hat" as wavelet function and identifies the significant coefficients by Monte Carlo simulations. The background level needed to empirically estimate the significance is taken directly from the negative annulus of the wavelet function. Source properties are computed inside the detection cell defined by minimizing the function $|\log r_{PSF} - \log \sigma_F|$, where r_{PSF} is the size of the PSF encircling a given fraction of the total PSF flux and σ_F is the size of the object at the scale closest to the PSF size. No detailed PSF shape information is needed to perform this minimization – just r_{PSF} as a function of the off-axis angle. The control parameters which need attention are the significance threshold and the set of scales. We have used a significance threshold of 10^{-4} corresponding to 1 false event in 10000 ($\sim 4\sigma$ in Gaussian case) and "$\sqrt{2}$ sequence" for the scales, where $a = 1, \sqrt{2}, 2, 2\sqrt{2}, 4, 3\sqrt{2} \ldots 16$.

`EWAVELET`: XMM-SAS package, based on a wavelet analysis. It is very similar to `WAVDETECT` but implements some new ideas. The sources are assumed to have a Gaussian shape in order to analytically derive their counts and extent. Currently, the PSF information is ignored, which can be regarded as a serious drawback. We have used the significance threshold of 10^{-4} ($\sim 4\sigma$) and wavelet scales 1, 2, 4, 8 and 16.

3.4. Mixed approach

This method combines a source detection by an elaborated procedure over filtered/smoothed raw photon images.

The use of such a mixed approach is motivated by the fact that procedures for source detection in astronomical images have been developed for many years and the steps and problems of deblending, photometry, classification of objects are now quite well understood. The raw photon

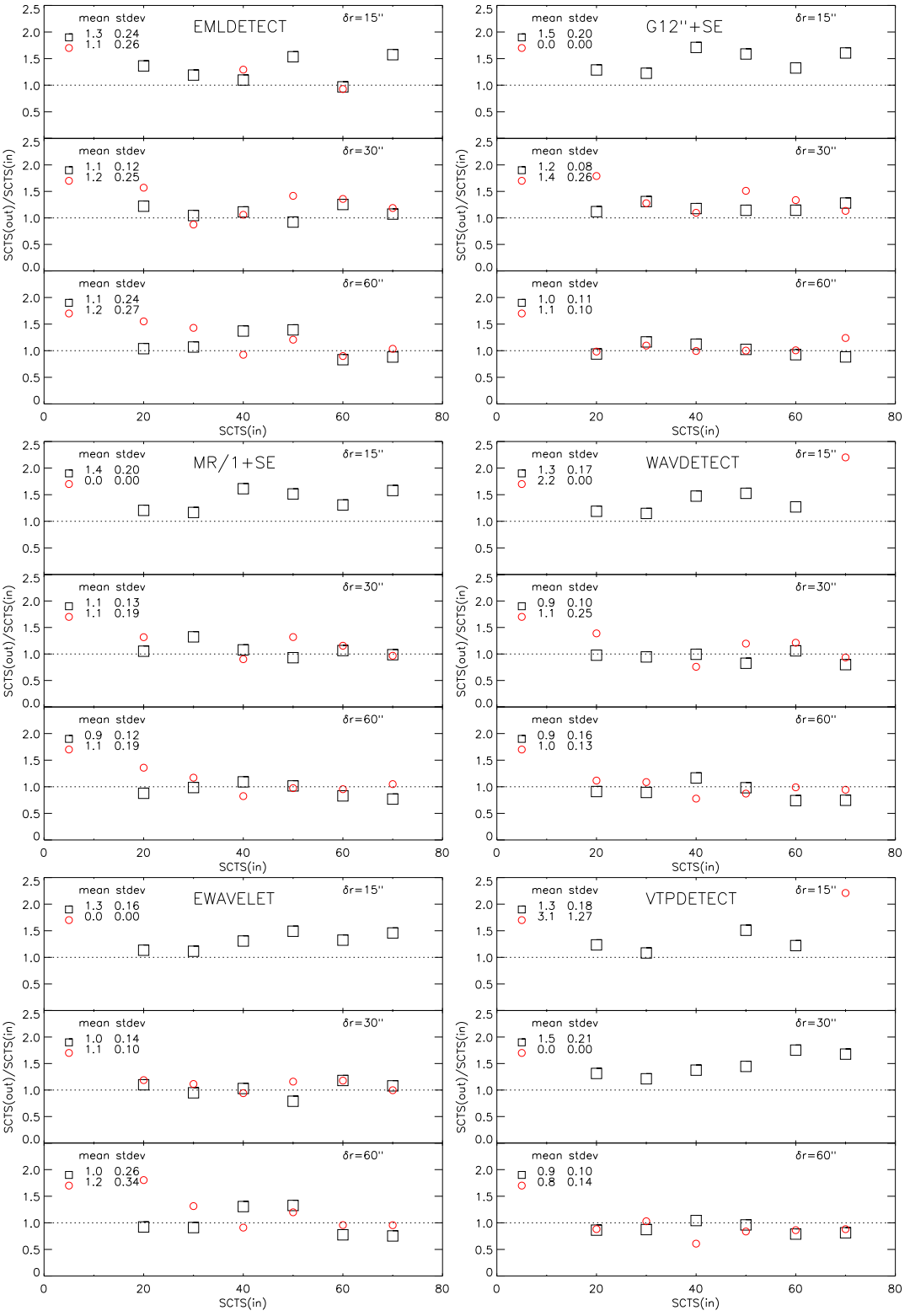

Fig. 3. Test 1. The three panels of each figure show the results in terms of the ratio of inferred counts $SCTS(out)$ and input counts $SCTS(in)$ as a function of the varying input counts for the three cases of object separations (indicated by δr). The mean and st.dev. of the corresponding points are also indicated. When there are no detections, the mean and the st.dev. are both zero. Objects with input counts fixed at 100 (squares) are placed beside their corresponding neighbors (circles), rather than being plotted at 100.

image manipulations can be performed with very simple smoothing procedures (for example a Gaussian convolution) or with more sophisticated methods like the "match-

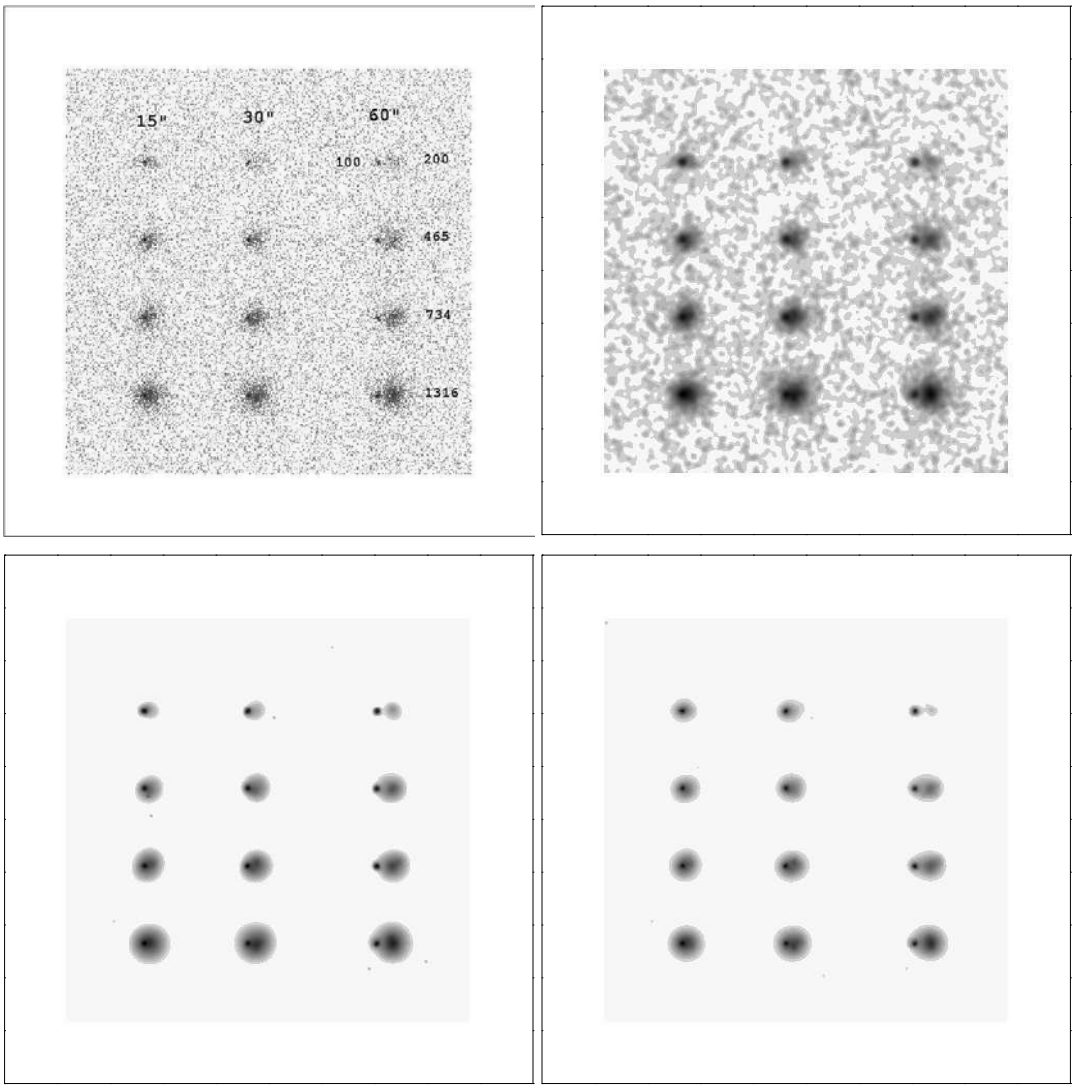

Fig. 4. Test 2. The raw X-ray photon image for 10 ks exposure time (upper left). As in Fig. 2 three cases of separations are indicated, as well as the corresponding input source counts. The extended objects are in the right columns. The Gaussian convolution with FWHM= 20″ (upper right), `MR/1` WT filtered image (lower left) and `WAVDETECT` reconstructed image both with a significance threshold of 10^{-4} (lower right) are shown.

ing filter" technique, adaptive smoothing or multiresolution (wavelet) filtering.

We have used two different types of raw image filtering:

(1) Gaussian convolution. For our simulated images we applied two convolutions with FWHM=12″ and 20″ constrained by the image characteristics (see Sec. 2).
(2) Multiresolution iterative threshold filtering (`MR/1` package, Starck et al. 1998) by means of "à trous" (with holes) wavelet method and Poissonian noise model (Slezak et al. 1993, Starck & Pierre 1998) to flag the significant wavelet coefficients (also known as autoconvolution or wavelet function histogram method). The control parameters are the significance threshold, wavelet scales and the number of iterations for the image reconstruction. We took 10^{-4} significance threshold (corresponding to $\sim 4\sigma$ for Gaussian distribution), 6 scales for the "à trous" method allowing analysis of structures with characteristic sizes up to 2^6 pixels ($\sim 4'$). We have used 25 iterations or a reconstruction error less than 10^{-5}. More iterations can improve the photometry but can also lead to the appearance of very faint real or sometimes false features. Optionally the last-scale wavelet smoothed image in the iterative restoration process is used for analysis of large-scale background variations or very extended features.

Source detection over the filtered images was performed with `SExtractor` (Bertin & Arnouts 1996) – one of the most widely used procedures for object detection in astronomy with a simple interface and very fast execution time. Originally, `SExtractor` was developed for optical images but it can be applied very successfully on X-ray images after they are properly filtered. The flexibility of `SExtractor` is ensured by a large number of control parameters requiring dedicated adjustments. In the following

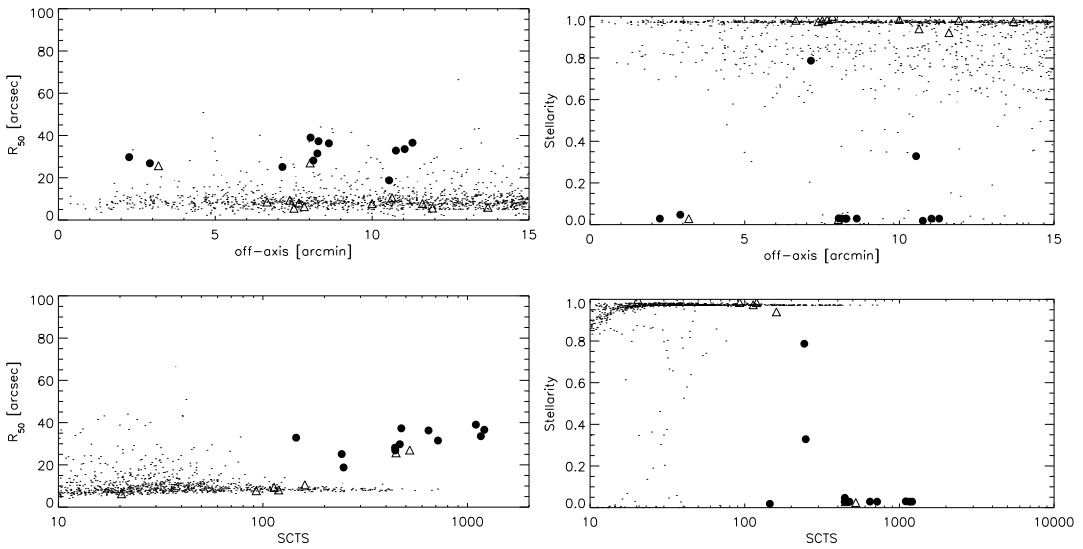

Fig. 5. Test 2. `MR/1+SE` detection classification based on R_{50} (left panels) and stellarity (right panels) as a function of the off-axis angle (upper panels) and detected source counts (lower panels). Identified extended (filled circles) and point-like objects (triangles) are plotted over the results from 10 simulated images with only point-like sources (see Sec. 6).

we will briefly outline those having a significant influence on our results:

- Detection and analysis threshold – important parameters for Gaussian convolved images. It is preferable to use a value greater than 4σ, even sacrificing very faint sources but reducing the number of false detections. For `MR/1` filtering this is irrelevant because the features in the images are already at 4σ significance.
- Background mesh size – influences object detection as well as photometry. Using too coarse a background grid (less grid points) will lead to a smoother background image but some faint objects will be missed in the detection. While too detailed a map (more grid points) will lead to many false detections and worse photometry, depending on the local noise properties. We have found after many experiments that local background meshes with 32 to 64 nodes give best results balancing both effects.
- Minimum detection area – in some cases this parameter can help to avoid spurious detections especially when one uses wavelet scales below the characteristic size of objects.
- Deblending parameters – the number of the deblending levels and the minimum contrast. We used the extreme values of 64 levels and zero contrast so that any saddle point will lead to object splitting.
- Photometry – we have decided to use the automatic aperture photometry procedure implemented in `SExtractor` following Kron (1980) and Infante (1987) which gives better results than the fixed aperture or isophotal methods.
- Classification – we discuss the classification in the next subsection.

3.5. Classification

The problem of classifying sources as resolved or unresolved (or stars/galaxies, extended/point-like) has a long history and discussions can be found in widespread detection packages like `FOCAS` (Valdes et al. 1990), `INVENTORY` (Kruszewski 1988), `SExtractor` (Bertin & Arnouts 1996), Neural Extractor (Andreon et al. 2000). This task becomes even more difficult for X-ray images – we have already mentioned various X-ray telescope effects that blur and distort the images as a function of the off-axis angle.

`EMLDETECT` – the extension likelihood is calculated by the deviation of the object fitted from the PSF model when varying the size (extension) of the object. It was used with *ROSAT* observations to flag possible extended objects and in most of the cases the results were positive. The extension likelihood depends on the chosen PSF model and for faint objects is not reliable (De Grandi et al. 1997).

`WAVDETECT` – the ratio between object size and the PSF size (R_{PSF}) is used for classification purposes. It depends on the adopted definition for object size and can be misleading, especially for faint objects.

`SExtractor` – one parameter for classification is the stellarity index. It is based on neural-network training performed over set of some 10^6 simulated optical images. There are 10 parameters included in the neural network training – 8 isophotal areas, the maximal intensity and the "seeing". The only controllable parameter is the "seeing" which, however, has no meaning for space observations. It can be tuned to the mean PSF size.

The half-light radius R_{50} is another classification parameter. It can be used as a robust discriminator because it depends only on the photon distribution inside

Table 4. Test 1. Detection results. The total number of input objects is 36.

Method	Missed	False
EMLDETECT	4	13
G+SE (4σ)	6	1
MR/1+SE	7	1
WAVDETECT	7	21
EWAVELET	6	4
VTPDETECT	12	19

the object ("luminosity profile"), which is assumed to be different for resolved and unresolved objects.

Additional indications might be taken into account when the classification is ambiguous – e.g. the wavelet scale at which object's wavelet coefficient is maximal or even spectral signatures.

4. Test 1 – point-like sources

4.1. Input configuration

We address the problem of point-like sources separated by $15''$ (half-energy width of the on-axis PSF), $30''$ and $60''$ with different flux ratios. We include the PSF model and background but do not apply the vignetting effect.

The raw input test image is shown in Fig. 2 together with its Gaussian convolution, MR/1 wavelet filtering and WAVDETECT output image. Visually, the Gaussian image is quite noisy, while there are few spurious detections in the WT images.

4.2. Detection rate and positional errors

The number of missing detections and false objects are shown in Tab. 4.

The one sigma input-detect position differences are less than the FWHM of the PSF ($6''$) for all procedures and the maximum occurs for the blended objects, as expected. Note the large number of spurious detections with WAVDETECT, VTPDETECT and EMLDETECT.

4.3. Photometric accuracy

The results for the photometry in terms of the inferred to the input counts are shown in Fig. 3.

$\delta r = 15''$. Only EMLDETECT detects two of the six fainter objects. None of the other procedures separates the objects and consequently the inferred counts are a blend from both sources.

$\delta r = 30''$. The proximity of objects influences the detection and the photometry. EMLDETECT and EWAVELET show the best detection rate results while all the other procedures miss one of the faintest objects.

$\delta r = 60''$. We can safely assume that the objects are well separated. The recovery of the properties is informative for the performance of the tested procedures. It is clear that the general flux reconstruction error (taken to be the spread of the points around the unity line in Fig. 3) is about 15% for brighter sources and goes down to 20-25% for the faintest ones. [In our 10 ks exposure tests and with the adopted background in band [0.5-2] keV, we assume the objects with input counts of 20 photons ($\sim 10^{-15}$ erg/s/cm^2) to be at the detection limit when there is no confusion by nearby sources.]

4.4. Discussion

After this simple test we can eliminate the VTPDETECT: in addition to the very large execution time, some of the VTP-detected object centres were shifted by more than $20''$ from their input positions – a consequence of its ability to detect sources with different shapes where the object center can be far from the input position. Moreover, VTPDETECT percolates all the double sources into single objects at $\delta r = 30''$, which all other procedures were able to separate.

No procedure unambiguously shows best results – both in terms of the detection rate, spurious sources and photometric reconstruction. EMLDETECT outperforms the others in terms of detection rate but with the price of many spurious detections. Using exactly the same PSF model as the one hard-coded in EMLDETECT leads to much better photometric reconstruction.

All other procedures are comparable: EWAVELET showing better detection but its photometric reconstruction is far from satisfactory – about half of the photons were lost at $\delta r = 30''$ and $60''$, because of the assumed Gaussian shape used to derive analytically extension and counts. We have applied a simple correction for the object size to arrive at the good photometric results for EWAVELET presented on Fig. 3.

5. Test 2 – point-like plus extended objects

5.1. Input configuration

This test is similar to Test 1, but we have replaced some of the point-like sources by extended ones generated as described in Sec. 2. The raw photon image with input counts indicated and its representations are shown in Fig. 4.

5.2. Detection rate and positional errors

The number of missed and false detections are shown in Tab. 5. An increase of the searching radius to $20''$ was needed: at $\delta r = 15''$ the blending tends to shift the centroid towards the point-like source. Note that this situation is a clear case for source confusion: if we take the closest neighbour (the point-like source in some cases) as the cross-identification from the input list, we shall overestimate the flux more than two-fold, while the true representation is the extended object.

Some changes were needed for the procedures not based on the wavelet technique in order to avoid splitting

Table 5. Test 2 results for the detection rate. The first number in the "Missed" column is for point sources while the second is for extended ones. The total number of input sources is 24=12+12.

Method	Missed	False
EMLDETECT	1+1	89
G+SE 4σ	6+0	1
MR/1+SE	6+0	6
WAVDETECT	6+0	18
EWAVELET	4+2	5

of the bright extended objects into sub-objects: increase of the Gaussian convolution FWHM to $20''$, and multi-PSF fit for EMLDETECT. In the Gaussian case, the larger smoothing length smears some of the point-like sources, leading to non-detection. EMLDETECT splitting persists even with the maximum number of the PSFs fitted to the photon distribution (currently it is capable of simultaneously fitting up to 6 PSFs).

5.3. Photometric reconstruction

The inferred-to-input source counts ratio is shown in Fig. 6. We will not consider EWAVELET as its photometric results and detection of extended sources were quite unsatisfactory. The simple correction technique (as in Test 1) based on the PSF does not work – the extended objects profile has different shape from the PSF.

$\delta r = 15''$. Only MR/1+SE gives good results for the flux restoration of the extended objects, but overestimating the counts for the faintest one. WAVDETECT misses almost half of the input photons while EMLDETECT splitting leads to very poor results.

$\delta r = 30''$. All procedures give bad restoration results with MR/1+SE performing best again for the extended sources. The proximity of the objects leads to an overestimation of the point-like source counts and an underestimation of the extended object counts. There is no simple way to correct for this effect, but can be done using a rather elaborated iterative procedure involving extended object profile fitting.

$\delta r = 60''$. Point-like source results are relatively similar with all procedures – the source counts are slightly overestimated due to the extended object halo even at $60''$. The problems of WAVDETECT and EMLDETECT and the recovery of the extended objects counts are quite obvious. Again MR/1+SE is the best performing procedure with extended objects flux uncertainty about 25-30%.

5.4. Object classification

An important test is the ability of the procedures to classify objects and to allow further analysis of complicated cases of blending. The MR/1+SEresults for the clasification by means of the half-light radius and stellarity index (c.f. Sec. 3.5) are shown in Fig. 5, overlayed over the results from 10 simulated images with only point-like sources. Clearly the detected extended objects with MR/1+SE fall into zones not occupied by point-like sources. Note, however, that the two detected point-like sources at $30''$ will be mis-clasified as extended objects – the proximity not only influences the source counts, overestimated by more than 4-5 times (Fig. 6), but also the object profile and consequently the classification.

Fig. 8 shows the WAVDETECTclassification – the ratio of the object size to the PSF size (R_{PSF}). The results are more ambiguous with WAVDETECT (Fig. 8) compared to MR/1+SE. The results with EMLDETECT and its classification parameter (extension likelihood) were very unsatisfactory due to the extended object splitting. More comprehensive discussion of the simulations and the classification is left for Sec. 7.

5.5. Discussion

Clearly EMLDETECT and WAVDETECT have problems in restoring the fluxes of extended objects. We have already discussed the splitting difficulties of EMLDETECT. The explanation for WAVDETECT's bad results is that the wavelet scale at which the detected object size is closer to the PSF size defines the source detection cell (in which the flux is computed). If the characteristic size of an object is larger than the PSF size (i.e. an extended object) this procedure will tend to underestimate the flux.

We can safely accept the MR/1+SE procedure as the best performing for detection and characterization both for point-like and extended objects. We must stress however that one cannot rely on the flux measurements when there are extended and point-like sources separated by less than $30''$. The proximity affects also the classification of the point-like sources. Using the classification and then performing more complicated analysis like profile fitting and integration for the extended sources can improve a lot the restoration. In realistic situations we can expect very often problems of this kind, especially with *XMM-Newton* .

6. Test 3 – Realistic model with only point-like sources

6.1. Input configuration

We simulate an extragalactic field including only point-like sources with fluxes drawn from the $\log N - \log S$ relation (Hasinger et al. 1998, 2001, Giacconi et al. 2000). PSF, vignetting and background models are applied as described in Sec. 2. The aim is to test the detection procedures in more realistic cases where confusion and blending effects are important and not controlled. The raw photon image is shown in Fig. 7 together with its visual representation – the same input configuration for a much larger exposure time and no background, only keeping the objects with counts greater than 10. It displays better the input object

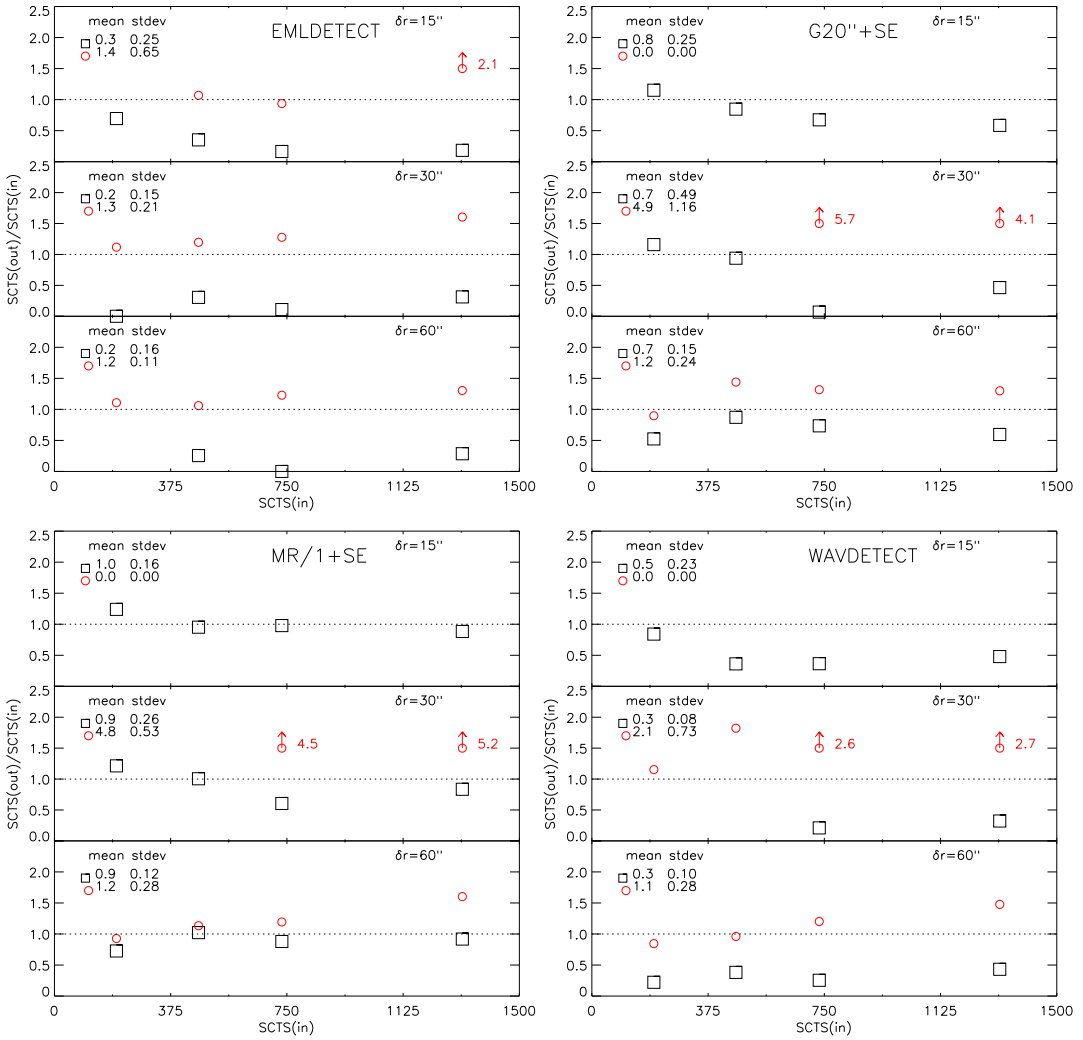

Fig. 6. Test 2. As in Fig. 3 except that the squares now represent extended objects and the point-like sources at fixed counts of 100 (circles) are put beside their corresponding neighbors (rather than being put at 100). Circles with arrows and numbers denote the ratio when it is above 2.

sizes, fluxes and positions and it is instructive to compare it to the `MR/1` filtered and `WAVDETECT` images shown on the same figure.

6.2. Cross-identification and positional error

We need to define a searching radius in order to cross-identify the output and the input lists. The input list contains many objects with counts well below the detection limit ($\log N - \log S$ extends to very faint fluxes) and a lower limit must be chosen. For each detected object, we search for the nearest neighbour inside a circle within the reduced input list.

The positional difference for the brightest detected sources (more than 100 counts) in the inner $10'$ from the center of the FOV is shown in Tab. 6. The region beyond $10'$ is subject to serious problems caused by the vignetting and PSF blurring, the detected object centroid can be few PSFs widths from the true input identification.

Table 6. One sigma positional error and number of detected objects inside the inner $10'$ from the center of the FOV and more than 100 counts for a 10 ks exposure.

Procedure	$\Delta r''$	number
`EMLDETECT`	2.9	13
`G+SE`	3.5	14
`MR/1+SE`	3.2	13
`WAVDETECT`	4.1	12

We therefore adopt the following cross-identification parameters: the input list is constrained to counts greater than 10; a $6''$ searching radius; we consider only the central $10'$ of the FOV.

6.3. Detection rate and photometric reconstruction

The detection rate and flux reconstruction results are shown in Fig. 9. There are different effects playing a role

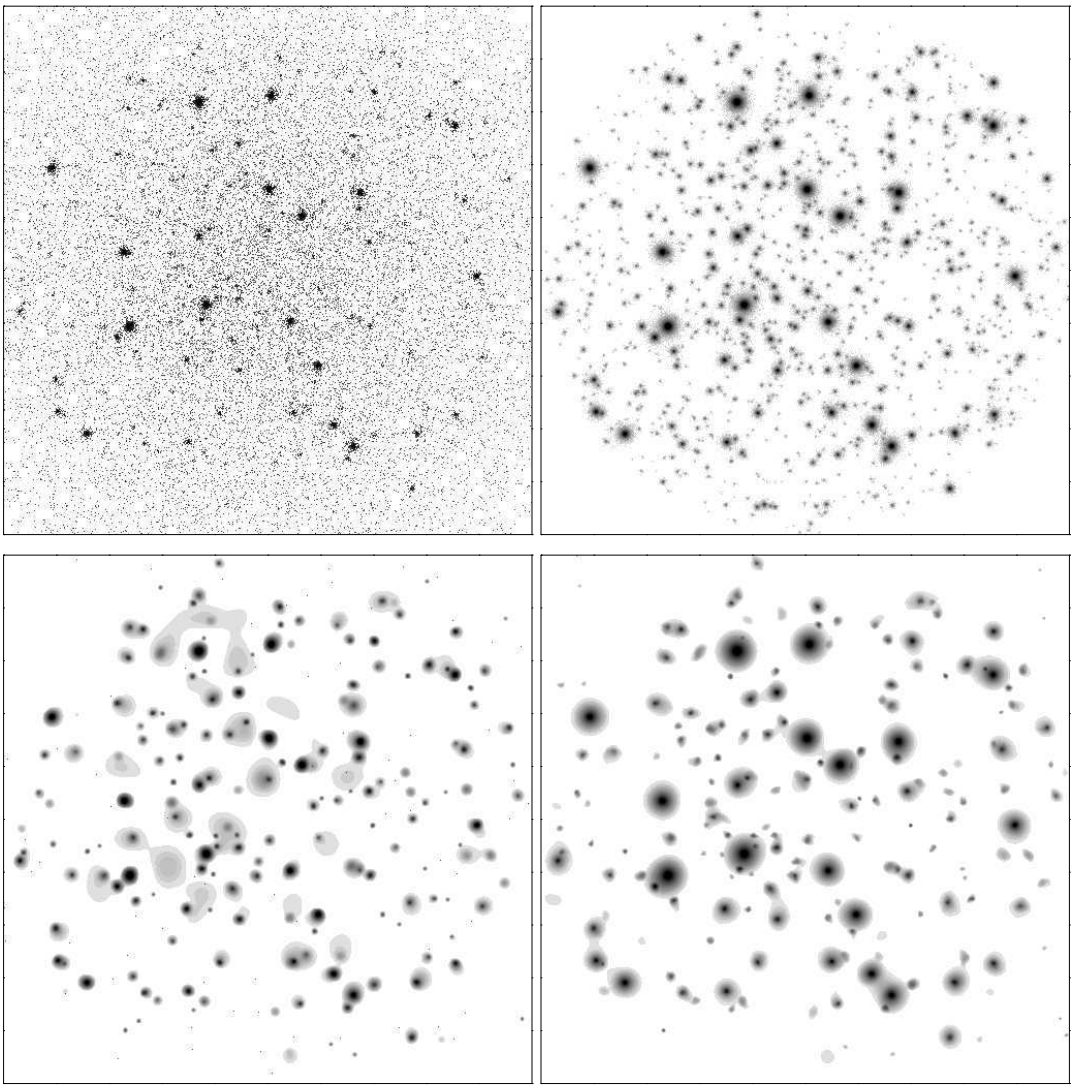

Fig. 7. Test 3. A simulated *XMM-Newton* extragalactic field with only point-like sources for 10ks exposure time and the total sensitivity of the three EPIC instruments (upper left), its representation for much larger exposure time and no background (upper right). The `MR/1+SE` filtering (lower left) and `WAVDETECT` images both with 10^{-4} significance threshold (lower right) are shown.

in the distribution and the numbers of missed and false detections:

(1) "false" detections – non-existent objects, or two or more sources blended into a single detected object. The result will be a "false" detection if the blended objecs are not in the input list (count limit) or the merged object centroid is beyond the searching radius.
(2) source confusion – in the cross-identification process the nearest neighbour to the detected source is not the true assignment; or as in case (1), when a blend of objects is wrongly identified by one input source.
(3) missed detections – depending on the local noise properties, some objects can be missed even if their input counts are above the adopted limiting counts for cross-identification.

6.4. Discussion

The results in terms of detection rate are similar for all procedures. The best detection rate shows `G+SE` but at the price of twice as many false detections.

The photometry reconstruction for the sources above 50 counts shows a spread about 10-15% for the WT based methods and $\sim 25\%$ for `EMLDETECT`. However, `EMLDETECT` clearly outperforms the other procedures when we use the same PSF model as the one hard-coded into the programme. This fact shows that using a correct PSF representation has a crucial importance for the ML technique. More discussion about the detection limits, completeness and confusion is left for Sec. 8.

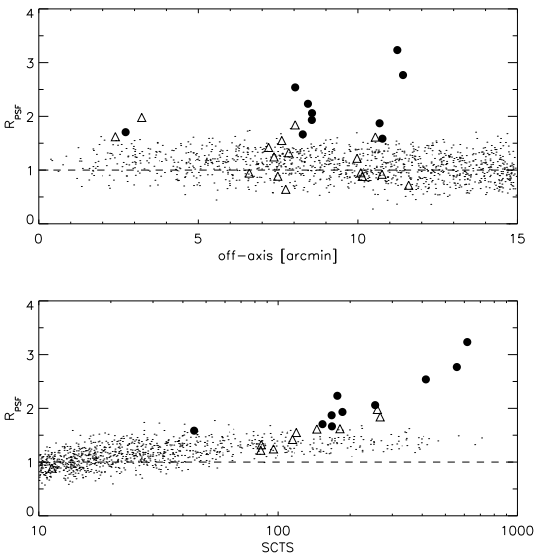

Fig. 8. Test 2. `WAVDETECT` classification based on object size to PSF size ratio – R_{PSF}. The identified extended (filled circles) and point-like sources (triangles) are plotted over the results from 10 simulated images with only point-like sources (see Sec. 6), the dashed line marks a ratio of unity .

7. Test 4 – sky models with point-like and extended objects

7.1. Input configuration

We have chosen exactly the same input point-like sources configuration as in Test 3 and we have added 5 extended objects. They may be regarded as clusters of galaxies at different redshifts with the same β-profiles and moderate X-ray luminosity $L_{[2-10]keV} \sim 3 \times 10^{44}$ erg/s (c.f. Tab. 2). Now the objective is to estimate the capabilities of the procedures to detect and identify extended objects. The difference from Test 2 is the arbitrary positions of the point-like sources leading to different local and global background properties and to uncontrolled confusion effects.

The input configuration and wavelet filtered and output images are given in Fig. 10.

7.2. Positional and photometric reconstruction

Results for the point-like sources will not be presented, because the input configuration (position, $\log N - \log S$, background) is exactly the same as in the previous test. It was shown in Test 2 that the presence of a point source even with moderate counts in the vicinity of a faint extended source could lead to confusion and even non-detection. Of course, the presence of a cluster will affect the detection and photometry of the point-like objects in its vicinity, but this effect is of minor concern for this test and has been already discussed (Test 2).

The detection rate, input-detect position offsets, detected counts and detected-to-input counts ratio are shown in Tab. 7.

As to the positional errors, it was already concluded that the centres of the extended object can be displaced by more than the adopted searching radius for point-like sources (Sec. 5). The differences in positions shown in Tab. 7, especially for fainter objects, are 3-4 times larger than the one sigma limit for point-sources inside the inner $10'$ of the FOV (Tab. 6).

It is confirmed again that `EMLDETECT` and `WAVDETECT` are not quite successful in charactering extended objects. But note that this time the results for `MR/1+SE` and `G+SE`

Table 7. Recovery of position and flux of the extended objects.

redshift	Δr [arcsec]	Input [counts]	Detect [counts]	Detect/Input [%]
		`EMLDETECT`		
0.6	2.1	1316	94	7
1.0	8.0	465	12	3
1.5	12.3	200	161	81
1.8	4.6	136	228	167
2.0	14.8	109	32	29
		`G+SE`		
0.6	1.2	1316	1043	79
1.0	5.2	465	355	76
1.5	1.9	200	220	110
1.8		Not detected		
2.0	15.3	109	80	73
		`MR/1+SE`		
0.6	0.2	1316	1016	77
1.0	2.3	465	340	73
1.5	1.8	200	223	111
1.8	11.8	136	83	61
2.0	10.8	109	185	169
		`WAVDETECT`		
0.6	5.8	1316	344	26
1.0	10.6	465	193	41
1.5	0.1	200	39	19
1.8		Not detected		
2.0	15.3	109	27	24

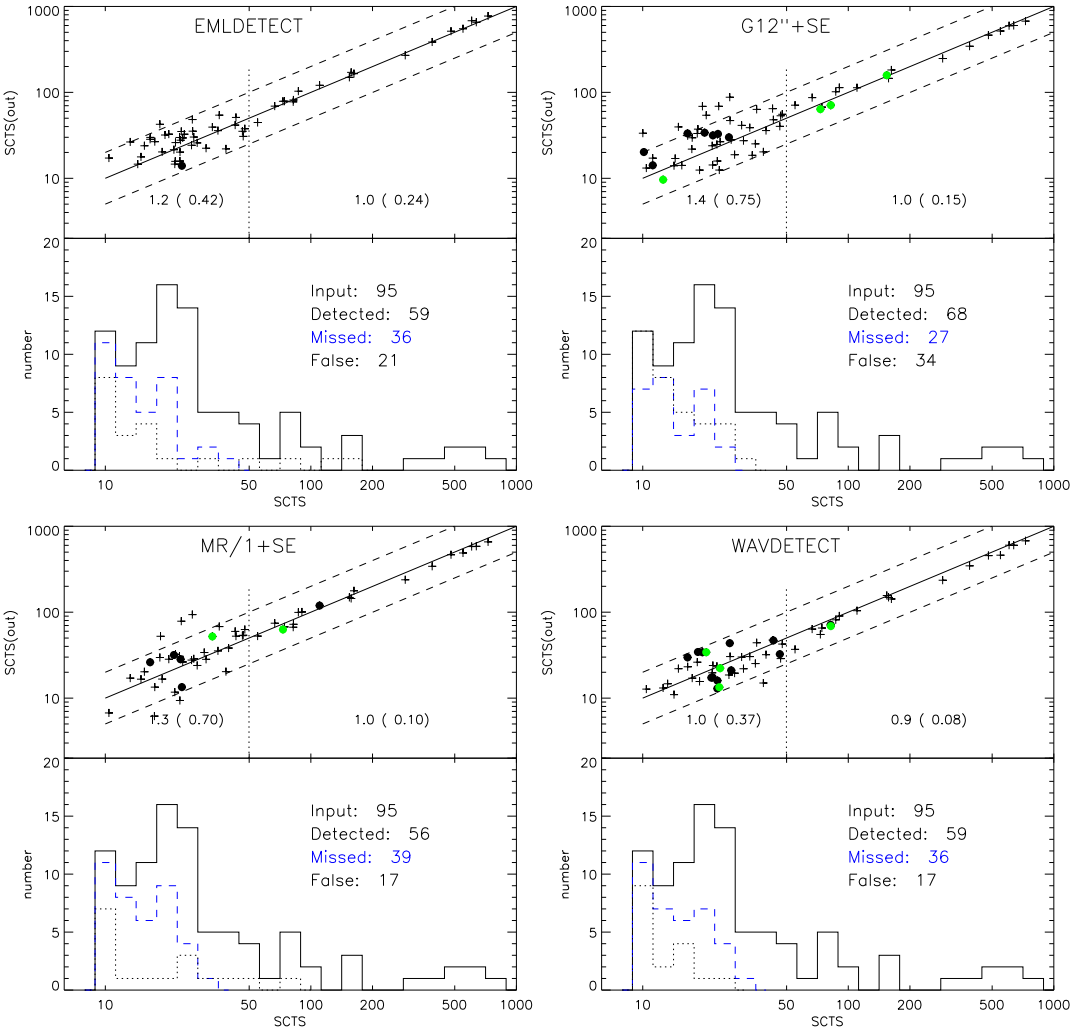

Fig. 9. Test 3. Recovery of the input flux (upper panel of each figure). The continuous line is exact match between detected and input counts while the dashed lines are for two times differences. The limit of 50 input counts is shown by a vertical dotted line and the mean and the st.dev. (in brackets) of $SCTS(out)/SCTS(in)$ for the two regions are indicated. The black circles denote objects with detect-input position difference larger than $4''$, suggesting blending effects; the grey circles denote objects with more than one neighbour inside the searching radius. In the bottom panels, the corresponding rate and distribution of input counts (continuous histogram), missed input objects (dashed histogram) and possible false detections (dotted histogram) are shown.

are worse than the results in Test 2 – the rate of lost photons being about 20-30%. Also, the flux of the clusters at $z = 1.5$ and 2 is overestimated, suggesting blending with faint nearby point-like sources.

7.3. Classification

To classify the detected objects we have performed many simulations with only point-like sources as in Test 3. Ten simulated images were generated with the same $\log N - \log S$ and background, but with different and arbitrary positions of the input sources. Exactly the same parameters were used for filtering, detection and characterization.

Two classification parameters were used: the half-light radius (R_{50}) and the stellarity index from `SExtractor` based procedures. The results are shown in Fig. 11. We do not show results with `WAVDETECT` and `EMLDETECT` classification parameters because their unsatisfactory results were confirmed, as in Test 2.

We can see the excellent classification based on the stellarity index and half-light radius: in the inner $10'$, for objects with more than 20 detected counts, stellarity less than 0.1 and $R_{50} \geq 20''$ we have 15 incorrect assignments from 1287 detections ($\sim 1\%$).

8. Test 5 – completeness and confusion

In this section we investigate the confusion and completeness problems for *XMM-Newton* shallow and deep observations like the first XMM Deep X-ray Survey in the Lockman Hole (Hasinger et al. 2001).

A set of 10 images with exposure times of 10 ks and 100 ks in the energy bands [0.5-2] and [2-10] keV were generated; the fluxes were drawn using the latest $\log N - \log S$

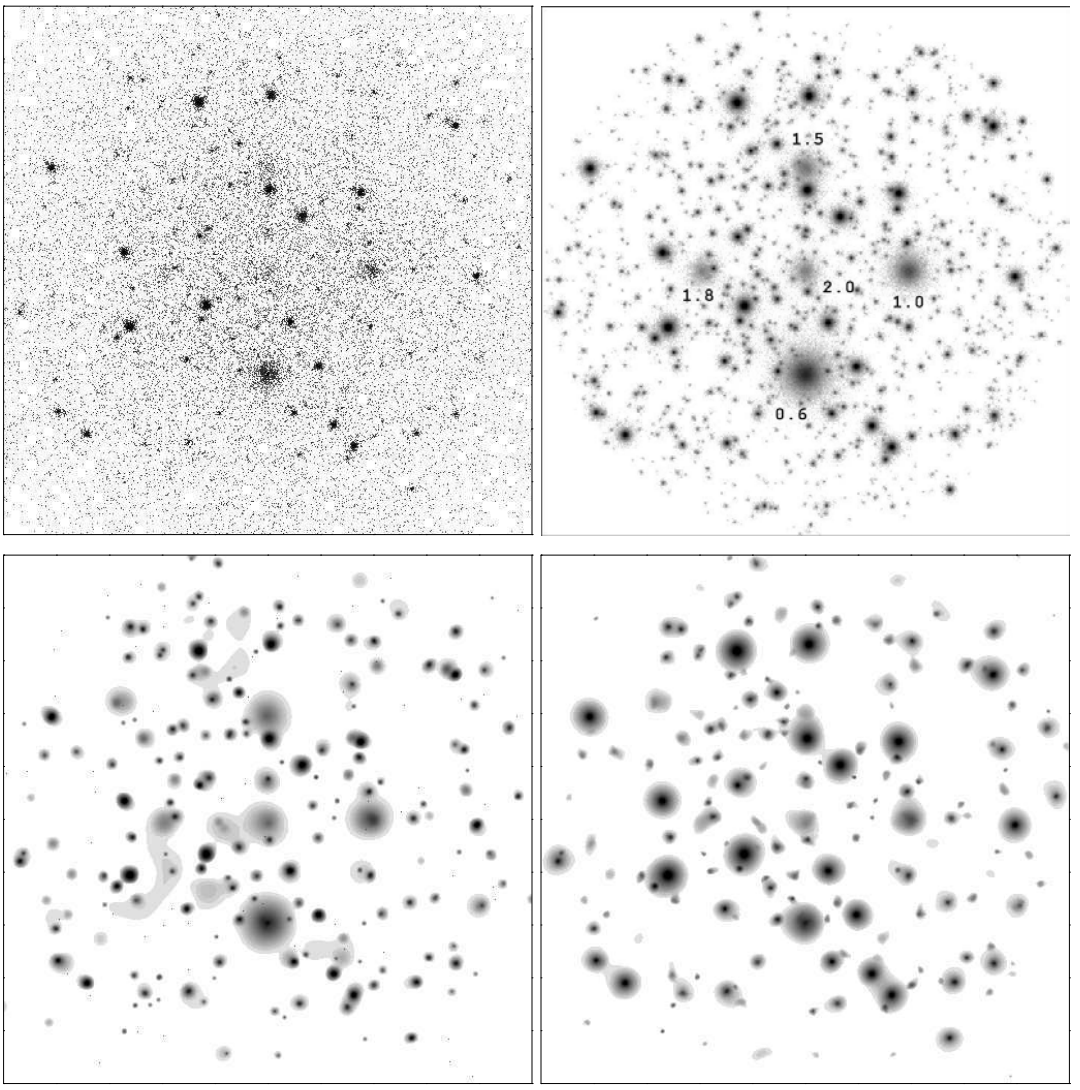

Fig. 10. Test 4. The raw X-ray photon image with point-like and extended objects for 10ks exposure time (upper left) and its visual representation for much larger exposure and no background (upper right). The corresponding redshifts for the clusters are indicated. The `MR/1+SE` filtering (lower left) and `WAVDETECT` both with 10^{-4} significance threshold (lower right) are shown.

relations from Hasinger et al. (2001) and Giacconi et al. (2000). Detection and analysis were performed with exactly the same parameters for all simulations: detection threshold, analysis threshold, background map size, detection likelihood, etc. (see Sec. 3). Cross-identification was achieved using the input sources above 10 counts and 30 counts for 10 ks and 100 ks exposures respectively. Lowering the count limits yields more cross-identifications but increases considerably the number of spurious detections.

The input image for 100 ks and [0.5-2] keV band is shown in Fig. 12. The inner $10'$ zone where all analysis is performed is indicated, as well as the total *XMM-Newton* field-of-view. It is informative to compare it with the images for 10 ks in Fig. 7.

In order to estimate the effect of confusion we have generated images with only point-like sources, distributed on a grid such to avoid close neighbours, and with fixed fluxes spanning the interval $[10^{-16}, 10^{-13}]$ erg/s/cm^2.

In the following we discuss some important points.

– *Confusion and completeness*
The detection rate of the input sources as a function of flux (Fig. 13) indicates that confusion problems are significant for 100 ks exposures in the [0.5-2] keV band. They are marginal for 100 ks exposures in [2-10] keV band and absent for 10 ks in both bands.
Energy conversion factors and the limiting fluxes below which more than 10% of the input objects are lost are shown in Tab. 8.
– *Differential flux distribution*
The differential flux distributions for 100 ks in [0.5-2] keV obtained by `MR/1+SE` and `EMLDETECT` are shown on Fig. 14. Spurious detections appears to be numerous with `EMLDETECT` below 5×10^{-16} erg/s/cm^2 and tend to compensate the loss of sensitivity and confusion. `MR/1+SE` appears to be less affected and allows us to set a conservative flux limit of 6×10^{-16} erg/s/cm^2($\sim$ 90

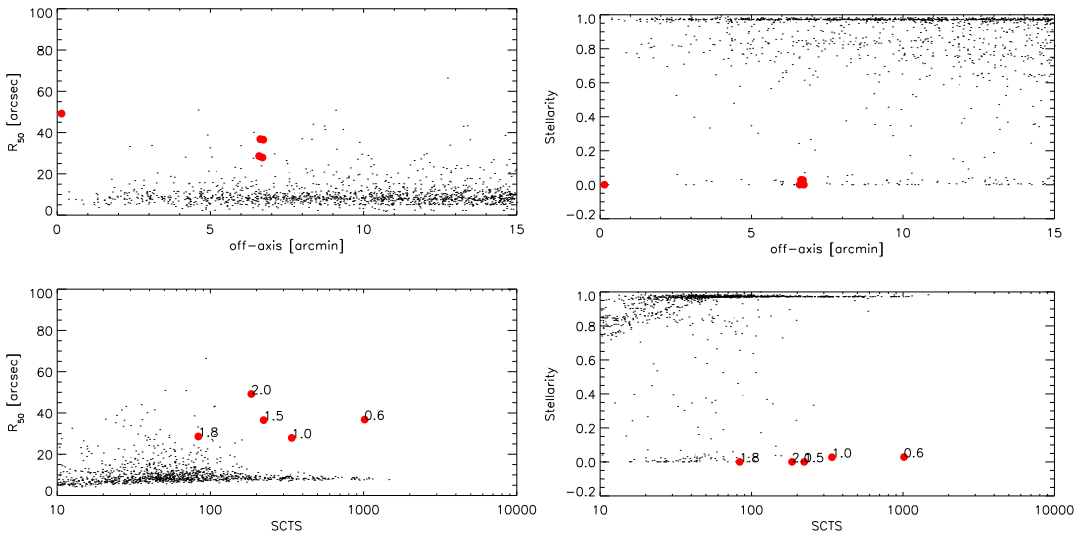

Fig. 11. Test 4. Half-light radius R_{50} (left figures) and stellarity index (right) as a function of the off-axis angle (up) and detected counts (down) for 10 generations. The detection was performed with `SExtractor` after `MR/1` multiresolution filtering. There are in total 1287 detections indicated by points. The extended objects from this test are shown with filled circles.

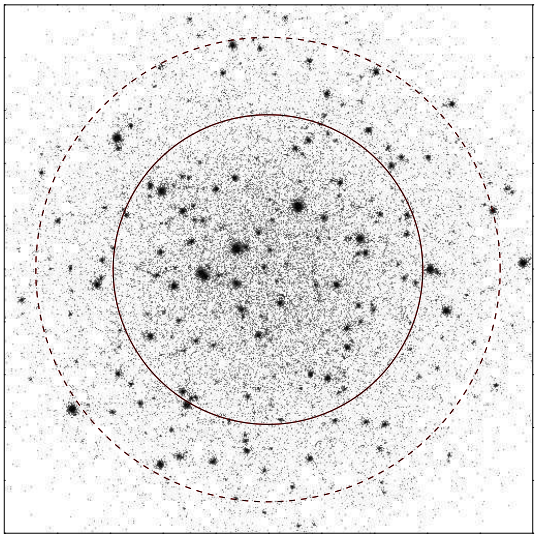

Fig. 12. Simulated 100ks *XMM-Newton* deep field in [0.5-2] keV with the same parameters (N_H, $\log N - \log S$, Γ, background) as in the Lockman Hole (Hasinger et al. 2001, Watson et al. 2001). We restrict the analysis to the inner $10'$.

Table 8. The energy conversion factors (ECF) and the 90% completeness limits for detections. ECF is computed assuming power-low spectrum with photon index $\Gamma = 2$, $N_H = 5 \times 10^{19}$ cm^{-2} (Hasinger et al. 2001) and the three EPIC instruments (pn+2MOS) with thin filters.

	[0.5-2] keV	[2-10] keV
ECF (cts/s per erg/s/cm^2)		
	6.70×10^{-13}	3.66×10^{-12}
Flux limits (erg/s/cm^2)		
10ks	2×10^{-15}	10^{-14}
100ks	6×10^{-16}	3×10^{-15}

photons for 100 ks), below which the incompleteness becomes important – 65% of the input sources are lost between 3×10^{-16} and 6×10^{-16} erg/s/cm^2.

– $\log N - \log S$
The $\log N - \log S$ functions in [0.5-2] keV for 10 ks and 100 ks exposures are shown in Fig. 15. The inferred $\log N - \log S$ (by simple source counting) are in very good agreement with the input ones down to fluxes about 2×10^{-15} and 6×10^{-16} erg/s/cm^2 with `MR/1+SE`and 10^{-15} and 3×10^{-16} erg/s/cm^2 for `EMLDETECT`for 10 ks and 100 ks respectively. Although there are confusion and completeness problems for 100 ks starting at $5 - 6 \times 10^{-16}$ erg/s/cm^{2}as discussed above, their effect is completely masked in the `EMLDETECT` integral distribution, which seems to be in very good agreement down to 3×10^{-16} erg/s/cm^2(the lower flux limit for the Lockman Hole Deep Survey analysis of Hasinger et al. 2001).

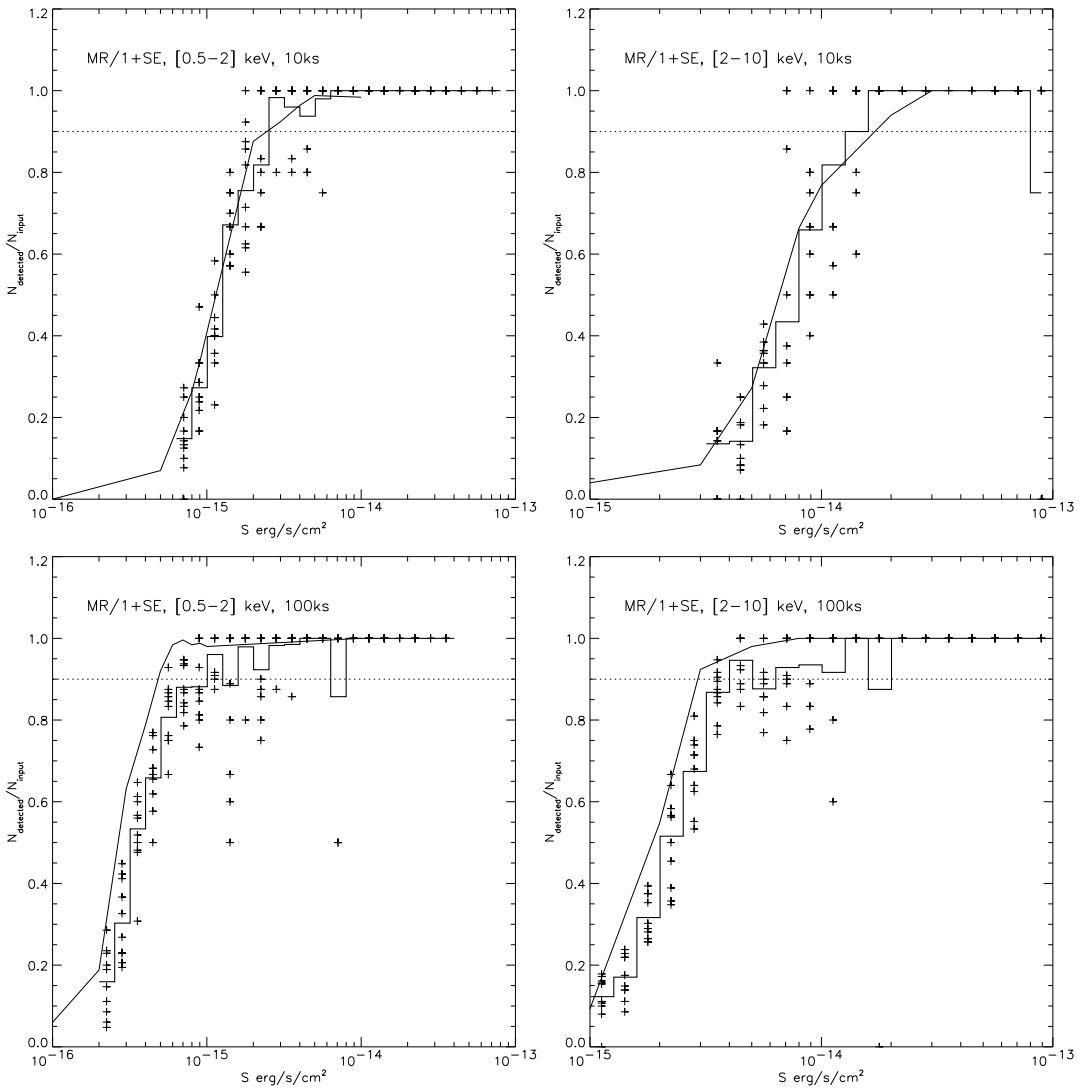

Fig. 13. Ratio of number of cross-identified objects to the number of input objects, with counts greater than 10 and 30 for 10 ks and 100 ks exposures respectively, as a function of the input flux. The results of 10 generations are shown by crosses, the heavy histogram is the corresponding average; the curve indicates the detection rate if confusion is absent and the dotted line marks 90% completeness.

– *Photometric accuracy*
The photometric reconstruction is relatively similar for 10ks and 100ks in for fluxes greater than 2×10^{-15} and 6×10^{-16} erg/s/cm^2 respectively (the 90% completeness limit, Fig. 16). The flux uncertainties are about 25-30 % and going down to fainter fluxes leads to very poor photometry.

9. Conclusions

Various procedures for detecting and characterizing sources were tested by simulated X-ray images. We have concentrated our attention mainly on images with *XMM-Newton* specific characteristics, because the problems arising from its high sensitivity and relatively large PSF are new and challenging.

We have analyzed the detection rate and the recovery of all characteristics of the input objects: flux, positional accuracy, extent measurements and the recovery of the input $\log N - \log S$ relation. We have also investigated confusion problems in large exposures.

Concerning detection rate and characteristics reconstruction, we have shown that the `VTPDETECT` implementation of the Voronoi Tessellation and Percolation method is not suited to *XMM-Newton* images. `EWAVELET` provides very good detection rate and photometric reconstruction for point-like sources after a simple correction, but shows unreliable results for extended sources.

One of the best methods for point-like source detection and flux measurements is `EMLDETECT` but we stress again that the PSF model used for the ML procedure needs to be close to the image PSF for the most accurate photometry. Serious drawbacks are the relatively large number of spurious detections as well as the splitting of the extended sources, which we were not able to suppress even with 6

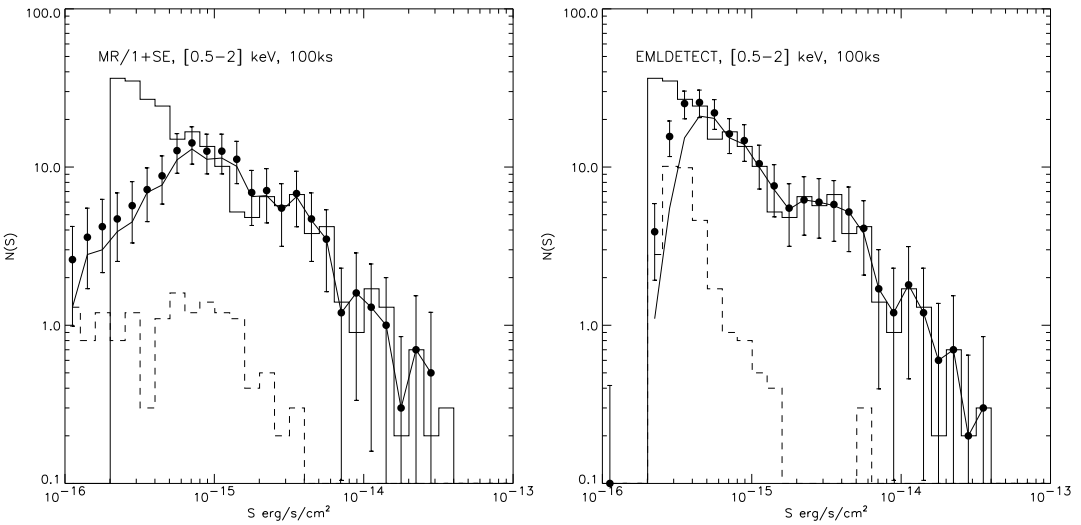

Fig. 14. Differential number counts as a function of flux. The continuous histogram is the input distribution, the dots with error bars (Poissonian) are the measured distribution (without any cross-identifications), the dashed histogram indicates the false detections and the continuous line is the corrected distribution excluding the false detections. Left for `MR/1+SE`, right for `EMLDETECT`– all averaged from 10 simulations

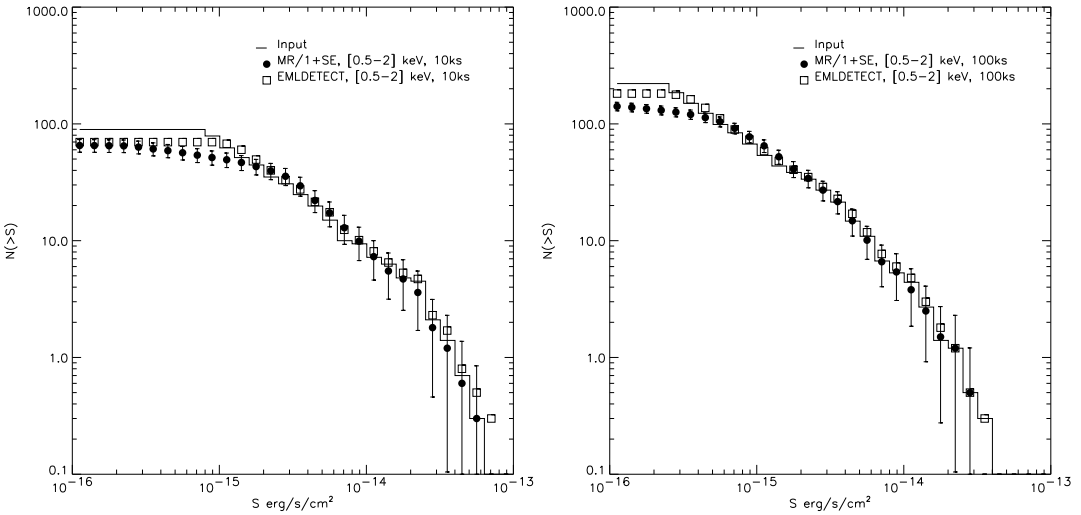

Fig. 15. The integral number of objects in the inner $10'$ (surface 0.087 sq.deg.) as a function of the flux for [0.5-2] keV and two exposures: 10 ks and 100 ks. The points with error bars (Poissonian) are the detections (without cross-identification) with `MR/1+SE` boxes are `EMLDETECT`results, while the histogram is the input $\log N - \log S$ function.

simultaneous PSF profile fits in the multi-PSF mode; this seriously hampers the analysis of the extended sources.

`WAVDETECT` is a flexible method giving good detections even in some complicated cases. But, here again, spurious detections are quite numerous. `WAVDETECT` does not assume a PSF model but requires the PSF size as a function of the encircled energy fraction and the off-axis distance in order to define the object detection cell. However, the way the detection cell is defined leads to bad photometry for extended objects.

Our choice is the `MR/1+SE` method. The mixed approach involving first a multiresolution iterative threshold filtering of the raw image followed by detection and analysis with `SExtractor`. Our tests have shown that this is the best strategy for detecting and characterizing both point-like and extended objects . Even though this mixed approach consists of two distinct steps, it is one of the fastest procedures (Tab. 9), allowing easy checks of different stages in the analysis (filtering, detection, photometry).

Without blending or confusion effects, the photometry is accurate within 10-20% for both point-like and extended objects. This uncertainty can be regarded as an intrinsic error due to the Poissonian nature of the X-ray images. For extended objects, only the `MR/1+SE` method gives satisfactory photometric results.

Blending between extended and point-like sources is quite serious at separations below $\sim 30''$. Better results for photometry may eventually be obtained if the intrinsic shape of the extended objects is known, and if the two objects are detected. However, in most of the cases with small separation, there is no indication of blending

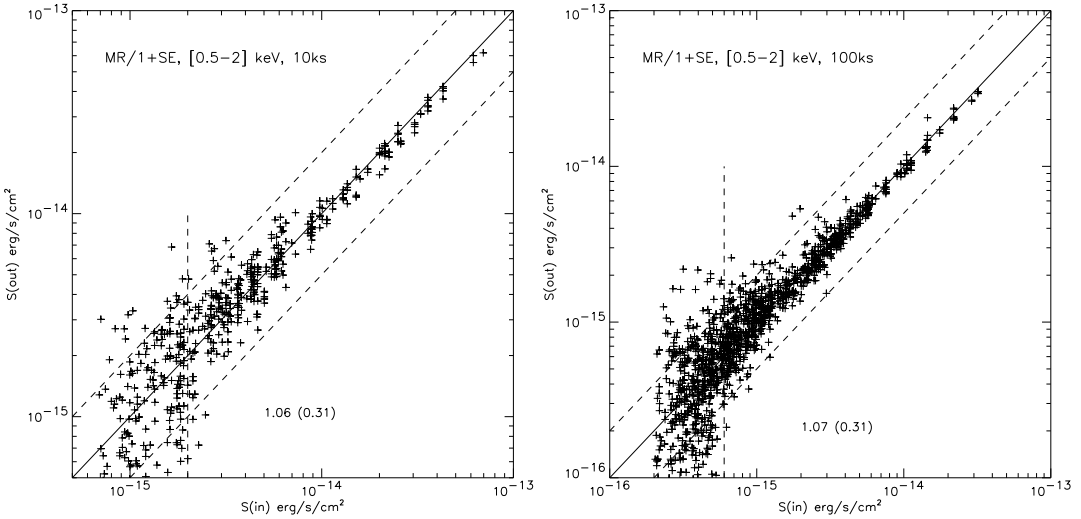

Fig. 16. Photometry reconstruction for all 10 simulated images at 10 ks (left) and 100 ks (right) in the [0.5-2] keV band. The solid line is exact match between detected and input counts while the dashed lines are for two-fold differences. The vertical dashed line marks the 90% completeness limit (see Tab. 8) and mean and st.dev. (in brackets) above this limit are denoted.

Table 9. CPU times for performing Test 5 for 100ks. The procedures were run on a Pentium III-Xeon, 550MHz, Linux. `G+SE` and `MR/1+SE` CPU time is the total of filtering and detection passes. For `EMLDETECT` the number of input objects is given.

Procedure	Number of detections	CPU time [min.]
`EMLDETECT`	528	12.0
`EWAVELET`	364	0.4
`MR/1+SE`	370	1.9
`G+SE`	365	0.1
`WAVDETECT`	378	10.3
`VTPDETECT`	1307	10.7

– which is a dangerous situation for flux reconstruction. In such cases, there may exist some spectral signatures of the effect.

The identification process of X-ray sources relies on their positional accuracy. We have shown that for objects with more than 100 counts in 10 ks exposure images and within the inner $10'$ of the field-of-view, the one sigma positional error is of the order of one half of the FWHM of the PSF ($\approx 3-4''$, Tab. 6). For extended objects, because of their shallower profiles and depending on the number of photons and the off-axis distance, the detected centre could even be at about $15''$ from its input position.

Comparing series of simulations with 100 ks and 10 ks in two energy bands – $[0.5-2]$ and $[2-10]$ keV, we show that the effects of confusion and completeness are absent for 10 ks, but quite significant for 100 ks in the lower energy band. Moreover, for faint fluxes, these effects tend to be masked by the large number of spurious detections with `EMLDETECT`. Although this method seems to give correct results for the $\log N - \log S$ down to fainter fluxes than `MR/1+SE`, in real situations it is impossible to asses the contribution of the numerous spurious detections. From our simulations, we estimate that about 60-65% of the sources are lost between 3×10^{-16} and 6×10^{-16} erg/s/cm^2 for a 100 ks exposure with the current best method (`MR/1+SE`).

One of the most important conclusions that will have deep cosmological impact concerns the detection and classification of extended objects. We have shown that the `MR/1+SE` mixed approach is capable of detecting galaxy cluster-like objects with moderate luminosity ($L_{[2-10]keV} \sim 3 \times 10^{44}$ erg/s) at redshifts $1.5 < z < 2$ in 10 ks *XMM-Newton* simulated images. A criteria based on the half-light radius and the stellarity index classifies them correctly, with a confidence level greater than 98%.

Acknowledgements. We are thankful to J.-L. Starck for many discussions regarding wavelet filtering and detections and for the `MR/1` software, R. Ogley and A. Refregier for valuable comments on the manuscript, H. Bruner and J. Ballet for comments and help on XMM-SAS and `EMLDETECT`, E. Bertin for help on `SExtractor`. We thank also the referee for valuable comments and suggestions on the manuscript.

References

Andreon S., Gardiulo G., Longo G., et al, 2000, MNRAS, 319, 700 (NExt)

Arnaud K.A., 1996, in ASP Conf. Ser., Vol. 101, Astronomical Data Analysis Software and Systems V,eds. Jacoby G.H. & Barnes J. (San Francisco: ASP), 17 (XSPEC)

Aschenbach B., Briel U., Haberl F., et al., 2000, SPIE 4012, 731 (astro-ph/0007256)

Bertin E., Arnouts S., 1996, A&AS 117, 393 (`SExtractor`)

Brunner H., 1996, Technical Note (SSC-AIP-TN-0001), http://xmmssc-www.star.le.ac.uk/documents/

Cavaliere A., Fusco-Femiano R., 1976, A&A 49, 137

Cruddace R.G., Hasinger G.R., Schmitt J.H., 1988, In: Astronomy from large databases, eds. F. Murtagh & A. Heck (Garching:ESO)

Cruddace R.G., Hasinger G.R., Trümper J. et al., 1991, Exp.Astron. 1, 365

Damiani F., Maggio A., Micela G., Sciortino S., 1997, ApJ 483, 350

De Grandi S., Molendi S., B̈horinger H., et al., 1997, ApJ 486, 738
Dobrzycki A., Ebeling H., Glotfelty K. et al., 1999, In *Chandra* DETECT User Guide: http://asc.harvard.edu/
Erd C., Gondoin P., Lumb D., et al., 2000, XMM Calibration Access and Data Handbook, XMM-PS-GM-20 Issue 1.1, http://xmm.vilspa.esa.es/calibration/
Giacconi R., Rosati P., Tozzi P. et al., 2000, astro-ph/0007240v2
Gioia I.M., Maccacaro T., Schild R.E., et al., 1990, ApJSS 72, 567
Grebenev S.A., Forman W., Jones C., Murray S., 1995, ApJ 445, 607
Ebeling H., 1993, Ph.D. thesis, MPE Report 250.
Ebeling H., Wiedenmann G., 1993, Phys. Rev. 47, 704
Ebeling H., Jones L.R., Perlman E., et al., 2000, ApJ 534, 133
Freeman P., Kashyap V., Rosner R. et al., 1996, in ASP Conf. Ser., Vol. 101, Astronomical Data Analysis Software and Systems V, eds. Jacoby G.H. & Barnes J. (San Francisco: ASP), 163
Hasinger G., Burg R., Giacconi R., et al., 1993, A&A, 275, 1 (erratum 1994, A&A 291, 348)
Hasinger G., Burg R., Giacconi R., et al., 1998, A&A, 329, 482
Hasinger G., Altieri B., Arnaud M., et al. 2001, A&A, 365, L45
Infante L., 1987, A&A 183, 177
Kolaczyk E., Dixon D., 2000, ApJ 534, 490
Kron R.G., 1980, ApJS 43, 305
Kruszewski, A., 1988, in 1st. ESO/ST-ECF Data Analysis Workshop, eds. Grosbol P.J., Murtagh F., Warmels R.H., ESO Munchen, 29
Lazzati D., Campana S., Rosati P., et al., 1999, ApJ 524, 414
Pierre M., Bryan G., Gastaud R., 2000, A&A 356, 403
Raymond J.C., Smith B.W., 1977, ApJS 35, 419
Scharf C.A., Jones L.R., Ebeling H., et al., 1997, ApJ 477, 79
Slezak E., de Laparent V., Bijaoui A., 1993, ApJ 409, 517
Slezak E., Durret F., Gerbal D., 1994, AJ 108, 1996
Starck J.-L., Pierre M., 1998, A&AS 128, 397
Starck J.-L., Murtagh F., Bijaoui A., 1998, Image Processing and Data Analysis: The Multiscale Approach, Cambridge Univ. Press, Cambridge (UK) (MR/1)
Valdes F.G., Campusano L.E., Velasquez J.D., Stetson P.B., PASP 107, 1119 (FOCAS)
Vikhlinin A., Forman W., Jones C., 1997, ApJ 474, L7
Voges W., Aschenbach B., Boller Th., et al., 1999, A&A 349, 389
Watson M.G., Auguères J.-L., Ballet J., et al. 2001, A&A, 365, L51
Zimmermann H.U., Becker W., Belloni T., et al., 1994, EXSAS User's Guide, MPE Report 257 (EXSAS)